

# Development of a Cold Atom Pressure Standard

by

Pinrui Shen

B.Sc., Dalian University of Technology, 2015

M.Sc., Northwestern University, 2016

A THESIS SUBMITTED IN PARTIAL FULFILLMENT OF  
THE REQUIREMENTS FOR THE DEGREE OF

DOCTOR OF PHILOSOPHY

in

The Faculty of Graduate and Postdoctoral Studies

(Physics and Astronomy)

THE UNIVERSITY OF BRITISH COLUMBIA

(Vancouver)

April 2022

© Pinrui Shen 2022

The following individuals certify that they have read, and recommend to the Faculty of Graduate and Postdoctoral Studies for acceptance, the dissertation entitled: **Development of a Cold Atom Pressure Standard** submitted by **Pinrui Shen** in partial fulfilment of the requirements for the degree of **Doctor of Philosophy in Physics**.

**Examining Committee:**

Prof. Kirk W. Madison, Department of Physics and Astronomy, UBC

*Supervisor*

Prof. Valery Milner, Department of Physics and Astronomy, UBC

*Supervisory Committee Member*

Prof. Joshua Alexander Folk, Department of Physics and Astronomy, UBC

*University Examiner*

Prof. Mark Thachuk, Department of Chemistry, UBC

*University Examiner*

**Additional Supervisory Committee Members:**

Prof. Roman Krems, Department of Chemistry, UBC

*Supervisory Committee Member*

Prof. Edward Grant, Department of Chemistry, UBC

*Supervisory Committee Member*

# Abstract

In this thesis, we report the realization of the world's first cold atom based pressure standard for the high- and ultra-high vacuum (UHV) regimes,  $< 10^{-6}$  Pa (1 Pa=1N/m<sup>2</sup>). This standard is a fundamentally new approach to vacuum metrology as it is based on a universal law governing quantum diffractive collisions between particles. We show that a measurement of trap loss rate versus trap depth provides the velocity averaged total collision cross-section,  $\langle\sigma_{\text{tot}}v\rangle$ , - the only parameter required to quantify the pressure of background particles given a measurement of the collision rate with a sensor atom. This new quantum measurement standard is fully empirical, based on unchanging and fundamental atomic constants, and does not rely on computations of total collision cross-sections based on theoretical interaction potentials. We demonstrate, using a sensor ensemble of <sup>87</sup>Rb atoms, that this new quantum pressure standard can be applied to gases of both atomic species (He, Ar, and Xe) and molecular species (N<sub>2</sub>, CO<sub>2</sub>, and H<sub>2</sub>), surpassing the scope of existing orifice flow pressure standards. The accuracy of this new standard was also verified by comparing it with an N<sub>2</sub> calibrated ionization gauge traced back to an orifice flow standard. They agree within 0.5%. A complete uncertainty analysis of this cold atom pressure standard is provided here. Moreover, using this standard, we are able to observe and quantify the performance limits of two industry-standard ionization gauges. Using this universal law, we can precisely measure the total collision cross-section  $\langle\sigma_{\text{tot}}v\rangle$  for the collision system of interest. As an example, we show a precision measurement of  $\langle\sigma_{\text{tot}}v\rangle$  for collisions between Rb and Ar. The experimentally determined value of  $\langle\sigma_{\text{tot}}v\rangle$  agrees with the theoretical computation result within 1.0 %. Next, we demonstrate the use of a magneto-optical trap (MOT) as a transfer pressure standard to extend the operational range of the cold atom pressure standard by a factor of 100, from  $P < 10^{-7}$  Pa to include pressures up to  $P < 10^{-5}$  Pa. Finally, a proposal for using a MOT as a primary pressure standard is presented.

# Lay Summary

*“Imagine measuring a meter with a ruler that has a scale varying from time to time”*

— *Dr. James L. Booth*

Unfortunately, this is the current situation in the everyday use of pressure gauges to measure the pressures in the high vacuum ( $10^{-1}$  to  $10^{-6}$  Pa) and ultra-high vacuum ( $10^{-6}$  to  $10^{-10}$  Pa). This is because existing pressure gauges are subject to uncontrolled calibration drift due to environmental changes, including heat, vibration, gas contamination, and radiation. Luckily, nature provides us with an accurate ‘ruler’ that does not suffer from calibration changes – atoms. We can make the ‘ruler’ even more accurate by cooling the atoms down to near absolute zero. This thesis introduces the ways of using cold atoms as a pressure sensor and shows how we realized the world’s first HV/UHV primary cold atom pressure standard (CAPS).

# Preface

All the work presented in this thesis was conducted on an apparatus in the Quantum Degenerate Gas laboratory at the University of British Columbia, Vancouver campus. I was heavily involved in the work presented in this thesis. The work presented herein that has not been specifically credited to someone else was undertaken by me.

The schematic shown in figure 1.3 is made by Dr. Kirk W. Madison and me. The review of quantum scattering theory in chapter 2 is reorganized and refined based on the notes written by Dr. James L. Booth. Figure 2.1 was modified based on the figure in Dr. James L. Booth's notes.

In Chapter 3, the coil system and the vacuum chamber are designed and initially assembled by Dr. Janelle van Dongen [1]. Figure 3.19 was made by Dr. Janelle van Dongen. I was heavily involved in benchmarking the apparatus and reconstructing the apparatus after several vacuum failures. I was heavily involved in designing and upgrading the laser system to laser cool and trap Rb atoms.

Section 4.1 and 4.2 in Chapter 4 are heavily based on a manuscript that has been published in J.L. Booth et al., *New Journal of Physics*, **21**(10):102001, (2019)[2] on which I am the first co-author. Figure 4.2 is produced by Dr. Roman V. Krems, and figure 4.3 is produced by Dr. James L. Booth. The atom-molecule coupled channel computations were done by Dr. Roman V. Krems, and the atom-atom quantum scattering computations were done by Dr. James L. Booth and me. The theoretical analysis of the quantum diffractive universality in this work was done by Dr. Kirk W. Madison, Dr. James L. Booth, Dr. Roman V. Krems, and me. The data in this work was taken by me and analyzed under the guidance of Dr. Kirk W. Madison and Dr. James L. Booth.

Section 4.2 and 4.4 in Chapter 4 is heavily based on a manuscript that has been published in P. Shen et al., *Metrologia*, **57**(2):025015, (2020) [3] on which I am the first author. The data in this work was taken by me and analyzed under the guidance of Dr.

Kirk W. Madison and Dr. James L. Booth. Section 4.3 in Chapter 4 is heavily based a manuscript that has been published in P. Shen et al., *Metrologia*, **58**(2):022101, (2021) [4] on which I am the first author. The analysis was done by Dr. James L. Booth and me.

The work in Chapter 5 will lead to a future publication. The work of trapping  $^{87}\text{Rb}$  atoms in  $F = 2$  state and the work of accounting for the heating rate were done by Riley Stewart and me under the guidance of Dr. Kirk W. Madison and Dr. James L. Booth. The final uncertainty analysis in Chapter 5 was done by Avinash Deshmukh and me.

Section 6.1 in Chapter 6 is heavily based on a manuscript that has been published in P. Shen et al., *Metrologia*, **57**(2):025015, (2020) [3] on which I am the first author. The excited-state fraction measurement in section 6.2 was done by Riley Stewart and me based on the work in Yue Shen's master thesis [5]. The trap depth control of the MOT and the excited state loss rate measurement were done by me under the guidance of Dr. Kirk W. Madison and Dr. James L. Booth.

In Chapter 8, the explorations of the quantum diffractive universality were done by me with the assistance of Dr. Kirk W. Madison, Dr. James L. Booth, and Riley Stewart. The portable CAPS is mainly designed and assembled by Perrin Waldock with my assistance. Figure 8.4 is made by Perrin Waldock.

Appendix C and B are are heavily based on a manuscript that has been published in J.L. Booth et al., *New Journal of Physics*, **21**(10):102001, (2019)[2]. Appendix B was written by Dr. Roman V. Krems and appendix C was written by Dr. James L. Booth.

# Table of Contents

<b>Abstract</b> . . . . .	iii
<b>Lay Summary</b> . . . . .	iv
<b>Preface</b> . . . . .	v
<b>Table of Contents</b> . . . . .	vii
<b>List of Figures</b> . . . . .	x
<b>List of Tables</b> . . . . .	xiv
<b>List of Abbreviations</b> . . . . .	xviii
<b>Acknowledgements</b> . . . . .	xx
<b>Dedication</b> . . . . .	xxiii
<b>1 Introduction</b> . . . . .	1
1.1 Background . . . . .	1
1.1.1 Pressure Standards . . . . .	1
1.1.2 A New Definition of the Pascal . . . . .	4
1.1.3 Recent Developments in cold atom pressure standard . . . . .	7
1.2 Thesis Overview . . . . .	14
<b>2 Review of Quantum Scattering Theory</b> . . . . .	17
2.1 Hamiltonian of a Two-body System . . . . .	17
2.2 Loss cross section . . . . .	20
2.3 Partial Wave Analysis . . . . .	23
2.3.1 Log-derivative method . . . . .	25

*Table of Contents*

---

2.3.2	Jeffreys-Born approximation . . . . .	27
2.4	Thermally Averaged Collision cross section . . . . .	29
<b>3</b>	<b>Experimental Apparatus . . . . .</b>	<b>33</b>
3.1	Choice of Sensor Atoms . . . . .	33
3.2	Laser System . . . . .	41
3.2.1	Laser units . . . . .	41
3.2.2	Frequency stabilization system . . . . .	42
3.2.3	Power amplification system . . . . .	46
3.2.4	Essential optics and additional lasers . . . . .	49
3.3	Magnetic Field Coils . . . . .	58
3.3.1	2D MOT coils . . . . .	58
3.3.2	3D MOT coil . . . . .	59
3.3.3	Compensation coils . . . . .	61
3.3.4	RF coil . . . . .	63
3.4	Vacuum Chamber . . . . .	67
3.4.1	Source chamber . . . . .	67
3.4.2	Measurement chamber . . . . .	68
3.4.3	Vacuum Baking . . . . .	69
3.5	Control System . . . . .	73
<b>4</b>	<b>Magnetic Trap (MT) Based Cold Atom Pressure Standard (CAPS) . . . . .</b>	<b>75</b>
4.1	Quantum Diffractive Collisions Universality . . . . .	77
4.1.1	Analytical computations . . . . .	77
4.1.2	Numerical computations . . . . .	80
4.2	Experimental Demonstration . . . . .	86
4.2.1	Loss rate measurements . . . . .	87
4.2.2	Trap depth Characterization . . . . .	91
4.2.3	Experiment results . . . . .	94
4.3	Rigorous Universal Fitting . . . . .	105
4.4	Uncertainty Analysis . . . . .	107
4.4.1	Systematic Errors . . . . .	108
4.4.2	Random Errors . . . . .	109

<b>5 Application of QDU: Precision Measurements of <math>\langle\sigma_{\text{tot}}v\rangle</math></b>	111
5.1 Trapping Rb Atoms in F=2 Ground State.	111
5.1.1 Optical pumping	112
5.1.2 Gravitational filtering	114
5.1.3 Two-body elastic collisions	116
5.2 Two-point Decay Rate Measurement	119
5.3 Heating Rate Correction	124
5.4 Experiment Results	128
5.5 Error Analysis	130
<b>6 Magneto Optical Trap (MOT) Based CAPS</b>	133
6.1 The Use of a MOT as a Transfer Standard.	134
6.2 Proposal of Using a MOT as an Absolute Pressure Standard	136
6.2.1 Excited state fraction characterization	137
6.2.2 Control of the trap depth of atoms in the MOT	141
6.2.3 Determination of loss rate coefficient of excited state Rb atoms	148
<b>7 Conclusion</b>	152
<b>8 Future Outlook</b>	156
8.1 Complication	156
8.2 Simplification	161
<b>Bibliography</b>	163
 <b>Appendices</b>	
<b>A Motorized Iris Calibration</b>	178
<b>B Quantum Scattering Calculation</b>	181
<b>C Analytical Derivation of the Universal Form</b>	185
<b>D Scattering Angle</b>	189

# List of Figures

1.1	A schematic of the orifice flow vacuum standard. . . . .	2
1.2	Vacuum 'spectrum' and types of pressure standard . . . . .	4
1.3	A schematic of glancing collisions that happen in a pressure measurement by the CAPS. . . . .	12
2.1	A diagram of the collision process. . . . .	18
2.2	A plot of the total collision cross section, $\sigma_{tot}$ , versus the velocity of the incoming particle, $v$ , in the Rb-Ar system. . . . .	30
3.1	The vapor pressures of Li and Rb at different background temperatures.	34
3.2	Hyperfine energy diagrams for $^{85}\text{Rb}$ ( $I = 5/2$ ) and $^{87}\text{Rb}$ ( $I = 3/2$ ). . . . .	35
3.3	Hyperfine energy diagrams for $^7\text{Li}$ ( $I = 3/2$ ) and $^6\text{Li}$ ( $I = 1$ ). . . . .	36
3.4	Zeeman splitting of the ground state of an Rb or Li atom. . . . .	40
3.5	A photo and schematic of the leading laser unit . . . . .	43
3.6	A diagram of the laser system. . . . .	44
3.7	A plot of laser locking signal. . . . .	46
3.8	A schematic of the following laser setup. . . . .	48
3.9	Hyperfine splitting and Zeeman sublevel energy diagrams for $^{87}\text{Rb}$ ( $I = 3/2$ ). . . . .	51
3.10	A schematic of the lasers going into the 2D and 3D MOT region. . . . .	52
3.11	A detailed schematic showing the inside of the tabletop optics. . . . .	53
3.12	A plot of laser power versus the driving frequency of the AOM. . . . .	54
3.13	A plot of the laser power stability measurement with and without the PID control system. . . . .	55
3.14	A 'catalysis laser' excites the ground state atoms to a repulsive excited molecular potential . . . . .	56

*List of Figures*

---

3.15 Normalized $^{87}\text{Rb}$ atom number versus the MT coil current. . . . .	61
3.16 A diagram of the compensation coil and the RF coil. . . . .	62
3.17 The potential energy of $^{87}\text{Rb}$ atoms moving along the z-axis and in different Zeeman sublevels $ m_F = 0, \pm 1\rangle$ . . . . .	64
3.18 A figure of the overall design of the experiment apparatus. . . . .	66
3.19 A cut view of the differential pumping tube. . . . .	68
3.20 A block diagram of the control system. . . . .	74
4.1 A schematic of a CAPS connected to an orifice flow standard. . . . .	76
4.2 Theoretical demonstration of collision universality. . . . .	82
4.3 A plot of the Lennard-Jones PES for different collision systems. . . . .	84
4.4 Velocity averaged collision loss cross sections versus trap depth for He (red triangles), Ar (black circles), and Xe (blue squares) colliding with Li (dashed lines) and Rb (solid lines). . . . .	85
4.5 A plot of the photodetector reading for the atoms recaptured from the magnetic trap, $V_{\text{MT}}$ , versus the 3D MOT signal, $V_{\text{MOT}}$ . . . . .	88
4.6 The signal of the 3D MOT fluorescence as a function of the experiment time. . . . .	89
4.7 The decay of the MT population with holding time is measured by recording the fluorescence upon MOT recapture of the $^{87}\text{Rb}$ sensor atoms and normalizing it by the fluorescence after a negligibly short hold time. . . . .	91
4.8 Fraction of atoms remaining in a MT (blue dots) as a function of truncation energy, $hf_{\text{RF}}$ , set by an RF pulse that ejects sensor atoms with a magnetic potential energy above this. . . . .	94
4.9 A plot of experimental results. . . . .	96
4.10 A plot of experiment results for all the collision species (He (triangles), Xe (squares), $\text{H}_2$ (stars), $\text{N}_2$ (right triangles), and $\text{CO}_2$ ) . . . . .	97
4.11 A plot of the uncertainty in the determination of $\langle \sigma_{\text{tot}} v \rangle$ as a function of the range of $\frac{U}{U_d}$ accessed for the measurement. . . . .	99
4.12 IG pressure readings as a function of measurement time. . . . .	103
4.13 A plot of $\langle \sigma_{\text{tot}} v \rangle_a$ versus $\langle \sigma_{\text{tot}} v \rangle_b$ measured against the two ionization gauges (IG “a” and IG “b”). . . . .	104

*List of Figures*

---

5.1	Fraction of atoms remaining in a MT as a function of energy, set by an RF pulse that ejects sensor atoms with energy above this. . . . .	113
5.2	Fraction of atoms remaining in a MT as a function of energy after performing a gravitational filter step of various durations. . . . .	115
5.3	Average and minimum energy as a function of the GF times at two different GF coil currents, 15 A and 20 A. . . . .	117
5.4	A plot of recapture fraction as a function of holding time in the MT . . .	119
5.5	Decay rate versus the trap depth at different magnetic field gradients. . .	120
5.6	Relative uncertainty in the decay rate versus the number of runs. . . . .	121
5.7	The log of the recapture fraction versus the holding time when atoms are trapped in $F = 2$ state and the magnetic trapping is current, $I = 200$ A. . . . .	123
5.8	The average temperature of the cloud versus the holding time for atoms trapped in $F = 1$ state at the magnetic trapping current, $I = 60$ A and $I = 200$ A and in $F = 2$ state at the magnetic trapping current, $I = 60$ A and $I = 200$ A. . . . .	126
5.9	Fitted $\langle\sigma_{\text{tot}}v\rangle$ results as a function of the iteration step for atoms trapped in $F = 2$ state. . . . .	128
5.10	Measured $\frac{\langle\sigma_{\text{tot}}v\rangle}{i_g}$ as a function of trap depth for atoms trapped in both $F = 2$ (blue markers) and $F=1$ state (red markers). . . . .	130
6.1	IG readings versus MOT decay rate for Ar gas (pressure up to $6 \times 10^{-7}$ Torr). . . . .	136
6.2	The fluorescence of a MOT (captured by a PD) versus time. . . . .	140
6.3	$G$ values as a function of the pump power for different laser detunings. . .	142
6.4	$G$ value as a function of the pump power at different detunings. . . . .	144
6.5	MOT fluorescence as a function of time. . . . .	146
6.6	Excited state fraction of a MOT at different trap depths, controlled by the repump beam size. . . . .	147
6.7	Ar collisions induced loss rate versus the density of Ar gas. . . . .	149
8.1	Lennard-Jones form PES for Li-He and Rb-He, Ne, Ar, Kr, and Xe collisions systems. . . . .	157

*List of Figures*

---

8.2	Velocity averaged collision loss cross sections versus trap depth for Rb-He (green circles), Ne (black stars), Ar (red diamonds), Kr (yellow right triangles), and Xe (blue up triangles), and Li-He (purple squares). . . .	159
8.3	Averaged deviations from the universal curve as a function of the $Q$ value.	160
8.4	A schematic of the portable CAPS. . . . .	162
A.1	A picture of the motorized iris. . . . .	178
A.2	Calibration results of the motorized iris . . . . .	180
D.1	Newton diagram . . . . .	190

# List of Tables

3.1	Atomic parameters for magnetic trapping. Column 1 lists the atomic species, column 2 provides the hyperfine quantum number of the state, column 3 has the approximate Landé g-factor for this state, column 4 lists the state being trapped, column 5 gives the minimum field gradient to support the atom under gravity (The calculation methods are presented in section 3.3.2 ). Column 6 provides the maximum magnetic field that can support a trapped state, and the values are quoted from [6]. Column 7 provides the maximum Zeeman energy associated with the $B_{\max}$ values. The methods of calculating the maximum magnetic field and the maximum Zeeman energy can be found in section 3.1 . . . . .	39
4.1	The theoretically computed values of the universal coefficients, $\beta$ . We reported $\beta_1$ to $\beta_6$ from the full quantum scattering computations (averaged over Rb-[He,Ar,Xe] and Li-[He, Ar, Xe] collisions). Using the analytical expressions in Eq. 4.7, we only calculated the values of $\beta_1$ and $\beta_2$ (averaged over Rb-[He, Ar, Xe] and Li-[He, Ar, Xe] collisions) [2, 3]. .	80

- 4.2 Values for  $\langle\sigma_{\text{tot}}v\rangle$  and the gauge calibration factor  $i_{ga,exp}$  and  $i_{gb,exp}$  derived from fitting the data shown in Fig. 4.10 to Eq. 4.16, here  $\bar{\sigma} = \langle\sigma_{\text{tot}}v\rangle/v_p$ . The first bracket in the column of  $\langle\sigma_{\text{tot}}v\rangle_a$  indicates the statistical error and the second one indicates the systematic error. The gauge factor,  $i_g$ , for  $\text{N}_2$  (blue) is the value calibrated by NIST’s orifice flow pressure standard with an uncertainty of 2.8%. Here the estimates of gauge correction factor for He, Ar, Xe,  $\text{H}_2$  and  $\text{CO}_2$  in the column of  $i_g$  are provided by MKS Instruments [7] with at least 10% uncertainties according to [8]. The numbers in the column of  $i_{ga}$  and  $i_{gb}$  are the experimentally measured ion gauge “a” and “b” correction factors.  $C_{6,\text{theory}}$  is the theoretical prediction for the  $C_6$  value given by [<sup>1</sup>Derevianko *et al* [9], <sup>2</sup>Thomas *et al* [10], or <sup>3</sup>Arponthip *et al* [11]] in units of  $E_H a_0^6$ , where  $E_H$  is the Hartree energy and  $a_0$  is the Bohr radius.  $\langle\sigma_{\text{tot}}v\rangle_a$  and  $C_{6,\text{exp}}$  are the experimentally measured values using IG “a”. . . . . 101
- 4.3 A comparison of the experimentally determined values of  $\langle\sigma_{\text{tot}}v\rangle$  for Rb-X collisions ( $X = \text{He}, \text{Ar}, \text{Xe}, \text{H}_2, \text{N}_2, \text{and } \text{CO}_2$ ). The values of  $\langle\sigma_{\text{tot}}v\rangle$  in the second column, reported in table 4.2, are extracted by fitting the experimentally determined loss rate coefficients to the approximate expression, Eq. 4.29. The values in the column of  $\langle\sigma_{\text{tot}}v\rangle^*$  are determined by fitting the experimental data to the rigorous expression, Eq. 4.31. The discrepancy between the two values in column 2 and 3 is defined as  $\Delta\langle\sigma_{\text{tot}}v\rangle/\langle\sigma_{\text{tot}}v\rangle^* = (\langle\sigma_{\text{tot}}v\rangle^* - \langle\sigma_{\text{tot}}v\rangle)/\langle\sigma_{\text{tot}}v\rangle^* \times 100\%$  and is presented in column 4. The first bracket in the columns of  $\langle\sigma_{\text{tot}}v\rangle_a$  and  $\langle\sigma_{\text{tot}}v\rangle_a^*$  indicates the statistical error and the second one indicates the systematic error reported in table 4.2. The column of  $U_d$  presents the quantum diffractive energy of each collision pair, derived from the newly determined value of  $\langle\sigma_{\text{tot}}v\rangle^*$ . The last column reports the updated calibration factor,  $i_g$ , for the ionization gauge operated in the experiment, which was previously calibrated against NIST’s orifice flow pressure standard only for the gas of  $\text{N}_2$ . The statistical error of the calibration factor is shown in the bracket. . . . . 107

4.4	Relative uncertainties for the total velocity averaged cross section $\langle\sigma_{\text{tot}}v\rangle$ when the test species is $\text{N}_2$ . The statistical uncertainty results from fitting the data, including variations due to fluctuations in the decay rate measurement 1.8% and fluctuations in the IG “a” readings 0.2% (1.0% for IG “b” readings). Note that the sizes of both the statistical and the systematic errors depend on collision species. . . . .	110
5.1	The fitted values for $\langle\sigma_{\text{tot}}v\rangle$ for collisions between Rb and Ar atoms and the ion gauge calibration factor for Ar gas. The first bracket in the column of $\langle\sigma_{\text{tot}}v\rangle_{\text{Rb-Ar}}^{\text{exp}}$ indicates the total statistical error and the second one indicates the total systematic error. The numbers in the column of $\langle\sigma_{\text{tot}}v\rangle_{\text{Rb-Ar}}^{\text{num}}$ are the numerically computed $\langle\sigma_{\text{tot}}v\rangle$ for Rb-Ar collisions. The long-range coefficient, $C_6 = 336.4\text{E}_h\text{a}_0^6$ , and the depth of the potential, $\epsilon = 38.06\text{cm}^{-1}$ , are quoted from Ref.[12]. <sup>[1]</sup> represents the numerical result using the L-J PES form, while <sup>[2]</sup> represents the numerical result using the modified Morse PES in [12]. . . . .	131
5.2	Relative uncertainties for the total velocity averaged cross section $\langle\sigma_{\text{tot}}v\rangle$ for $^{87}\text{Rb-Ar}$ collisions. The Rb atoms are trapped in $F = 2$ ground state. The statistical uncertainty results from fitting the data which include variations due to fluctuations in the decay rate measurement 1.0% and fluctuations in the IG “a” readings 0.2% (1.0% for IG “b” readings). . .	132
8.1	Column 2 and 3 show the long-range coefficients, $C_6$ , and the depths, $\epsilon$ , of the PES for different collision systems, respectively. The values for Li-He are quoted from ref. [13], while the values for Rb colliding with noble gas species are quoted from ref. [12]. These coefficients are used to perform full quantum scattering computations to calculate $\langle\sigma_{\text{tot}}v\rangle$ are presented in column 4. The $Q$ factors, computed based on Eq. 8.3, are presented in the last column. . . . .	158
A.1	The calibration results of the MI at three different times. The last column shows the factory data. . . . .	179

C.1	The coefficients $\beta_1$ and $\beta_2$ from the full quantum scattering computations averaged over 6 species (see text), based on the analytical expression for the small angle scattering amplitude from Ref. [14] (which predicts that all collision partners will have the same coefficients), and based on the analytical expressions used in this Appendix. The variation arising from the different $C_6$ and masses of the collision partners from this analysis is shown for the different species listed. . . . .	187
C.2	The values of $\xi(n)$ , $c(n)$ , and $d(n)$ as a function of $n$ for potentials of the form, $V(R) = -C_n/R^n$ . . . . .	188

# List of Abbreviations

<b>CAPS</b>	Cold atom pressure standard
<b>QDU</b>	Quantum diffractive universality
<b>MT</b>	Magnetic trap
<b>MOT</b>	Magneto optical trap
<b>XHV</b>	Extreme-high vacuum
<b>UHV</b>	Ultra-high vacuum
<b>HV</b>	High vacuum
<b>OFC</b>	Orifice flow standard
<b>SRG</b>	Spinning-rotary gauge
<b>IG</b>	Ionization gauge
<b>EM</b>	Electromagnetic
<b>FLOC</b>	Fixed-length optical cavity
<b>VLOC</b>	Variable-length optical cavity
<b>F-P</b>	Fabry-Perot
<b>MB</b>	Maxwell Boltzmann
<b>ODT</b>	Optical dipole trap
<b>CoM</b>	Center of mass
<b>J-B</b>	Jeffreys-Born
<b>EOM</b>	Electro-optical modulator
<b>AOM</b>	Acousto-optic modulator
<b>ECDL</b>	Extended-cavity diode laser
<b>SAS</b>	Saturated absorption spectroscopy
<b>PBS</b>	Polarizing beam splitter
<b>PFD</b>	Phase frequency detector
<b>TA</b>	Tapered amplifier
<b>3D</b>	Three dimensional

<b>2D</b>	Two dimensional
<b>HWP</b>	Half waveplate
<b>QWP</b>	Quarter waveplate
<b>GT</b>	Glan-Thompson prism
<b>RCP</b>	Right-hand circular polarization
<b>LCP</b>	Left-hand circular polarization
<b>OP</b>	Optical pump
<b>CAL</b>	'Catalysis' laser
<b>DFB</b>	Distributed feedback
<b>PD</b>	Photodetector
<b>DDS</b>	Direct digital synthesizer
<b>SWC</b>	Six-way cross
<b>IP</b>	Ion pump
<b>PS</b>	Pumping station
<b>RGA</b>	Residual gas analyzer
<b>FPGA</b>	Field-programmable gate array
<b>PC</b>	Personal computer
<b>AO</b>	Analog output
<b>DP</b>	Digital output
<b>ADC</b>	Analog-to-digital converter
<b>TCG</b>	Thermcouple gauge
<b>PES</b>	Potential energy surface
<b>L-J</b>	Lennard-Jones
<b>SNR</b>	Signal-to-noise ratio
<b>ESF</b>	Excited state fraction
<b>MI</b>	Motorized iris

# Acknowledgements

I received so much support throughout this Ph.D. from many people I am immensely grateful to. I first want to thank my supervisor Dr. Kirk Madison who took me in and offered me this opportunity of working on the cold atom sensing project. He is kind, patient, and an inspiring person. I enjoyed very much working with him and learned tremendously through the discussions with him. To this day, I am still surprised by his knowledge of physics and his expertise in electrical engineering. His ability to grasp the essence of a problem and offer valuable thoughts immediately is beneficial to me as an international student who sometimes cannot express myself clearly. This helped me gain confidence and become a better presenter and communicator.

I was also lucky enough to have co-supervisor, Dr. James Booth. My great thanks also go to him. His optimism, enthusiasm, and intuition are very inspiring. Working with him was an enjoyable experience that let me grow as a scientist. Not only did his rich knowledge in collision physics help me make progress in my project, but also his direct involvement in the operation of the apparatus was essential, especially in the beginning. I also want to thank him for his great patience when revising my manuscripts. His feedback has helped me to become a better writer. Finally, I want to thank both Jim and Kirk for their deep caring for my development, both academically and personally, and their willingness to do anything to help me achieve my goals.

Throughout my graduate career, I have also met lots of great researchers. I want to thank Dr. Roman Krems for his theory support to my Ph.D. project and for the valuable discussions with him. I also want to thank Dr. Katrin Dulitz, who is willing to take risks in trusting me with an important laser project in her lab during my exchange time in the University of Freiburg and thank her for the help. Finally, I also thank my committee members, Dr. Valery Milner and Dr. Edward Grant, for their insight over the years.

I was fortunate enough and am grateful to have the apparatus designed and assem-

## *Acknowledgements*

---

bled by Dr. Janelle Van Dongen. Without her efforts, I would need to spend two or more years to achieve the results I have had today. I am also grateful to have some overlapped time with Kais Jooya, who taught me experimental skills and helped me get going on the project.

During my time in the lab, I worked with many great colleagues along the way. Yue Shen who joined the lab at the same time as me, helped me make progress in using a MOT based pressure standard. I also had the great pleasure of having her as a friend in the lab. I have had the opportunity to work with Perrin Waldock for over two years closely. His talent in engineering and programming was beneficial to me, especially when I was trying to upgrade the control system of the apparatus. I want to thank him for that. I really hope that his portable pressure standard will be finished very soon and have an excellent performance. I also enjoyed valuable and interesting discussions with Erik Freiling and Denis Uhland who work on the MOL experiment. Their expertise in ultra-cold atoms/molecules has inspired me to think deeper into the application of cold atoms and provided me with useful insights into approaching physics problems I encountered.

I am also excited for the next generation of Madison group students. Riley Stewart took over the MAT apparatus when I was still in the lab. I was thrilled to witness how he had upgraded the apparatus and became an experienced researcher. His talent and research progress often inspired and helped me solve my experiment's problems. I enjoyed very much working with him and the way we iterated the new ideas with each other until they became feasible. I know he will have a bright future when he joins the MOL apparatus in the future. During the last time of my graduate study, I enjoyed working with Avinash Deshmukh, a new addition to the lab. I can imagine his talent in theory and mathematics will help him thrive and benefit the whole lab.

Equally important was the support I received outside of work. I am thankful to have made many great friends in Vancouver, Ruoxi, Shuailiang, Yue, and Ruoyu, etc. I have no idea how such a diverse group of personalities ended up spending so much time together, but these individuals provided me with great memories.

I lastly want to thank my family members. My fiancée Yifan who is also my best friend had spent many important life moments with me. I thank her for her accompany in my graduate study, especially the “dark” times during the pandemic. My final

## *Acknowledgements*

---

gratitude goes to my parents Lihua and Bibo who worked so hard to provide me with every possible advantage. Their unconditional love and support were with me every step of the way. Without your support, I could not finish my Ph.D. study.

# Dedication

獻給我的父母沈碧波先生和鄧麗華女士。

To my parents Mr. Bibo Shen and Mrs. Lihua Feng.

# Chapter 1

## Introduction

### 1.1 Background

#### 1.1.1 Pressure Standards

Detection and measurement of pressures have been of great importance to civilization, beginning with the invention of the barometer (manometer) by Torricelli circa in 1643, which also provided the first measurement of pressure [15]. Traditionally, pressure is defined as force,  $F$ , per unit area  $A$ ,

$$P = \frac{F}{A}, \quad (1.1)$$

where the SI unit of pressure is the pascal ( $1 \text{ Pa} = 1 \text{ N/m}^2$ ). In the area of structural engineering, where force is the primary concern, this is a good definition of pressure. One of the most accurate primary pressure standards is the piston gauge which measures the pressure by comparing the force generated by the test pressure with the weight of a calibrated mass object applied on a known area,  $A_0$ ,  $P_{\text{test}} = mg/A_0$ . The operating range of the piston gauge is from a few hundred megapascals (MPa) down to hundreds of pascals [16, 17]. With the help of mercury-based U-tube manometers [18], this calibration can be extended to lower pressures below 1 Pa. When using the mercury-based U-tube manometer, a test pressure,  $P_{\text{test}}$  is applied on one side of the U-tube, while the other side is evacuated to a pressure,  $P_0 \ll P_{\text{test}}$ . Therefore the test pressure is determined by the difference  $\Delta h$  of the mercury columns in the two tubes with respect to a horizontal plane,  $P_{\text{test}} = \rho g \Delta h$ , where  $\rho$  is the mass density of the Mercury. This method has been incrementally refined and improved for centuries, and it can measure pressures down to 1.0 Pa with an uncertainty on the level of a few parts in  $10^6$  [19].

As the pressure goes even lower to the high vacuum (HV) regime ( $10^{-1}$  to  $10^{-6}$  Pa), the static expansion vacuum standard [20] can be used to create a known pressure of

certain gas species. In the static expansion standard, a gas is introduced at pressure  $P_1$  to a chamber with a known volume,  $V_1$ . The pressure  $P_1$  is high enough to be accurately measured with a gauge calibrated by a mercury manometer. The gas is then expanded into a total volume of  $V = V_1 + V_2$ , so that  $P_1V_1 = P_2(V_1 + V_2)$  where  $P_2$  is the pressure after expansion. Given that  $V_1$ ,  $V_2$ , and  $P_1$  are known accurately, then  $P_2$  can be determined. A pressure gauge such as the spinning-rotary gauge (SRG) can be connected to the total volume so that it can be calibrated.

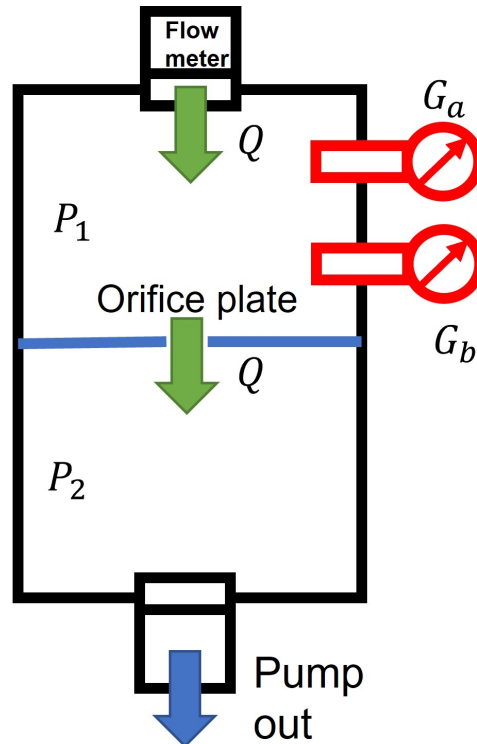


Figure 1.1: A schematic of the orifice flow vacuum standard. Two chambers are separated by an orifice of known conductance  $C$ . The flow rate is  $Q = C(P_1 - P_2)$ , which is the same as the flow rate input to the upper chamber. Given the equal flow rate, the pressure in the upper chamber is stable at  $P_1$  (outgassing is negligible). Two gauges are connected to the upper chamber. Gauge A ( $G_a$ ) is calibrated on another higher pressure range standard. Gauge B ( $G_b$ ) is the gauge that is to be calibrated by the orifice flow standard. The flow rate  $Q$  is measured with a flowmeter. The ratio,  $r = P_1/P_2$ , is determined by sending a large enough flow through the system so that gauge a can measure  $P_1$ . Then, the flow is reduced so that the upper pressure is brought down to a pressure  $P_1$  at which one wishes to calibrate gauge b. The ratio  $r$  is constant within the molecular flow regime so that the pressure  $P_1$  in the upper chamber can be determined using  $P_1 = \frac{Q}{C(1-r)}$ , thus gauge b is calibrated.

Finally, for the pressure measurements in the ultra-high vacuum (UHV) regime

( $10^{-6}$  to  $10^{-10}$  Pa), the orifice flow vacuum standard (also known as dynamic expansion vacuum standard) is used [21, 22]. A typical setup of the orifice flow method is shown in figure 1.1. Two vacuum chambers are separated by a plate in which has a carefully machined orifice connecting the chambers. A steady gas flow is fed into the upper chamber and pumped out at the lower chamber. In equilibrium, the volume flow rate of gas through the orifice plate,  $Q$ , is the same as the flow fed into the upper chamber, which is measured by the flowmeter. Given the equal flow rate, the pressure in the upper chamber is stable at  $P_1$  (outgassing is negligible). Initially, the pressure in the upper chamber is kept high so that it can be measured by a pressure gauge  $G_a$  that has been calibrated against another pressure standard that can operate in the higher pressure range. Through the orifice plate, the flow rate to the lower chamber can be expressed as,

$$Q = C(P_1 - P_2), \quad (1.2)$$

where  $C$  is the conductance provided by the orifice that can be independently measured or calculated [23]. Therefore, the pressure in the lower chamber can be obtained as  $P_2 = P_1 - Q/C$ . Then the flow is reduced so that the pressure in the upper chamber  $P_1$  is below the measuring range of the calibrated gauge  $G_a$ . However, in the molecular flow regime (where the gas atoms or molecules hit the walls before hitting each other) the ratio of the lower chamber pressure  $P_2$  to the upper chamber pressure  $P_1$  is a constant at different flow rates,  $r = P_2/P_1$ . Then the new upper pressure  $P_1$  can be determined using Eq. 1.2 with controlled the flow rate  $Q$ , the measured ratio  $r$ , and the known conductance  $C$ . Thus, the attached uncalibrated pressure gauge  $G_b$  (usually the ion gauge) can be calibrated [24]. Ar and N<sub>2</sub> gas are typically used in this orifice flow pressure standard since they are inert. By contrast, the ‘sticky’ or reactive gases are not favored in this system since they can be stuck to or react with the chamber walls which makes the gas flow rate through the orifice different from the flow rate into the system.

### 1.1.2 A New Definition of the Pascal

As one can see, the pressure calibrations in the HV/UHV regime are traceable to the mercury-based pressure standard that relies on the definition of the pressure in Eq. 1.1. However, Eq. 1.1 is not a practical definition for vacuum measurements since the forces exerted are exceedingly small. On the contrary, the number density of gas molecules in the vacuum would be a better definition [25], where ideal gas law can be applied. This also follows the recent changes for the SI units. In 2018, the base SI units were redefined based on atomic properties accessed via quantum measurements [26, 27, 28]. Relevant to our work, the Kelvin has been newly defined by the amount of energy  $k_B T$  [29, 30], where  $k_B$  is the Boltzmann constant whose value has been fixed in the new definitions of the SI units. This makes the ideal gas law,  $P = nk_B T$ , a more attractive, alternative, route for National Metrology Institutes to realize the pressure unit by measuring gas density. This redefines Pascal with measurements at the microscope level. The development of the new pressure standards, in particular, aligns with the scope of the new SI definitions: *The new definitions do not prescribe particular realization methods and hence will allow the development of new and more accurate measurement techniques*[26].

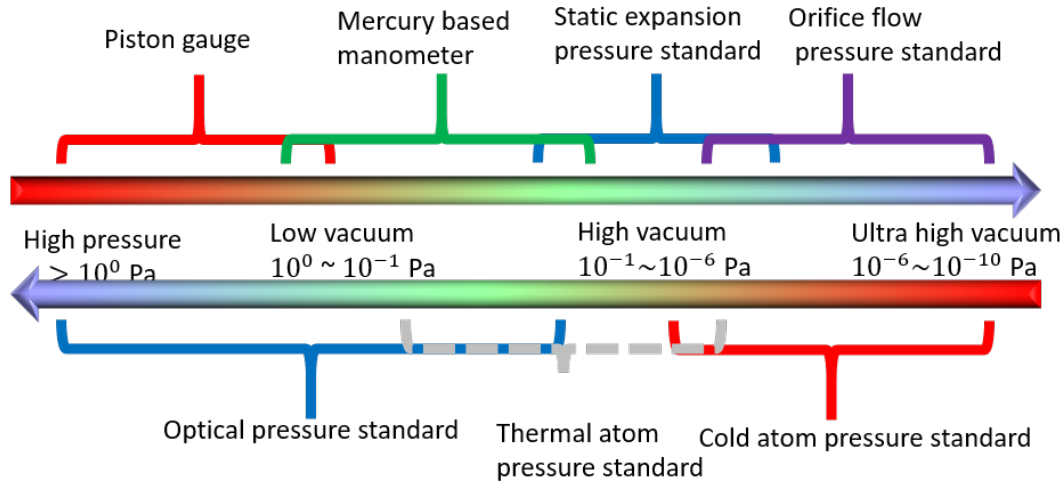


Figure 1.2: The vacuum ‘spectrum’ shows the current/potential pressure standards with their operating ranges. The top part of the plot shows the traditional pressure standards based on the definition of the pascal (force per area) in Eq.1.1. The bottom plot shows the new types of pressure standards that offer the possibility of using a thermodynamic definition—specifically the ideal gas law to realize the pressure unit.

The recent developments in laser technologies provide us with the methods of directly measuring the gas density. When electromagnetic (EM) waves (e.g., laser beams) travel

through a gaseous medium, they interact with the electrons and to a lesser extent with the nuclei of the molecules in that medium. Depending on the frequency of the EM wave, either absorption or dispersion occurs. In the case of dispersion, the frequency is far from resonance, the EM wave polarizes the molecules with the net effect of reducing the EM wave speed  $c$  and altering the wavelength  $\lambda$ . The reduction depends on the frequency  $\nu$  of the EM wave and is described by the refractive index  $R(\nu)$ :

$$c = \frac{c_0}{R(\nu)}, \quad (1.3)$$

where  $c_0$  is the speed of light in an ideal vacuum. The relation of the gas density  $n$  to the refractive index  $R$  can be obtained by the Lorentz-Lorenz equation [31],  $R = \frac{\alpha}{2\epsilon_0}n + 1$ . Here,  $\alpha$  is the dynamic polarizability of the gas species, can be calculated, and  $\epsilon_0 = 8.854187 \times 10^{-12}\text{F/m}$  is the vacuum permittivity. Therefore, Eq. 1.3 provides a way of measuring the density of gas particles by measuring the ratio of the speed of light in a vacuum divided by the speed of light in the gas. This principle is the basis of new types of pressure standards, such as the FLOC (the fixed-length optical cavity) based pressure standard [32, 33, 34, 35]. This optical pressure standard uses a gas-filled fixed-length Fabry-Perot (F-P) cavity. A laser can be servo-locked in resonance with this F-P cavity, and the frequency  $f$  of the laser is given approximately by

$$f = \frac{mc_0}{2RL}, \quad (1.4)$$

where  $m$  is the integer number of wavelengths in the cavity, and  $L$  is the length of the cavity. Therefore, if the gas density inside the cavity changes, causing  $R$  to change, the servo adjusts  $f$  to maintain resonance with the cavity. Hence frequency changes track changes in the refractive index, which reflects the gas density changes. One can also fix the laser frequency, then the length of the cavity can be tracked as the gas density changes. This is the principle of a variable-length optical cavity (VLOC) based pressure standard [36]. These pressure standards relying on measuring the refractive of the gas have a very broad range of operation from less than one pascal to 3 MPa.

Another type of optical pressure standard can be built based on the absorption of EM waves through the gas medium. In this case, the frequency  $\nu$  of the EM wave is in resonance with one of the allowed molecule quantum state transitions of the gas

molecules in the medium through which the EM wave is traveling. The relationship between the EM wave frequency,  $\nu$ , and the energy of the two quantum levels involved in the transition,  $E_1$  and  $E_2$ , is,

$$h\nu = E_2 - E_1, \quad (1.5)$$

where  $E_1$  and  $E_2$  are the energies associated with the quantum states  $|1\rangle$  and  $|2\rangle$  coupled by the EM wave. Absorption happens when the molecule absorbs the photon with energy  $h\nu$  and transfers it from the state  $|1\rangle$  to the state  $|2\rangle$ . Due to the absorption of the molecules, the laser power will drop after transmitting through the molecule gas region. For a dilute medium, the reduction in the intensity,  $\Delta I$ , can be expressed as,

$$\Delta I = -k(\nu)I_0\Delta z, \quad (1.6)$$

where  $k(\nu)$  is the absorption coefficient describing the reduction of the power, which is proportional to the molecule gas density.  $I_0$  in Eq. 1.6 is the initial intensity of the laser, and  $\Delta z$  is the distance the laser beam has traversed.

Therefore, one can measure the drop of the laser intensity after transmitting through a glass cell filled with the gas to infer the gas density. Based on this method, people have developed the laser absorption spectroscopy-based pressure standard [37, 38, 39]. Furthermore, the multi-pass glass configuration [37], the cavity ring-down spectroscopy method [39] and the saturated absorption method [40] can be used to increase the interaction time between the laser and the gas particles. This helps this laser absorption spectroscopy-based pressure standard measure the pressure from about 10 Pa to 1 kPa.

So far, these optical pressure standards can only measure the pressure as low as 1 Pa. As the pressure goes even lower, especially in the HV/UHV regime, optical pressure standards won't work due to the low gas density being unable to produce a measurable dispersion or absorption of the laser beams. Therefore, creating a new pressure standard based on the ideal gas law that can operate in the HV and UHV, even the XHV regime, is required and urgent. It will also be a boon to fundamental scientific research, to commercial fabrication technologies such as those used for modern semiconductor devices [41, 42, 43], and to the study of dynamics and processes of the upper atmosphere, with practical consequences for satellite technology [44, 45, 46]. Fortunately,

the recent development of cold atom technology and the study of the collisions between cold atoms and the background particles have provided us with a solution-cold atom pressure standard (CAPS).

### 1.1.3 Recent Developments in cold atom pressure standard

In 1985, Migdall et al. [47] first reported the magnetic trapping of Na atoms and discovered that the lifetime of the Na atoms held in the trap was limited by the collisions between the trapped atoms and the background gas particles in the vacuum environment. Later, Bjorkholm [48] theoretically modeled the lifetime of the trapped particles and showed that the loss rate (the lifetime is the inverse of this) is linearly proportional to the density of the background particles for a general interaction potential,  $V(r) = -C_n/r^n$ . Taking the long-range part of the Van der waals interactions ( $n = 6$ ), he derived an approximated expression for the loss rate of trapped atoms  $\Gamma$ ,

$$\Gamma_{\text{loss}} = 5.376 \left( \frac{C_6}{U} \right)^{\frac{1}{3}} \bar{v} n, \quad (1.7)$$

where  $U$  is the trap depth, and  $\bar{v}$  is the most probable speed of the background particles. This expression nicely predicted the measured loss rates in some of the cold atom experiments [49, 50, 51, 52]; however, it fails in the limit of small trap depth because it is a purely classical result.

The coefficient  $5.376 \left( \frac{C_6}{U} \right)^{\frac{1}{3}}$  in Eq. 1.7 can be viewed as the averaged collision loss cross-section between the trapped atoms and the background particles,  $\bar{\sigma}_{\text{loss}}(U)$ , at a given trap depth. Most importantly, the approximated expression in Bjorkholm's work [48] captured the feature that the loss rate coefficient decreases as the depth of the trap increases. This was supported by some later cold atom loss rate measurements at large trap depths ( $\sim 1$  K) [53, 54]. They showed that the measured loss rates are radically different at different trap depths set by various trapping parameters. This is because the retention of the trapped atoms caused by small-angle elastic collisions is significant at large trap depths. These small angle elastic collisions are called quantum diffractive collisions since they reveal the wave nature of the collisions in a manner that is similar to light diffracting through an aperture which is small compared to its wavelength. These quantum diffractive collisions impart a very small amount of momentum to the trapped

atoms, which results in ensemble heating instead of trap losses at large trap depths. Therefore, the loss rate measured at large trap depths is smaller than it measured at shallower trap depths. Later, the relationship between the loss rate coefficient  $\sigma_{\text{loss}}v$  and the trap depth  $U$  was more carefully studied by Bali et al. and Beijerinck et al. [10, 55, 56]. They started by computing the scattering amplitude based on the Jeffreys-Born approximation and the long-range part of the interaction potential (the details of the Jeffreys-Born approximation can be found in section 2.3.2). Then, they computed analytically the total collision cross section,  $\sigma_{\text{tot}}$  by integrating the scattering amplitude over all the scattering angles,  $\sigma_{\text{tot}} = 8.482 \left( \frac{C_6}{\hbar v} \right)^{\frac{2}{5}}$ . Similarly, the collision loss cross section can be obtained by only integrating the scattering amplitude from the minimum scattering angle  $\theta_{\text{min}}$  to  $\pi$ . Based on this, the loss cross section,  $\sigma_{\text{loss}}$ , can be expressed in terms of the total cross section  $\sigma_{\text{tot}}$  and the minimum scattering angle  $\theta_{\text{min}}$ ,

$$\sigma_{\text{loss}} = \sigma_{\text{tot}} \left( 1 - 0.37 \frac{U}{U'_d} \right), \quad (1.8)$$

where

$$\begin{aligned} U &= \frac{(1 - \cos \theta_{\text{min}}) \mu^2 v^2}{m} \\ U'_d &= \frac{4\pi \hbar^2}{M \sigma_{\text{tot}}}. \end{aligned} \quad (1.9)$$

Here, the trap depth  $U$  is a function of the minimum scattering angle (details can be found in appendix D),  $M$  is the mass of the trapped particle,  $m$  is the mass of the background particle, and  $\mu$  is the reduced mass of the collision system. Finally, the decay rate of the atoms can be expressed as,

$$\Gamma_{\text{loss}} = \sigma_{\text{loss}} \bar{v} n = 8.482 \left( \frac{C_6}{\hbar \bar{v}} \right)^{\frac{2}{5}} \left( 1 - 0.37 \frac{U}{U'_d} \right) \bar{v} n. \quad (1.10)$$

This expression was not investigated experimentally until 2009 by Fagnan et al. [57]. They experimentally characterized the change of the loss rate coefficient across a wide range of the trap depths. The factor,  $\sigma_{\text{loss}} \bar{v}$ , in Eq. 1.10 is usually referred as the loss rate coefficient. However, more precisely, the loss rate coefficient should be defined as the

collision cross-section averaged over the Maxwell Boltzmann (MB) velocity distribution,  $\langle\sigma v\rangle$ . The ' $\langle\rangle$ ' denotes that this quantity is averaged over the MB velocity distribution of the background particles impinging on the trapped atoms. This is an important correction to the expression of the loss rate coefficient and was reported in later work [57].

From the preceding, we can see the importance of trap depth and of knowing the expression of the loss rate coefficient as a function of trap depth. If both the trap depth and the loss rate coefficient at that trap depth are known, this offers a way of measuring the background gas density from a measurement of the loss rate. **This is the idea of the cold atom pressure standard and was first proposed by Madison et al. in 2011 [58].** Key to this application is knowing the value of the loss rate coefficient at a certain trap depth. One approach is to use a quantum scattering calculation to determine the loss rate coefficient (thermally averaged collision cross-section) using an *ab initio* computed potential energy surface between the trapped particle and the collision partner.

This method was later adopted by national metrologia groups and reported in ref. [6, 59, 60]. They have calculated the loss rate coefficients for Li-He and Li-H<sub>2</sub> as reported by [61, 13]. The plan is to use the Li-H<sub>2</sub> calculation and loss rate measurements to determine the loss rate coefficients for other collision partners using a ratio-metric technique (details can be found in chapter 4 of this thesis). This determination will involve the use of an orifice flow pressure standard as described in [6].

In 2019, a novel approach for determining the loss rate coefficient was proposed by Booth et al.[2]. Rather than computing it from an *ab initio* computed potential, this new method relies on an experimental measurement to determine the loss rate coefficient. This is the revolutionary characteristic of our pressure standard. The details of this quantum based pressure standard, and its realization are the main topics of this thesis. For the range of trap depths achievable with a magnetic trap, collisions that do not eject atoms out of the trap are quantum diffractive collisions. It is well known that the cross-sections of the quantum diffractive collisions are dominated by the long-range part of the interaction potential and have been studied by [14, 62].

Booth et al. have found that the loss rate of cold atoms in a shallow trap follows a universal scaling law whose characteristic energy is set by the total collision cross

section as dictated by the Heisenberg uncertainty principle [2, 3], namely,

$$\begin{aligned}\Gamma_{\text{loss}} &= n \langle \sigma_{\text{loss}}(U) v \rangle \\ &= n \langle \sigma_{\text{tot}} v \rangle \left[ 1 - \sum_j \beta_j \left( \frac{U}{U_d} \right)^j \right].\end{aligned}\quad (1.11)$$

Here,  $\beta_j$  in Eq. 1.11 are the universal coefficients, and  $U_d = \frac{4\pi\hbar^2}{M\bar{\sigma}}$ , where  $\bar{\sigma} = \langle \sigma_{\text{tot}} v \rangle / \bar{v}$  is a thermally averaged total collision cross-section. This is different from the previous definition by Bali et al. and Beijerinck et al since the cross-section is averaged over the velocity distribution of the particles impinging on the trapped atoms. In addition, in contrast with the approximate Eq. 1.10, we used full quantum scattering computations to calculate the values of total and loss collision cross sections and then numerically determined the relationship between the total collision cross section and the loss collision cross section.

A conceptual illustration of this process is shown in figure 1.3. Initially, the cold trapped sensor atom has a small momentum uncertainty and a correspondingly large position uncertainty. When a background particle passes near enough to the trapped sensor atom that a collision occurs, the sensor atom's position becomes localized to a spatial region with characteristic length  $\sqrt{\sigma}$ . Because of complementarity, this collision-induced spatial localization leads to a new momentum uncertainty with a characteristic width  $\hbar/m\sqrt{\sigma}$ . This position-measurement-induced momentum kick is the most gentle momentum exchange allowed by quantum mechanics, and it encodes empirical information about the total cross section due to the uncertainty principle. Collisions that transfer momenta on this small localization scale are referred to as quantum diffractive collisions and are mediated by the long range tail of the interaction potential between the sensor atom and the incident particle.

When the trap depth is sufficiently shallow, the momentum gained through a quantum diffractive collision can eject the sensor atom out of the trap. Therefore, one can measure the trap loss rate as a function of the trap depth at exceedingly low depths to discover the spectrum of the momentum transfer for quantum diffractive collisions. The width of this momentum distribution is related to the spatial localization region,  $\sigma_{\text{tot}}$ , through the uncertainty principle, while the shape of the distribution encodes the

underlying physical process that led to the localization, the interaction potential between the trapped sensor atom and the background particle. This is the key idea to discovering  $\sigma_{tot}$  by measuring the post-collision momentum distribution.

For combinations of incident particle and sensor particle with large polarizability, the Van der Waals interactions (induced dipole-dipole interactions) will dominate, and the long-range interaction,  $C_6/r_6$ , will determine the collision-induced localization process. In this case, the resulting shape of the post-collision momentum distribution will be dictated by the  $C_6$  interaction potential. Specifically, if the measured post-collision energy distribution is scaled by the quantum diffractive energy ( $U_d$  in equation 1.11), the scaled distribution will follow the universal law characteristic of  $C_6$  interactions. Knowing that the collision partners have a long range  $C_6$  interaction allows the discovery of this scale factor and thus the total cross section by finding the scale factor that matches the scaled measured loss rate to the universal function. In the case where the polarizability of the species combination is small, the  $C_6$  interaction may not dominate the interactions, and the resulting loss rate versus trap depth may deviate from the  $C_6$  universal shape. However, most species of interest should have sizable polarizability, thus most should follow the  $C_6$  universality.

To use this universal law in the CAPS, one needs to create a shallow trap with a variable depth. A magnetic trap is an effective platform for performing these universality based pressure measurements, which leads to the MT-based CAPS. Once the cross section has been determined, any trap can be used to perform a pressure measurement. An optical dipole trap (ODT) based CAPS has also been demonstrated by Makhlov et al. in [63, 64]. They performed pressure measurements using  $^6\text{Li}$  atoms confined in a far-detuned optical dipole trap. However, the systematic errors in the pressure measurements introduced by the sensor atom's interactions with the trapping laser have not yet been quantified. It is known that sensor ensemble heating can occur in an optical dipole trap, and this can, in turn, change the effective trap depth and the resulting loss rate. Heating can occur from photon scattering or beam intensity or direction fluctuations that lead to parametric heating of the trapped atoms [65]. Careful precautions can be taken to eliminate those effects, but the requirement of high-power trapping laser can make it more expensive to build than a MT-based CAPS where the MT can be created using the MOT coils.

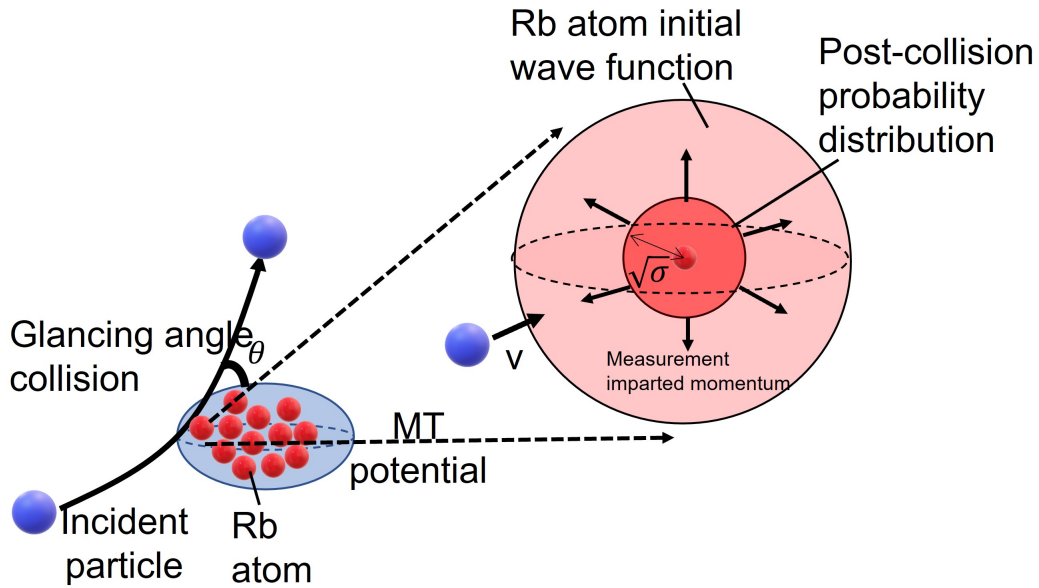


Figure 1.3: A schematic of glancing collisions that happen in a pressure measurement by the CAPS. An incident particle with velocity,  $v$ , collides with a trapped atom with a total collision cross section,  $\sigma$ . The collision localizes the sensor atom's position to a region of characteristic size  $\sqrt{\sigma}$ . Complementarity implies that this position localization leads to a broadening of the momentum distribution. This post-collision momentum distribution broadening encodes information about the collision cross section  $\sigma$ .

In addition to the MT and the ODT-based CAPS, researchers have also demonstrated pressure measurements using atoms trapped in a magneto-optical trap (MOT) [66, 67, 68, 69]. However, the accuracy is limited for pressure measurements in a MOT based CAPS. This is because using a magneto-optic trap to confine sensor particles is more complicated than using a purely magnetic trap, as the MOT introduces several factors that confound the pressure measurement. First, there are rapid two-body loss channels for atoms in a MOT that are absent for atoms in a magnetic trap, including fine structure changing collisions and light-assisted losses (radiation escape mechanisms) as shown by [53, 70, 54]. Second, the trap depth of the MOT is challenging to determine and to hold constant as it is sensitive to slight misalignments of the MOT laser beams. This confounds the determination of background pressure from sensor particle loss rate since the loss rate is trap-depth dependent. Nevertheless, [71, 72, 66] have demonstrated the use of light-assisted collisional loss to measure the trap depth of a MOT. Third, the determination of pressure from sensor particle loss rate from a MOT is further confounded by the fact that the trapping mechanism of the MOT forces

the sensor particles to move between different quantum states (the ground and excited electronic states), and these states have different collision cross-sections with the background particles being measured. In this case, knowledge of the cross sections and the occupation of the various quantum states is essential for an accurate determination of pressure from the loss rate. Methods of determining the excited-state fraction have been demonstrated in [73, 74, 75, 76].

Although using a MOT to perform accurate pressure measurements seems challenging, the MOT provides important advantages over other traps. Due to its large trap depth ( $\sim 1$  K), the loss rate from a MOT can be significantly lower than that from a magnetic or far-detuned optical dipole trap (depth  $< 10$  mK), and this can allow measurements at much higher pressures. For example, we have demonstrated accurate pressure measurements up to  $10^{-4}$  Pa, two orders of magnitude higher than that achieved with a magnetic trap, using a MOT as a transfer pressure standard calibrated by a magnetic trap [3]. An alternative method of using a MOT as a primary pressure standard is presented at the end of this thesis.

The operating ranges of the optical pressure standards ( $< 1$  Pa) and the cold atom pressure standards ( $< 10^{-4}$  Pa) are summarized at the bottom of figure 1.2. There appears to be a gap in the vacuum 'spectrum' in which neither the optical pressure standards nor the cold atom pressure standards can operate. However, an atom-based pressure standard operating at room-temperature could potentially fill the gap. This atom-based pressure standard could use the phenomena of photon echoes to measure collisions with the background vapor and thus determine the pressure. When an ensemble of atoms is prepared in a linear superposition of two electronic ground state energy levels by a  $\pi/2$  radiation pulse, this coherence can persist for some time. If the superposition includes states in the electronic excited state, the coherence can relax due to spontaneous emission. The atom coherence will dephase due to the different velocities within the ensemble (Doppler shifts). If, after a fixed waiting time  $T$ , another  $\pi$  pulse is applied to completely reverse the coherence phase, this dephasing process becomes a rephasing process, and the atomic coherence will revive at a time  $T$  after the  $\pi$  pulse when the atoms are in phase again. Thus the "echo" of the atomic coherence occurs at  $t = 2T$ .

However, if there are background collisions in the dephasing and rephasing process,

the velocity of those atoms are changed and thus they do not contribute to the "echo" at  $t = 2T$ . This leads to a drop in the echo signal. Therefore, by measuring the echo amplitude as a function of the waiting time, one can determine the background collision rate, thus, the gas density. The same collision theory involving the cold atoms can also be applied here, and the measured loss rate coefficients with the CAPS.

Researchers have demonstrated the feasibility of measuring background collisions using atomic coherence, for example references [77, 78, 79] report the collision cross section between the coherence atoms and the background particles using the photon-echo techniques. Early results have also shown that using the photon echo method can measure the pressure from 1 Pa to  $10^{-2}$  Pa [78, 80]. The hope is that this photon-echo method could measure the pressures as low as  $10^{-4}$  Pa with improved techniques such as the grating stimulated echo method [81, 82]. With all these new types of density-based pressure measurements, one can hope a new definition of Pascal using the ideal gas law is possible at all pressures.

## 1.2 Thesis Overview

This thesis presents the work of realizing the world's first cold atom pressure standard. This is a primary pressure standard since it operates based on the immutable, universal, and fundamental constant- total collision cross section  $\langle\sigma_{\text{tot}}v\rangle$ . It does not rely on any calibrations against other standards, which separates it from the transfer standard or the pressure gauges. Moreover, relying on the fundamental quantity  $\langle\sigma_{\text{tot}}v\rangle$  makes it superior to other, traditional pressure standards since the traditional pressure standards rely on the human fabricated parts. For example, the orifice flow standard is based upon machining an orifice plate with a precisely known conductance, which is reliable solely for inert gas flows, limiting its range of applications. The static expansion standard requires knowing the volume of the expansion chamber. Neither of these is based on fundamental, immutable physical constants. By contrast, the CAPS, based on a single fundamental, immutable,  $\langle\sigma_{\text{tot}}v\rangle$ , is applicable to a wide range of binary collision partners, revolutionizes and modernizes the definition of pressure, in accordance with the new SI mandates.

The MT-based CAPS is realized based on the universal behavior of the quantum

diffractive collisions. In summary, the trap loss rate of atoms from shallow traps as a function of the trap depth, is dictated by the momentum distribution of the trapped atoms which were subjected to quantum diffractive collisions. This distribution is dominated by the long-range part of the interaction potential and defined by a single parameter,  $\langle\sigma_{\text{tot}}v\rangle$ . The measured loss rate is described for all collision partners through, Eq. 1.11. Thus, by measuring the loss rate of the cold atoms  $\Gamma_{\text{loss}}$  as a function of the trap depth  $U$ , one may fit these data to Eq. 1.11 to extract  $\langle\sigma_{\text{tot}}v\rangle$ . Once  $\langle\sigma_{\text{tot}}v\rangle$  is determined for a collision pair, the pressure in the vacuum system can be determined from the ideal gas law and the decay rate of the cold atoms.

Chapter 2 reviews the quantum scattering theory and explains the physics of the quantum diffractive collisions. The Jeffreys-Born long-range approximation of collision cross section introduced in Chapter 2 also implies the universal behavior of the quantum diffractive collisions. Chapter 2 also states the correct expression of the loss rate coefficient is to integrate the collision cross over the Maxwell-Boltzmann velocity distribution.

Chapter 3 firstly explains the reason for choosing Rb as a sensor atom in the MT-based CAPS since it can allow us to map out a wider range of the post-collision momentum distribution, which leads to a more accurate determination of  $\langle\sigma_{\text{tot}}v\rangle$ . Then it discusses the details of building a MT-based CAPS, which involves the laser system used to cool and capture Rb atoms, the magnetic coil system to provide the trapping field, the vacuum chamber design to house the cold atoms, and the control system to program the experiment procedure.

Chapter 4 presents the work of predicting the universal behavior of the quantum diffractive collisions both analytically and numerically. Later this universal behavior is verified experimentally by measuring the trap loss as a function of trap depth, which is equivalent to mapping out the post-collision momentum distribution. We have found the measured pressure using this method with the CAPS agrees with the measurement using the NIST calibrated ion gauge (IG) within 0.5% for a gas of  $\text{N}_2$ . This method is then generalized to measure the values of  $\langle\sigma_{\text{tot}}v\rangle$  between Rb atoms and other test gas species  $x$  ( $x=\text{He}, \text{Ar}, \text{Xe}, \text{H}_2$ , and  $\text{CO}_2$ ). These results are presented in Chapter 4. Finally, all these measurements are reported with quantifiable statistical and systematic uncertainties.

Chapter 5 introduces the precision measurement of  $\langle\sigma_{\text{tot}}v\rangle$  using the MT-based CAPS and the universal behavior of the quantum diffractive collisions. The details of improving the precision have been thoroughly discussed. One direction is to reduce the systematic uncertainty, we have achieved this by eliminating the two-body loss process in the MT. The other direction is to reduce the statistical uncertainty, which has been done by reducing the shot-to-shot noise and reducing the fitting uncertainty. The latter is achieved by increasing the trap depth range of the confined atoms, facilitating higher precision determination of  $\langle\sigma_{\text{tot}}v\rangle$  from the experimental data. The increase in trap depth was achieved by trapping the Rubidium atoms in their  $|F = 2, m_F = 2\rangle$  hyperfine state. We showed an example of precision measurements of  $\langle\sigma_{\text{tot}}v\rangle$  for Rb-Ar collisions with these methods applied. The experimentally determined  $\langle\sigma_{\text{tot}}v\rangle$  value agrees within 0.5% with the theoretically computed result.

To increase the pressure measurement range of the CAPS, chapter 6 demonstrates the realization of the MOT-based CAPS. First, we demonstrate using a MOT-based CAPS as a transfer pressure standard calibrated against MT-based CAPS. As a result, we are able to measure the Ar pressure up to  $10^{-7}$  Torr ( $10^{-5}$  Pa) (In North America, particularly in the US, a commonly used pressure unit is Torr where  $1 \text{ Torr} = 133.32 \text{ Pa}$ ). Next, we propose a way of using a MOT-based CAPS as a primary pressure standard, which involves solving the excited-state fraction and controlling the depth of the MOT. Finally, we show a measurement of the excited state loss rate coefficient and the ground state loss rate coefficient that are key in realizing a MOT-based CAPS.

Finally, chapter 7 summarizes all the work presented in this thesis. Also, a list of future outlooks for the development of the CAPS is presented in chapter 8. This chapter explores two promising, albeit opposing, directions: the complications and the simplifications of the quantum pressure standard. The complications section focuses on finding the limitations of the universality of quantum diffractive collisions and aiming to find a solution when the universality doesn't apply. The simplifications section presents the ongoing effort in making portable CAPS that can be easily operated and shipped. This is an essential direction of the CAPS and has also raised other groups' attention [60, 83, 84, 85].

## Chapter 2

# Review of Quantum Scattering

## Theory

The core principle of the cold atom pressure standard is the description of elastic collisions between the trapped atoms and the background particles. The loss rate of the trapped atoms from the background collisions,  $\Gamma_{\text{loss}}$ , can be formulated as,

$$\Gamma_{\text{loss}} = n \langle \sigma v \rangle, \quad (2.1)$$

where  $n$  is the density of background particles<sup>1</sup>. The quantity  $\langle \sigma v \rangle$ , usually referred as the rate coefficient, represents the collision cross section,  $\sigma$ , velocity averaged over the Maxwell-Boltzmann velocity distribution of the background particles. Based on Eq. 2.1, One can see that knowing the value of  $\langle \sigma v \rangle$  is key to determining the pressure in the vacuum, given the loss rate of the trapped atoms can be measured. Therefore, it is essential to understand the collision mechanism in order to use collisions in realizing a fundamental pressure standard. A quick review of the quantum scattering theory by a central force in a two-body system is helpful.

### 2.1 Hamiltonian of a Two-body System

In the two-body collision model, there is a trapped particle with mass  $m_1$  and a background gas-particle with mass  $m_2$ , as shown in figure 1.3. The collision particle has an initial velocity,  $\vec{v}_2$ , towards the trapped particle, where the trapped particle is moving at a negligible velocity  $\vec{v}_1$ . The interaction potential between the two particles is  $V(\vec{r}_1 - \vec{r}_2)$ , where  $\vec{r}_1$  and  $\vec{r}_2$  represent the positions of the trapped particle and the collision partner separately in the lab frame. Then, we can construct the interacting

---

<sup>1</sup>One then can obtain the pressure using the ideal gas law,  $p = nk_B T$

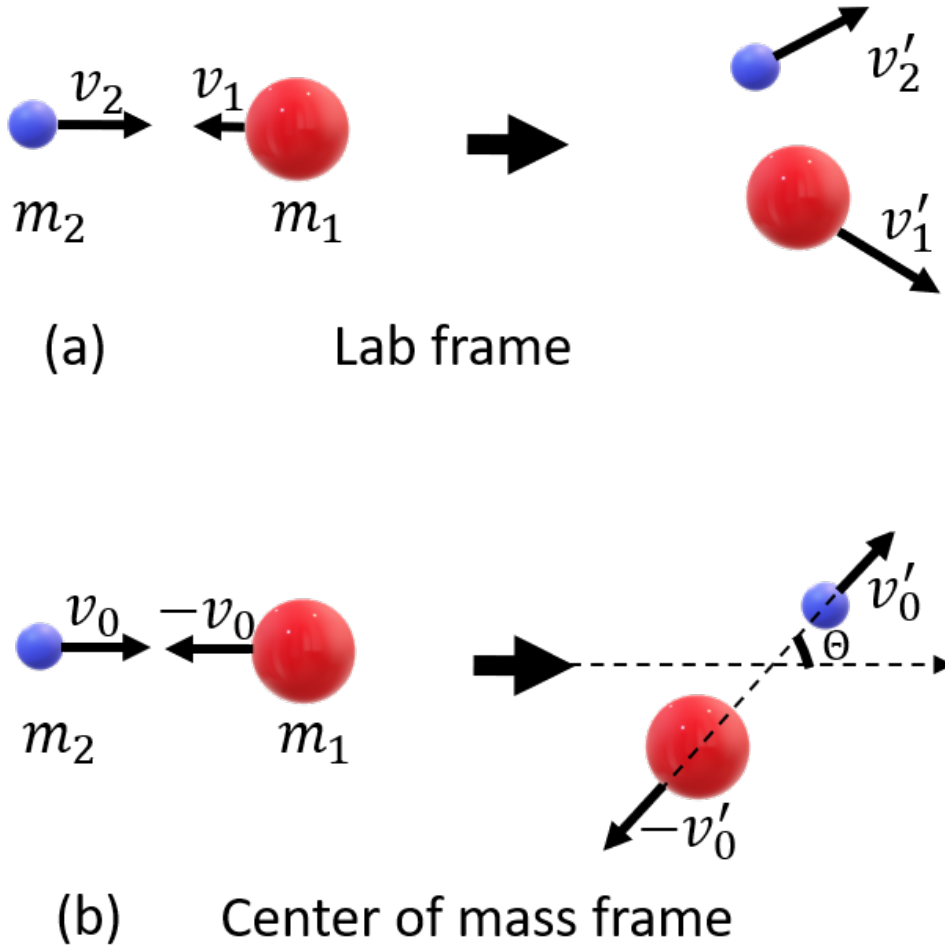


Figure 2.1: A diagram of the collision process. Plot (a) represents that an incoming particle with a mass  $m_2$  and a velocity  $v_2$  collides with a trapped atom with a mass  $m_1$  and a negligible velocity  $v_1$  in the lab frame. After the collision, the incoming particle is scattered out with a new velocity  $v'_1$  and the trapped atom gains a new velocity  $v'_2$ . Plot (b) represents the same collision process in the center of mass frame and demonstrates the scattering angle,  $\theta$ .

Hamiltonian as,

$$H = \frac{\vec{p}_1^2}{2m_1} + \frac{\vec{p}_2^2}{2m_2} + V(\vec{r}_1 - \vec{r}_2). \quad (2.2)$$

Here, the momentum can be expressed as,  $\vec{P}_1 = m_1\vec{v}_1$  and  $\vec{P}_2 = m_2\vec{v}_2$ . We can switch from the lab frame to the center of mass (CoM) frame to analyze the Hamiltonian.

Classically, we can define the coordinate of the CoM as

$$\vec{R} = \frac{m_1 \vec{r}_1 + m_2 \vec{r}_2}{M}, \quad (2.3)$$

where  $M = m_1 + m_2$ . The relative position coordinate can be written as  $\vec{r}' = \vec{r}_1 - \vec{r}_2$ . Similarly, the CoM velocity can be expressed as

$$\vec{v}_C = \frac{m_1 \vec{v}_1 + m_2 \vec{v}_2}{M} = \frac{\vec{P}_1 + \vec{P}_2}{M}, \quad (2.4)$$

and the relative velocity between the two collision partners is  $\vec{v}_r = \vec{v}_1 - \vec{v}_2$ . Given the expression of the CoM velocity, we can write the total momentum as  $\vec{p} = \vec{p}_1 + \vec{p}_2 = M\vec{v}_C$ . Given the very low energy range of collisions we studied in this thesis, the inelastic collisions contribute very little to the whole collision process, thus, we only consider the case of elastic collisions here. In the case of elastic collisions, the momentum is conserved before and after the collision, and the CoM velocity  $\vec{v}_C$  is a constant. In the CoM frame, we will have  $\vec{v}_C = 0$ , and the particles have equal and opposite momenta. Since the total energy is also conserved in an elastic collision, the magnitude of the relative velocity in the CoM frame is constant before and after the collision (details of the derivations can be found in the appendix C),  $|\vec{v}_r| = |\vec{v}_1 - \vec{v}_2|$ . However, the direction of the relative velocity changes before and after the collision, as illustrated in figure 2.1 (a). The angle between the post-collision velocity vector and the pre-collision velocity vector is defined as the scattering angle,  $\theta$ . Then we can write the Hamiltonian in Eq. 2.2 in terms of the quantities defined in the CoM frame,

$$\begin{aligned} H &= \frac{\vec{p}^2}{2M} + \frac{\vec{p}_r^2}{2\mu} + V(\vec{r}_1 - \vec{r}_2) \\ &= -\frac{\hbar^2}{2M} \nabla_R^2 - \frac{\hbar^2}{2\mu} \nabla_r^2 + V(\vec{r}'), \end{aligned} \quad (2.5)$$

where  $\mu = \frac{m_1 m_2}{m_1 + m_2}$  is the reduced mass of the two colliding particles, and  $\nabla_R^2 = -\vec{p}^2/\hbar^2$  and  $\nabla_r^2 = -\vec{p}_r^2/\hbar^2$  are the laplacian corresponding to the center of mass and relative coordinates, respectively. As a result, we can find that the Hamiltonian in the center of the mass frame is composed of a CoM part and a relative motion part.

## 2.2 Loss cross section

To find a solution to the Hamiltonian in the CoM frame, one can solve the time-independent Schrödinger equation,  $H\psi = E\psi$ , with the time-independent approach. A common wavefunction solution to this Schrödinger equation is a product of the wavefunction of CoM and the wavefunction of the relative motion,  $\psi = \psi_R\psi_r$ . The wavefunction of CoM  $\psi_R$  satisfies the Schrödinger equation,

$$-\frac{\hbar^2}{2M}\nabla_R^2\psi_R = E_R\psi_R, \quad (2.6)$$

while the wavefunction corresponding to the relative motion,  $\psi_r$ , satisfies,

$$\left[-\frac{\hbar^2}{2\mu}\nabla_r^2 + V(\vec{r})\right]\psi_r = E_r\psi_r. \quad (2.7)$$

If we treat the system in the CoM frame, we can ignore Eq.2.6 and focus on the Schrödinger Eq.2.7. Also, we know the energy of the particle can be expressed in terms of the momentum,  $E_r = \frac{\hbar^2\vec{k}^2}{2\mu}$ , where the wavevector,  $\vec{k} = \mu\vec{v}_r/\hbar$ , describes the momentum of the reduced mass particle in the interaction potential. Thus, one can write Eq. 2.7 into the following form,

$$\left[-\frac{\hbar^2}{2\mu}\nabla_r^2 + V(\vec{r}) - \frac{\hbar^2k^2}{2\mu}\right]\psi_r = 0 \quad (2.8)$$

The form of this equation models a single particle of reduced mass  $\mu$  in the presence of the potential  $V(\vec{r})$  which, in Eq. (2.8), is assumed to be spherically symmetric in the CoM frame and goes to zero as  $r \rightarrow \infty$ . From now, we drop the directional dependence in the potential,  $V(\vec{r}) \rightarrow V(r)$ . For the large distance regime, the solution to Schrödinger Eq. 2.8,  $\psi_r$ , is expected to be the superposition of an incoming plane wave and an outgoing spherical wave (details can be found in Ref. [86]),

$$\psi_r \sim e^{i\vec{k}\cdot\vec{r}} + f(k, \theta, \phi) \frac{e^{ikr}}{r}. \quad (2.9)$$

The first term represents the state of the system in the absence of the scattering potential, which is determined by the physical conditions of the experiment, expressed in the form of a plane wave. The second term in Eq. 2.9 describes the form of the outgoing

## 2.2. Loss cross section

---

scattered wave with a scattering amplitude  $f(k, \theta, \phi)$ , which depends on the interaction potential,  $V(r)$ . The square of the scattering amplitude,  $|f(k, \theta, \phi)|^2$ , indicates the probability of scattering into different directions,  $\theta$  and  $\phi$ , which is consistent with the definition of the classical differential collision cross section,  $d\sigma/d\Omega$  ( $d\Omega$  is the solid angle scattered into). Therefore, one can obtain the relationship between the scattering amplitude,  $f(k, \theta, \phi)$ , and the differential cross section by comparing the incident flux (number of particles per unit area per unit time) with the rate of scattering into a given solid angle  $d\Omega$ . The differential cross section,  $\frac{d\sigma}{d\Omega}$ , is defined as

$$\frac{d\sigma}{d\Omega} = \frac{\# \text{ of particles scattered per unit time per unit solid angle } d\Omega}{\text{flux of incident particles}}, \quad (2.10)$$

where the unit solid angle is  $d\Omega = \sin\theta d\theta d\phi$  and the flux has units of number per second. To calculate the flux density in the denominator, one can use the continuity equation in the absence of sources,

$$\frac{d\rho}{dt} + \vec{\nabla} \cdot \vec{J} = 0. \quad (2.11)$$

In the quantum regime, the density quantity  $\rho$  can be expressed as the probability density,  $|\psi_r|^2$ . With this replacement, it can be shown that the flux quantity  $\vec{J}$  for a particle of mass  $\mu$  has the form,

$$\begin{aligned} \vec{J} &= \frac{\hbar}{2\mu i} (\psi_r^* \nabla \psi_r - \psi_r \nabla \psi_r^*) \\ &= \frac{\hbar}{\mu} \text{Im}(\psi_r^* \nabla \psi_r). \end{aligned} \quad (2.12)$$

Now we can plug in the expression of the wave function  $\psi_r = e^{ikz \cos\theta}$  and obtain the flux of incident particles,  $\vec{J} = \frac{\hbar \vec{k}}{\mu}$ .

Next, we can calculate the numerator in Eq. 2.10. The number of particles scattered into the solid angle  $d\Omega$  per unit time can be calculated by

$$dn = |\psi(r)|^2 d^3r = \left| f(k, \theta, \phi) \frac{e^{ikr}}{r} \right|^2 r^2 d\Omega dr = |f(k, \theta, \phi)|^2 d\Omega dr. \quad (2.13)$$

## 2.2. Loss cross section

---

Therefore, the number of particles scattered per unit time per unit solid angle is

$$\frac{dn}{dt d\Omega} = \frac{|f(k, \theta, \phi)|^2 dr}{dt} = \frac{|f(k, \theta, \phi)|^2 dr}{dr/v} = \frac{\hbar \vec{k}}{\mu} |f(k, \theta, \phi)|^2. \quad (2.14)$$

Hence, the differential cross section equals  $\frac{d\sigma}{d\Omega} = |f(k, \theta, \phi)|^2$ , and the total collision cross section can be obtained by integrating the differential cross section over the entire solid angle,

$$\sigma_{tot} = \int \frac{d\sigma}{d\Omega} d\Omega = \int_0^{2\pi} d\phi \int_0^\pi |f(k, \theta, \phi)|^2 \sin \theta d\theta \quad (2.15)$$

$$\sigma_{tot} = 2\pi \int_0^\pi |f(k, \theta, \phi)|^2 \sin \theta d\theta. \quad (2.16)$$

However, in our case, this total collision cross section is not directly reflected in the loss rate measurements since the collision target is trapped in a confining potential with a finite trap depth,  $U$ . *The trap depth of an atom is defined as the energy required to eject the atom out of the trap.* Therefore, not every collision will force the trapped atom to leave the trap. If a collision that transferred energy,  $\Delta E$ , is smaller than the trap depth of the trapped atom. The trapped atom will gain the energy and stay in the trap, and this collision process cannot be detected. Thus, in order for the collision to be detected, the transferred energy should be larger than the trap depth, which can be mathematically expressed as  $\Delta E > U$ . Based on the classical analysis (details in Appendix D), we can find the relationship between the CoM scattering angle and the transferred energy,

$$\Delta E = \frac{(1 - \cos \theta) \mu^2 |\vec{v}_r^\rightarrow|^2}{m_1} \quad (2.17)$$

This relationship indicates that the larger the scattering angle, the larger the transferred energy. We can define the minimum scattering angle,  $\theta_{\min}$ , that represents the transferred energy exactly matching the trap depth of the atom and satisfies the relation  $U = (1 - \cos \theta_{\min}) \mu^2 |\vec{v}_r^\rightarrow|^2 / m_1$ . Thus, the scattering angles that are larger than the minimum scattering angle,  $\theta_{\min}$  will generate trap loss. This leads to a decrease in the loss collision cross section, so we define the cross section related to the loss process as the loss cross section, which can be obtained by integrating the differential cross section

only over the loss regime,  $\theta > \theta_{\min}$ ,

$$\sigma_{loss} = 2\pi \int_{\theta_{\min}}^{\pi} |f(k, \theta, \phi)|^2 \sin \theta d\theta. \quad (2.18)$$

Finally, as we can see, the value of the loss cross section decreases as the trap depth increases, reflecting the fact that fewer collisions transfer sufficient energy to liberate an atom from deeper traps. The loss cross section will converge to the total collision cross section as the trap depth goes to zero. To determine the value of both the total and the loss cross sections, we need to compute the expression of the scattering amplitude, which can be solved using the partial wave analysis method, shown in the following section.

## 2.3 Partial Wave Analysis

To solve for the scattering amplitude, we should start by finding a solution to the Schrödinger equation, Eq. 2.8. For convenience, we can rewrite Eq. 2.8 in terms of the spherical coordinates of the reduced mass particle,

$$\frac{\hbar^2}{2\mu} \left[ -\frac{1}{r^2} \frac{\partial}{\partial r} \left( r^2 \frac{\partial}{\partial r} \right) + \frac{\hat{L}^2}{r^2} + U(r) - k^2 \right] \psi_r = 0, \quad (2.19)$$

Where  $U(r) = 2\mu V(r)/\hbar^2$  and  $\hat{L}$  is the angular momentum operator of the reduced mass particle.

Similar to the treatment we did in separating the CoM coordinates and relative coordinates, in the spherical coordinates, we can separate the wavefunction into as a radial part and an angular part,

$\psi_r(r, \theta, \phi) = R_l(r), Y_{l,m}(\theta, \phi)$ , where the angular part can be expanded into a spherical harmonics series and are eigenfunctions of  $\hat{L}^2$  with  $\hat{L}^2 Y_{l,m}(\theta, \phi) = l(l+1)Y_{l,m}(\theta, \phi)$ .

Here,  $l$  is the orbital angular momentum of the reduced mass particle moving through the inter-particle potential. Then we can plug the solution for  $\psi_r(r, \theta, \phi)$  into Eq. 2.19, to obtain the following expression,

$$\frac{\hbar^2}{2\mu} \left[ -\frac{1}{r^2} \frac{d}{dr} \left( r^2 \frac{d}{dr} \right) + \frac{l(l+1)}{r^2} + U(r) - k^2 \right] R_l(r) = 0 \quad (2.20)$$

### 2.3. Partial Wave Analysis

---

After substituting  $\psi_l(r) = krR_l(r)$ , we can obtain the final form,

$$\left[ -\frac{d^2}{dr^2} + \frac{l(l+1)}{r^2} + U(r) - k^2 \right] \psi_l(r) = 0. \quad (2.21)$$

For very large inter-atomic separations, the interaction potential  $U(r) \rightarrow 0$ . In this limit, we can drop the interaction term, we can write the wavefunctions as linear combinations of spherical Bessel,  $j_l(kr)$ , and Neumann functions,  $n_l(kr)$ , corresponding to a free particle,

$$\psi_l(r) = kr[B_l j_l(kr) + C_l n_l(kr)]. \quad (2.22)$$

Asymptotically, these wavefunctions can be expressed in terms of sine and cosine,

$$j_l(kr) \rightarrow \frac{\sin(kr - l\pi/2)}{kr} \quad (2.23)$$

$$n_l(kr) \rightarrow -\frac{\cos(kr - l\pi/2)}{kr} \quad (2.24)$$

If the interaction potential is zero everywhere, the only boundary condition is at the origin, and  $U(0) = 0$  and only the sin term can be left. Thus, the wave function can be written as,  $\psi_l(r) = krB_l \sin(kr - l\pi/2)$ . However, if the interaction potential is not zero within some radial distance, then we no longer have the boundary condition. Therefore, the Neumann term is retained and has the asymptotic cosine form as  $r \rightarrow \infty$ . Therefore, the total asymptotic wave function can be expressed in terms of sine and cosine,

$$\psi_l(r) = B_l \sin(kr - l\pi/2) - C_l \cos(kr - l\pi/2) \quad (2.25)$$

$$= A_l \sin(kr - l\pi/2 + \eta_l), \quad (2.26)$$

where  $\eta_l = \arctan(-C_l/B_l)$  is the phase shift of the  $l$  partial wave and is determined by the interaction potential  $U(r)$ . The phase shift will become zero when the potential  $U(r)$  goes to zero. In our case, we assume cylindrical symmetry so that we can drop the  $\phi$  dependence, and the angular wave function can be expanded in terms of Legendre polynomials,  $Y_{l,m}(\theta) \propto 2\pi P_l(\cos\theta)$ . Therefore, the final solution to the relative wave

function,  $\psi(r)$ , is,

$$\psi_r(r) = \sum_{l=0}^{\infty} (2l+1) i^l A_l \sin(kr - l/2\pi + \eta_l) P_l(\cos \theta). \quad (2.27)$$

The general form of the wave function we have obtained, as shown in Eq. 2.9, can also be written as an expansion in terms of asymptotic Bessel functions,

$$e^{ikz \cos \theta} = \sum_{l=0}^{\infty} (2l+1) i^l \frac{\sin(kr - l/2\pi)}{kr} P_l(\cos \theta) \quad (2.28)$$

$$f(k, \theta) \frac{e^{ikr}}{r} = \sum_{l=0}^{\infty} f_l(k) \frac{e^{ikr}}{r} P_l(\cos \theta) \quad (2.29)$$

Now comparing the exact form of the wavefunction, Eq. 2.27, with the general form of the wavefunction, Eq. 2.29, we can obtain the expression for the scattering amplitude,

$$f(k, \theta) = \frac{1}{k} \sum_{l=0}^{\infty} (2l+1) T_l(k) P_l(\cos \theta). \quad (2.30)$$

Here  $T_l(k) = \sin(\eta_l) e^{i\eta_l}$  is the transmission matrix for the collision<sup>2</sup>. The scattering matrix can be defined as,  $S_l(k) = e^{2i\delta_l} = 1 + 2iT_l(k)$ . Then the exact expression of the total cross section can be obtained by plugging in the solution of the scattering amplitude into Eq. 2.16,

$$\sigma_{tot}(k) = 2\pi \int_0^\pi \left| \sum_{l=0}^{\infty} (2l+1) T_l(k) P_l(\cos \theta) \right|^2 \sin \theta d\theta \quad (2.31)$$

$$\sigma_{tot}(k) = 4\pi \sum_{l=0}^{\infty} \frac{(2l+1)}{k^2} \sin^2 \eta_l. \quad (2.32)$$

### 2.3.1 Log-derivative method

We can see that the key to obtaining the total cross section and  $f(k, \theta)$  is to compute the phase shifts of the scattered reduced mass particles,  $\eta_l$ , which depends on the interaction potential. One can numerically integrate Schrödinger Eq. 2.21 from a position where the reduced mass particle is close to the center of the potential and out to a very large distance. To achieve this, one can apply the log-derivative method described by Johnson

---

<sup>2</sup>For an elastic collision, the transmission matrix is a simple scalar.

[87]. As a start, we can simplify Eq. 2.21 by redefining a quantity,

$$W(k, r) = k^2 - U(r) - \frac{l(l+1)}{r^2}, \quad (2.33)$$

so we can have

$$\left[ -\frac{d^2}{dr^2} + W(k, r) \right] \psi_l(r) = 0. \quad (2.34)$$

Then we can define a parameter  $y = \psi'_l(r)/\psi_l(r)$ , so that we can find

$$y' = \frac{\psi''_l(r)}{\psi_l(r)} - \frac{|\psi'_l(r)|^2}{|\psi_l(r)|^2} \quad (2.35)$$

$$= -W(k, r) - y^2. \quad (2.36)$$

Therefore, the final differential equation can be iterated beginning at small  $r = r_0$  and assuming an initial large number for  $y(r_0)$ . The iterative solution is,

$$y_n = \frac{y_{n-1}}{1 + \Delta y_{n-1}} - \frac{\Delta}{3} w_n q_n. \quad (2.37)$$

Here,  $\Delta$  is the step size in the radial direction and,

$$q_n = \begin{cases} W(k, r_n) & n = 0, 2, 4, \dots, N \\ \frac{W(k, r_n)}{1 + \frac{\Delta^2}{6} W(k, r_n)} & n = 1, 3, 5, \dots, N-1 \end{cases} \quad (2.38)$$

with the weights,  $w_n$ ,

$$w_n = \begin{cases} 1 & n = 0, N \\ 4 & n = 2, 4, 6, \dots, N-2 \\ 2 & n = 1, 3, 5, \dots, N-1. \end{cases} \quad (2.39)$$

Recall the solution for  $\psi_l(r)$  given in Eq. 2.22, we can define the reactance matrix,

$K_l = \tan \eta_l = -C_l/B_l$ . Then we can find the relationship between the  $K_l$  matrix and  $y$ ,

$$\begin{aligned}
 y &= \frac{\psi'_l(r)}{\psi_l(r)} = \frac{\frac{d}{dr} \left( krB_l[j_l(kr) - K_l n_l(kr)] \right)}{\psi_l(r)} \\
 &= \frac{kB_l[j_l(kr) - K_l n_l(kr)] + krB_l[j'_l(kr) - K_l n'_l(kr)]}{krB_l[j_l(kr) - K_l n_l(kr)]} \\
 &= \frac{1}{r} + \frac{[j'_l(kr) - K_l n'_l(kr)]}{[j_l(kr) - K_l n_l(kr)]}
 \end{aligned} \tag{2.40}$$

Therefore, we can solve for the  $K_l$  matrix

$$K_l = \frac{[(y - \frac{1}{r})j_l - j'_l]}{[(y - \frac{1}{r})n_l - n'_l]}. \tag{2.41}$$

For each partial wave, we can compute its  $K_l$  matrix element by numerically integrating Eq. 2.36. Once the  $K_l$  matrix has been found, the scattering matrix,  $S_l(k)$ , and the transmission matrix,  $T_l(k)$ , can be determined. Then, the scattering amplitude,  $f(k, \theta)$ , for a particular  $k$  and  $\theta$  can be found by substituting the transmission matrix into Eq. 2.30 and summing over the partial waves until convergence criteria are met. Finally  $f(k, \theta)$  is substituted into Eq. 2.32 to obtain the total cross section,  $\sigma_{tot}$ .

### 2.3.2 Jeffreys-Born approximation

Alternatively, one can obtain an approximate analytical solution of the total cross section based on the Jeffreys-Born (J-B) approximation, as previously discussed by Child (chapter 4 in [14]). From Eq. 2.9, we model the wavefunction as including a plane wave part and a scattering term. The idea of J-B approximation is to express the scattering part in terms of outgoing Green's function,  $G(r, r')$ , which allows us to obtain an expansion for the wavefunction in powers of  $U(r)$ ,

$$\psi_l(r) = \psi_l^0(r) + \int_0^\infty G(r, r')U(r')\psi_l(r')dr'. \tag{2.42}$$

Here the Green's function is given by,

$$\begin{aligned}
 G(r', r) &= -\frac{\psi_l^+(r)\psi_l^0(r')}{k} \quad (r > r') \\
 &= -\frac{\psi_l^0(r)\psi_l^+(r')}{k} \quad (r < r'),
 \end{aligned} \tag{2.43}$$

### 2.3. Partial Wave Analysis

---

where  $\psi_l^0(r) \sim krj_l(kr)$  and  $\psi_l^+(r) \sim krn_l(kr)$  represent the wavefunction of the plane wave and the scattering wave, respectively. When the inter-atomic separation is large, the effect of the interaction potential will be small, and Eq. 2.42 can be written as [14],

$$\psi_l(r) \sim \sin\left(kr - \frac{1}{2}\pi l\right) - \frac{\exp(ikr - \frac{1}{2}\pi l)}{k} \int_0^\infty U(r)\psi_l^0(r)dr. \quad (2.44)$$

Here, we take the asymptotic form of the incoming and outgoing wave functions. We can then compare the J-B approximation form with the previously derived form in Eq. 2.26, and get the approximate expression of the phase shift,

$$\eta_l = -\frac{\int_0^\infty U(r)[\psi_l^0(r)]^2}{k}dr. \quad (2.45)$$

Then we can substitute the solution to the incoming wave function,

$$\eta_l = -kr^2 \int_0^\infty U(r)[j_l(kr)]^2dr = -\frac{2\mu}{k\hbar^2} \int_0^\infty V(r)k^2r^2[j_l(kr)]^2dr. \quad (2.46)$$

For the high angular momentum collisions where the long-range part of the interaction potential has the dominant effect, we can solve for the phase shift. Usually, the long-range form of the interaction potential is in the form of  $V(r) \sim -C_s/r^s$ . Plugging the long-range form of the interaction potential into Eq. 2.46, we can have

$$\eta_l = -\frac{2\mu C_s}{k\hbar^2} \int_0^\infty \frac{1}{r^s} k^2 r^2 [j_l(kr)]^2 dr \quad (2.47)$$

$$\approx -\frac{2\mu C_s}{k\hbar^2} \int_0^\infty \frac{1}{r^s} \frac{1}{2} \left(1 - \frac{l^2}{k^2 r^2}\right)^{-\frac{1}{2}} dr \quad (2.48)$$

$$= \frac{\pi^{\frac{1}{2}} \Gamma(\frac{1}{2}s - \frac{1}{2})}{2\Gamma(\frac{1}{2}s)} \frac{\mu C_s k^{s-2}}{\hbar^2 l^{s-1}} \quad (2.49)$$

This solution is the so-called Jeffreys-Born approximation of the phase shift employed in the theory of small-angle scattering. Here, we also applied the approximation at long range,  $k^2 r^2 [j_l(kr)]^2 \approx \frac{1}{2} (1 - l^2/k^2 r^2)^{-1/2}$  [14]. For the case we study, the interaction is usually a van der Waals type potential, which has a long-range  $\frac{C_6}{r^6}$  attraction. For this long-range interaction potential, we derive the phase shift,

$$\eta_l = \frac{\pi^{\frac{1}{2}} \Gamma(\frac{5}{2})}{2\Gamma(3)} \frac{\mu C_6 k^4}{\hbar^2 l^5} \approx 0.589 \frac{\mu C_6 k^4}{\hbar^2 l^5} = \frac{\alpha}{l^5}, \quad (2.50)$$

If we replace the sum in Eq. 2.32 with an integral and plug in the approximations of the phase shift, Eq. 2.50, we can calculate the approximate total collision cross section

$$\sigma_{tot}(v) \approx 4\pi \int_0^\infty \frac{(2l+1)}{k^2} \sin^2\left(\frac{\alpha}{l^5}\right) dl \quad (2.51)$$

$$\approx 8.0828 \left(\frac{\mu C_6}{\hbar^2 k}\right)^{\frac{2}{5}} + 7.1889 \frac{1}{k} \left(\frac{\mu C_6}{\hbar^2 k}\right)^{\frac{1}{5}} \quad (2.52)$$

$$= 8.0828 \left(\frac{C_6}{\hbar v_r}\right)^{\frac{2}{5}} + 7.1889 \frac{\hbar}{\mu v_r} \left(\frac{C_6}{\hbar v_r}\right)^{\frac{1}{5}} \quad (2.53)$$

This is J-B long-range approximate form of the total collision cross section, but the (small) second term in  $\sigma(v)$  of Eq. 2.53 is usually neglected in other literature [62, 14]. The collisions resulting in small momentum transfer are predominantly determined by the long-range part of the interaction potential. Thus, we can notice that the J-B long-range approximation agrees with the actual total collision cross section computed using the log-derivative method very well, as demonstrated in figure 2.2 (for this numerical computation a L-J potential was used).

The dashed line in the figure is the J-B prediction, while the quantum scattering computed result is shown as the solid curve. The oscillations of the computed  $\langle\sigma_{tot}v\rangle(k)$  as a function of  $v$  are due to the interference between the long-range and short-range scattering of the interaction potential. It is the result of the interference between the forward traveling, unscattered part of the wavefunction with the partial waves which are scattered in the forward direction (i.e., the glory oscillations). The interference term disappears if we ignore the short-range contributions or when they are very small.

## 2.4 Thermally Averaged Collision cross section

In Section 2.3, we derived the expression of the total cross section and the loss cross section for each specific relative speed, as shown in Eq. 2.16 and Eq. 2.18, respectively. We can notice that the cross section is a function of the velocity of the relative motion,  $v_r = \hbar k/\mu$ . In our case, the velocity of the trapped particle is very small compared to the velocity of the incoming particle. Therefore, the relative velocity can be approximated with the velocity of the incoming particle. To simplify the following analysis, we replace the relative velocity  $v_r$  with  $v$ . Then we need to know the velocity of the

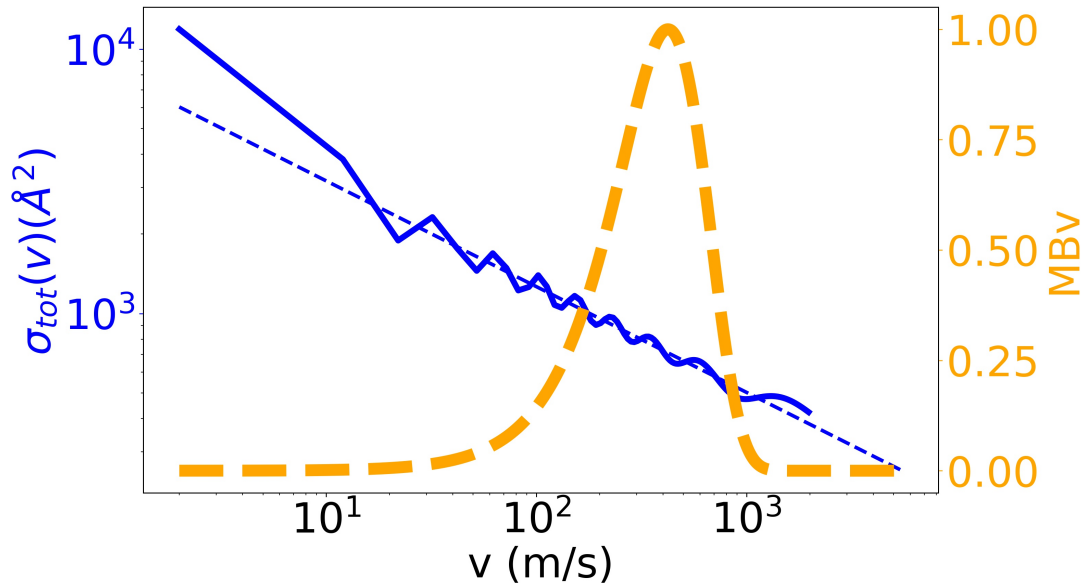


Figure 2.2: A plot of the total collision cross section,  $\sigma_{tot}$ , versus the velocity of the incoming particle,  $v$ , in the Rb-Ar system. Note that both the total collision cross section and the velocity are plotted in the log scale. The solid blue line represents the total cross section calculated using the J-B approximation, while the blue dashed line represents the total cross section computed numerically using the log-derivative method. The latter is more accurate. The orange dashed line shows the Maxwell-Boltzmann velocity distribution (scaled by the maximum value) of the background particles, Ar, at room temperature, 21°C, with the most probable speed of 349.6 m/s.

collision particle in order to report the total collision cross section. However, in the real world, it is difficult to have a single velocity source of particles. On the contrary, the collision particles usually have a velocity distribution and can be modeled as the Maxwell-Boltzmann distribution with the temperature at room temperature. The validation of using the room temperature as the temperature of the collision system is: The background gas particles are contained within the glass vacuum cell whose dimensions are on the order of several centimeters. These particles collide with the vacuum chamber walls, thus thermalizing with the temperature of the vacuum chamber, which is in equilibrium with room temperature. The mean speed of the background particles is on the order of a few hundred meters per second so that, in the absence of collisions, they traverse the vacuum system in approximately 250  $\mu\text{s}$ , undergoing thousands of wall collisions per second. At the pressures used in this work ( $\sim 10^{-9}$  Torr), the mean free path of the background particles is on the order of kilometers, and the rate for intra-vacuum particle collisions is on the order of several Hz. Therefore, the wall collisions

dominate the gas dynamics and thermalization under our operating conditions. Second, the cooling effect through the collisions with the trapped cold atoms is negligible. At the pressure of  $10^{-9}$  Torr, the density of the background gas is approximately  $3 \times 10^7/\text{cm}^3$ . In total, there are around  $10^{10}$  particles in the glass cell, which is much more than the total number of atoms ( $10^6$ ) trapped in the magnetic trap. Thus, the average temperature of the whole collision system is unaffected by the whole cold ensemble. Moreover, the collision rate between the background gas particles and the cold atoms is only on the order of 1 Hz, which is much slower than the collision rate with the glass cell. In addition, these cooled atoms will continue to collide with the cell walls, rethermalizing. In short, the collisions between the background particles and the trapped atoms have a negligible effect on the temperature of the overall background ensemble.

Hence, instead of determining the total cross section, we measure the thermally averaged total cross section,  $\langle \sigma_{\text{tot}} v \rangle$ , which will be the integration of the total cross section over the entire velocity distribution,

$$\begin{aligned} \langle \sigma_{\text{tot}} v \rangle &= \int_0^\infty 4\pi v^3 \int_0^\pi \sigma(k, \theta) d\theta \rho(v) dv \\ &= \int_0^\infty 4\pi v^3 \left[ \frac{2\pi}{k^2} \int_0^\pi \left| \sum_{l=0}^\infty (2l+1) T_l(k) P_l(\cos \theta) \right|^2 \sin \theta d\theta \right] \rho(v) dv. \end{aligned} \quad (2.54)$$

Here

$$\rho(v) = \left( \frac{m_1}{2\pi k_B T} \right)^{3/2} e^{-\frac{m_1 v^2}{2k_B T}}, \quad (2.55)$$

is the Maxwell-Boltzmann distribution. Similarly, based on Eq. 2.18, the velocity average loss cross section,  $\langle \sigma_{\text{loss}} v \rangle$ , can be written as,

$$\langle \sigma_{\text{loss}} v \rangle = \int_0^\infty 4\pi v^3 \left[ \frac{2\pi}{k^2} \int_{\theta_{\text{min}}}^\pi \left| \sum_{l=0}^\infty (2l+1) T_l(k) P_l(\cos \theta) \right|^2 \sin \theta d\theta \right] \rho(v) dv. \quad (2.56)$$

Here, we note that the integral over the scattering angle starts from  $\theta_{\text{min}}$  instead of zero. This reflects the fact that not all the collisions will liberate an atom from the trap, reducing the loss rate coefficient,  $\langle \sigma_{\text{loss}}(U) v \rangle$ , below the total collision loss rate

coefficient  $\langle\sigma_{\text{tot}}v\rangle$ . Figure 2.2 illustrates the range of speeds over which the total collision cross section is integrated over.

Naturally, one can imagine that if the information of the interaction potential,  $V(r)$ , is known, we can compute the resulting phase shifts using the log-derivative method or J-B approximations. Then, plugging in the phase shifts, we can obtain the values of  $\langle\sigma_{\text{loss}}v\rangle$  using Eq. 2.56. Then one can *measure* the density of the background particles,  $n = \Gamma_{\text{loss}}/\langle\sigma_{\text{loss}}v\rangle$ , from the measured trap loss rate. In fact, this is the most straightforward method to obtain the values of  $\langle\sigma_{\text{loss}}v\rangle$  and realize the CAPS. In addition, other methods allow us to determine the values of  $\langle\sigma_{\text{loss}}v\rangle$  and will be discussed in the later section 4.

# Chapter 3

## Experimental Apparatus

The techniques for producing cold ensembles of atoms are very mature and have been well described previously [88, 89]. This chapter will describe the details of cooling, trapping, and measuring the trap loss of specific species for our research goals. First, we will explain the reasons behind choosing Rb atoms and discuss its advantages and disadvantages as the "sensor" in a cold atom pressure standard (CAPS). Then we will present the details of building a CAPS apparatus, including the laser system, the magnetic coil system, the vacuum chamber, and the control system.

### 3.1 Choice of Sensor Atoms

While many candidate species can be laser cooled and trapped, two of the most popular species for pressure measurements have been Rb and Li due to their simplicity of atomic structures, which facilitates laser cooling and trapping. Therefore, we only compare Rb atoms and Li atoms and provide our reasons for choosing Rb atoms as sensor atoms over Li atoms.

#### Vapor pressure

The main advantage offered by Li is its low vapor pressure compared to Rb at room temperature. According to Clausius-Clapeyron law [90], the vapor pressure of the solid-state of the material can be modeled as,

$$\log(P/\text{Torr}) = A - \frac{B}{T} + 2.125, \quad (3.1)$$

where  $P$  is the vapor pressure in Torr,  $T$  is the temperature of the material,  $A$  and  $B$  are material-dependent constants. For solid Li,  $A = 10.673$  and  $B = 8310\text{K}$ , and for solid Rb,  $A = 9.863$  and  $B = 4215\text{K}$  [91, 92]. Therefore, one can find that the vapor

### 3.1. Choice of Sensor Atoms

pressure for Li at room temperature is  $\sim 10^{-19}$  Torr, while the vapor pressure for Rb at room temperature is  $\sim 10^{-7}$  Torr, as shown in figure 3.1. The low vapor pressure for Li means that this species will not contaminate the vacuum system to which a CAPS is attached. Moreover, it will potentially help extend the lower measuring limit of the CAPS to the extremely high vacuum regime (XHV,  $P_{\text{vap}} < 10^{-12}$  Torr).

To implement a CAPS, regardless of which species is used as the trapped sensor atom, it is prudent to separate the source of the sensor atoms from the measurement section of the standard to avoid contamination of the sensor atom source by the gas being measured and to provide a controlled loading rate of atoms in the test section. The usual solution is to place a differential pumping tube between the source chamber and the test chamber, isolating the higher pressure source region from the test chamber. This mitigates the contamination risk a Rb-based CAPS could pose to a vacuum system during measurements (See section 3.4 for details).

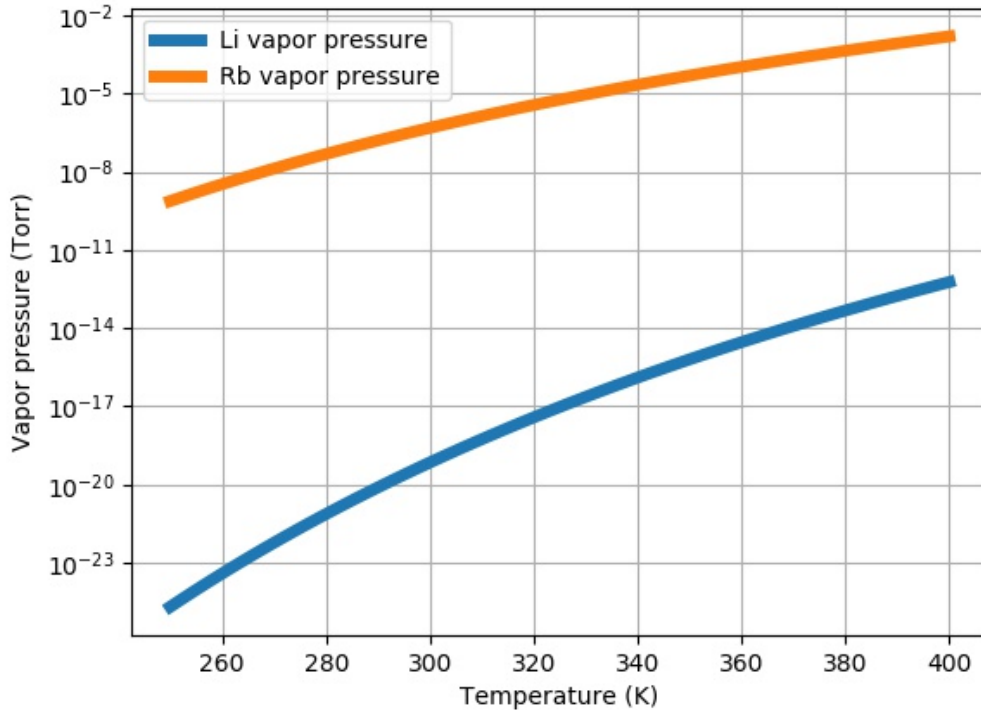


Figure 3.1: The vapor pressures of Li and Rb at different background temperatures. The orange line represents the vapor pressure for Rb, while the blue line represents the vapor pressure for Li. They are calculated based on Eq. 3.1.

### Atomic structures

For both Rb and Li atoms, the ground state electron configuration has a single valence electron with spin  $S = 1/2$  in an  $s$  orbital ( $L = 0$ ). Coupling between the spin of the electron,  $S$ , and the orbital angular momentum of the electron,  $L$ , gives rise to the fine structure, which leads to the sum of these angular momenta being a good quantum number,  $J$ , with a range from  $|L - S|$  to  $|L + S|$ . The spin-orbital coupling leads to a splitting of the first excited state ( $L = 1$ ) into two levels,  $^2P_{1/2}(J = 1/2)$  and  $^2P_{3/2}(J = 3/2)$ . The energy transitions between the ground state,  $^2S_{1/2}$ , and the  $^2P_{1/2}$  and  $^2P_{3/2}$  levels are respectively referred to as the D1 and D2 transitions.

These species have nuclear magnetic moments and nuclear electric quadrupole moments (characterized by their nuclear spin,  $I$ ) which couple to the electrons. These hyperfine interactions further split the atomic energy levels into total angular momentum states,  $F = I + J$ . The fine and hyperfine structure of the ground state and  $^2P_{3/2}$  excited states of Li and Rb are shown in figure 3.2 and figure 3.3 (Note that both Rb and Li atoms have two isotopes,  $^{87}\text{Rb}$ ,  $^{85}\text{Rb}$  and  $^7\text{Li}$  and  $^6\text{Li}$ , each of which has different total nuclear spins,  $I$ ). The theory of laser cooling and trapping has been thoroughly summarized and well presented in previous literature [93, 94, 1], thus, will not be discussed here. In short, two sets of lasers, pump and repump light, are required to cover D2 transitions in order to Doppler cool Rb or Li atoms, as shown in figure 3.2

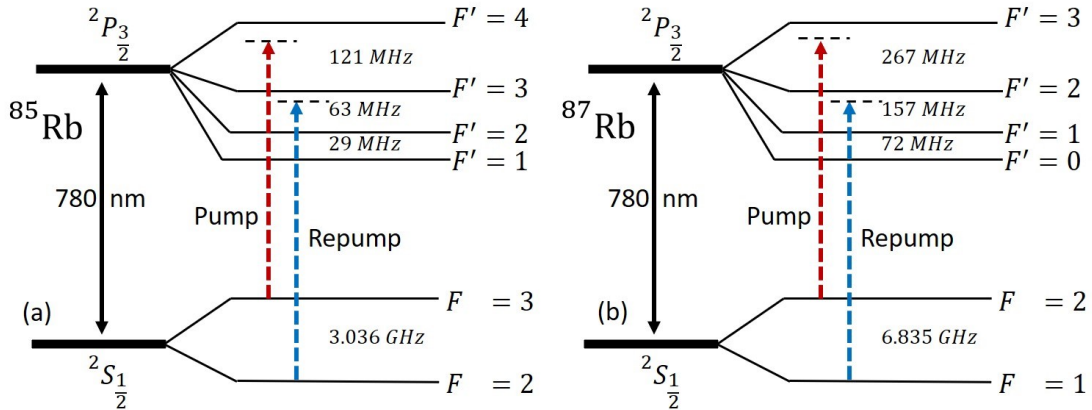


Figure 3.2: Hyperfine energy diagrams for  $^{85}\text{Rb}$  ( $I = 5/2$ ) and  $^{87}\text{Rb}$  ( $I = 3/2$ ). The hyperfine energy separations are indicated for each electronic state. The red dashed lines represent the pump light which covers the transition from the higher hyperfine ground state,  $F = |I + J|$ , to the corresponding excited state,  $F' = F + 1$ . Similarly, the blue dashed lines represent the repump light which covers the transition from the lower hyperfine ground state,  $F = |I - J|$ , to the corresponding excited state,  $F' = F + 1$ .

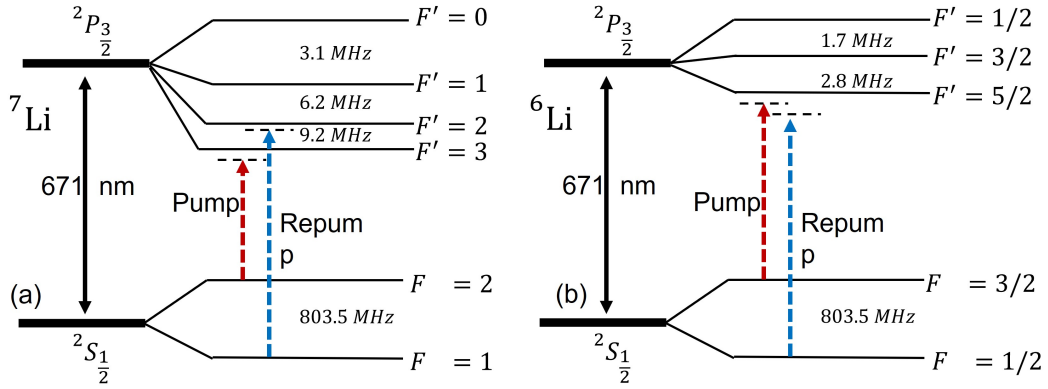


Figure 3.3: Hyperfine energy diagrams for  ${}^7\text{Li}$  ( $I = 3/2$ ) and  ${}^6\text{Li}$  ( $I = 1$ ) are shown above. The hyperfine energy separations are indicated for each electronic state. The red dashed lines represent the pump light which covers the transition from the higher hyperfine ground state,  $F = |I + J|$ , to the corresponding excited state,  $F' = F + 1$ . Similarly, the blue dashed lines represent the repump light which covers the transition from the lower hyperfine ground state,  $F = |I - J|$ , to the corresponding excited state,  $F' = F + 1$ .

Atoms trapped in a MOT are continuously absorbing and re-emitting the trapping light and thus spend some amount of time in the electronic excited and electronic ground states. However, atoms in the ground states and the excited states have different collision cross section with background particles. Therefore, using a MOT-based CAPS, one needs to know the fraction of the excited states, which can be studied by solving and simulating the rate equations [75]. For Rb atoms, the energy splittings between the two excited states are so large that each state can be accessed by the pump and repump light, respectively. Therefore, the population of Rb atoms distributed over those states can be calculated using rate equations. However, the energy splittings between Li excited states are very narrow, even smaller than the natural linewidth of the transition. It would be difficult to resolve them and, therefore, hard to know the population of Li atoms among the excited states.

### The maximum trapping magnetic field

The CAPS has been designed to study the collision-induced loss of atoms held in a magnetic trap (MT). These traps have the advantage of being very shallow which makes them amenable to studying quantum diffractive collision-induced losses. Also, the trapped ensemble can be prepared in a single quantum hyperfine state which simplifies the interpretation of the loss rate measurements. In the presence of an external

### 3.1. Choice of Sensor Atoms

---

magnetic field, each hyperfine state,  $F$ , will be split into  $2F + 1$  different sublevels that can be labeled by their hyperfine sublevel quantum numbers  $|F, m_F\rangle$ . To simplify the cold atom ensemble state preparation and the interpretation of the experimental data, the  $F = |I - J|$  states are generally chosen to be trapped states since these have fewer magnetic hyperfine sub-states suitable for magnetic trapping (one for  $^{87}\text{Rb}$ ,  $^7\text{Li}$ , and  $^6\text{Li}$ , two for  $^{85}\text{Rb}$ ).

In addition, when holding atoms in a MT, it is more advantageous to select atomic species for which there is a single low field seeking state<sup>3</sup>. This guarantees that the MT loss rate is being measured from a single trap depth rather than from an admixture of atoms in two states with different trap depths. Both  $^6\text{Li}$  and  $^7\text{Li}$  have a single ground state that can be trapped  $|F = 1/2, m_F = -1/2\rangle$  and  $|F = 1, m_F = -1\rangle$ , respectively. However, only  $^{87}\text{Rb}$  has the requisite single trappable state,  $|F = 1, m_F = -1\rangle$ , while  $^{85}\text{Rb}$  has two trappable states  $|F = 2, m_F = -1\rangle$  and  $|F = 2, m_F = -2\rangle$ . Holding the sensor atoms in a single state guarantees that the MT loss rate is being measured from a single trap depth rather than from an admixture of atoms in two states with different trap depths.

However, as shown in figure 3.4, there is a limited range of magnetic fields over which these quantum states remain trappable. At low fields, where the Zeeman shifts of the states are small compared to the hyperfine state splitting, these states are labeled by their hyperfine sublevel quantum numbers,  $|F = 1, m_F = \pm 1, 0\rangle$ . Taking  $^{87}\text{Rb}$  atoms as an example (since in this work, we chose  $^{87}\text{Rb}$  atoms as our sensor atoms to perform the self-calibrating pressure standard measurements), magnetic trapping can only occur when the atoms are in the “low-field seeking”  $|F = 1, m_F = -1\rangle$  state. As the external magnetic field increases, the Zeeman energy approaches the energy separation of the hyperfine states. This results in energy eigenstates which have a mixture of  $|F = 1\rangle$  and  $|F = 2\rangle$  character for each  $m_F$  sublevel. In this “intermediate” coupling regime, the eigenstate can change its character from trappable to untrappable. To find this maximum trappable magnetic field,  $B_{\text{max}}$ , and the corresponding maximum trap depth,

---

<sup>3</sup>Low field seeking: The energy of such state increases as the magnetic field increases.

### 3.1. Choice of Sensor Atoms

$E_{\text{Zeeman}} = E(B = B_{\text{max}}) - E(B = 0)$ , one can use the Breit-Rabi formula [60, 95, 96, 97],

$$E = -\frac{\Delta E_{\text{hfs}}}{2(2I + 1)} + g_I \mu_B m_F B - \frac{\Delta E_{\text{hfs}}}{2} \left[ 1 + \frac{4g m_F \mu_B B}{(2I + 1)\Delta E_{\text{hfs}}} + \left( \frac{g \mu_B B}{\Delta E_{\text{hfs}}} \right)^2 \right]^{\frac{1}{2}}. \quad (3.2)$$

Here,  $\Delta E_{\text{hfs}}$  is the ground state hyperfine splitting without the external magnetic field,  $g = g_J - g_I$ ,  $g_I$  and  $g_J$  are the nuclear and electronic gyromagnetic ratios, respectively,  $\mu_B$  is the Bohr magneton, and  $B$  is the magnetic field strength. We took the derivative of equation 3.2 with respect to  $B$  and calculated the maximum trappable magnetic field,  $B_{\text{max}}$ . The computed values of maximum magnetic field  $B_{\text{max}}$  and the corresponding maximum trap depth  $E_{\text{Zeeman}}$  are presented in column 6 and 7 of table 3.1.

Our numerical calculations also support these analytical results. We have written the Hamiltonian,  $H_{\text{tot}}$  for an atom in the electronic ground state, subjected to an external magnetic field as including hyperfine interactions,  $H_{\text{hfs}}$  and the magnetic field interaction,  $H_B$ . In equation 3.3, we are neglecting any terms (fine structure interactions) in the Hamiltonian that are common to all hyperfine and magnetic hyperfine sublevels. The axis of quantization (z-direction) is chosen to be along the direction of the local, external B-field:

$$\begin{aligned} H_{\text{tot}} &= H_{\text{hfs}} + H_B \\ &= A_{\text{hfs}} \mathbf{I} \cdot \mathbf{J} + \frac{\mu_B}{\hbar} (g_J J_z + g_I I_z) B_z, \end{aligned} \quad (3.3)$$

where  $A_{\text{hfs}}$  is the hyperfine magnetic dipole constant. This Hamiltonian is diagonalized for different magnitudes of the external B-field with the  $|I, J, m_I, m_J\rangle$  basis. For example, the eigenenergies for  $^{87}\text{Rb}$  atoms as a function of the magnetic fields are shown in the first plot of figure 3.4 for the 3 magnetic hyperfine sublevels that correlate to  $|F = 1, m_F = 0, \pm 1\rangle$  at zero field. The energy of the trappable state  $|F = 1, m_F = -1\rangle$  reaches a local maximum at  $B_{\text{max}} = 1221$  G with a corresponding maximum trap depth,  $E_{\text{Zeeman}}/k_B = 22.0$  mK. These calculations agree with the predictions of the Breit-Rabi formula. One can also perform the similar analysis for the  $F = |I - J|$  ground state of other sensor atoms  $^6\text{Li}$ ,  $^7\text{Li}$ , and  $^{85}\text{Rb}$ . The results are summarized in column 6 and 7 of table 3.1.

### 3.1. Choice of Sensor Atoms

Atom	F	$g_F$	State $ F m_F\rangle$	$(\frac{dB}{dz})_0/(G/cm)$	$B_{\max}/G$	$(E_{\text{Zeeman}}/k_B)/mK$
${}^6\text{Li}$	$\frac{1}{2}$	$-\frac{2}{3}$	$ \frac{1}{2} - \frac{1}{2}\rangle$	3.16	27.2	0.314
${}^7\text{Li}$	1	$-\frac{1}{2}$	$ 1 - 1\rangle$	2.46	144	2.59
${}^{87}\text{Rb}$	1	$-\frac{1}{2}$	$ 1 - 1\rangle$	30.5	1221	22.0
${}^{85}\text{Rb}$	2	$-\frac{1}{3}$	$ 2 - 2\rangle$	22.4	722.5	18.6

Table 3.1: Atomic parameters for magnetic trapping. Column 1 lists the atomic species, column 2 provides the hyperfine quantum number of the state, column 3 has the approximate Landé g-factor for this state, column 4 lists the state being trapped, column 5 gives the minimum field gradient to support the atom under gravity (The calculation methods are presented in section 3.3.2 ). Column 6 provides the maximum magnetic field that can support a trapped state, and the values are quoted from [6]. Column 7 provides the maximum Zeeman energy associated with the  $B_{\max}$  values. The methods of calculating the maximum magnetic field and the maximum Zeeman energy can be found in section 3.1

As one can observe in figure 3.4 and table 3.1,  ${}^6\text{Li}$  and  ${}^7\text{Li}$  has a maximum Zeeman energy,  $U/k_B$ , of only 0.314 mK and 2.59 mK, respectively, while  ${}^{87}\text{Rb}$  has a much higher critical energy of 22.0 mK for the  $|F = 1, m_F = -1\rangle$  state. In fact, the maximum trap depths for a trapped ensemble are even less than the values listed due to the effect of gravitational energy and the temperature of the sensor atom ensemble (details are explained in section 4.2.2). When using the self-calibration method with the MT-based CAPS, the greater the accessible range of the trap depth one could achieve, the higher the accuracy of the  $\langle\sigma_{\text{tot}}v\rangle$  values measured (details are explained in chapter 4). Therefore, one can achieve a higher trap depth with  ${}^{87}\text{Rb}$  as sensor atoms and achieve a higher precision in determining the value of  $\langle\sigma_{\text{tot}}v\rangle$ .

#### Cost

Finally, from the practical point of view, the cost of an Rb-based CAPS is lower than a Li-based CAPS, and the robustness of an Rb-based CAPS is higher than a Li-based one. Those advantages are directly related to the robustness of semiconductor laser media at 780 nm as opposed to 671 nm. A 780 nm laser system is much more reliable and longer-lived than a 671 nm. This helps to make the Rb-based cold atomic pressure standard easily portable, which could be shipped to other places in the world to directly compare with other UHV standards. For these reasons, we believe that it is easier to commercialize a Rb-based rather than a Li-based CAPS.

Based on the comparisons above, we believe  ${}^{87}\text{Rb}$  is a better fit to build the CAPS.

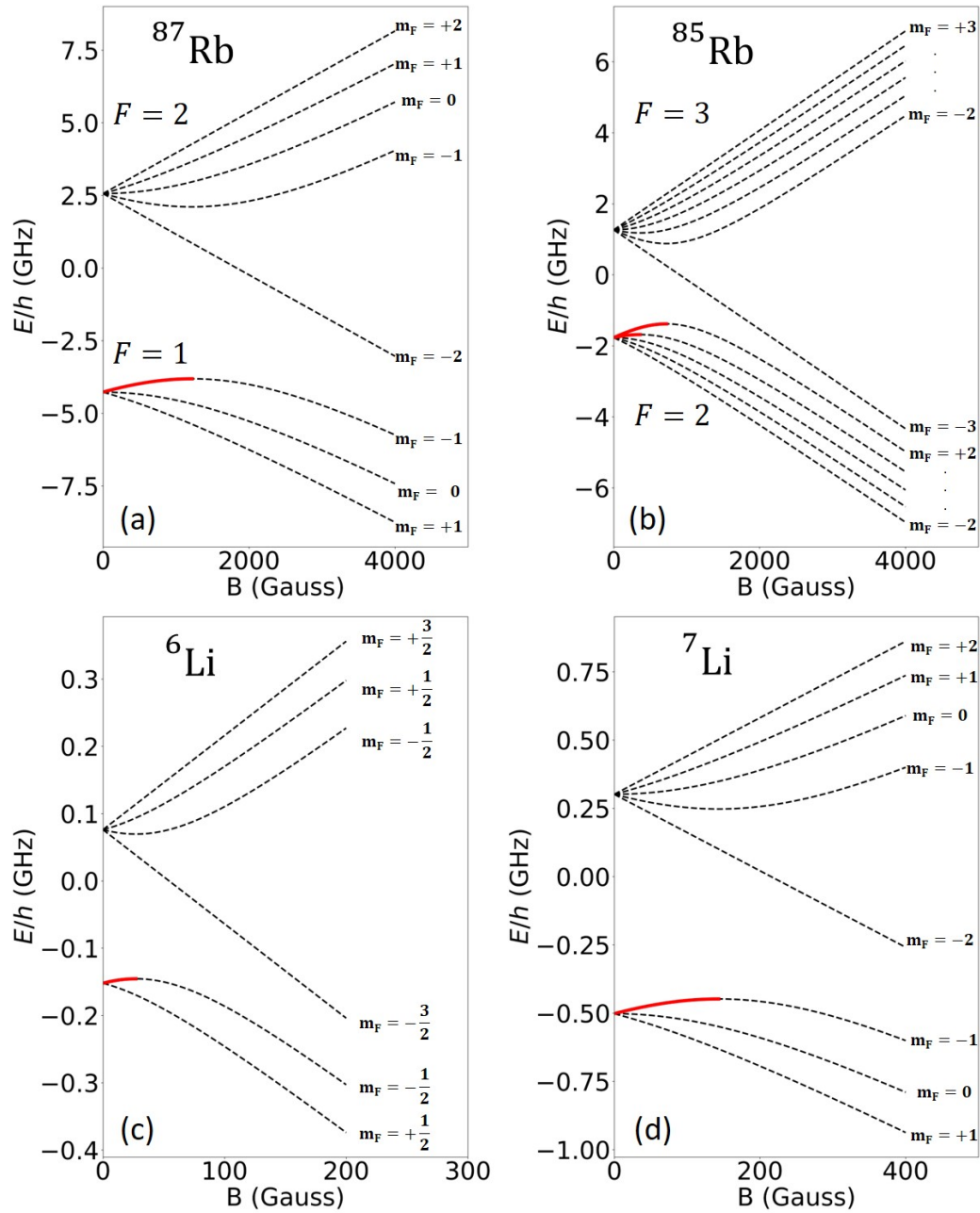


Figure 3.4: Zeeman splitting of the ground state of an Rb or Li atom. The red curves indicate the magnetic field range of the trappable states. For the atoms in their lower hyperfine state, both  $^6\text{Li}$  and  $^7\text{Li}$  have a single lower hyperfine ground state that can be trapped  $|F = 1/2, m_F = -1/2\rangle$  and  $|F = 1, m_F = -1\rangle$ , respectively.  $^{87}\text{Rb}$  has the requisite single trappable state,  $|F = 1, m_F = -1\rangle$ , while  $^{85}\text{Rb}$  has two trappable states  $|F = 2, m_F = -1\rangle$  and  $|F = 2, m_F = -2\rangle$ . Note the states are labeled using their sublevel quantum numbers when the external field is low.

All of the work presented in this thesis was obtained from an apparatus designed to work with Rb atoms.

## 3.2 Laser System

The first important part of the CAPS is the laser system, which consists of multiple leading laser units, a frequency lock system, a power amplification system, and essential optics. The output of the laser unit is frequency selected and stabilized. Then the light goes to one or more power amplification systems to obtain sufficient power for the magneto-optical trap (MOT). The amplified light will then be frequency shifted and magnified/demagnified through a group of optics in order to form the beams required for the MOT. In this section, I begin by introducing the leading laser units. Then I will introduce the frequency stabilization system and the laser power amplification system. Finally, I will present the details of the optics design.

### 3.2.1 Laser units

As discussed in section 3.1, two sets of lasers are required to Doppler cool and trap  $^{87}\text{Rb}$  atoms. One is the pump laser which drives the transition from  $5^2S_{1/2}|F = 2\rangle \rightarrow 5^2P_{3/2}|F' = 3\rangle$ , the other is the repump light driving the transition from  $5^2S_{1/2}|F = 1\rangle \rightarrow 5^2P_{3/2}|F' = 2\rangle$ .

The frequency difference ( $f_{\text{repump}} - f_{\text{pump}}$ ) between them is about 6.56 GHz, which falls in the operating range of the electro-optical modulator (EOM). Therefore, one can generate the repump light using an EOM to generate phase modulation induced sidebands of the pump light. This approach may be useful for building a portable cold atom system since it eliminates the need for a separate laser to generate repump light. However, we generate the pump and the repump light using two home-build extended-cavity diode lasers (ECDL), referred to as leading lasers. They are designed to have a wide ( $\sim 8$  GHz) mode-hop free range covering both the pump and repump transitions, making them interchangeable. The detailed design of home-build ECDL lasers can be found in [98, 99], but the original laser diodes have been replaced with ones from Thorlabs (L785P090). With this new type of diode, the output power after the grating is around 50 mW with the driving current at 90 mA. The Littrow configuration is used in the laser design, as shown in figure 3.5. In this configuration, 1<sup>st</sup> order diffraction beam is directly reflected directly back from the grating to select the frequency of injection, whereas the 0<sup>th</sup> order beam is sent out as the output of the laser.

Therefore changing the grating angle, the laser feedback frequency will be changed, which controls the laser output frequency. With this feature, one can stabilize the laser frequency by continuously adjusting the grating angle, which is achieved by using the angle piezo and the length piezo, as shown in figure 3.5 (a). However, the feedback from mechanically steering the grating is slow, so we also need to provide a fast control by adjusting the laser diode current via a home-built current controller. One of the disadvantages of using the littrow configuration is that the angle of the output light will be changed if the selected frequency varies. This will make the alignment of the beam through the downstream optics change with the laser frequency. Fortunately, the angle of the grating does not change significantly once the laser is locked, so the alignment of the optics need not be changed.

The horizontal and vertical knobs in figure 3.5 are used to manually align the injection of the laser diode and coarsely select the frequency. One should know that the vertical knob controls the direction of the reflected beam, thus, mainly determining the injection quality of the laser diode. The better injection, the wider the mode-hop free tuning range will be. The horizontal knob controls the relative angle of the grating to the laser diode, thus setting the reflected beam's frequency. One should adjust the vertical knob to obtain a good injection (determined by monitoring the reduction in the laser's threshold current) and then adjust the horizontal knob to select the desired frequency. Besides the mechanical control of the laser diode grating, the temperature of the diode is also controlled by a Peltier element attached to the bottom of the laser mounting frame, which is driven by a temperature controller. At room temperature, the fluctuations of the diode temperature is about  $\pm 1^\circ\text{C}$ , which is not ideal. Our lab is planning to build a temperature-controlled enclosure for the leading lasers, and the hope is that this will help reduce temperature fluctuations.

#### 3.2.2 Frequency stabilization system

Since the output light from the laser unit is frequency selected by the grating, the alignment and thus frequency can vary due to the environmental changes such as vibrations or variations of the temperature or the pressure. Therefore, an external locking system is needed to achieve active feedback control to the grating position to provide long-term stability of the laser frequency. The most common method for locking an Rb laser is

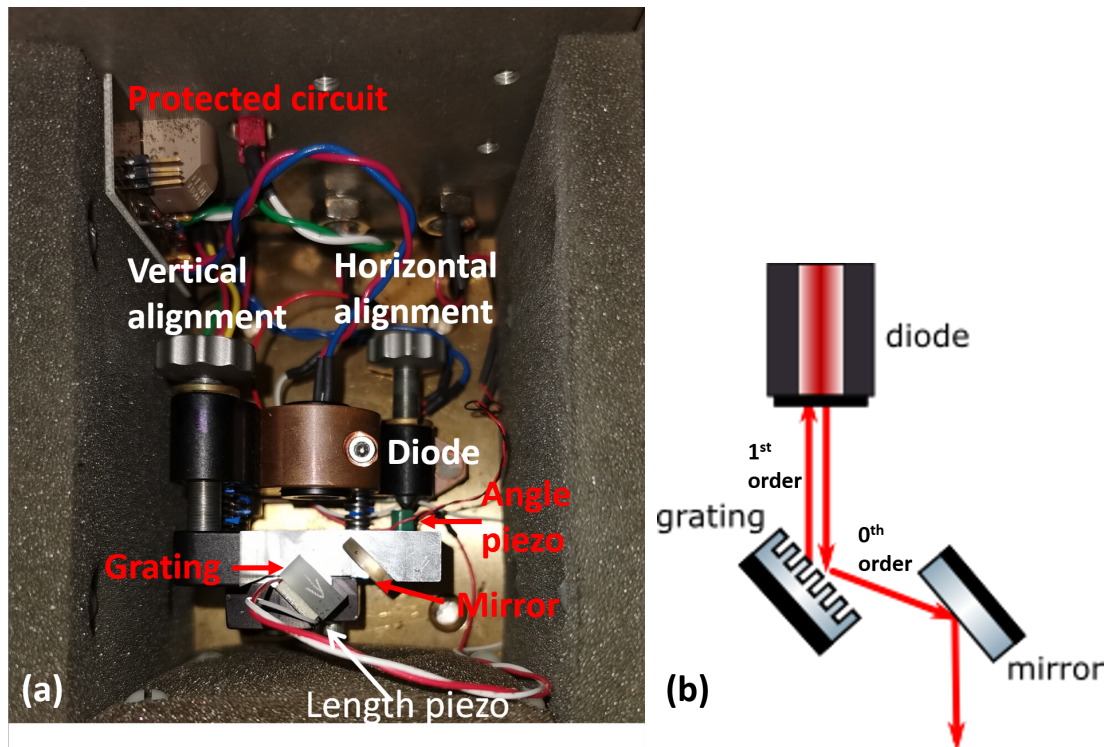


Figure 3.5: A photo and schematic of the leading laser unit. Panel (a) shows the internal design of the laser unit. Panel (b) shows the schematic of the Littrow configuration of the laser design.

called Saturated Absorption Spectroscopy (SAS) locking, also being used here, which relies on the Rb atoms' hyperfine transitions. The principle of this locking method has been widely discussed in the literature [100, 101, 102]. Here, I will only focus on the practical issues of its use in our setup. An intuitive picture of this method is that it uses the Rb atomic transition as a reference to continuously correct/adjust the laser's frequency.

To scan over all the possible atomic transitions, the laser current and the laser grating are ramped by an external input (shown by the yellow trace shown in figure 3.7). The transmission of the laser light through a cell filled with Rb vapor is monitored and reveals Doppler broadened absorption dips for both Rb isotopes (blue trace in figure 3.7). The schematic of the locking system is shown in figure 3.6. The light from the leading laser goes through a polarizing beam splitter (PBS) and is first split into two arms; One is used as the reference light to lock the repump leading laser, the other continues traveling. After another PBS, the latter one is also split into two beams; One is used as the seeding light for the following laser, and the other is sent to the SAS locking system.

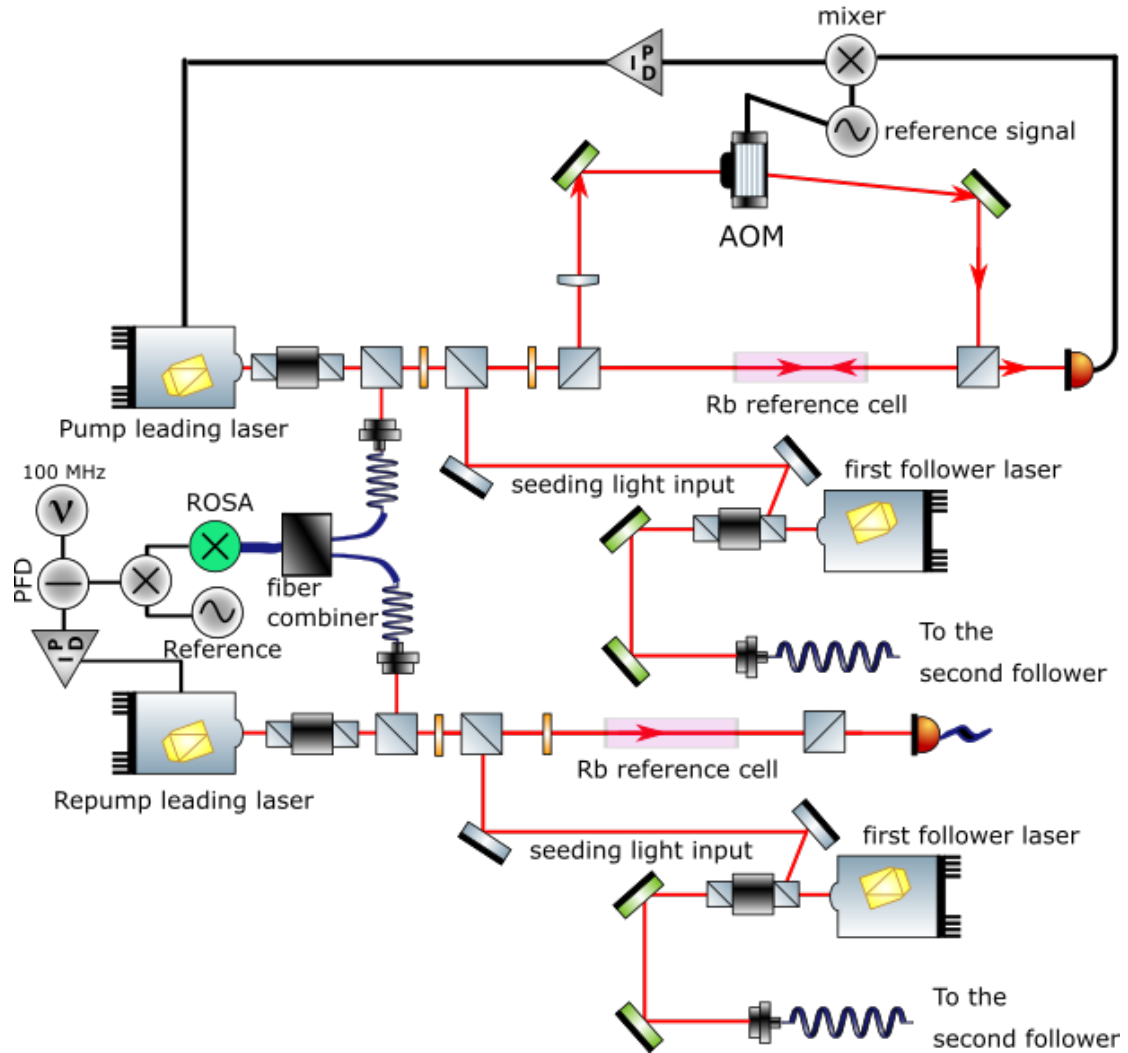


Figure 3.6: A diagram of the laser system. The top part shows the design of the pump leading laser, which drives the transition from  $5^2S_{1/2}|F = 2\rangle \rightarrow 5^2P_{3/2}|F' = 3\rangle$ . A portion of the light is sent to the SAS locking system. The remaining light is used as seed light to injection lock the first following laser. While the repump leading laser shown in the bottom part is offset locked to the pump leading laser, which drives the transition from  $5^2S_{1/2}|F = 1\rangle \rightarrow 5^2P_{3/2}|F' = 2\rangle$ . The "ROSA" in the diagram represents the optical to electrical converter, and the "PFD" represents the phase frequency detector and the reference signal is generated by an Analog Devices board (ADF 5355). The "100 MHz" signal is fed from a DDS, which is clocked by a GPS guided oscillator.

The one sent to the SAS system is further split into two beams; The weaker "probe" beam strikes a photodiode after being transmitted through a Rb vapour cell. The second, stronger, "pump" beam passes through an acousto-optic modulator (AOM) which shifts its frequency, then counter-propagates through the Rb vapour cell, overlapping the probe beam. The strong pump beam depletes the population of specific velocity

groups of atoms in the Rb vapour cell within the beam. When the probe beam interrogates the same velocity classes, the reduction in absorption is detected on the monitor photodiode. The signal of the probe beam on the PD is shown as the blue trace in figure 3.7, each peak represents each hyperfine transition, which is referred as the absorption spectroscopy.

The AOM here detunes the frequency of the pump arm by  $\nu_{\text{AOM}}$  so that the final frequency of the leading laser is  $\nu_{\text{lead}} = \nu_{\text{atomic}} - \nu_{\text{AOM}}/2$ , where  $\nu_{\text{atomic}}$  is the frequency of the selected atomic transition. In addition, the AOM is used to generate the derivative of the saturated absorption signal, shown in the pink trace in figure 3.7, so that we can isolate the frequency variation from the laser power variation. The modulated signal will then be demodulated by a mixer and sent to the PID controller to generate a laser current feedback signal and the grating angle/position feedback signal. We have found the linewidth of the leading laser under this locking scheme can be on the level of 2 to 3 MHz.

The same locking scheme can be applied to the repump leading laser. However, we chose to lock the repump light with the offset lock method. Different from the SAS lock, the offset lock method uses the pump laser as the reference and locks the repump light with respect to the pump laser, as demonstrated in figure 3.6. The pump light and the repump light are fiber-coupled and overlapped through a fiber combiner. The combined light is sent to an optical to electrical converter to generate a beatnote signal with the frequency at  $\Delta\nu_{\text{beat}} = |\Delta\nu_{\text{pump}} - \Delta\nu_{\text{repump}}|$ . For Rb cooling lasers, the frequency of the beatnote is in the range of 1 to 7 GHz, so we can easily generate a reference analog signal within the frequency range. Here, we use an analog board (ADF 5355) to generate a signal 100 MHz below the beatnote frequency. This is because the difference between the beatnote and the analog signal can later be compared to another precise signal at 100 MHz which is locked to the GPS. The comparison happens through a home-built phase frequency detector (PFD). The result of the comparison is used as an error signal and sent to a PID box to generate the feedback signal, which eventually locks the repump laser. After the offset locking, the linewidth of the repump laser can be achieved on the same level as the pump laser (reference laser). The advantage of the offset lock is that it is fairly easy to implement, while the disadvantage is the performance of the offset locked laser is highly determined by the referenced laser.

Besides these two mentioned locking schemes, there are many other locking methods. Suppose the desired frequency of the laser is nowhere near any natural atomic transitions. In that case, the Pound-Drever-Hall method can be used, which relies on the frequency selection property of the Fabry–Pérot cavity. More details can be found in [103, 104, 105].

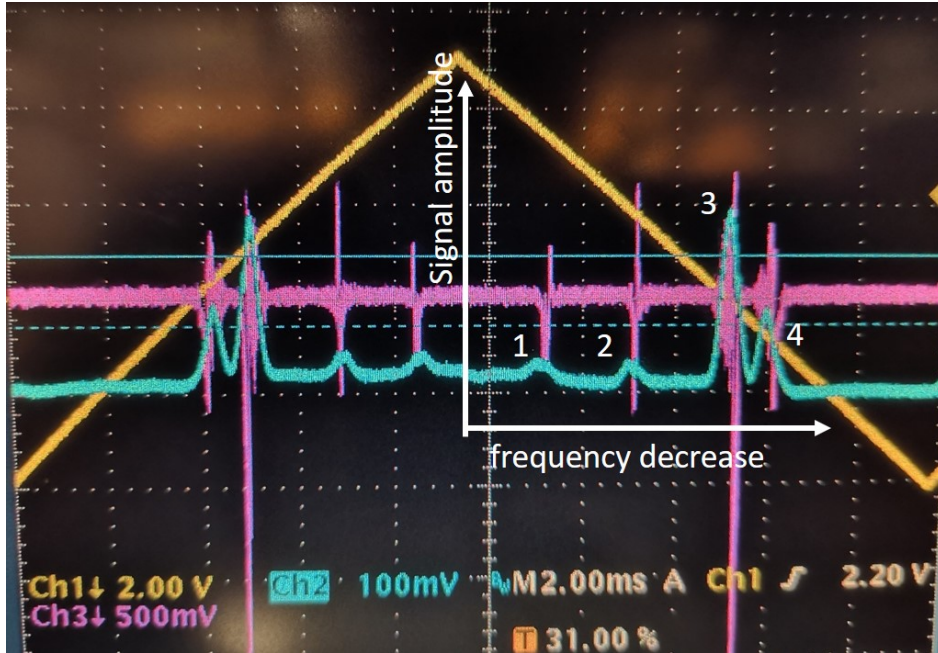


Figure 3.7: A plot of laser locking signal. The yellow trace shows the triangle ramp signal of the leading laser. The blue trace represents the Rb absorption signal, which reflects the signal of the probe beam on the PD. The pink trace is the derivative signal of the blue trace, also referred as the error signal. Peak 1 and 4 represent the transitions of  $^{87}\text{Rb}$  atoms from hyperfine ground state  $|F = 1\rangle$  and  $|F = 2\rangle$ , separately, to all the excited states in  $^2P_{3/2}$  level. Peak 2 and 3 represent the transitions of  $^{85}\text{Rb}$  atoms from hyperfine ground state  $|F = 2\rangle$  and  $|F = 3\rangle$ , separately, to all the excited states in  $^2P_{3/2}$  level.

### 3.2.3 Power amplification system

After sending the portion of the light from the leading laser to the locking system, the power available for running the experiment is only about 5 mW, too low to laser cool and trap Rb atoms. Therefore, an amplification system is required to amplify the laser power while maintaining the frequency of the laser at the same time. Here, we implemented the injection locking scheme [106, 107], as demonstrated in figure 3.6.

Some of the light from the leading laser is sent to the following laser as the seeding

light. Usually, the following laser can output a much higher power than the leading laser. Here, we use a high power diode L785H1 from thorlabs for the following laser, which can output up to 200 mW with an injection current of 200 mA. If the frequency of the seeding light is close to the frequency of the free-running following laser, then the following laser can output the light at the same frequency as the leading laser, which is called injection locking. The performance of the injection locking relies highly on the seeding light power and frequency. Usually, a seeding light with a higher power and whose frequency is closer to the frequency of the free-running following laser leads to a more robust performance of the injection locking. One good indicator of the performance is called injection factor,  $B$ , which can be calculated by the expression,

$$B = \frac{W_1 - W_b}{W_2}. \quad (3.4)$$

Here  $W_1$  and  $W_2$  represent the power of the following laser with and without the seeding light running at its threshold current <sup>4</sup>, which is 40 mA for L785H1 type diode.  $W_b$  represents the baseline power when there is only the seeding light and no following laser. The higher the injection factor,  $B$ , the better the injection-locking performance.

Suppose the power after the following laser is still not enough. In that case, we can add a second stage of the amplification system similar to the first one utilizing the injection locking scheme. We used the light from the first following laser as the seeding light distributed to different experiment apparatuses. We built a second-stage power amplification system for each apparatus to amplify the seeding light. The experiment apparatus introduced in this thesis requires a very high pump power, so a third-level amplification system is involved. In this third amplification system, we used a tapered amplifier (TA) as the following laser, bought from Toptica. The power of the seeding light injected into this TA cannot exceed 45 mW. Here, we use 38 mW of injection power. The TA can output about 2.2 W at the current 3100 mA. The maximum output power is 3.8 W at the maximum operating current 4500 mA. **Warning: This TA should not be operated (i.e. turned on) without seeding light applied and it should not be left off with seeding light incident on the chip for an extended period of time.**

---

<sup>4</sup>The threshold current means the minimum current required to initiate laser diode operation.

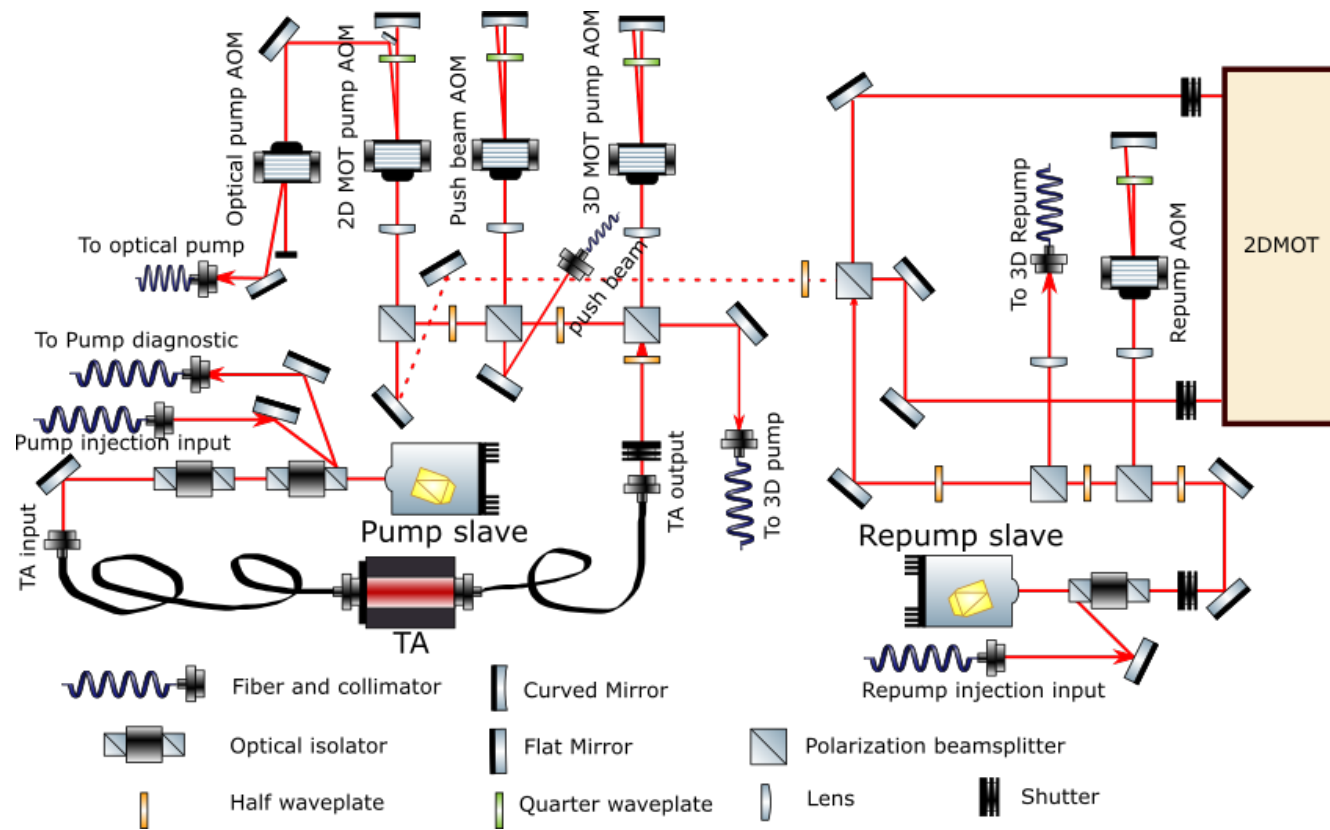


Figure 3.8: A schematic of the following laser setup. A seeding light from the leading laser unit first injection locks a following laser in the pump laser system. Next, the output from the pump following laser is guided into a tapered amplifier (TA) through a fiber. Then the output from the TA will be split into three parts, one is used as the 3D MOT pump light, the second one is used as the push light, and the third one is used as the 2D MOT pump light. Their frequencies are all being first shifted by the double-pass AOM system and then guided into the 3D and 2D MOT system. A similar power amplification setup is used in the repump laser system without a TA since the power requirement of the repump light is low. Instead of controlling the 3D and 2D repump laser frequencies separately, they have the same frequency by sharing a double-pass AOM system.

### 3.2.4 Essential optics and additional lasers

#### Tabletop optics

After the light is amplified by the power amplification system, it will be further split and sent to different regions of the apparatus, such as the 3 dimensional (3D) MOT section and the 2 dimensional (2D) MOT section. This is achieved using a combination of the half waveplates (HWP) and the polarizing beam splitter (PBS). As shown in figure 3.8, the pump light after the TA is divided into the 3 dimensional (3D) MOT pump light, the 2 dimensional (2D) MOT pump light, the push beam, and the optical pump beam. Next, the repump light is split into the 3D MOT repump light, and the 2D MOT repump light. Both the pump and repump laser beams going to the 2D MOT section travel in free space. They are combined through a PBS, then they are expanded through a telescope into a 1.5 inch  $1/e^2$  diameter beam before going into the 2D MOT section, as shown in figure 3.10 (a).

We send the laser beams to the 3D MOT region via fibers, which makes post-fiber alignments much easier if the optics before the fiber are changed. To avoid the variation of the polarization of the pump light over time, the pump light is sent through a Glan-Thompson (GT) prism after the fiber, as shown in figure 3.10 (b). Then it goes through a telescope so that the  $1/e^2$  diameter is expanded to 1 inch. However, the setup of the repump light is slightly different since Rb atoms are not very sensitive to the polarization of the repump light. This is because the energy splitting between the two hyperfine ground states,  $|F = 1\rangle$  and  $|F = 2\rangle$  is relatively large. As a result, the atoms cycling in the main transition  $|F = 2\rangle \rightarrow |F' = 3\rangle$  is less likely to leak out to the lower hyperfine ground state, thus depending less on the repump light. Therefore, we don't need to add a GT into the repump laser path, and we can use a large beam fiber collimator (F810FC-780) for the repump light, which makes the alignment easier.

The pump and the repump beams are overlapped through a PBS and sent to the 3D MOT glass cell along 3 perpendicular axes to form the MOT, as shown in figure 3.11. The HWPs in the combined laser path are used to adjust the power balance between two arms. Each arm of the combined light is sent through a quarter waveplate (QWP) to create the requisite right-hand circular polarization (RCP) in order to drive  $\sigma^-$  transition ( $|F, m_F\rangle \rightarrow |F, m_F - 1\rangle$ ) of the atoms with the help of the trap's magnetic

field. Note the vertical arm of the MOT light has an opposite polarization to the horizontal arms due to the opposite direction between the axial and radial magnetic fields generated by the magnetic coils in an anti-Helmholtz configuration. We also add QWPs in their retro-reflection path to keep the RCP polarization.

### Optical pumping light

Besides the pump and repump light here, we add an optical pump (OP) beam which is used to assist in driving Rb atoms from their lower stretched states  $|F = 2, m_F = -2\rangle$  to the higher stretched states  $|F = 2, m_F = +2\rangle$  since  $|F = 2, m_F = -2\rangle$  state is not trappable in the magnetic field, as shown in figure 3.9. Atoms trapped in the  $|F = 2, m_F = +2\rangle$  state experience a higher trap depth than atoms trapped in the  $|F = 1, m_F = -1\rangle$ , which will help determine  $\langle\sigma_{\text{tot}}v\rangle$  more accurately (details can be found in section 5.1). To transfer atoms from their lower stretched states  $|F = 2, m_F = -2\rangle$  to the higher stretched states  $|F = 2, m_F = +2\rangle$ , we should drive  $\sigma^+$  transitions ( $|F, m_F\rangle \rightarrow |F, m_F + 1\rangle$ ), as demonstrated in figure 3.9.

This can happen when the magnetic field points along with a right-hand circular polarized (RCP) light or the magnetic field points toward a left-hand circular polarized (LCP) light. Here, we choose the polarization of the OP light as RCP by using a QWP and adding an extra magnetic field pointing along with the OP light. The extra magnetic field is generated by a set of compensation coils will be introduced in the later section 3.3.3. However, the reflected OP light is not sent through a QWP, so the polarization of the reflected beam is LCP. In the presence of the same extra magnetic field, the reflected beam can also drive  $\sigma^+$  transitions, which will increase the OP efficiency. We have found that the polarization of the OP light significantly affects the OP efficiency, so we also add a GT in the path to keep the polarization clean.

The generation of the optical pumping light is shown in figure 3.8. We pick up the zeroth-order light of the 2D MOT pump after the AOM and send the light to another AOM to red detune this laser beam by 67 MHz, shifting it on resonance with the  $|F = 2\rangle \rightarrow |F' = 2\rangle$  transition. The light is then sent to the 3D MOT region via a fiber.

Similarly, both the pump and the repump light are also required further frequency shifted since the SAS locking system, and the offset locking system are designed to lock the frequencies of the pump and the repump at 180 MHz red detuned to the transitions

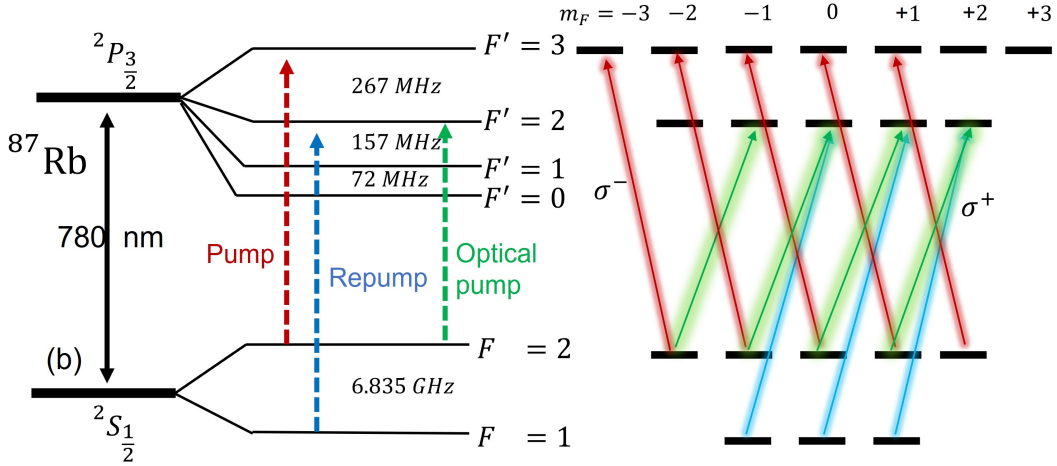


Figure 3.9: Hyperfine splitting and Zeeman sublevel energy diagrams for  $^{87}\text{Rb}$  ( $I = 3/2$ ). The hyperfine energy separations are indicated for each electronic state. The red dashed line represents the pump light which covers the transition from the upper hyperfine ground state,  $|F = 2\rangle$ , to the excited state,  $|F' = 3\rangle$ . Similarly, the blue dashed line represents the repump light which covers the transition from the lower hyperfine ground state,  $|F = 1\rangle$ , to the excited state,  $|F' = 2\rangle$ . The green dashed line represents the repump light which covers the transition from the hyperfine ground state,  $|F = 2\rangle$ , to the excited state,  $|F' = 2\rangle$ . Different color-coded is for distinguishing different lasers not representing the actual wavelength. The right panel shows the Zeeman sublevel splittings for the corresponding hyperfine states. Here, the pump laser drives the  $\sigma^-$  transition, repump and optical pump lasers drive the  $\sigma^+$  transitions. The details are presented in text.

$|F = 2\rangle \rightarrow |F' = 3\rangle$  and  $|F = 1\rangle \rightarrow |F' = 2\rangle$ , respectively. This is achieved by using acoustic-optical modulators (AOM). The AOMs are from IntraAction Corp. with the center driving frequencies at 80 MHz. To set the laser detuning back to resonance, we pass the light through an AOM driven with an RF signal at 90 MHz and in a double-pass configuration [108], as shown in figure 3.8. One can change the output laser frequency by adjusting the driving frequency of the AOM. The double-pass configuration provides several advantages: One is to prevent the beam from steering during the change of the driving frequency, the other benefit is to keep the power of the light after the AOM constant over a large range of driving frequencies. With careful alignment of the laser through the AOM, one can achieve a  $\sim 110$  MHz frequency range of power larger than 150 mW, as plotted in figure 3.12.

Although setting up the AOM in the double-pass configuration gives us a constant power range, we still find that the power of the light drifts over time due to the change of the temperature of the AOM or the variation of the amplitude of the AOM driving

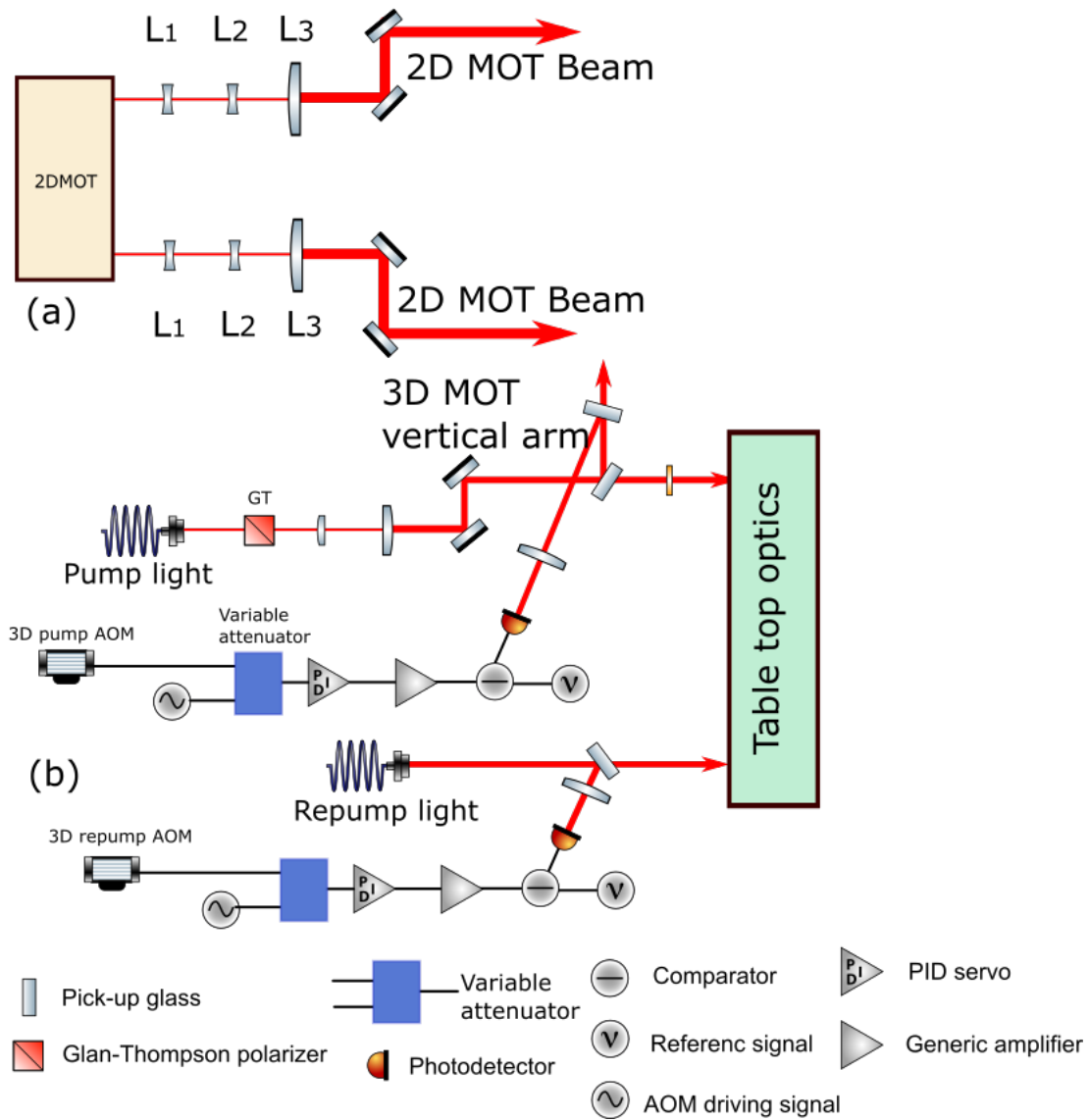


Figure 3.10: A schematic of the lasers going into the 2D and 3D MOT region. Panel (a) shows the optics design for the 2D MOT side. The optics design is mirror symmetry of both arms. The lens  $L_1$  is plano-concave with a focal length,  $f = -50$  mm.  $L_2$  is a  $f = -75$  mm plano-concave lens, and  $L_3$  is a  $f = +200$  mm plano-convex lens. Panel (b) shows the optics design for the pump and repump light going into the 3D MOT section. The pump and the repump beam are combined through a PBS.

signal. To achieve a more stable power during the experiment time, we implement a PID power stabilization system. Figure 3.10 (b) shows the schematics of PID power stabilization systems for both the pump and the repump light. They share the same design: First, we used a piece of glass to pick up a small portion of the light ( $< 2$  mW) after the GT. It was thick to avoid interference fringes being superimposed on the

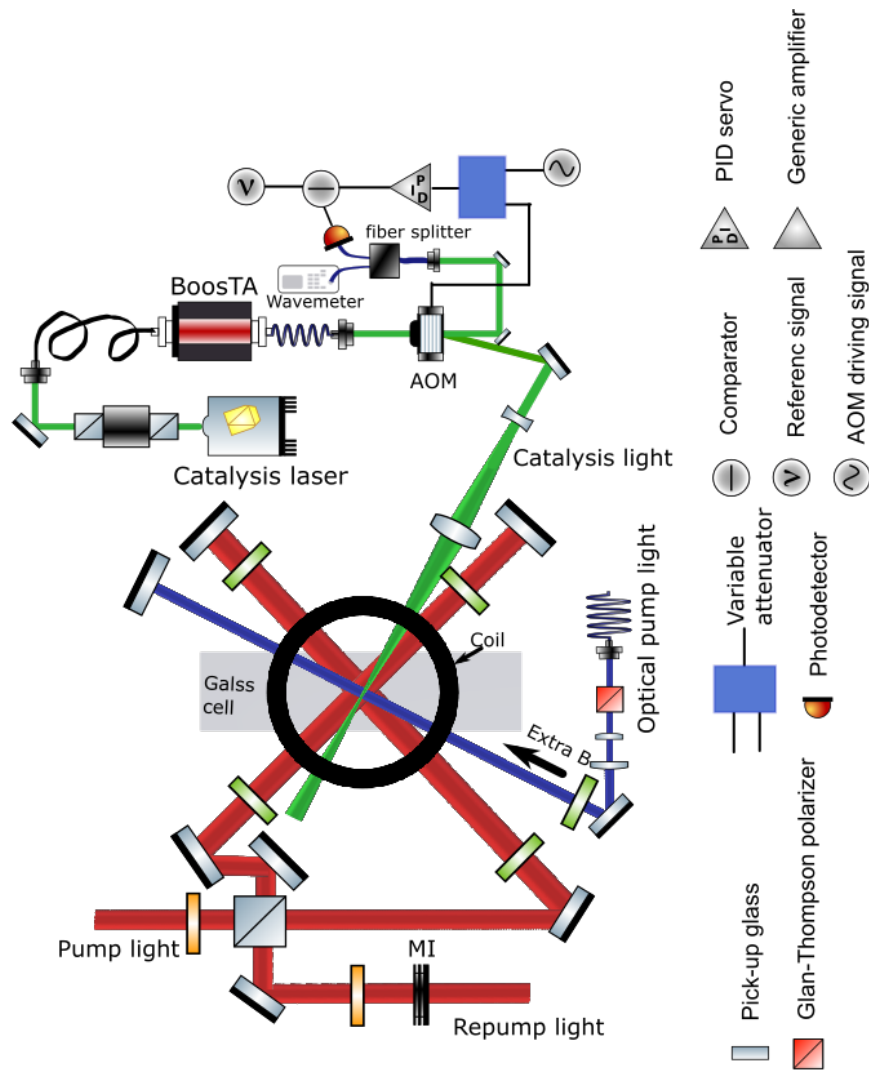


Figure 3.11: A detailed schematic showing the inside of the tabletop optics in figure 3.10. The pump and the repump light (red lines) are combined through the HWPs (orange plates) and a PBS and sent to the MOT region. The QWPs (green plates) are added to create the circular polarization needed (RCP) to drive  $\sigma^-$  transitions of the atoms. However, the OP light (blue line) is used to drive  $\sigma^+$  transitions in  $|F = 2\rangle \rightarrow |F' = 2\rangle$  in order to help atoms accumulate in  $|F = 2, m_F = 2\rangle$  state to optimize the transfer into the magnetic trap. The polarization of the incident optical pump light is set RCP with a QWP, but an extra magnetic field is added along the same direction (this additional field is generated by the compensation coils, shown in figure 3.16). The reflected OP light will not go through a QWP so that it has the left-hand circular polarization (LCP) and also drives  $\sigma^+$  transitions with the same magnetic field. This improves the optical pumping efficiency. The catalysis light (green line) is focused on the atoms through a short-focus lens ( $f = 100$  mm). The details of the catalysis setup can be found in the text (section 3.2.4). The ‘MI’ (black block) in the repump beam path represents the motorized iris, which is used to vary the size of the repump beam to control the trap depth of a MOT (details can be found in section 6.2.2).

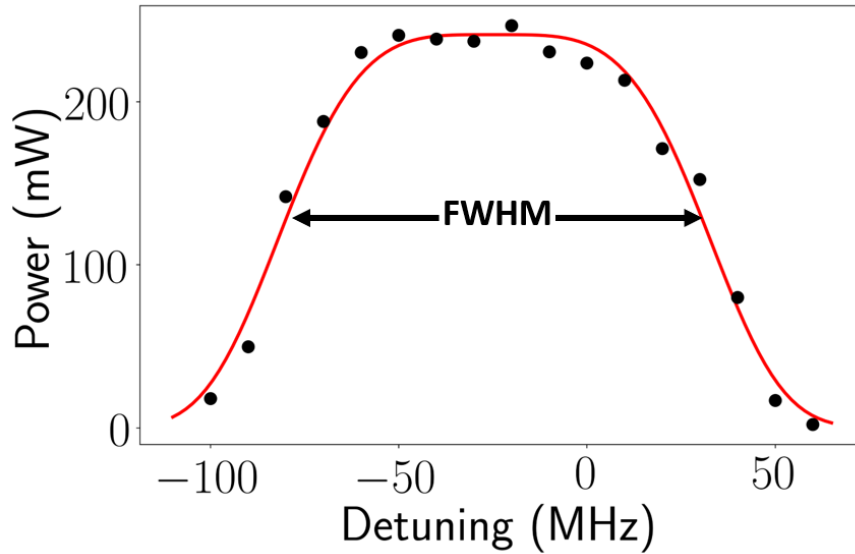


Figure 3.12: A plot of laser power versus the driving frequency of the AOM. The black dots are experiment data, the red line is fit to guide eyes. The FWHM is found to be around 110 MHz, which means the system can output up to 150 mW of laser power over this range.

feedback signal to a PID box. Then, the picked-off light is focused on a PD through a single lens. The PD signal is compared with an analog DC voltage, which indicates the power set point. The comparison result, referred to as the error signal, is then sent to the PID control box. Finally, the output of the PID box will adjust the attenuation of the driving amplitude of the AOM through a variable attenuator. Varying the driving amplitude of the AOM will change the power of the light, which provides the power control option.

With the PID power stabilization system, we found that the laser power's short- and long-term stability has been greatly improved. Figure 3.13 shows a measurement of the power stability of the pump light with and without the PID control. As one can see, the power of the pump laser power drifts significantly over time with the uncertainty of around 40 % if the PID control system is not implemented. In contrast, the uncertainty drops to about 0.1 % under the control of the PID system. The short-term stability is also increased by more than a factor of 2 when the PID control system is in use. Similar results can be found in the Allan deviation measurements for both cases, as shown in figure 3.13 (b).

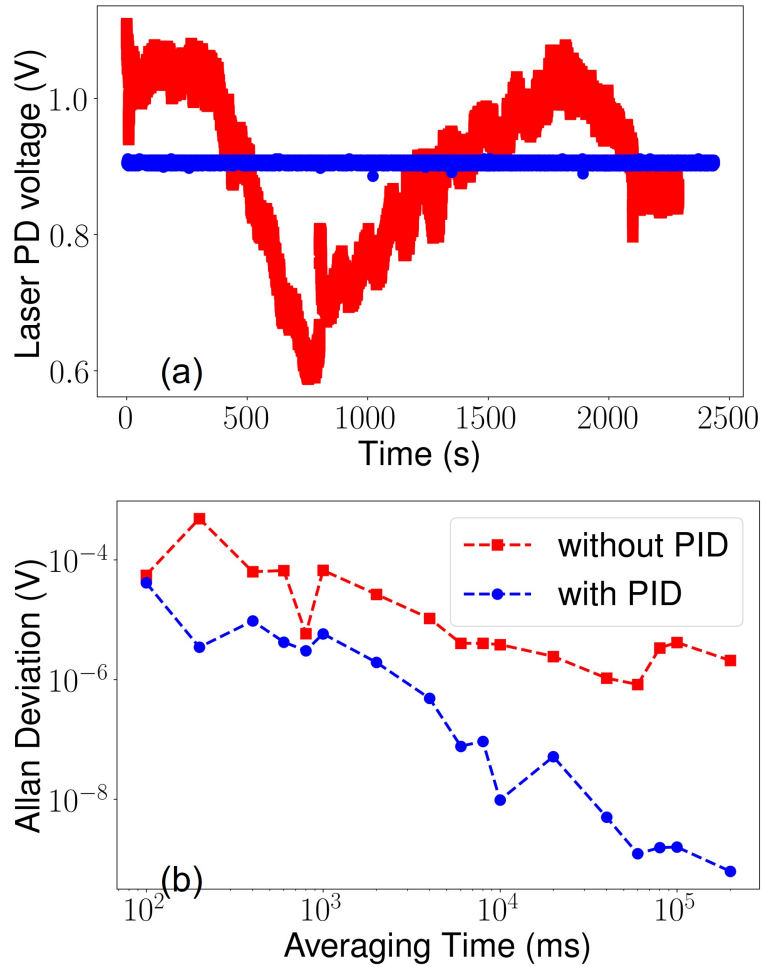


Figure 3.13: A plot of the laser power stability measurement with and without the PID control system. Panel (a) shows the laser power as a function of time. Blue circles and red squares represent the case with and without the PID control, respectively. The laser power is measured with a photodetector (PD), and the voltage level of the PD is proportional to the laser power. Panel (b) shows the Allan deviation of measurements in (a).

### Photoassociation laser

Finally, we added an additional photoassociation laser, referred as the ‘catalysis’ laser, to the system. This ‘catalysis’ laser (CAL) is used to measure the trap depth of the MOT [71, 66]. In a MOT, two colliding cold ground state atoms can resonantly absorb a photon from the CAL, which excites them to a repulsive molecular state. The molecule quickly dissociates, and the atoms move apart, picking up kinetic energy and then spontaneously emitting back to the ground state. The mechanism of the photoassociation process is illustrated in figure 3.14. The kinetic energy picked up by each atom in the

case of homonuclear collisions is  $h\Delta_{cl}/2$  where  $\Delta_{cl}$  is the detuning of the CAL above the atomic resonance between the ground and the excited state ( $5^2S_{1/2}$  to  $5^2P_{3/2}$  in the case of  $^{87}\text{Rb}$ ). If  $h\Delta_{cl}/2 > U$ , where  $U$  is the trap depth, then the CAL will cause a loss of the atoms from the trap. Therefore, by measuring the trap loss as a function of the CAL's detuning, the average MOT trap depth can be determined from the peak loss rate (more details of the trap depth measurements are discussed in section 6.2.2).

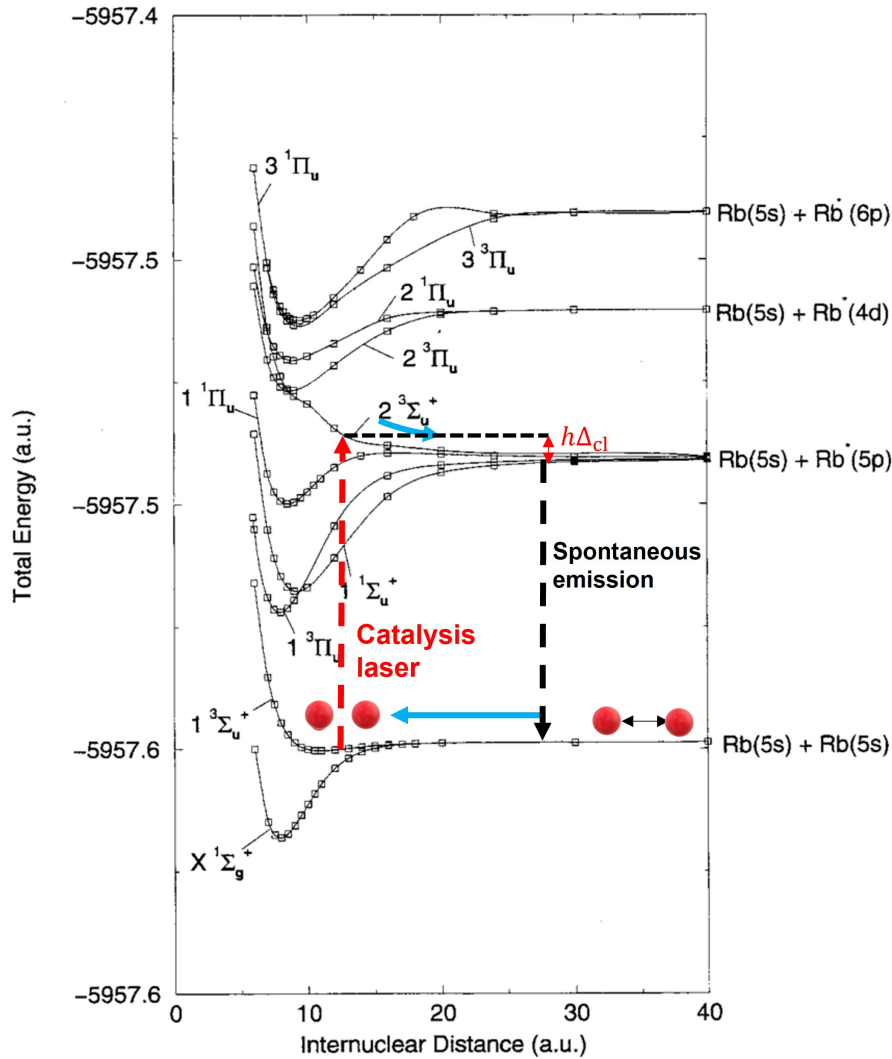


Figure 3.14: A ‘catalysis laser’ excites the ground state atoms to a repulsive excited molecular potential. The  $\text{Rb}_2$  molecular potential energy curves shown are taken from reference [109]. The atoms quickly repel each, picking up  $h\Delta_{cl}/2$  in kinetic energy for the homonuclear case.  $\Delta_{cl}$  is the detuning of the catalysis laser above the  $5^2S_{1/2}$  to  $5^2P_{3/2}$  atomic resonance for  $^{87}\text{Rb}$ . A loss will result if the kinetic energy imparted to the atoms is greater than the trap depth.

The experimental setup of the CAL is presented in the top part of figure 3.11. A

distributed feedback (DFB) laser is used to generate the seeding light for the CAL. The DFB laser diode (EYP-DFB-0780-00080-1500-TOC03-0005) is purchased from Toptica Eagleyard. The output frequency of the DFB diode can be varied as a function of the operating current and the temperature. We have measured that the frequency varies by  $-1.15$  GHz/mA and  $-20.5$  GHz/ $^{\circ}$ C, and the output light is on resonance with the pump transition ( $F = 2$  to  $F' = 3$  in the case of  $^{87}$ Rb) when the current is at 183 mA and the temperature is  $36.8^{\circ}$ C. The current and the temperature of the CAL are both controlled by the controller from Vescent (D2-105) and are programmed by the external analog inputs. We can vary the temperature from  $15^{\circ}$ C to  $40^{\circ}$ C (max temperature) and vary the current from 100 mA to 180 mA. Below 100 mA, the output power of the DFB laser is not enough to injection lock the TA system, as discussed next.

The output of the light from the DFB laser is not enough to induce the photoassociation process in a MOT, especially when the detuning is far away. Therefore, we amplified the DFB laser power through a tapered amplifier (TA) purchased from Toptica (BoosTA). The frequency of the TA output follows the frequency of the DFB laser through the injection lock, as mentioned in section 3.2.3. The output power of the DFB laser is 70 mW at maximum. After the power stabilization system and the fiber coupling loss, about 20 mW of power is sent into the TA and amplified to 500 mW.

However, as we change the current of the DFB laser to adjust the frequency, we also change the power. This leads to the power change of the TA as well. To mitigate the power variation, we also implemented a power stabilization system here. The output of the TA is sent through an AOM. The zeroth-order is sent to a fiber splitter (PN780R5A1, Thorlabs). One of the fiber splitter outputs is sent to a wavemeter which is used to monitor the frequency of the CAL during the measurements. The other output is sent to a fiber-coupled PD (DET02AFC). The signal of the PD is then sent to the PID lock system, as we did for pump and repump light. With this PID stabilization system, we have achieved the power of the CAL stable over 500 GHz frequency tuning, which allows us to measure the trap depth as large as 14 K.

The first order of the AOM has a power of around 230 mW and is sent to the MOT region. The beam is first expanded through a concave lens, then focused down to 0.1 mm in  $1/e$  radius through a convex lens ( $f=250$  mm). This convex lens is placed on a translation stage so that we can finely adjust the beam size at the position of atoms.

The intensity of the CAL onto the atoms is over  $650\text{W}/\text{cm}^2$ . The alignment of the CAL needs to be carefully adjusted so that it can overlap with the region of atoms and involve more atoms in the photoassociation process.

## 3.3 Magnetic Field Coils

Lasers can apply velocity dependent optical forces that slow the atoms, but due to gravity, atoms can still drift away from the laser interaction region. Therefore, we need to apply a confining potential to the atoms so that they can be trapped. This confining potential can be formed in a variety of ways, such as using an optical trap [110, 111] or a magnetic trap (MT) [112, 113]. Here, we chose to use the magnetic trap, which avoids the additional photon scattering from the dipole trap light [63]. For example, the scattering of photons can heat the atoms, which causes loss after enough energy is deposited. Also, ODT light induced spontaneous and stimulated Raman transitions can populate higher-energy ground states that can then suffer single spin-changing collisions with other trapped atoms. To generate such a confinement trapping field, we use a pair of the anti-Helmholtz coil. In addition to these primary trapping coils, we also add a set of compensation coils to generate an additional quantization magnetic field to assist the optical pumping stage. It can also help cancel out the earth's magnetic field for precision measurements. Finally, I will add a single turn radio frequency (RF) coil to control the trap depth of the atoms in the MT.

### 3.3.1 2D MOT coils

A detailed discussion of the 2D MOT coils can be found in Dr. Van Dongen's thesis [1], including the design and the dimensions of the 2D MOT coils. Thus, here I will provide a summary. A picture of the 2D MOT coils installed on the 2D MOT chamber is shown in figure 3.18 (b). These consist of four rectangular coils that generate a magnetic field gradient along the two perpendicular arms of the four-way cross of the 2D MOT chamber.

The coils can be removed from the chamber if the vacuum chamber needs to be baked out. The dimensions of the coils are the following: The inside dimensions of each coil are 8 by 26 cm. The coil pair surrounding the viewports in the y-direction

is separated by 8.5 cm, and the pair surrounding the viewports in the z-direction are separated by 14 cm. There are approximately 10 layers with 12 turns per layer, totaling 120 turns. The wire used was 16 AWG magnet wire from Superior Essex (H GP/MR-200). With 5A going through all the coils, the magnetic field gradient was measured using a gaussmeter (model Bell 620) to be 16.6 G/cm along the transverse direction and 0.29 G/cm along the axial direction. An analog channel separately controls the current of each rectangular coil, and the current range is from -5.0 to 5.0 A.

#### 3.3.2 3D MOT coil

A pair of anti-Helmholtz coils are used here to generate the magnetic field for the 3D MOT. They are constructed from quarter-inch outer diameter copper tubing with a quoted 0.03 inch wall thickness and 0.0032 inch thick PVC coating from Alaskan Copper (part NO. 142797). [1]. The outer diameter of the copper tubing, including the PVC is approximately 8.3 mm, and the inner hollow core is 4.5 mm. The coil has a 188 mm outer diameter and 38 mm inner diameter. The height of each coil is 73 mm, and the distance between them is 5 cm, as shown in figure 3.18 (c). There is enough clearance between the coils and the glass cell to place an RF coil in between. However, this large separation will reduce the magnetic field gradient generated at the center of the coils. Therefore, to achieve enough strength, the coils require running a high current, which will result in generating heat. To remove the heat, we flow water through the hollow coils at 70-80 psi, and the flow rate of each coil is about 30 liter/s.

The coil is powered by a 60 V, 250 A power supply (Sorensen, LX1), and the resistance of each coil is 38.5  $\Omega$ . The original power outlet we have is 20 A and 208 V so the maximum power from the outlet is 4160 W less than the maximum power output of the power supply. However, we found that the breaker goes off very often if we run the current at 200 A. Therefore, we upgraded the power outlet to 40 A and 208 V to handle much higher power.

#### Magnetic field gradient calibration using atoms

One can characterize the magnetic field gradient by measuring the minimum field required to trap Rb atoms in different hyperfine ground states,  $|F = 1\rangle$ , and  $|F = 2\rangle$ . In the low field regime, the energy of an Rb atom in the magnetic field can be expressed

as

$$E_B = -\vec{\mu}_B \cdot \vec{B}(r, I) = -\mu_B g_F m_F b' I \sqrt{\frac{x^2}{4} + \frac{y^2}{4} + z^2}. \quad (3.5)$$

Here,  $\mu_B$  is the Bohr magneton,  $g_F = 1/2$  is the Lande factor, and  $m_F$  indicates the Zeeman sublevels of the hyperfine state (the quantization axis is chosen to be along the direction of the local magnetic field). The coordinate system is centered at the location where  $B=0$  between the coils.  $r = (x, y, z)$  in Eq. 3.5 represents the position from the center of the field.  $I$  is the current running through the coil, and  $b' = \frac{dB}{dZdI}$  is the magnetic field axial gradient along the z-direction. Then the magnetic force along z-axis can be calculated by

$$F_{B,z} = -\frac{dE_B}{dz} = \mu_B g_F m_F b' I. \quad (3.6)$$

We can see that the minimum magnetic field required to trap an atom happens when  $F_{B,z}$  equals the gravitational force  $F_g = mg$ , which leads to

$$\begin{aligned} F_g &= F_{B,z} \\ mg &= \mu_B g_F m_F b' I \\ b' &= \frac{mg}{\mu_B g_F m_F I}. \end{aligned} \quad (3.7)$$

Therefore, we can determine the magnetic field axial gradient by scanning the magnetic coil current to find when the atoms start being trapped. An example measurement of the number of atoms in the magnetic trap as a function of the magnetic field set by the coil current,  $I$ , is shown in figure 3.15. We can see the minimum trapping current for  $|F = 1, m_F = -1\rangle$  state is 22.4 A, and the minimum trapping current for  $|F = 2, m_F = 2\rangle$  state is 11.2 A. The ratio of the two minimum trapping currents matches the ratio of the quantum numbers of the sublevels. Therefore, we can solve the magnetic axial field gradient  $b' = 1.36$  G/cm/A, and we can get the radial field gradient,  $2b' = 0.68$  G/cm/A, given the coil is in the anti-Helmholtz configuration. Those quantities can be used to determine the strength of the magnetic field gradient,  $dB/dz$ . Usually, we run  $I = 10$  A ( $b'I = 13.6$  G/cm) in the coil to trap atoms in the MOT, while we run  $I = 200$  A ( $b'I = 272$  G/cm) in the coil to confine atoms in the

MT.

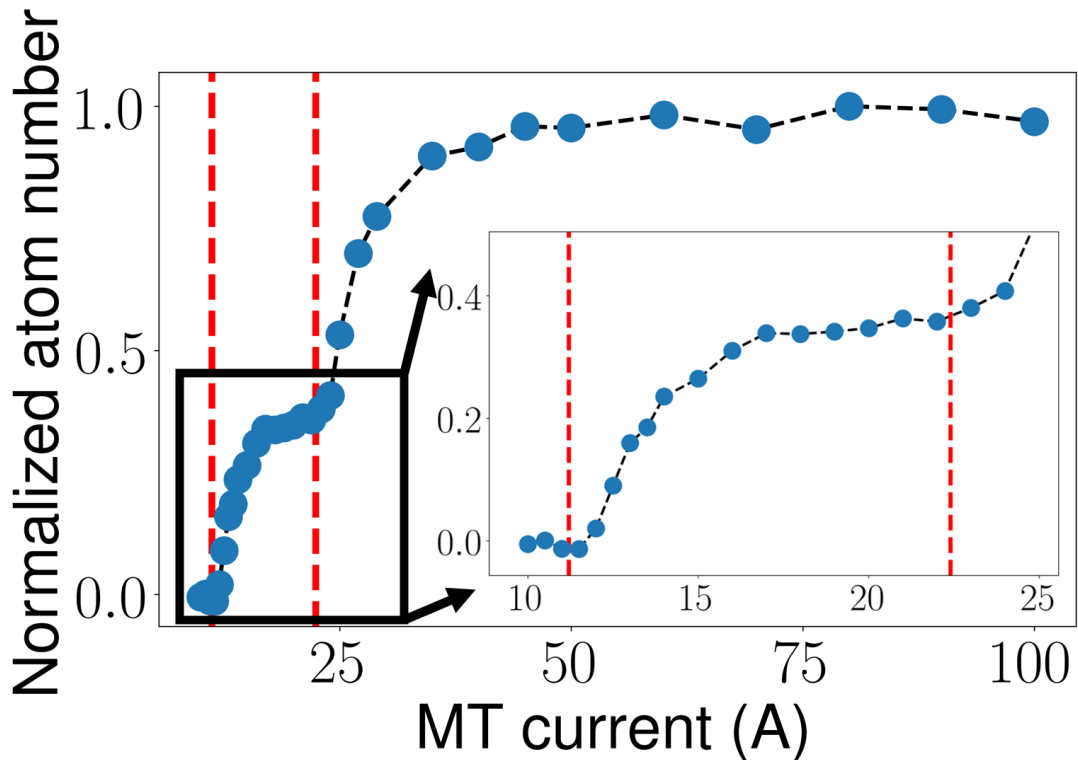


Figure 3.15: Normalized  $^{87}\text{Rb}$  atom number versus the MT coil current. The two vertical lines represent the threshold current at 11.2 A and 22.4 A for trapping  $m_F = 1$  and  $m_F = 2$  states, respectively. No atoms can be trapped below 11.2 A because the magnetic force of the MT is not enough to overcome gravity for any atomic state. As the current increases past 11.2 A, atoms in  $m_F = 2$  state can be trapped in the MT and then level off. As the current passes 22.4 A, atoms in  $m_F = 1$  state start being trapped since the minimum magnetic field gradient to trap  $m_F = 1$  state is twice as trapping  $m_F = 2$  state.

### 3.3.3 Compensation coils

Besides the 3D and 2D MOT coils, we also add a set of compensation coils around the glass cell. The set of compensation coils consists of six rectangular coils that are made of the same magnet wire as the 2D MOT coils. A schematic of the compensation coil is shown in figure 3.16. The coils facing the same direction are connected in series, for instance coil 1 and 2 are connected in series. We use a home-built current controller to control the current running through the coil ranging from -5.0 to 5.0 A. The change of the sign of the current changes the direction of the magnetic field.

### 3.3. Magnetic Field Coils

One can use these six coils to offset the earth's field to perform precision atom interferometries. Here, we use the compensation coils to provide a strong magnetic field to improve the optical pumping by defining a quantization axis that points along the OP light propagation direction. As introduced in section 3.2.4, the purpose of the OP light is to drive Rb atoms from all  $m_F$  states to the stretched state  $|F = 2, m_F = +2\rangle$  since  $|F = 2, m_F = -2\rangle$  state is not trappable in the magnetic field. Therefore, we should drive  $\sigma^+$  transitions ( $|F, m_F\rangle \rightarrow |F, m_F + 1\rangle$ ). The polarization of the OP light is RCP, so we need to set the magnetic field to follow the direction of the OP light. Therefore, we run the compensation coil 1 and 2 at the current -3.0 A and run the compensation coil 5 and 6 at also -3.0 A. The currents running through the coils have been optimized. Note that the coil pair can be separated and controlled independently by an analog signal, which can provide more precise control of the magnetic field.

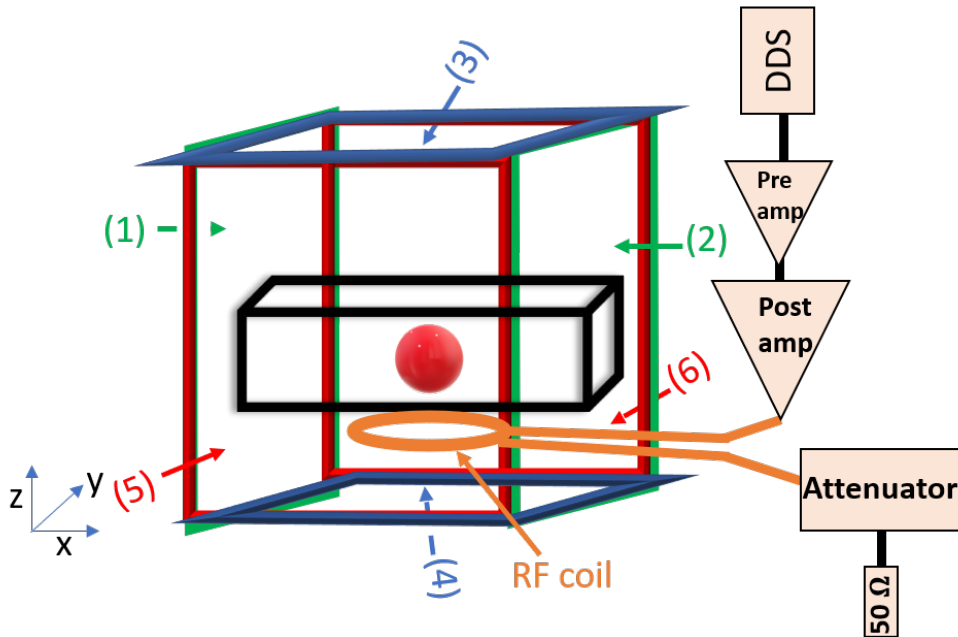


Figure 3.16: A diagram of the compensation coil and the RF coil. Coil pairs 1-2, 3-4, and 5-6 are connected in series. The RF coil is placed directly under the trapping region in the glass cell. The RF signal is generated by a home-built DDS and amplified through a pre-amp (home-built) and a post-amp (Lzy-22+). The signal later gets dumped into an attenuator and a 50 ohm load after transmitting through the RF coil.

### 3.3.4 RF coil

We apply RF radiation to the trapped atom ensemble to eject those above certain energy, which sets the maximum trap depth energy of atoms. As discussed in section 3.3.2, the magnetic potential energy of an Rb atom in the magnetic trap is  $E = -\mu_{BGF} m_F b' I \sqrt{x^2/4 + y^2/4 + z^2}$ , and the energy difference between the adjacent sub-levels is  $\Delta E = \mu_{BGF} b' I \sqrt{x^2/4 + y^2/4 + z^2}$ . Therefore, if the atom absorbs an RF photon with energy,  $h\nu_{RF}$ , matching the energy difference of the adjacent sublevels, it will likely be flipped to the adjacent state. If this new state is not trappable in the MT, the atom will leave the trap eventually. This process is illustrated in figure 3.17. The resonant RF frequency  $\nu_{RF}$  can be expressed as,

$$h\nu_{RF} = h\mu_{BGF} b' I \sqrt{\frac{x^2}{4} + \frac{y^2}{4} + z^2}. \quad (3.8)$$

As one can see, this sets an oblate spheroid surface in space where the RF field is resonant with  $|F, m_F\rangle \rightarrow |F, m_F \pm 1\rangle$  magnetic dipole atomic transition. Atoms with sufficient energy to traverse this surface will, with high probability, make the transition to a non-trapped state and leave the cloud. Then, one can sweep the RF from low,  $\nu_l$ , to high  $\nu_h$  and eject all the atoms with the energy above  $h\nu_l$ . This method is usually named as RF “knife”.

Therefore, we need an RF coil to emit the sweeping radiation. Here, we build a one-loop coil by striping off a BNC cable. Although we can use more turns, we find that the stronger radiation emitted by the multi-loop coil strongly affects the current of the leading lasers. This temporarily unlocks the lasers and affects other running experiments in the lab. Building a complete Faraday cage around the RF coil would eliminate this effect, which could be designed in the future. Alternatively, one can move the leading lasers far from the RF coils. Since we are limited by the turns we can use, we decided to put the RF coil as close to the atoms as possible. It is placed under the glass cell and 2 cm away from the atoms, as illustrated in figure 3.16.

The RF signal is generated by a home-built direct digital synthesizer (DDS), which outputs from 0 to 150 MHz. The output signal of the DDS is only -20 dBm which is far from enough to flip atoms' transitions. Therefore, we use a home-built pre-amplifier to

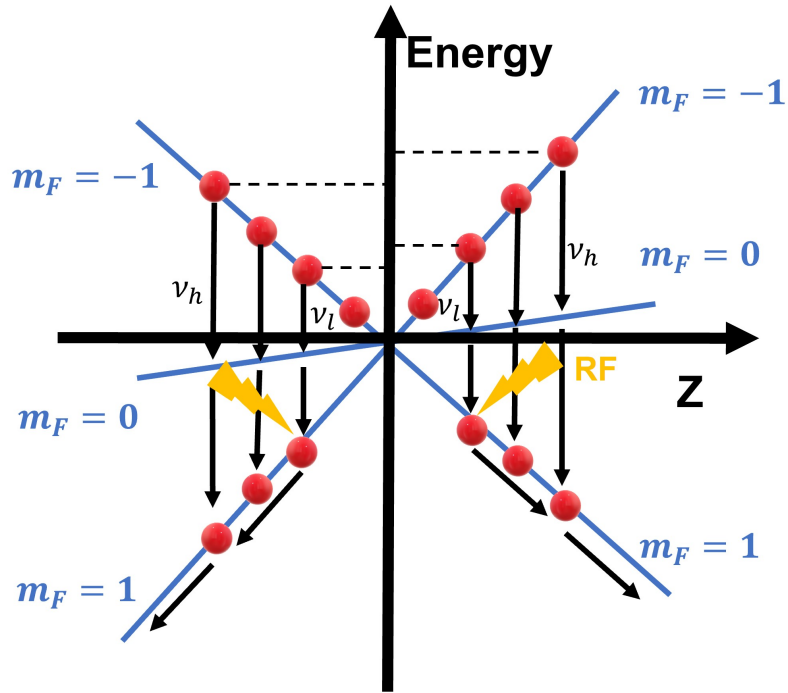


Figure 3.17: The potential energy of  $^{87}\text{Rb}$  atoms moving along the  $z$ -axis and in different Zeeman sublevels  $|m_F = 0, \pm 1\rangle$ . The RF frequency is swept between  $\nu_l$  and  $\nu_h$  ejecting atoms from the magnetic trap whose Zeeman energy lies within the range  $h\nu_l$  and  $h\nu_h$ . When the energy of the RF photon matches the energy difference between adjacent states, the atoms can absorb the photon and make a transition to a different state. There is an asymmetry to the energy surfaces introduced by the gravitational potential energy. Atoms reaching the RF surface near the lowest position in the  $Z$ -direction have less potential energy than atoms reaching any other point of the RF surface. The energy difference is here referred to as the "gravitational sag". A similar illustration can be shown for the  $X$  and  $Y$  directions, but there is no asymmetry in the energy surface.

amplify this signal to about 10 dBm. We then add a high-power post-amplifier (Lzy-22+) to further increase the amplitude to about 40 dBm. After transmitting through the RF coil, the signal gets dumped into an attenuator and a 50-ohm load. The connection is shown in figure 3.16. Given the power running in the RF coil, we can calculate the Rabi frequency of the transition,

$$\Omega = \left| g_F \frac{\mu_B}{2\hbar} B_{rf} \right|. \quad (3.9)$$

Here  $B_{rf}$  is the magnetic field generated by the RF radiation and can be calculated by

### 3.3. Magnetic Field Coils

---

(if the coil is in a circular shape),

$$B_{rf} = \frac{\mu_0}{4\pi} \frac{2\pi R^2 i}{(d^2 + R^2)^{3/2}}, \quad (3.10)$$

where  $\mu_0 = 4\pi \times 10^{-7}$  T·m/A is permeability,  $R = 1.5$  cm is the radius of the RF coil, and  $i = 0.45$  A is the current running through the coil calculated using the Ohm's law.  $d \approx 2.0$  cm in Eq. 3.10 is the vertical distance between the center of the coil and the atoms. We can find the magnetic field is about 0.032 Gauss, so the Rabi frequency  $\Omega \approx 0.1$  MHz. Given the Rabi frequency is not so large, we apply the RF signal for a total duration of  $> 0.5$  s while sweeping the RF frequency between the lower and upper limit with a sweep rate of 1 GHz so that all target atoms within the cut range can experience resonant RF radiation and are thereby ejected.

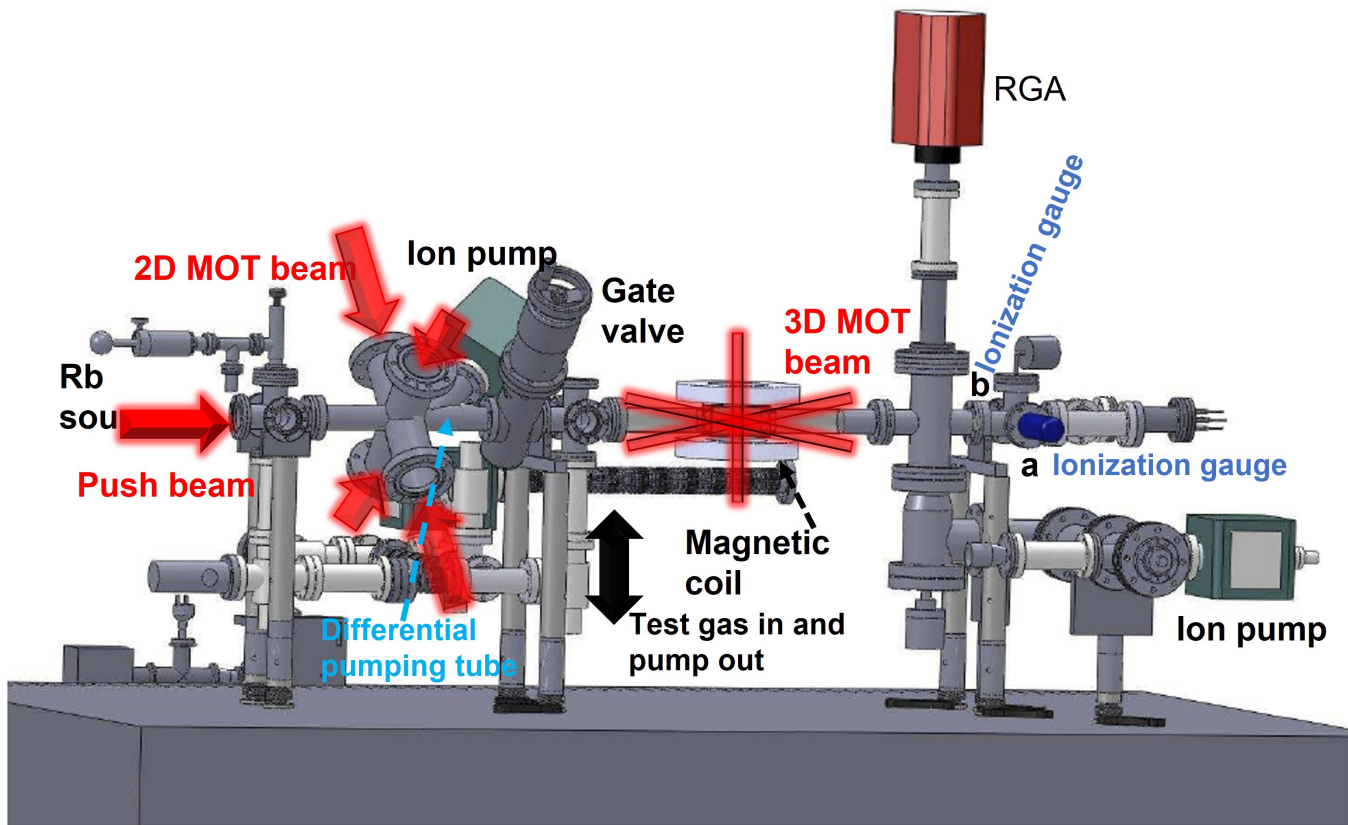


Figure 3.18: A figure of the overall design of the experiment apparatus. The apparatus consists of a Rb source stage, a 2D MOT section, a 3D MOT section (measurement section), and the pumping section. Red arrows indicate 2D, 3D MOT beams, and the push beam. The black arrow shows the port through which the test gas is introduced. A residual gas analyzer is attached to the 3D MOT section to analyze the gas composition inside the vacuum to examine the purity of the test gas. Also, two ionization gauges (IGs), labeled as 'a' and 'b' (placed across to the IG 'a'), are connected to the measurement section.

## 3.4 Vacuum Chamber

The next important part of the CAPS is the vacuum chamber which provides the vacuum environment for trapping Rb atoms. It is constructed of two stages: The source and measurement stages. A CAD schematic of the whole apparatus is shown in figure 3.18 (a).

### 3.4.1 Source chamber

Rb atoms are released from a Rb ampoule sitting in the Rb source stage. A UHV valve (X3202-60098, Agilent) is placed between the source chamber and the 2D MOT chamber in order to prevent Rb vapor from contaminating the whole system. The source valve can be opened during the experiment to provide a constant Rb flux so that the Rb vapor pressure does not drift over time. After finishing the measurements, this valve needs to be closed. **Warning: If one forgets to close the valve and leaves it on for days, the Rb atoms will corrode the threads of the valve and prevent the valve from being closed.**

The Rb atoms from the source chamber are first captured in the 2D MOT region. This 2D MOT region is constructed of a six-way cross (SWC 1) and a seven-way cross, as shown in figure 3.18 (b). The six-way cross has three viewports; two of them are used to look for Rb fluorescence when filling the chamber with Rb, and the other one on the back is used to image the 2D MOT through a CCD camera and provide optical access to the push beam. Note that the push beam and the CCD camera imaging cannot co-exist since the push beam will saturate the CCD camera and potentially damage the camera.

The seven cross chamber was custom built by Johnsen Ultravac. Two of the longitude ports are connected to the six-way cross chamber and the measurement section separately. In addition, four of the ports have the viewports (VPZL-450, kurt Lesker) installed in order to provide the optical access for the trapping lasers. We have found that Rb atoms are likely to be condensed on the viewports and crack the seals between the glass and the steel, resulting in a vacuum leak. The lifetime of the seal is around two and half years, so one should prepare new viewports before the end of the lifetime (The last time the viewports were replaced in Mar, 2019). The last port of the 2D MOT chamber is connected to an ion pump (IP2 9191145, Agilent), which is used to maintain

the low pressure in the differential pumping tube.

The differential pumping tube is used to separate the source stage and the measurement stage. The Rb vapor pressure in the source chamber and the 2D MOT chamber are on the level of  $10^{-8}$  Torr at room temperature. Using two low-conductance differential pumping tubes allows the base pressure in the “measurement” chamber to reach the  $10^{-10}$  Torr level when the ion pump and NEG in that region are on. Figure 3.19 shows a cutaway of the differential pumping section. The first tube in the differential pumping design separates the 2D MOT chamber from the ion pump. A second tube then connects the region with the ion pump to the 3D MOT region. The second tube has a graduated opening to allow for divergence in the atomic beam as it propagates towards the 3D MOT. Having the ion pump separated from the Rb vapor helps preserve the ion pump’s lifetime.

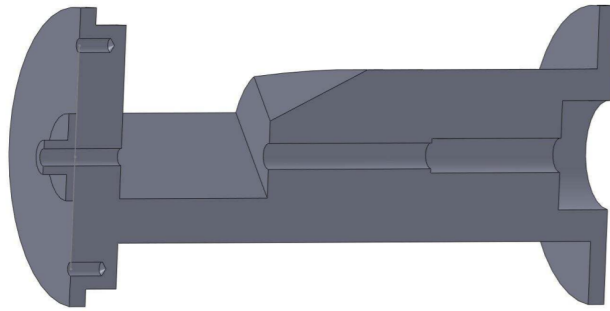


Figure 3.19: A cut view of the differential pumping tube. Atoms travel from left to right through one tube and then through another series of tubes before exiting and going to the 3D MOT cell. Atoms in the atomic beam have a high directionality and will make their way through the tubes. Atoms that randomly enter the tubes from the vapour on either side of the 2D or 3D MOT regions will tend to bounce around in the section between the two different tube sections and be pumped away by an ion pump.

### 3.4.2 Measurement chamber

There is a gate valve (48132-CE01-0002, VAT valve) between the 2D MOT section and the 3D MOT section, which is used to preserve the vacuum in the measurement chamber while only baking the 2D MOT section. Another six-way cross (swc2) with viewports is attached to the other end of the gate valve for diagnosing the 2D MOT beam characteristics exiting the differential pumping tubes. The bottom of this six-way cross connects to a pumping station (PS1), including a leak valve 59024-GE01, VAT and

a turbo and scroll pump. This pumping station (“test gas in” arrow in figure 3.18) is used to introduce the test gases into the chamber and maintain the vacuum level during the loss rate measurements. The right-hand side of swc2 is attached to a rectangular glass cell inside where we trap atoms and perform loss rate measurements. The cross section of the cell is square with inner dimensions of 40 mm by 40 mm. The other side of the glass cell is connected to a four-way cross. The top port of the four-way cross is connected to a residual gas analyzer (RGA), which is used to analyze the gas composition inside the vacuum to examine the purity of the test gas.

The bottom port of the four-way cross is attached to a metal isolation valve. The other side of the metal isolation valve is connected to an ion pump (IP, VacIon Plus 20) and a getter pump (NEG, C400-2-DSK ,SAES getters) used to maintain the vacuum in the measurement chamber. **Warning: We have found that the ion pump and the getter pump need to be valved off during the loss rate measurements since the pumping flow generated by the IP and the NEG will compete with the pumping flow from the turbopump station. This creates a pressure gradient and pressure fluctuations inside the measurement region of the glass cell.**

The last port of the four-way cross is attached to a five-way cross which is used to connect with the ionization gauges (IG). This connection is designed to ensure that the test gas is introduced, the region of the 3D MOT and IGs experience a stagnant, constant pressure, with no pressure gradients between the MOT and the IGs. One of the IGs (a), as shown in figure 3.18, is directly purchased from the industry (MKS) without calibrations, NIST sent the other one (b) (placed across to the IG ‘a’) after calibration against their orifice flow standard for Nitrogen. The top port of the five-way cross is connected to a SRGs that is used to measure the pressure in the HV regime. The last port of the five-way cross is connected to an isolation valve. The other side of the isolation valve is an open port that is designed to connect with the future portable CAPS to perform side-by-side comparisons.

#### 3.4.3 Vacuum Baking

Once the vacuum chamber is assembled, the UHV environment can be achieved through a process of high-temperature baking. The initial baking procedure has been fully explained in Dr. Van Dongen’s thesis [1]. However, after the initial baking, the vacuum

of the apparatus has been breached many times due to the breakage of the viewports and the failures of the pumps. We have successfully restored the vacuum level after experiencing those failures. Therefore, I will present the details of rebaking and the lessons we learned from that.

Once the apparatus is exposed to the atmosphere, even for a short amount of time, the water and other gas species,  $\text{H}_2$ ,  $\text{CO}_2$ , and  $\text{O}_2$ , etc in the air will contaminate the vacuum. These species are very sticky and difficult to remove at room temperature with the turbopump. Therefore, baking the apparatus will increase its vapor pressures and leads to higher pumping efficiency.

#### **Pre-baking**

During the baking, the whole apparatus needs to be heated up to at least  $200^\circ\text{C}$ . Since some of the hardware on the apparatus cannot stand such high temperature, before the baking, all the high temperature-sensitive parts need to be taken out, including the 2D and 3D magnetic coils, the optics, the ion gauges' connectors, the spinning-rotary gauges' connectors, the RGA, and all the labels.

After removing the items, a separate pumping station (PS 2) should be attached to the apparatus. This baking station contains a scroll pump, a turbopump, an ion gauge (843 Varian) to indicate the pressure, a residual gas analyzer (RGA, SRS200A), and a logger for the thermocouple gauges. First, we should turn on the scroll pump and wait until the pressure drops below  $10^{-2}$  Torr. Then we can turn on the turbopump, and the pressure will asymptote to  $10^{-7}$  Torr before baking the apparatus. At this point, one should turn on the RGA and run a Helium leak test to make sure there is no leak in the apparatus, especially when the viewports have been replaced. One should also run a leak test after the baking.

Once the apparatus has passed the leak test, we can heat up the apparatus to about  $200^\circ\text{C}$ . Since the whole apparatus is not in a regular shape, using heating tapes would not be ideal and result in temperature gradients. Here, we used fire bricks (K23 Firebrick and 3 feet by 1 foot Fibre Block Insulation from Greenbarn Potters Supply) to build an oven around the apparatus. The oven lid was made from 3 feet by 1 foot Fibre block insulation with double layers put on top. Inside the oven, we placed four infrared heaters to convection heat the system. The glass cell and the viewports need

to be wrapped up with aluminum foils to protect against temperature gradients and anything that melts dropping onto them. All the valves, except the Rb source valve should be opened up to ensure the pumping flow can reach everywhere. **Warning: If the Rb source valve is open during the bake, this can lead to a migration of Rb into the entire chamber and contaminate it with Rb atoms.** However, there are still some parts that cannot be contained in the oven, for example, the UHV bellows and the ion pumps. For those parts, one could use heating tapes to wrap around them. To monitor the temperatures of the apparatus during the baking, we placed a few thermocouples at various places in the chamber and read them out using a digital data logger.

#### During the baking out

Before baking the whole apparatus, the Rb source chamber should be baked and pumped out first with the gate valves in between the 2D and the 3D MOT section closed. The purpose is to remove the water vapor inside the source chamber, and the source chamber will be valved off during the later baking process to protect the science chamber from contamination from the source chamber. To clean the source chamber, the valve in the Rb source chamber should be opened, and the temperature of the source chamber should be brought up over 100 °C. A 24 hr baking will be enough to remove the water vapor inside the chamber. Then one should be careful to close the isolation valve in the source chamber and keep it closed during the later baking stages.

Then we can start increasing the temperature of the whole apparatus by increasing the voltage to the infrared heaters and heating tapes with a rate of 5 V/hr. The temperature will reach a steady value,  $\sim 170^\circ$  C in around 6 hours. The temperature needs to be constantly monitored, as if there is a power failure that will cause unsuccessful baking. The temperature of the main chamber inside the oven should be brought up first while the outside bellows connected to the turbo station is lagging behind in temperature so that the temperature gradient is in the right direction. The aim is that outgassed species from the main chamber will be pumped out without the bellows and turbo station being a large source of contamination to the main chamber.

At the beginning of the baking, the pressure of the chamber increases due to the outgassing from the steel chamber [114]. The pressure will reach a maximum of about

$10^{-6}$  Torr when the temperature reaches the maximum and slowly drops as the baking continues. At this point, the NEG pump [link](#) needs to be activated by applying a DC voltage in steps of 1 V/min up to 16 V. The voltage is parked at 16 V for 60 minutes, and the pressure will rise to  $10^{-4}$  Torr due to outgassing of the NEG. Then the voltage is brought down to 7 V, which corresponds to 250 °C, and is left at that voltage for the duration of the bakeout so that the NEG would be the hottest spot in the whole system. To increase the pumping efficiency, the PS1 can be operated as well. This baking process will last 2 weeks, and the pressure will reach about  $7 \times 10^{-8}$  Torr. At this point, the ion pumps can be turned on (the cables are connected during the baking since they can sustain the temperature up to 250 °C) and baked for another week. At first, the LED light on the ion pump controllers would be railing but will drop down to the final light after 24-hour baking.

#### **After the baking out**

After baking for three weeks, the system can be slowly cooled down over the course of two days. The baking station should be cooled down before the main chamber. The NEG pump should be reactivated again at 16 V for 60 minutes when the chamber temperature was below 100 °C. Then the system and the NEG pump can be completely cooled down, and the pressure reading on the ion gauge should be  $1.0 \times 10^{-8}$  Torr, the lowest reading indicated by the ion gauge. At this point, we should valve off all the pumping stations and use the ion pumps solely. One can estimate the pressure of the vacuum chamber by measuring the output voltage of the ion pump, which is proportional to the pressure of the vacuum. This last IP pumping should last two days.

Finally, the part of the oven that covers the ion gauges in the main chamber can be removed, and the ion gauges can be turned on. The ion gauges need to be first degassed by pressing the "degas" button on the ion gauge controllers, which will help remove the junk on the filament. In the beginning, the readings of the ion gauges will increase and then decrease after a while. After 10 minutes (default maximum) degassing period, the degassing process will end. If the ion gauge readings never drop during the degassing, one should run the degas. If the ion gauge reading drops to about  $2.0 \times 10^{-10}$  Torr over a day, the baking is successful, and one can remove all the bricks and install all the parts that have been removed.

## 3.5 Control System

The final part of the CAPS is the control system, which is used to control the laser, optics, and electronic components and record the status of the apparatus. The central part of the control system is an FPGA (field-programmable gate array) based controller. The details of the FPGA controller have been discussed in [115]. The FPGA system takes the byte code (generated with Python 3) from a personal computer (PC) and translates them into the execution commands. Following the commands, the FPGA system controls analog outputs (AO), digital outputs (DO), and the DDS channels sequentially, which completes the full cycle of the measurements. Therefore, one can program the FPGA with Python 3 to launch measurements with different purposes.

One should note that an FPGA can only handle a certain amount of devices due to the amplitude decrease of the communication signal after going through many devices. In our case, there are 16 AOs, 32 DOs, and 24 DDS channels, which are more than an FPGA can handle. To solve this, we add a "repeater" to amplify the communication signal so that all the devices can receive it.

Once the FPGA launches the execution commands, the measurement begins, and the result of the measurements and the status of the apparatus need to be recorded. The conditions of the atoms are recorded by a PD and a CCD camera. The signal of the PD is logged by an analog-to-digital converter (ADC) and sent to the PC, and the PC directly captures the images of the camera. Thermocouple gauges (TCG) read the temperatures of the apparatus, and the data are sent to PC through another ADC. Finally, the pressures inside the vacuum are read by IGs and sent to the PC through an ethernet connection.

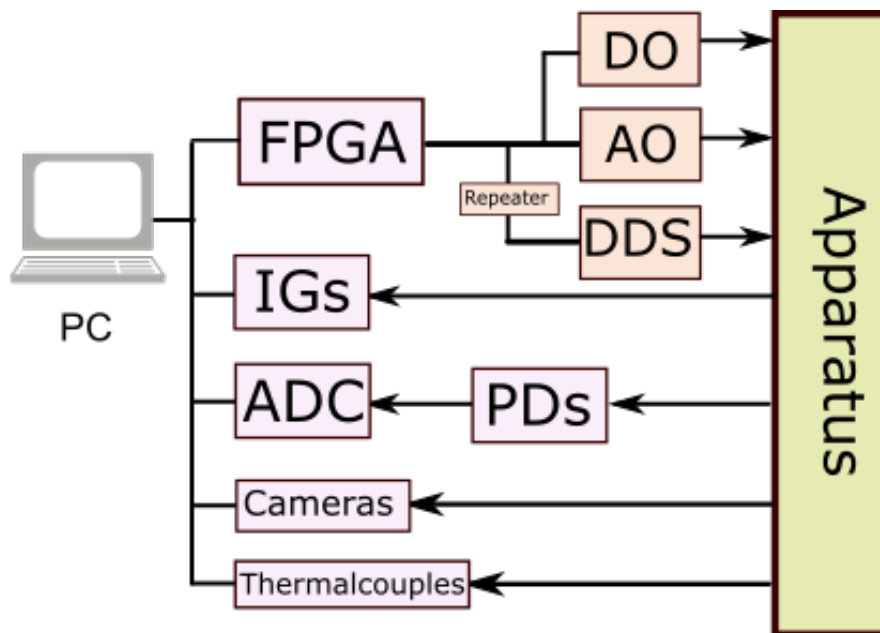


Figure 3.20: A block diagram of the control system. First, a PC sends the programmed execution codes to the FPGA system. Upon receiving the commands, the FPGA starts controlling the DOs, AOs, and the DDS channels sequentially, which launches a measurement cycle. The repeater is added here to amplify the command signal. Then, the status of the apparatus and the conditions of atoms are captured by a set of devices such as the PDs, cameras, IGs, and thermocouple gauges (TCG). Then the data are sent back to the PC. This completes a measurement cycle.

## Chapter 4

# Magnetic Trap (MT) Based Cold Atom Pressure Standard (CAPS)

The collision-induced loss rate of cold atoms from a trap is modeled as,  $\Gamma_{\text{loss}} = n \langle \sigma_{\text{loss}} v \rangle$ . Here  $n$  is the density of the background gas impinging on the trapped atoms and  $\langle \sigma_{\text{loss}} v \rangle$  is the loss rate coefficient. Therefore, if one can measure the loss rate of the atoms,  $\Gamma_{\text{loss}}$ , and know the value of the loss rate coefficient,  $\langle \sigma_{\text{loss}} v \rangle$ , then the pressure in the vacuum can be determined based on the ideal gas law,

$$P = \frac{\Gamma_{\text{loss}}}{\langle \sigma_{\text{loss}} v \rangle} k_B T. \quad (4.1)$$

In this chapter, I will focus on discussing the methods of determining the loss rate coefficient, which leads to a realization of a MT based CAPS.

As discussed in section 2.3.1, one can compute the scattering phase shifts using the log-derivative method if the information of the potential energy surface (PES) of the collision system is known. Plugging in the phase shifts into Eq. 2.56, one then can calculate the value of the loss rate coefficient. Fortunately, previous researchers have shown the method of constructing the PES accurately, *ab initio* method, a numerical computation method based on first principles [116, 117, 118, 61, 13]. Alternatively, others have developed several physical models to approximately describe the PES for a system with van der Waals interactions [119, 120, 121, 12]. These include modeling the PES as a Lennard-Jones potential and as a Morse potential. For systems with small numbers of electrons, the theoretical methods can be used to construct the PESs accurately. However, if the total number of electrons in a collision system increases, for instance, the atom-molecule or the molecule-molecule collision system, theoretically constructing the PES and computing the loss rate coefficient is computationally difficult. The current computation power limits the collision system that can be computed by *ab*

*initio* methods. On the other hand, the physical PES models are challenging to verify and have large uncertainties.

A second method of determining the value of the loss rate coefficient is using another independent pressure standard. Inspired by Eq. 4.1, if one can measure the trap loss rate while measuring the pressure of the vacuum simultaneously using another pressure standard, then the rate coefficient can be found empirically. Practically, this can be achieved by connecting the CAPS to an orifice flow standard (OFS), as shown in figure 4.1. Here, the CAPS is connected to the OFS upper chamber. The pressure in the OFS upper chamber,  $P_{OFS}$ , can be determined using the flow method as explained in section 1.1.1. In equilibrium, the pressure in the CAPS chamber is the same as the pressure in the OFS chamber,  $P_{CAPS} = P_{OFS}$ . Meanwhile, the loss rate of the cold atoms in the CAPS can be measured,  $\Gamma_{\text{loss}}$ . Then one can solve the loss rate coefficient for the test gas in the chamber using,

$$\langle \sigma_{\text{loss}} v \rangle = \frac{\Gamma_{\text{loss}} k_B T}{P_{OFS}}. \quad (4.2)$$

However, this method won't apply to gas species that are not compatible with the OFS system due to their large viscosity or reactivity.

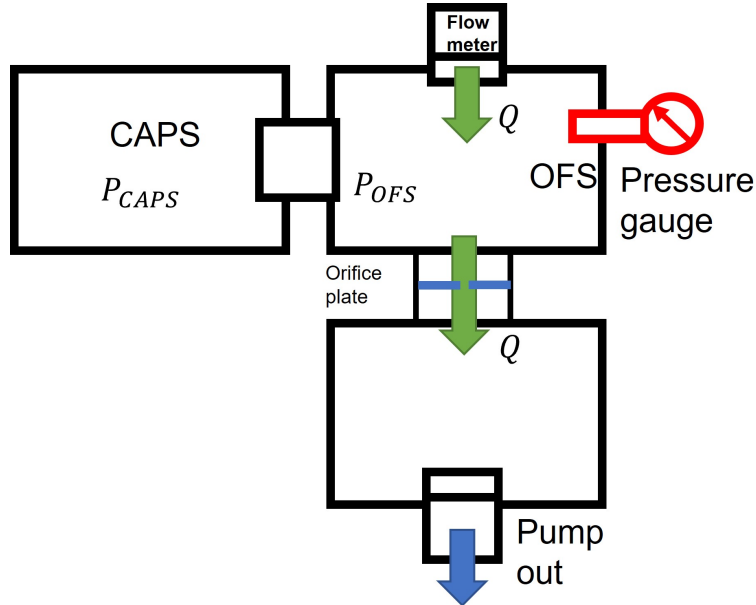


Figure 4.1: A schematic of a CAPS connected to an orifice flow standard. The operating principle of the orifice flow standard has been explained in section 1.1.1.

## 4.1 Quantum Diffractive Collisions Universality

In addition to the two methods above, we choose to examine the nature of the physics of the quantum diffractive collisions that dominate the trap loss variation with trap depth. We have shown that the loss rate at small trap depths follows a universal scaling law whose characteristic energy scale is determined by the total collision cross section dictated by the Heisenberg uncertainty principle. Initially, the trapped sensor atoms have a small momentum and a large de Broglie wavelength. A collision leads to the spatial localization of the sensor atom to a region whose size is determined by the total collision cross section,  $\sigma_{\text{tot}}$ . Complementarity requires that this position localization be accompanied by a change in the momentum distribution, even in the absence of direct momentum exchange, through the interaction potential. Those collisions that impart the least energy and momentum to the sensor atoms are referred as quantum diffractive collisions, and we measure the resulting low energy tail of the sensor atoms' post-collision distribution function by observing the trap loss probability versus trap depth - the cumulative energy distribution of the sensor atom post-collision. Thus, measuring the trap loss rate as a function of trap depth for shallow traps provides the spectrum of energies transferred by the quantum diffractive collisions. This approach allows us to define characteristic energy for the collision system based on the total collision cross section  $\langle\sigma_{\text{tot}}v\rangle$ . Finally, we then can rely on the value of  $\langle\sigma_{\text{tot}}v\rangle$  to solve the loss rate coefficient at the trap depth of atoms in the MT so that we can determine the pressure based on Eq. 4.1. The following sections will present more rigorous discussions of this method and the designed experiment to demonstrate this universal law.

### 4.1.1 Analytical computations

It has been shown that collisions resulting in small momentum transfer are dominated by quantum diffractive scattering [10, 57]. Such collisions occur with small scattering angles  $\theta \rightarrow 0$  and are predominantly determined by the long-range part of the interaction potential (see, for example, the discussion in [14]). Therefore, they are expected to be independent of the short-range interactions between the colliding particles. A qualitative relationship between the long-range interaction parameters,  $C_6$  coefficients, and the scattering amplitude can be established by an analysis based on the Jeffreys-Born (J-B)

approximation, as shown in section 2.3.

Moreover, we can express the loss rate coefficient in terms of the long-range interaction parameters,  $C_6$  coefficients. From Eq. 2.53, we know the J-B approximate form of  $\sigma(v)$ . Thus, we can obtain an approximation of the total collision cross section,

$$\begin{aligned}
 \langle \sigma_{\text{tot}} v \rangle &= \int_0^\infty 4\pi v^3 \left[ \frac{2\pi}{k^2} \int_0^\pi \left| \sum_{l=0}^\infty (2l+1) \sin(\eta_l) e^{i\eta_l} P_l(\cos\theta) \right|^2 \sin\theta d\theta \right] \rho(v) dv \\
 &\approx \int_0^\infty 4\pi v^3 \left[ 8.0828 \left( \frac{C_6}{\hbar v} \right)^{\frac{2}{5}} + 7.1889 \frac{\hbar}{\mu v} \left( \frac{C_6}{\hbar v} \right)^{\frac{1}{5}} \right] \left( \frac{m_2}{2\pi k_B T} \right)^{3/2} e^{-\frac{m_2 v^2}{2k_B T}} dv \\
 &= \langle \sigma_{\text{tot}} v \rangle_0 \left[ 1 + \frac{0.84728}{\bar{v}^{\frac{4}{5}}} \left( \frac{\hbar}{\mu} \right) \left( \frac{\hbar}{C_6} \right)^{\frac{1}{5}} \right], \tag{4.3}
 \end{aligned}$$

where

$$\langle \sigma_{\text{tot}} v \rangle_0 = 8.4946 \bar{v}^{\frac{3}{5}} \left( \frac{C_6}{\hbar} \right)^{\frac{2}{5}}. \tag{4.4}$$

This approximation form is obtained by plugging the J-B phase shift (Eq. 2.50),  $\eta_l = \alpha/l^5$  into Eq. 2.54. Note, here,  $\bar{v} = \sqrt{2k_B T/m_2}$  is the most probable speed for the test gas with a mass,  $m_2$ , at temperature,  $T$ .

Next, we can compute the loss rate coefficient,  $\langle \sigma_{\text{loss}} v \rangle$ , which considers that the atoms are held in a trap of depth  $U$ . That is, in order to be liberated from the trap, the momentum transferred to the trapped atom due to the collision must result in the atom's total energy exceeding the trap depth. In the center of mass frame, this condition reduces to a statement that the reduced mass particle must be scattered outside a minimum angle,  $\cos(\theta_{\min}) = 1 - m_2 U / (\mu^2 v^2)$ , as demonstrated in section 2.2. Thus,  $\langle \sigma_{\text{loss}} v \rangle$  is computed in the same manner as  $\langle \sigma_{\text{tot}} v \rangle$  from Eq. 4.3 except that the integral ranges from  $\theta_{\min}$  to  $\pi$  rather than  $[0, \pi]$ . Substituting  $x = \cos\theta$  in Eq. 2.56, one has

$$\begin{aligned}
 \langle \sigma_{\text{loss}}(U) v \rangle &= \int_0^\infty 4\pi v^3 \rho(v) dv \left[ \frac{2\pi}{k^2} \int_{-1}^{x_{\min}} \left| \sum_{l=0}^\infty (2l+1) \sin(\eta_l) e^{i\eta_l} P_l(x) \right|^2 dx \right] \\
 &= \langle \sigma_{\text{tot}} v \rangle - \left\langle v \cdot \left[ \frac{2\pi}{k^2} \int_{x_{\min}}^1 \left| \sum_{l=0}^\infty (2l+1) T_l(k) P_l(x) \right|^2 dx \right] \right\rangle. \tag{4.5}
 \end{aligned}$$

Here " $\langle \rangle$ " denotes the velocity averaging over the Maxwell-Boltzmann distribution,  $\rho(v)$ ,

and the transmission matrix (T-matrix),  $T_l(k) = \sin(\eta_l)e^{im}$ . In the small angle scattering regime, the Legendre polynomials in Eq. 4.5 can be expanded

$$P_l(x) \approx 1 - \frac{l(l+1)}{4}(1-x) + \dots \quad (4.6)$$

By plugging in the Legendre polynomial approximation, one can perform the integral in Eq. 4.5 over  $dx$ , results in

$$\begin{aligned} \langle \sigma_{\text{loss}}(U) v \rangle &\approx \langle \sigma_{\text{tot}} v \rangle - \left\langle v \cdot \frac{2\pi}{k^2} \sum_{l,l'} (2l+1)(2l'+1) T_l(k)^* T_{l'}(k)' \times \right. \\ &\quad \left. \left[ \left( \frac{m_2 U}{\mu^2 v^2} \right) - \frac{l(l+1) + l'(l'+1)}{4} \left( \frac{m_2 U}{\mu^2 v^2} \right)^2 + \dots \right] \right\rangle \end{aligned} \quad (4.7)$$

This description makes it clear that  $\langle \sigma_{\text{loss}}(U) v \rangle$  can be expanded in powers of  $U$  for shallow traps. The exact form of the expansion will depend on the T-matrix,  $T_L(k)$ , which encodes the specific form of the long-range interaction into the loss rate coefficient. Using the J-B approximation, we have the analytical expression of the T-matrix,

$$T_L(k) = \sin(\eta_l)e^{im} = \frac{1}{2} \sin\left(\frac{2\alpha}{L^5}\right) + i \sin^2\left(\frac{\alpha}{L^5}\right). \quad (4.8)$$

Note that this form of the phase shift is only valid when the velocity-dependent phase associated with core repulsion scattering, leading to glory oscillations, is eliminated through averaging over velocity. Performing the integrations with this form of the phase shift leads to a quasi-universal behavior (detailed derivations are presented in appendix C),

$$\langle \sigma_{\text{loss}}(U) v \rangle = \langle \sigma_{\text{tot}} v \rangle \left[ 1 - \beta_1 \left( \frac{U}{U_d} \right) - \beta_2 \left( \frac{U}{U_d} \right)^2 - \dots \right] \quad (4.9)$$

$$= \langle \sigma_{\text{tot}} v \rangle (1 - p_{\text{QDU6}}), \quad (4.10)$$

Here, we define

$$p_{\text{QDU6}} = \sum_{j=1}^{\infty} \beta_j \left( \frac{U}{U_d} \right)^j, \quad (4.11)$$

which represents the probability that the sensor atom remains in the trap after the

collision. As  $U \rightarrow 0$ ,  $p_{\text{QDU6}} \rightarrow 0$  and the loss rate approaches the total collision rate. The quantity  $U_d$  is the characteristic quantum diffraction energy and is defined as [10, 2],

$$U_d = \frac{4\pi\hbar^2}{m_1\bar{\sigma}}, \quad (4.12)$$

where  $\bar{\sigma} = \langle \sigma_{\text{tot}} v \rangle / \bar{v}$  is a thermally averaged total collision cross section. The system-dependent parameters, such as the strength of the van der Waals interaction, the long-range details of the potential, and the masses of the trapped and incident particles, have been included in  $U_d$ . If low angle scattering does not depend on the short-range part of the potential, one would expect the shape of  $p_{\text{QDU6}}$  (the values of  $\beta_j$  coefficients) is universal. The analytical coefficients  $\beta_j$  up to second-order are calculated after averaging over multi-collision systems (Rb-[He, Ar, Xe] and Li-[He, Ar, Xe]) and are provided in column 2 of table 4.1 [2, 3].

	Numerical Computation	Analytical solution
$\beta_1$	0.673(7)	0.693(3)
$\beta_2$	-0.477(3)	-0.669(9)
$\beta_3$	0.228(6)	-
$\beta_4$	-0.0703(42)	-
$\beta_5$	0.0123(14)	-
$\beta_6$	-0.0009(2)	-

Table 4.1: The theoretically computed values of the universal coefficients,  $\beta$ . We reported  $\beta_1$  to  $\beta_6$  from the full quantum scattering computations (averaged over Rb-[He,Ar,Xe] and Li-[He, Ar, Xe] collisions). Using the analytical expressions in Eq. 4.7, we only calculated the values of  $\beta_1$  and  $\beta_2$  (averaged over Rb-[He, Ar, Xe] and Li-[He, Ar, Xe] collisions) [2, 3].

### 4.1.2 Numerical computations

Analytical predictions can be used for the qualitative characterization of the universality of quantum diffractive scattering. However, the velocity averaged cross section is influenced by partial wave mixing (the glory oscillations), which is truncated by the J-B approximations used in previous analytical predictions. Therefore, rigorous quantum scattering computations are needed to demonstrate and to predict the universal shape of  $p_{\text{QDU6}}$ .

To demonstrate this universality, the time-independent coupled channel (CC) approach was used (described in Appendix B and in [122, 123]) to compute an atom-

diatomic molecule collision for three different PES. Each PES, shown at a  $90^\circ$  Jacobi angle of approach in the inset of figure 4.2 (a), has the same long-range van der Waals potential but radically different short-range core potentials, differing in depth by more than a factor of  $10^4$ .

The cross sections exhibit core-dependent oscillations superimposed on a trend defined by the long-range part of the potential <sup>5</sup>. The oscillations arise from the velocity-dependent glory phase shift, and therefore the locations of the maxima and minima are dependent on the short-range physics [14]. The effect of thermal averaging is clear: while an accurate prediction of the collision rate for a given velocity requires detailed knowledge of the core potential, averaging the cross section over one or more oscillations removes the core-dependent effects. In particular, for the 3 different PESs, we find  $\langle\sigma_{\text{tot}}v\rangle = [0.361, 0.361, 0.363] \times 10^{-8} \text{ cm}^3/\text{s}$  for the dark solid, dotted, and dashed PESs respectively. Because all three PESs have identical long-range character, the thermally averaged total cross sections are identical (differing by much less than 1%). However, the short-range physics of the interactions and the corresponding inelastic collision rates are radically different.

The shape of  $p_{\text{QDU6}}$  and corresponding loss cross section for small  $U$  is independent of the short-range part of the potential because inelastic and small impact parameter elastic collisions that probe the core always lead to large energy transfer and loss for shallow traps. Thus, the loss rate departs from the total collision rate due only to quantum diffractive collisions. This departure is a direct measure of the low-angle scattering cross section, which is expected to be independent of the short-range potential when averaged over the velocity distribution of the colliding partners [14]. Fig. 4.2(b) shows the cross section versus total angular momentum,  $J$ , for the three PESs at a collision energy of  $300 \text{ cm}^{-1}$ . The curves exhibit the same universal shape, independent of the core potential above  $J = 125\hbar$ . The scattering angles of such collisions are tiny ( $< 1 \text{ mrad}$  for  $U = 1 \text{ mK}$  and collision energy of  $300 \text{ cm}^{-1}$ ) where the differential cross section, shown in the inset of Fig. 4.2 (b), is dominated by large impact parameter elastic scattering, more than a 1000 times larger than inelastic scattering (arising primarily from low  $J$  collisions) for scattering angles below  $10 \text{ mrad}$ .

---

<sup>5</sup>For a long-range potential varying as  $C_n/r^n$  the trend is approximately a power-law,  $\sigma(v) \sim (\frac{C_n}{\hbar v})^{\frac{n-4}{5}}$ , that only depends on  $C_n$  (see Ref. [14]).

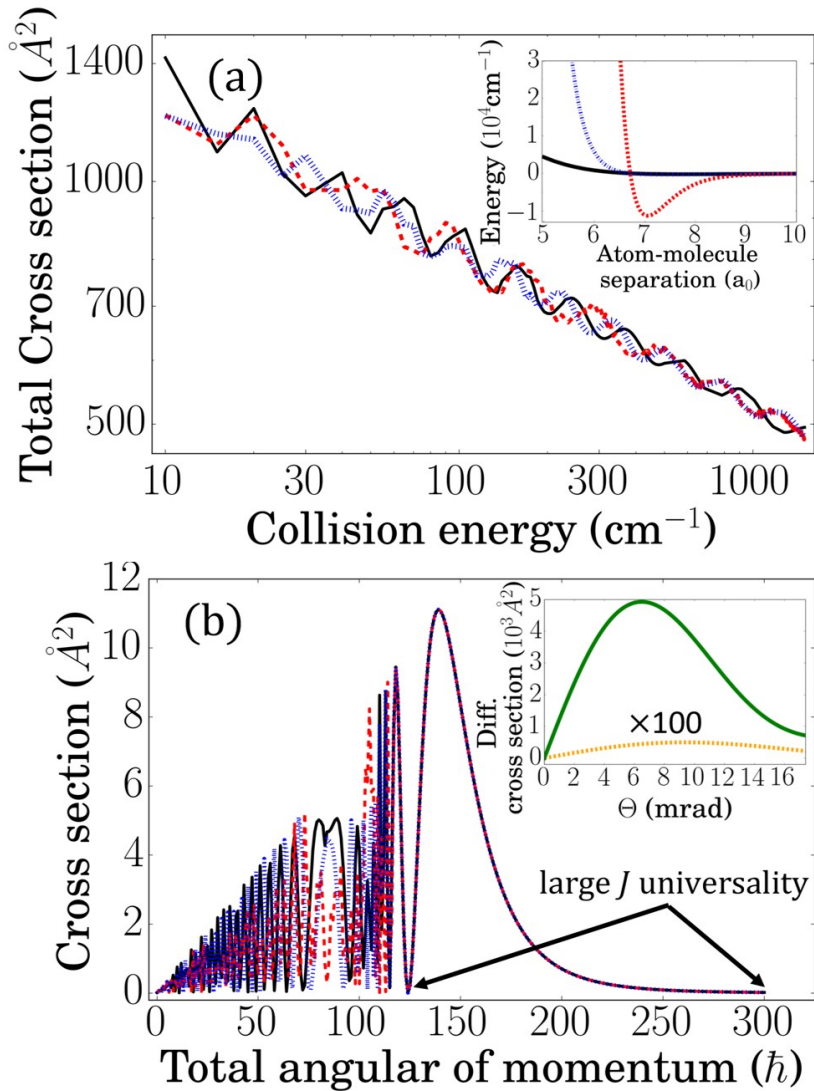


Figure 4.2: Theoretical demonstration of collision universality. Atom-molecule cross sections vs. collision energy in (a) are for PESs (see inset) with different cores but the same long-range potential. The thermally averaged total cross section is the same for all three (within 0.6%, see text) despite the radical differences in the potentials. The cross sections versus  $J$  are shown in (b) for a collision energy of  $300 \text{ cm}^{-1}$  and exhibit a universal shape above  $J = 125\hbar$  and core-dependent oscillations below. For small scattering angles, the differential cross section (inset of b) is dominated by elastic scattering (solid), more than 1000 times larger than inelastic (dashed) scattering for  $\theta < 10$  mrad.

Next, we numerically determine the universal coefficients,  $\beta_j$ , by using the log-derivative method to compute the collisions between Rb or Li and X (X=He, Ar, and Xe). In section 2.3.1, we introduced the way of computing the total cross section with the log-derivative method. However, if we want to compute the velocity averaged loss

cross section, we also need to numerically integrate Eq. 2.56 over the scattering angles that generate atom loss. Here, the phase shifts in Eq. 2.56 are computed using the log-derivative method with the PES modeled with L-J potential,

$$V(R) = \frac{C_{12}}{R^{12}} - \frac{C_6}{R^6} = 4\epsilon \left[ \left( \frac{r_0}{R} \right)^{12} - \left( \frac{r_0}{R} \right)^6 \right], \quad (4.13)$$

where  $C_{12}$  and  $C_6$  are the short and long-range coefficients of the L-J PES, respectively. Here, we also define  $\epsilon = C_6^2/4/C_{12}$  the depth of the potential well and  $r_0 = (C_{12}/C_6)^{1/6}$  is the range of the core repulsion. The long-range coefficients  $C_6$  for Rb, Li-X (X=He, Ar, and Xe) collisions are quoted from ref.[9], and the potential depths were fixed at  $\epsilon = 50 \text{ cm}^{-1}$ . Each PES as a function of the interatomic distance is shown in figure 4.3.

Then the computed phase shifts are plugged into Eq. 2.56, which is then numerically integrated over the accessible range of the scattering angles determined by the trap depth. Finally, the velocity-dependent collision cross sections are further integrated over the MB velocity range. The upper limit of the velocity should be three times larger than the most probable velocity at the background temperature,  $T$ , to ensure that the results converge. Here, we run quantum scattering computations for collisions at the background temperature 21 °C.

The results of the rate coefficients as a function of trap depths for collisions between Rb or Li and X (X=He, Ar, and Xe) are presented in figure 4.4 (a). As we can see, they have different values of  $\langle \sigma_{\text{tot}} v \rangle$ . However, if we normalize the loss rate coefficients,  $\langle \sigma_{\text{loss}} v \rangle / \langle \sigma_{\text{tot}} v \rangle$ , and plot them as a function of  $U/U_d$ , as shown in figure 4.4 (b). All the results collapse to the universal curve,  $(1 - p_{\text{QDU6}})$ , with coefficients given in the first column of Table 4.1. The universal curve coefficients,  $\beta_j$ , are obtained by the best fit to these six calculations. The residuals between the universal curve and the individual QS computations are shown in the inset and are all below 0.1% for trap depths up to  $U = 2.2 \text{ mK}$ , which is the range of our experimental measurements as indicated by the orange shadow region in figure 4.4 (a).

The trap depths explored in this calculation were from 0 to 15 mK and are far beyond those realized experimentally (0.2 to 2.2 mK). The corresponding scaled trap depth values ( $U/U_d$ ) differ depending on the total cross sections. For example, the maximum scaled trap depth for Rb-He at 15 mK was 0.06 compared to the Rb-Xe

value of 3.0. The purpose of exploring the behavior of the universal curve at values of  $U/U_d \geq 1$  was to demonstrate the convergence of the series expansion, ensuring that it faithfully captures the universal behavior for our experimentally accessible values  $U/U_d \leq 0.4$ .

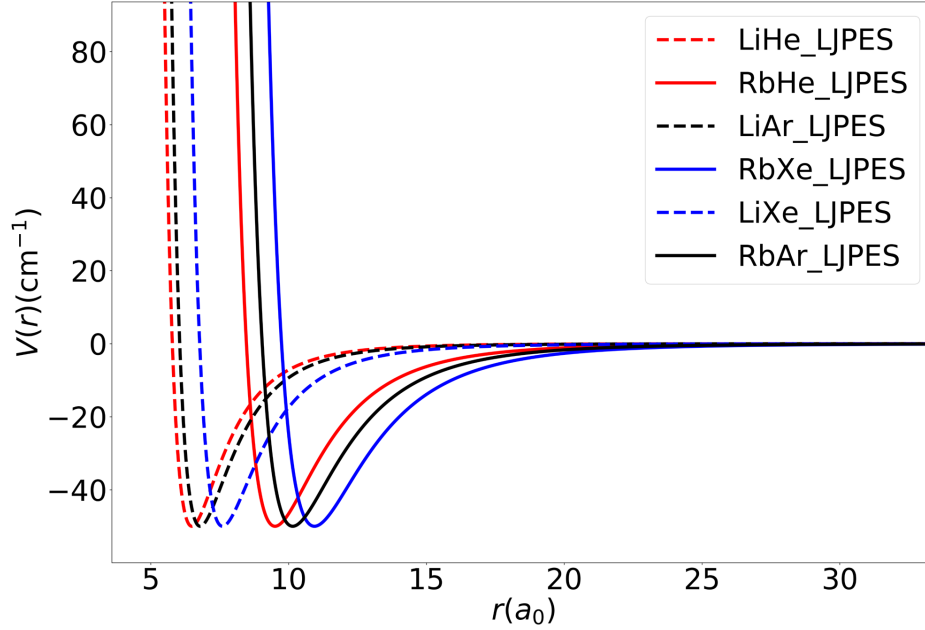


Figure 4.3: A plot of the Lennard-Jones PES for different collision systems. The solid lines represent the PESs for Rb atoms colliding with He (red), Ar (black), and Xe (blue). The dashed lines represent the PESs for Li atoms colliding with He (red), Ar (black), and Xe (blue). The long-range coefficients,  $C_6$  are quoted from ref. [9], and the depth of L-J PESs are fixed at  $50 \text{ cm}^{-1}$ .

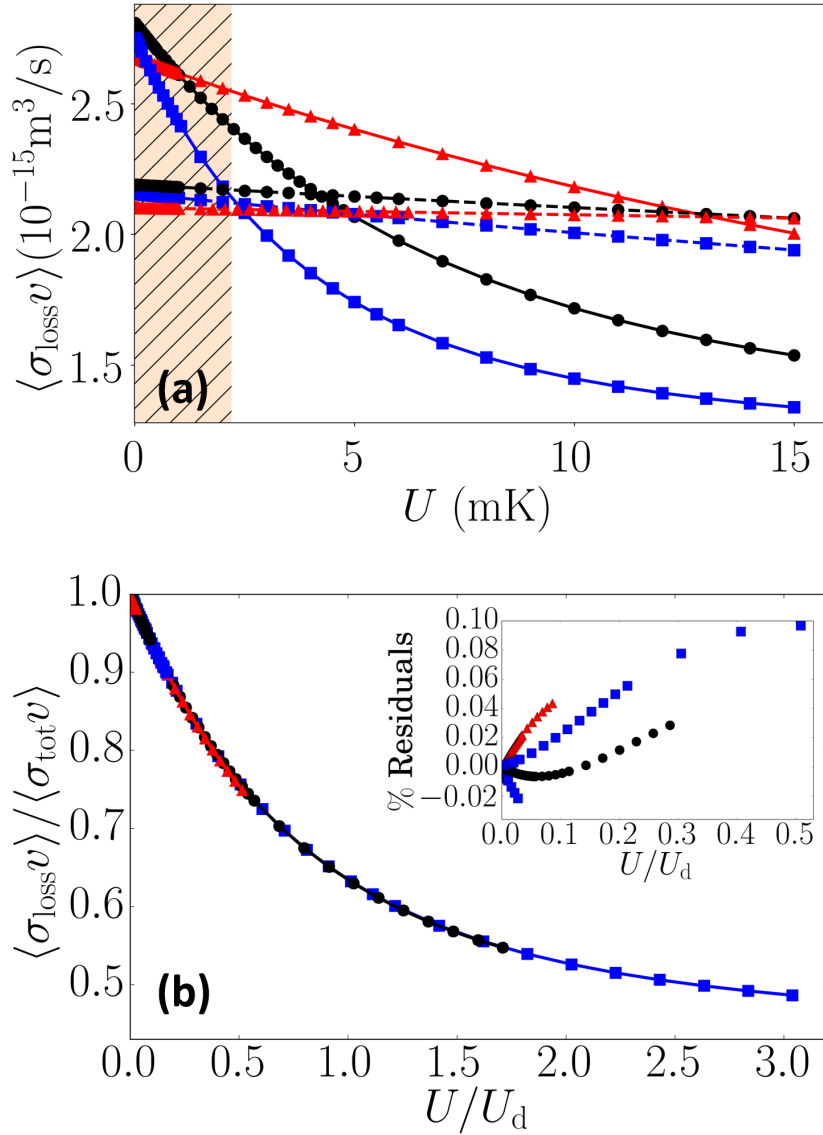


Figure 4.4: Velocity averaged collision loss cross sections versus trap depth for He (red triangles), Ar (black circles), and Xe (blue squares) colliding with Li (dashed lines) and Rb (solid lines). In (b), these loss rate coefficients are normalized by their value at  $U = 0$  and plotted versus the scaled trap depth. All of the results collapse to the universal curve for  $(1 - p_{\text{QDU6}})$  in Eq. 4.10 with coefficients provided in Table 4.1. The inset shows the residuals for each calculation from the universal curve, and all are below 0.1% for trap depths up to  $U = 2.2$  mK, which is the range of our measurements as indicated by the orange shadow region in (a).

## 4.2 Experimental Demonstration

So far, we have seen analytically and numerically demonstrations of the quantum diffractive universality. We have also found the universal coefficients,  $\beta_j$ , with the full quantum scattering computations. However, the next question is how to demonstrate the universality experimentally. As shown in Eq. 4.10, the loss rate coefficient,  $\langle\sigma_{\text{loss}}v\rangle$ , can be expanded into a universal equation as a function of the trap depth,  $U$ . Therefore, Eq. 4.10 can be rewritten as,

$$P = \frac{\Gamma_{\text{loss}}}{\langle\sigma_{\text{tot}}v\rangle(1-p_{\text{QDU6}})}k_{\text{B}}T \quad (4.14)$$

$$\begin{aligned} \frac{\Gamma_{\text{loss}}}{P}k_{\text{B}}T &= \langle\sigma_{\text{tot}}v\rangle(1-p_{\text{QDU6}}) \\ \frac{\Gamma_{\text{loss}}}{P}k_{\text{B}}T &= \langle\sigma_{\text{tot}}v\rangle\left[1 - \beta_1\left(\frac{U}{U_d}\right) - \beta_2\left(\frac{U}{U_d}\right)^2 - \dots\right]. \end{aligned} \quad (4.15)$$

Here,  $T$  is the environment temperature that can be measured easily using TCGs. Note  $\Gamma_{\text{loss}}$  only indicates the loss rate of the atoms that is caused by the collisions with the test gas species.  $P = P_x/i_{\text{g}}$  is the actual pressure of the test gas, X, and  $P_x$  is the pressure reading from the ion gauge (IG) connected to the apparatus, as described in section 3.4.2. The actual pressure of the test gas and the IG readings are related through the gauge calibration factor,  $i_{\text{g}}$ , which needs to be calibrated. Then, substituting  $P = P_x/i_{\text{g}}$  into Eq. 4.15, we will have,

$$\frac{\Gamma_{\text{loss}}}{P_x}k_{\text{B}}T = \frac{\langle\sigma_{\text{tot}}v\rangle}{i_{\text{g}}}\left[1 - \beta_1\left(\frac{U}{U_d}\right) + \beta_2\left(\frac{U}{U_d}\right)^2 - \dots\right]. \quad (4.16)$$

Therefore, we can map out the universal shape by measuring the loss rate of the atoms as a function of the trap depth while recording the values of the pressure and the environment temperature. The two unknown parameters in Eq. 4.16,  $i_{\text{g}}$  and  $\langle\sigma_{\text{tot}}v\rangle$  can be obtained by fitting the data to the universal equation with the numerical computed  $\beta_j$  coefficients. To verify the universal law, one can compare the fitted  $i_{\text{g}}$  parameters with prior calibrated results against the orifice flow standard. Moreover, the fitted  $\langle\sigma_{\text{tot}}v\rangle$  results can be compared with the existing theoretical predicted values.

### 4.2.1 Loss rate measurements

Rb atoms are loaded from the vapour into a MOT formed along two spatial dimensions (2D MOT). As described in section 3.4.1, the source section is separated by two low-conductance differential pumping tubes, which ensures a low base pressure in the 3D MOT region. The result is that the base pressure in the standard quantum region is 500 times lower than that in the source region. Then, the atoms in the 2D MOT are propelled towards the 3D MOT region using a horizontal laser beam (push beam) aligned along the axis, joining the 2D and 3D MOTs.

During the operation of the pressure standard, approximately  $10^7$  atoms are loaded into the 3D MOT, producing a fluorescence signal detected by an amplified photodetector of  $V_{\text{MOT}}$ . Using an optical pumping technique described in Ref. [75], we have verified that below the range  $V_{\text{MOT}} \leq 1.2$  V, our photodetector signal is linear in the atom number, as shown in figure 4.5. This is because the phase-space density of the MOT increases as the atoms accumulate at the beginning [124]. Once the density of the MOT has passed a limiting value, the trapping light is depleted by the outer atomic cloud resulting in the atoms inside the cloud not being properly illuminated, which leads to undercounting the atom number. Experimentally, we have found this limit is  $V_{\text{MOT}} \leq 1.2$  V in our case. This is a key factor for the proper operation of the CAPS.

Then, the atoms in the MOT are cooled by turning down the pump laser power and shifting the pump laser frequency to 60 MHz below the  $F = 2 - 3'$  transition for 50 ms. The repump laser is extinguished while the pump laser light is still on, transferring all of the atoms to the  $F = 1$  ground state of  $^{87}\text{Rb}$ . After 4 ms, the pump laser is extinguished, and the atoms in the diamagnetic (low-field seeking) state,  $|F = 1, m_F = -1\rangle$  are captured in the MT. We then increase the axial magnetic field gradient from 13.6 G/cm to 272 G/cm in 10 ms. Fig. 4.6 illustrates the MOT capture, atom cooling, and MT transfer timing sequence. Approximately 20% of the atoms are transferred to the MT with this procedure ( $N_{\text{trapped}} \approx (2.00 \times 10^6) \pm 1.2\%$ ). The atoms in the MT are held for a time  $t$ . At the end of this hold time, an RF “knife” is energized to set the trap depth of the MT by ejecting all atoms above certain energy (see the next section of the trap depth discussion). The remaining atoms are recaptured in the 3D MOT using the same settings as used for the initial MOT loading, and the signal,  $V_{\text{MT}}$ , is recorded. This procedure is repeated over a range of MT hold times,  $t$ .

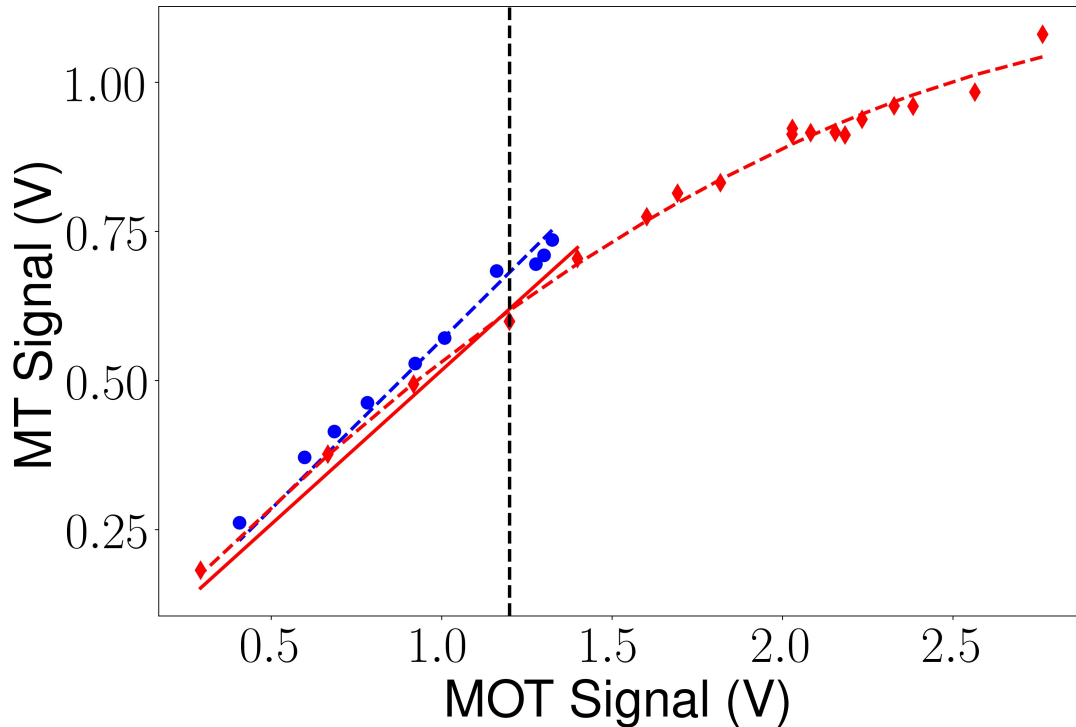


Figure 4.5: A plot of the photodetector reading for the atoms recaptured from the magnetic trap,  $V_{\text{MT}}$ , versus the 3D MOT signal,  $V_{\text{MOT}}$ . Two data sets, acquired on separate days, are shown. The linear region of the plot, where the densities of the ensembles are low enough to ensure there is single scattering of photons from the trapped atoms, corresponds to 3D MOT readings below 1.2 V.

Therefore, one can get the time-dependent variation of the atom number in the MT,

$$N(t) = N_0 \exp(-\Gamma t), \quad (4.17)$$

where  $N_0$  is the initial number of atoms in the MT. Here, we use the ratiometric quantity,  $V_{\text{MT}}(t)/V_{\text{MOT}}$  ( $V_{\text{MOT}}$  is the MOT loading reading prior to transferring the atoms to the MT), as a proxy for the atom number in the MT and compute it for each hold time  $t$ . The linearity of the photodiode signal with atom number ensures that this ratio is equal to the ratio of the number of atoms in the magnetic trap to the initial number in the MOT. *From here on, we refer to this ratiometric quantity as the recapture fraction.* Using the recapture fraction instead of the absolute atom number in the MT greatly reduces the effects of shot-to-shot variation in the number of atoms initially loaded into

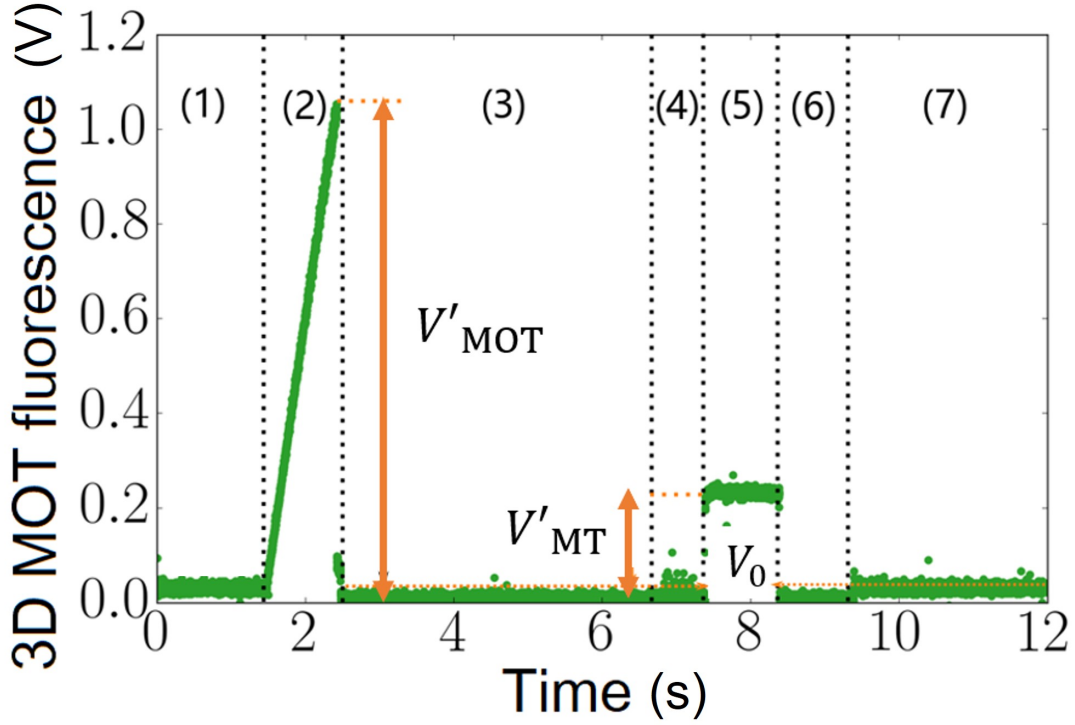


Figure 4.6: The signal of the 3D MOT fluorescence as a function of the experiment time. (1) is the pre-stage of the whole experiment where all the lasers are off and magnetic fields are off. (2) Rb atoms are loaded into the 3D MOT after turning on all the lasers and the magnetic fields. The MOT fluorescence signal is recorded by a photodetector as  $V'_{\text{MOT}}$ . (3) Next, we detune the pump light by 60 MHz below resonance to cool the Rb atoms and then turn off the repump light 4 ms before turning off the pump laser to pump all the atoms from  $|F = 2\rangle$  state to  $|F = 1\rangle$  state. Then we increase the magnetic field gradient to transfer atoms into a magnetic trap and atoms undergo collisions with the background particles. (4) After a certain amount of time (called holding time), we turn on the RF coil to remove atoms above a certain energy. (5) We restore the 3D MOT light and turn the magnetic field back to the MOT setting, to record the fluorescence of the remaining atoms as  $V'_{\text{MT}}$ . (6) We then extinguish the light and magnetic field to empty all the residual atoms. (7) Only tuning back on the lasers to record the background scattered light signal as  $V_0$ . Then, the actual MOT and MT fluorescence signals are  $V_{\text{MOT}} = V'_{\text{MOT}} - V_0$ , and  $V_{\text{MT}} = V'_{\text{MT}} - V_0$ .

the MOT. Then we can have,

$$\frac{V_{\text{MT}}(t)}{V_{\text{MOT}}} = \left( \frac{V_{\text{MT}}(t)}{V_{\text{MOT}}} \right)_{t=0} e^{-\Gamma t}. \quad (4.18)$$

Here,  $\Gamma$  in Eq. 4.18 is the total loss rate of the atoms as opposed to the loss rate due to collisions with the test gas. In the MT, sensor atoms are subject to several loss

mechanisms: Majorana spin-flip losses (characterized by an ensemble loss rate of,  $\Gamma_{\text{Maj}}$ ) that occur when the trapped atoms traverse a region of low B-field where their spin no longer follows the changing field direction adiabatically and they transition to a quantum state that is not trapped [125], loss induced by collisions with background particles in the vacuum (at rate  $\Gamma_{\text{bg}}$ ), loss due to collisions with the gas particles being studied (at rate  $\Gamma_{\text{loss}}$ ), and intra-trap 2-body collisions ( $\Gamma_{\text{two}}$ ), for which two trapped atoms collide and one or both atoms are liberated from the trap, these include both elastic [126], and inelastic collisions [127]. Thus, the total loss rate can be decomposed as,

$$\Gamma = \Gamma_{\text{loss}} + \Gamma_{\text{bg}} + \Gamma_{\text{Maj}} + \Gamma_{\text{two}}. \quad (4.19)$$

The two-body loss rate depends on the density of the ensemble, which is low in our case ( $\sim 10^7 \text{ cm}^{-3}$ ), so the two-body intra-trap loss rate is negligible ( $\sim 10^{-5} \text{ s}^{-1}$ ). Also, the Majorana spin-flip loss and the background collision-induced loss are not dependent on the density of the test gas [128], so they are constant as we increase the density of the test gas and combine as  $\Gamma_0 = \Gamma_{\text{bg}} + \Gamma_{\text{Maj}}$ . Then the experimentally measured loss rate is,  $\Gamma_{\text{exp}} = \Gamma_0 + \Gamma_{\text{loss}}$ . An example of the decay rate measurement is shown in figure 4.7. We can extract the total loss rate by fitting the data to an exponential equation. To extract the loss rate due to the collisions with the test gas, we can perform the baseline subtraction measurement: Firstly, we measure the loss rate without the test gas,  $\Gamma_1$  and record the reading from the IG,  $P_1$ . Then we can introduce the test gas, X, into the system and measure the new loss rate,  $\Gamma_2$  and record IG's new reading  $P_2$ . By subtracting  $\Gamma_1$  from  $\Gamma_2$  and  $P_1$  from  $P_2$ , we can get the pure loss rate due to the collisions with the test gas,  $\Gamma_{\text{loss}} = \Gamma_2 - \Gamma_1$ , and the IG's reading only for the test gas,  $P_x = P_2 - P_1$ .

So far, we have measured the left-hand side in Eq. 4.16. Next, we need to repeat the decay rate measurements at different trap depths to map out the right-hand side in Eq. 4.16. The method of characterizing and controlling the trap depth will be presented in the next section.

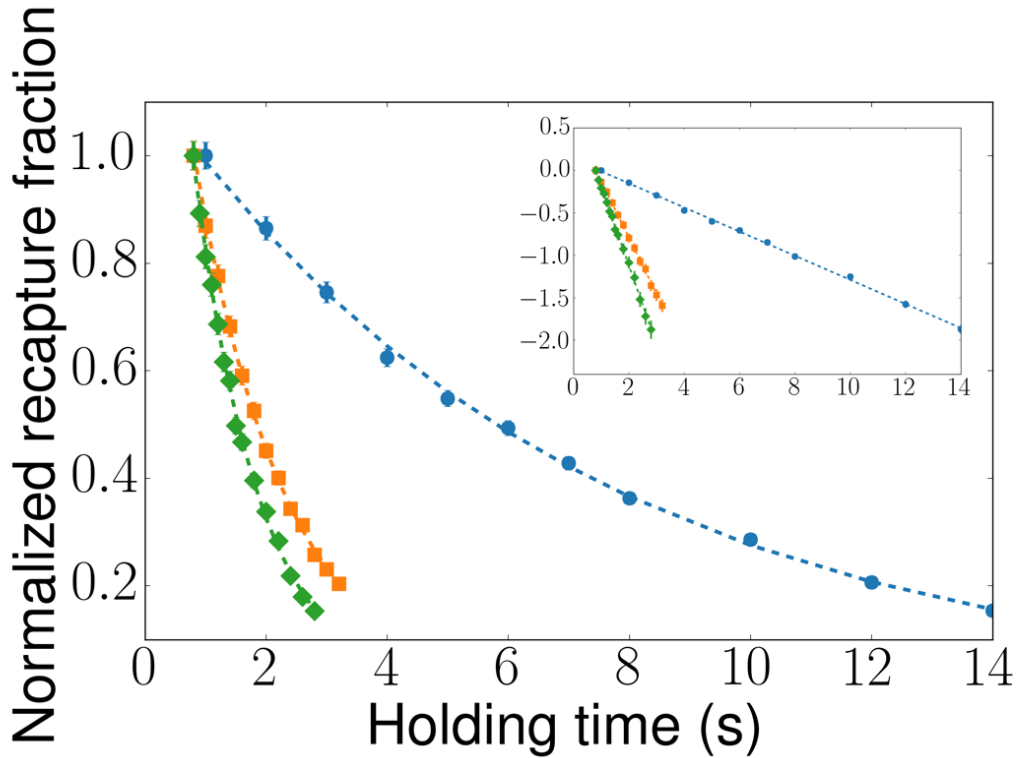


Figure 4.7: The decay of the MT population as a function of the holding time is measured by recording the fluorescence upon MOT recapture of the  $^{87}\text{Rb}$  sensor atoms and normalizing it by the fluorescence after a negligibly short hold time. In the absence of introduced gas, the ensemble exhibits an exponential decay (blue circles) due to a variety of loss mechanisms, including collisions with the residual background gases. The decay slope steepens when an Ar partial pressure is added (orange squares and green diamonds).

#### 4.2.2 Trap depth Characterization

We loaded  $^{87}\text{Rb}$  atoms into the magnetic trap in the  $|F = 1, m_F = -1\rangle$  state relative to the local field. These atoms evolved freely in the trap over the hold time until being recaptured and imaged in a MOT. In a classical sense, the atoms with energy,  $E$ , travel out to a spatial location where their kinetic energy is zero and their potential energy is,

$$E = -\vec{\mu} \cdot \vec{B} + mgz = h\mu_B g_F |m_F| \left( \frac{dB}{dz} \right) \sqrt{\frac{x^2}{4} + \frac{y^2}{4} + z^2} + mgz. \quad (4.20)$$

Here, the first term is the magnetic potential energy, and the second is the gravitational potential energy of the atom. The MOT coils are arranged so that the axial B-field

gradient,  $(\frac{dB}{dz})$ , is aligned along the vertical- or z-direction. For a spherical quadrupole field, the axial gradient is twice the radial gradient, and the field is zero at the center of the two coils,  $\vec{r} = 0$ . In this coordinate system, the gravitational potential energy is taken as zero at  $z = 0$ .

As discussed in section 3.3.2, the axial gradient can be expressed as,  $(\frac{dB}{dz}) = b'I$ , where  $I$  is the current in the trapping coils. There is a minimum current required,  $I_0$ , to support the weight of the atoms against gravity,

$$I_0 = \frac{mg}{h\mu_B g_F |m_F| b'}. \quad (4.21)$$

The depth of the magnetic trap confining the Rb atoms was set by a radio-frequency (RF) B-field created by a single loop coil placed below the trapping region. The driving signal to the loop was frequency scanned over the range  $[\nu_{\min}, \nu_{\max}]$  for the last 700 ms of each hold duration in the magnetic trap. For each RF frequency,  $\nu$ , there is a corresponding oblate spheroid surface where the RF field is resonant with  $|F, m_F\rangle \rightarrow |F, m_F \pm 1\rangle$  magnetic dipole atomic transition,

$$\begin{aligned} h\nu &= h\mu_B g_F \left( \frac{dB}{dz} \right) \sqrt{\frac{x^2}{4} + \frac{y^2}{4} + z^2} \\ &= \frac{mg}{|m_F|} \frac{I}{I_0} \sqrt{\frac{x^2}{4} + \frac{y^2}{4} + z^2}. \end{aligned} \quad (4.22)$$

Atoms with sufficient energy to traverse this surface will, with high probability, make the transition to a non-trapped state and leave the cloud. There is an asymmetry to the energy surfaces introduced by the gravitational potential energy. That is, atoms reaching the RF surface near the position,  $\vec{r} = [0, 0, -z_{\min}]$  have less energy than atoms reaching any other point of the RF surface.

$$\begin{aligned} |z_{\min}| &= \frac{h\nu_{\min}}{h\mu_B g_F |m_F| \left( \frac{dB}{dz} \right)} \\ &= \frac{h\nu_{\min}}{mg} \frac{I_0}{I} \end{aligned} \quad (4.23)$$

Provided that atoms in the trap explore the entire trap volume, the trap depth – or the

maximum energy of the remaining atoms – is given by,

$$\begin{aligned}
 E_{\max} &= h\mu_B g_F |m_F| \left( \frac{dB}{dz} \right) |z_{\min}| - mg|z_{\min}| \\
 &= h\nu_{\min} \left[ 1 - \frac{I_0}{I} \right].
 \end{aligned} \tag{4.24}$$

In our apparatus, the maximum current used to trap the atoms is 200 A, providing a field gradient of 272 G/cm, and the minimum trapping current is  $I_0 = 22.4$  A. The maximum RF frequency,  $\nu_{\max}$ , used here was 90 MHz, sweeping away atoms in the  $|F = 1, m_F = -1\rangle$  state with an energy greater than 3.84 mK ( $E/k_B T$ ), well above the measured trapped ensemble temperature  $< 1$  mK.

Equation 4.24 describes the maximum trap depth for a particular minimum RF frequency, assuming that the ensemble of trapped atoms does not have any average energy when loaded into the magnetic trap. In reality, the atoms are loaded with energy approximated by a Maxwell-Boltzmann distribution of temperature,  $T$ , shifted by an amount  $E_{\min}$ , owing to the offset between the center of the magnetic trap and the MOT. Thus, the actual trap depth is,

$$U = E_{\max} - \frac{\int_{E_{\min}}^{E_{\max}} E \rho(E - E_{\min}) dE}{\int_{E_{\min}}^{E_{\max}} \rho(E - E_{\min}) dE}, \tag{4.25}$$

where  $\rho(E - E_{\min})$  is the zero-point shifted Maxwell-Boltzmann distribution describing the trapped ensemble.

To measure the energy distribution, we first load the atoms into the MT, hold them for a fixed length of time, then apply the RF “knife” to truncate the ensemble by ejecting atoms with energies above that set by the RF pulse. The remaining atoms are then recaptured in the MOT, and their number is determined from the fluorescence produced. By repeating this process for various truncation energies, one can determine the cumulative energy distribution of the atom ensemble. An example measurement is shown in Fig. 4.8. By taking the derivative of this distribution, one can find the energy distribution  $\rho(E - E_{\min})$  of the atoms in the trap, shown in Fig. 4.8. The ensemble average trap depth is computed by averaging each particular atom’s trap depth over the normalized energy distribution, as demonstrated in Eq. 4.25. The integrals are performed from  $E_{\min}$  to  $E_{\max}$  set by the RF “knife”. Therefore, for each RF frequency

and trap current, one can accurately calculate the trap depth. For  $^{87}\text{Rb}$  atoms trapped in its  $|F = 1, m_F = -1\rangle$  state, the range of the trap depth can be realized from 0.02 mK to 2.0 mK, which corresponds to the shadow region in figure 4.4 (a).

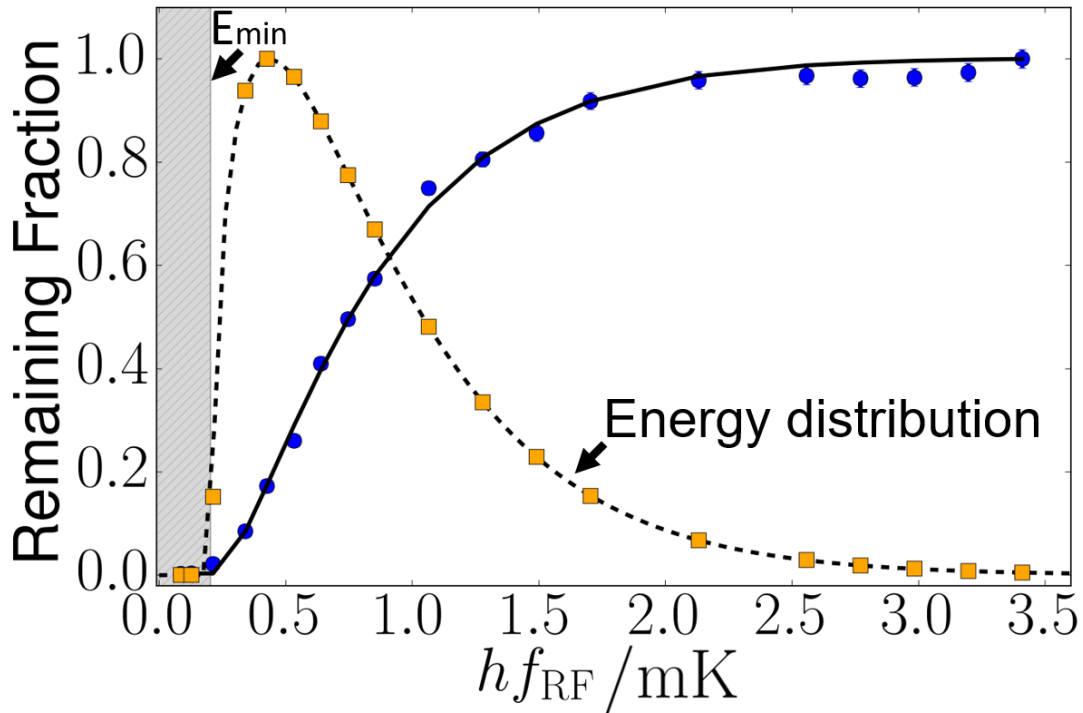


Figure 4.8: Fraction of atoms remaining in a MT (blue dots) as a function of truncation energy,  $hf_{\text{RF}}$ , set by an RF pulse that ejects sensor atoms with a magnetic potential energy above this. These data are fit to a cumulative MB distribution (solid line) for the trapped atom ensemble. The orange squares represent the corresponding energy distribution, which is obtained by taking the derivative of the cumulative MB distribution. Here, the mean energy of this distribution is  $444.32 \mu\text{K}$ , and the minimum energy (below which we find no atoms) is  $E_{\text{min}} = 225 \mu\text{K}$ .

### 4.2.3 Experiment results

Finally, We measured the loss rate as a function of trap depths for collisions between trapped  $^{87}\text{Rb}$  and atomic (He, Ar, and Xe) and molecular ( $\text{H}_2$ ,  $\text{N}_2$ , and  $\text{CO}_2$ ) gases. We introduced each test gas into the chamber from a 99.999 % pure source and we used an RGA to ensure that there is no other gas species introduced into the chamber. Then, for each test gas, the loss rates,  $\Gamma_{\text{loss}}(U)$ , were measured as a function of trap depths to verify that the measured normalized loss rate coefficients ( $\langle \sigma_{\text{loss}}(U) v \rangle / P_x$ ) versus  $U$  are independent of gas pressure. The Fig. 4.9 (a) shows the raw data for the Ar gas

study with corresponding IG readings of  $P_{\text{Ar}} \approx 8.9 \times 10^{-9}$  Torr and  $1.1 \times 10^{-8}$  Torr. Fig. 4.9 (b) shows the pressure normalized loss rates,  $\langle \sigma_{\text{loss}}(U) v \rangle / P_x$ , and the two data sets overlap, as expected, since this ratio removes the effects of changing the density of the test gas, Ar (the situation is different when the test gas is  $\text{CO}_2$ , as discussed in Section 4.2.3).

This overlap verifies (i) that the background pressure did not vary significantly during the measurements, (ii) that the measured  $\langle \sigma_{\text{loss}}(U) v \rangle$  values do not vary with the gas pressure, in agreement with equation 4.16, and (iii) that the IG pressure readings were linear (albeit inaccurate) with the test gas density. The same calibration procedure was applied to three molecular species, Hydrogen ( $\text{H}_2$ ), Nitrogen ( $\text{N}_2$ ), and Carbon Dioxide ( $\text{CO}_2$ ). They were selected because of their importance in many vacuum systems [114, 129]. Unlike atoms, these species have a rich internal structure and can undergo both elastic and inelastic collisions. Later, the same data in figure 4.9 (b) are then averaged and normalized by the extrapolated loss rate at zero trap depth,  $\Gamma_{\text{loss}}(U)/\Gamma_{\text{loss}}(U = 0)$ , and shown in figure 4.10 (a). Since we can obtain the PESs of atom-atom collisions more easily, we run the quantum scattering computations to generate the rate coefficients at different trap depths for collisions between Rb and atomic species (He, Ar, and Xe). The results are shown as dashed lines in figure 4.10 (a). We can find the experimental results agree with the theoretical predictions very well.

Next, the data in figure 4.10 are fitted to the universal Eq. 4.16 to extract the values of  $\langle \sigma_{\text{tot}} v \rangle$  and  $i_g$ . The fitting results are shown in table 4.2. Based on the  $\langle \sigma_{\text{tot}} v \rangle$  values, we can calculate the characteristic energy and normalize the trap depth by the characteristic energy  $U_d$ , as shown in figure 4.10 (b). As expected, all the data follow the same universal shape. This is a manifestation of the universality of quantum diffractive collisions that only depend on the analytic form of the long-range part,  $C_6$ , of the potential. Namely, quantum diffractive collisions responsible for the trap depth variation of the loss rate impart too little energy to lead to changes of the internal states of the collision partners over the range of trap depths studied here. Thus, inelastic collisions (although they are occurring) play no role in the trap depth dependence measured [2]. Moreover, because of universality, the energy scaling of the trap depth-dependent loss rate reveals the total cross section  $\langle \sigma_{\text{tot}} v \rangle$ .

By following the calibration procedure described in this work, one can determine

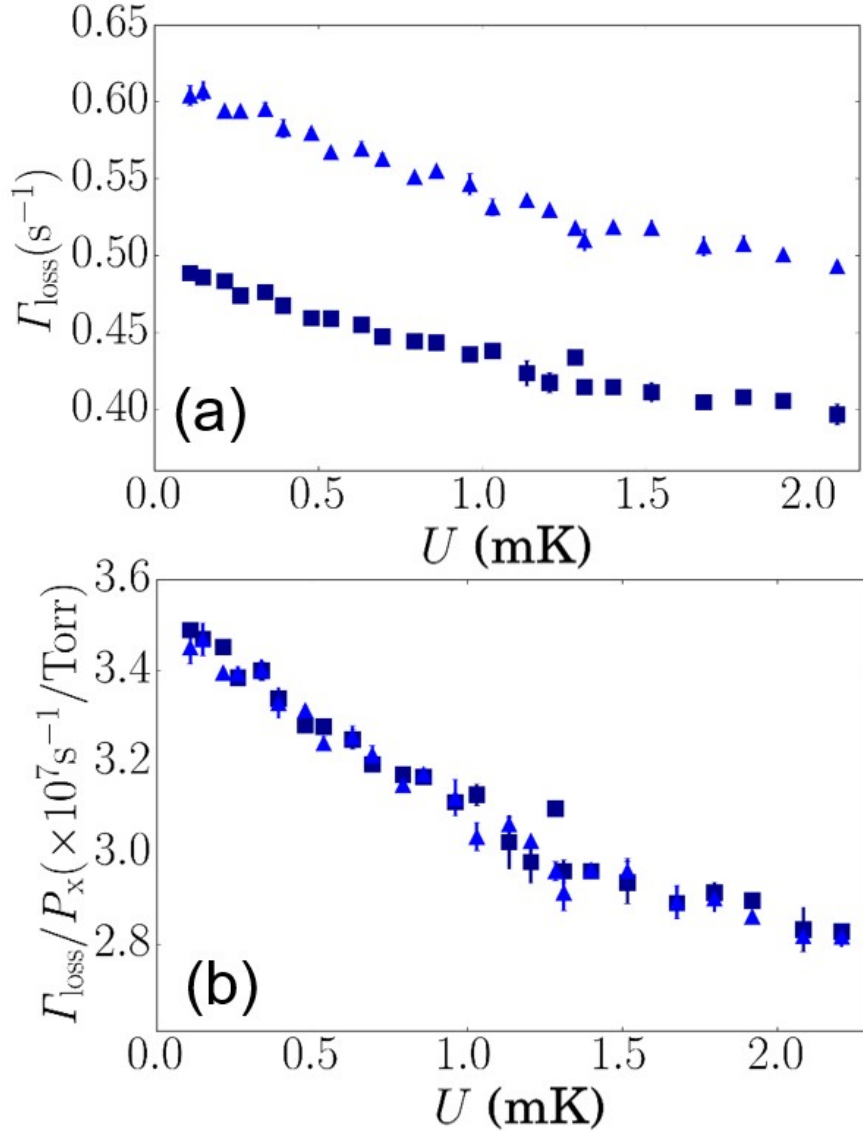


Figure 4.9: A plot of experimental results. In (a), the trap loss rate increase for  $P_{\text{Ar}} \approx 8.9 \times 10^{-9}$  Torr (triangles) and  $P_{\text{Ar}} \approx 1.1 \times 10^{-8}$  Torr (squares) are shown for different trap depths, those loss rates divided by the pressure reading for each measurement are shown in (b). The error bars in (b) are the statistical errors, including the uncertainties associated with the fit to extract decay rates,  $\Gamma_{\text{loss}}$ , from the atom number decay measurements and the uncertainties from the pressure measurements, while the error bars in (a) only represent the uncertainties from decay rate measurements.

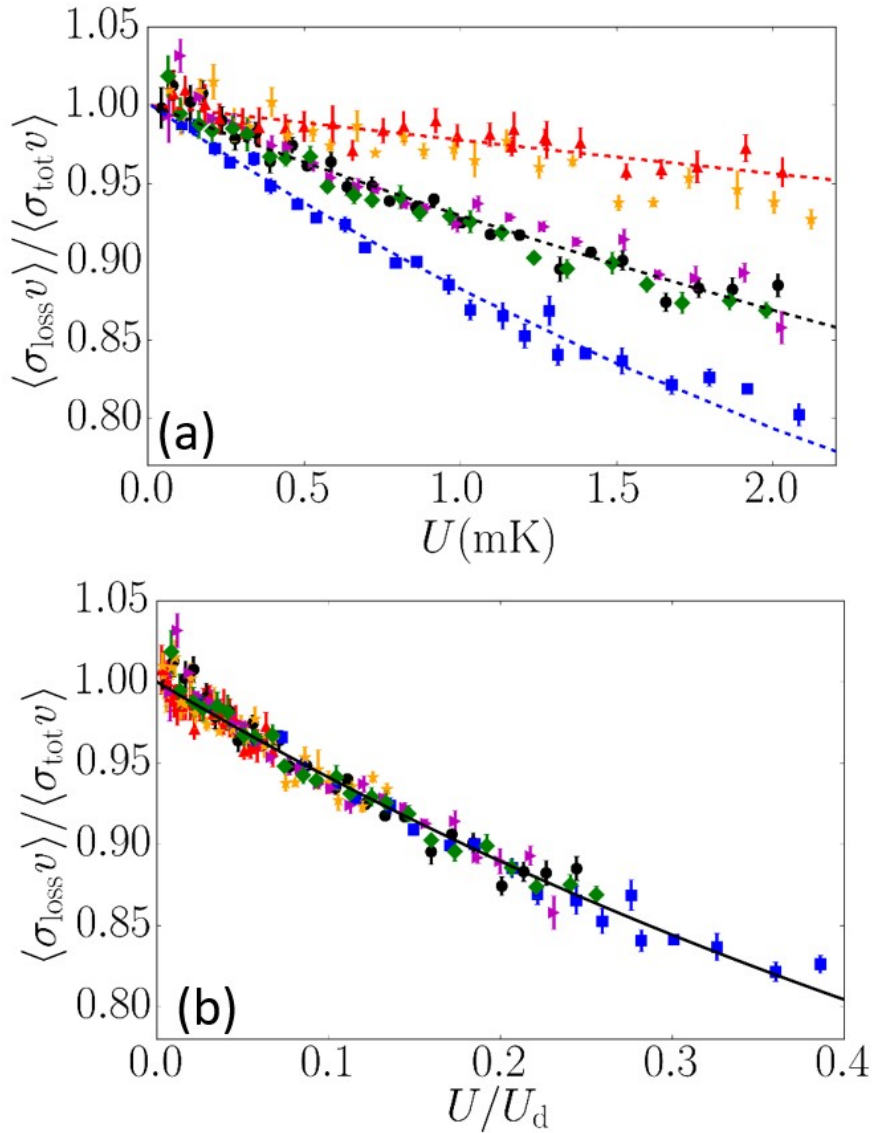


Figure 4.10: A plot of experimental results for all the collision species. Panel (a) shows the data in figure 4.9 (b) are normalized by the extrapolated loss rate at zero trap depth for all collisions species, He (triangles), Xe (squares), H<sub>2</sub> (stars), N<sub>2</sub> (right triangles), and CO<sub>2</sub> (diamonds). The dashed lines represent the theoretical predictions using the quantum scattering computations. All the data are then scaled by the fitted results,  $U_d$ , and shown in (b). As expected, they fall on the universal curve.

$\langle \sigma_{\text{tot}} v \rangle$  for the background gas species that cannot be easily computed due to the difficulty of computing the PES for systems with a large number of electrons. The measurement of  $\langle \sigma_{\text{tot}} v \rangle$  also provides the gauge factor reading for any IG attached to the quantum pressure standard. In our apparatus, two gauges, IG “a” and IG “b”, are connected to the system, as demonstrated in figure 3.18. The results for the six gases

calibrated (He, Ne, Xe, H<sub>2</sub>, N<sub>2</sub>, and CO<sub>2</sub>) are given in Table 4.2.

### $\langle\sigma_{\text{tot}}v\rangle$ Measurements

The second column of Table 4.2 lists the measured values of  $\langle\sigma_{\text{tot}}v\rangle$ . They show a trend of increasing precision with increasing mass of the collision partner (see Fig. 4.11). This mass dependence arises from the most probable velocity term,  $v_p$ , in the quantum diffractive energy,  $U_d$ . As the collision partner mass increases,  $v_p$  decreases, decreasing  $U_d$ , in turn. This leads to an increase in the range of  $U/U_d$  explored experimentally for our fixed maximum trap depth of  $U = 2.2$  mK. A larger range explored directly improves the experimental fit to the universal polynomial, Eq. 4.16, reducing the statistical uncertainty in the measured  $\langle\sigma_{\text{tot}}v\rangle$  value. The statistical (fitting) uncertainty as a function of the range of  $\frac{U}{U_d}$  is shown in figure 4.11.

The measurement technique presented here also provides a new method to measure the long-range dispersion coefficients for any species. Using Eq. 4.3, the dispersion coefficients,  $C_6$ , are extracted from the loss rate measurements and compared to the values listed in the literature [11, 9]. The latter is calculated based on the polarizabilities of the ground and excited electronic states using the Casimir Polder integral or Slater-Kirkwood formula. The experimental  $C_6$  values extracted from the measured  $\langle\sigma_{\text{tot}}v\rangle$  are consistent with the values reported in the literature or from the polarizabilities of the theoretical predictions for all species except CO<sub>2</sub>. The anomalous result for the CO<sub>2</sub> called for closer inspection. To verify this finding, the CO<sub>2</sub> measurements were repeated 7 times at different pressures and acquired over a five-month period, yielding consistent values for the  $\langle\sigma_{\text{tot}}v\rangle$  between CO<sub>2</sub> and trapped Rb of  $2.82 \times 10^{-15} \text{cm}^3/\text{s}$  ( $\pm 2\%$ ). Therefore, despite the discrepancy in the  $C_6$  value for CO<sub>2</sub>, the  $\langle\sigma_{\text{tot}}v\rangle$  results proved to be reproducible. The consistently measured value of  $\langle\sigma_{\text{tot}}v\rangle$  is the fundamental quantity required to measure the pressure of CO<sub>2</sub>. We speculate that the  $C_6$  discrepancy may arise from the fact that CO<sub>2</sub> is a triatomic molecule for which the long-range dispersion coefficient has a more complex relationship to the polarizabilities of its ground and excited electronic states than that for a diatomic molecule.

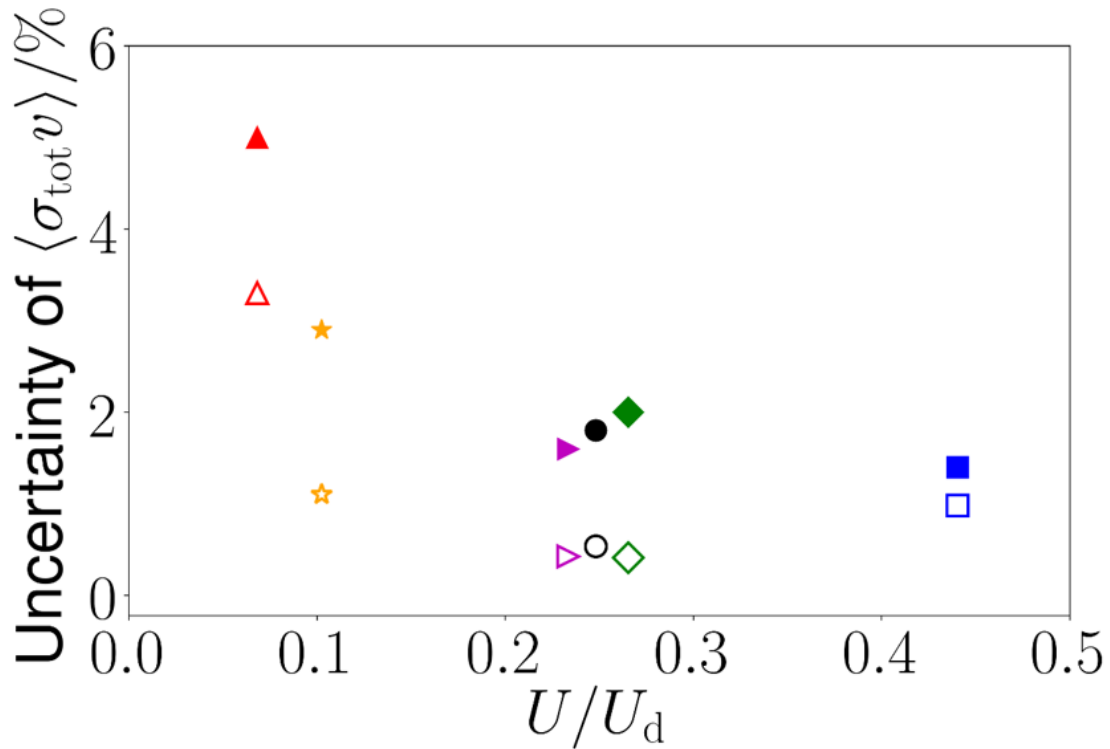


Figure 4.11: A plot of the uncertainty in the determination of  $\langle \sigma_{\text{tot}} v \rangle$  as a function of the range of  $\frac{U}{U_d}$  accessed for the measurement. For the lighter collision partners, He (triangles) and  $\text{H}_2$  (stars),  $U_d$  is significantly larger compared to the other species calibrated, Ar (circles), Xe (squares),  $\text{CO}_2$  (diamonds), and  $\text{N}_2$  (right triangles), limiting the range of  $\frac{U}{U_d} \leq 0.1$ , resulting in larger statistical fitting errors (filled markers). The open markers indicate the estimated systematic uncertainty, which is dominated by ensemble heating in the trap and base pressure changing in the vacuum. The filled markers indicate the estimated statistical uncertainty including the fitting uncertainty and the shot-to-shot noise.

### Validation of the Primary Quantum Pressure Standard

The standard practice for comparing the performance of vacuum pressure standards is to calibrate an ionization gauge (IG) with one standard, send the gauge to a second standard, and redo the calibration [23]. The figure of merit is the gauge factor,  $i_g$ , which relates the gauge readings,  $P_{\text{exp}}$ , to the pressure standard values,  $P_{\text{std}}$ .

$$P_{\text{exp}} = i_g P_{\text{std}} \quad (4.26)$$

Typically, this standard comparison is only carried out for two inert species, Argon and/or Nitrogen, dictated by the limitations of the state-of-the-art orifice flow stan-

dards currently in use [23]. Two IGs were attached to the quantum pressure standard apparatus. IG “a” was calibrated by NIST for N<sub>2</sub> using their orifice flow standard. The excellent agreement between the NIST gauge factor,  $0.94 \pm 2.8\%$ , and the value of  $0.943 \pm 2\%$  calibrated by the new standard demonstrate the quantum standard’s accuracy. Note that the 2.8% uncertainty quoted for the NIST calibration includes the calibration uncertainty (2.0%) and the calibration drift uncertainty (2.0%) [130]. It is essential to note that prior to calibration, the IG was “conditioned” with N<sub>2</sub> gas. That is, the gauge was exposed to a high pressure ( $10^{-4}$  Torr/ $10^{-2}$  Pa) of N<sub>2</sub> for one hour, then the vacuum system was evacuated back to its base pressure. This conditioning procedure ensures that the adsorption of N<sub>2</sub> into the IG filament is saturated. Thus, only this gas will be emitted by the hot filament during the gas calibration measurements. If gauge conditioning is not performed, the gauge factor can vary with time and with pressure reading, leading to the  $i_g$  for the specific species to differ from its previously calibrated value [23, 130].

	$\langle\sigma_{\text{tot}}v\rangle_a/10^{-15}\text{m}^3/\text{s}$	$\bar{\sigma}/\text{\AA}^2$	$C_{6,\text{theory}}/E_H a_0^6$	$C_{6,\text{exp}}/E_H a_0^6$	$i_g$	$i_{g_a,\text{exp}}$	$i_{g_b,\text{exp}}$	$U_d/mK$
N <sub>2</sub>	3.11 (5) (2)	744 (12)	302 <sup>3</sup>	325 (14)	0.94 (2)	0.943 (19)	0.823 (46)	9.4
He	2.40 (12) (8)	217 (11)	44.07 (11) <sup>1</sup> , 36.6 <sup>2</sup>	37.5 (4.9)	0.18 (2)	0.163 (8)	0.195 (39)	32.3
Ar	2.77 (5) (2)	792 (14)	334 (2) <sup>1</sup>	317 (14)	1.29 (13)	1.238 (26)	1.203 (74)	8.9
Xe	2.71 (3) (3)	1404 (17)	776 (4) <sup>1</sup>	738 (19)	2.85 (29)	2.511 (30)	2.484 (72)	5.0
H <sub>2</sub>	5.09 (14) (6)	327 (9)	140 <sup>3</sup>	145 (11)	0.46 (5)	0.559 (18)	0.534 (71)	21.5
CO <sub>2</sub>	2.82 (6) (2)	846 (17)	482 <sup>3</sup>	346 (11)	1.43 (14)	0.958 (14)	0.893 (54)	8.3

Table 4.2: Values for  $\langle\sigma_{\text{tot}}v\rangle$  and the gauge calibration factor  $i_{g_a,\text{exp}}$  and  $i_{g_b,\text{exp}}$  derived from fitting the data shown in Fig. 4.10 to Eq. 4.16, here  $\bar{\sigma} = \langle\sigma_{\text{tot}}v\rangle/v_p$ . The first bracket in the column of  $\langle\sigma_{\text{tot}}v\rangle_a$  indicates the statistical error and the second one indicates the systematic error. The gauge factor,  $i_g$ , for N<sub>2</sub> (blue) is the value calibrated by NIST’s orifice flow pressure standard with an uncertainty of 2.8%. Here the estimates of gauge correction factor for He, Ar, Xe, H<sub>2</sub> and CO<sub>2</sub> in the column of  $i_g$  are provided by MKS Instruments [7] with at least 10% uncertainties according to [8]. The numbers in the column of  $i_{g_a}$  and  $i_{g_b}$  are the experimentally measured ion gauge “a” and “b” correction factors.  $C_{6,\text{theory}}$  is the theoretical prediction for the  $C_6$  value given by [ <sup>1</sup>Derevianko *et al* [9], <sup>2</sup>Thomas *et al* [10], or <sup>3</sup>Arponthip *et al* [11]] in units of  $E_H a_0^6$ , where  $E_H$  is the Hartree energy and  $a_0$  is the Bohr radius.  $\langle\sigma_{\text{tot}}v\rangle_a$  and  $C_{6,\text{exp}}$  are the experimentally measured values using IG “a”.

## IG Performance

One of the strengths of this CAPS is that it can be used to calibrate IGs for any gas whose long-range interaction potential with the trapped sensor atom is described by a van der Waals potential. Two gauges were attached to the quantum pressure standard. As stated above, IG “a” was calibrated by NIST for N<sub>2</sub> and served as a direct comparison to their orifice-flow standard. IG “b” was an uncalibrated gauge attached to the system after purchase. Having two gauges attached to the quantum pressure standard allowed us to evaluate the performance of two gauges side by side. As noted above, IG conditioning was carried out prior to calibration with different gas species. However, for the inert gases such as He, Ar, and Xe, the conditioning procedure is unnecessary as these gases do not tend to absorb into the filament.

The calibrated gauge factors of IG “a” ( $i_{ga}$ ) and IG “b” ( $i_{gb}$ ) are listed in Columns 8 and 9 in Table. 4.2. Note that the shot-to-shot noise in the readings of IG “b” was found to be a factor of 5 larger than that of IG “a” during the calibration shown in Fig. 4.12, which produces much higher statistical uncertainty in the value of  $\langle\sigma_{tot}v\rangle$  derived from a calibration using this gauge.

As illustrated in Table. 4.2, the noble gas gauge factors determined for each IG agree with their measured uncertainties. The measured noble gas gauge factors also agree with their approximate (expected) values quoted by the gauge manufacturers within their stated 10% uncertainties [8]. By contrast, the other species we tested, CO<sub>2</sub> and N<sub>2</sub>, demonstrated much larger inter-gauge variations as well as large discrepancies between the calibrated  $i_g$  values and the manufacturers’ values. For example for N<sub>2</sub>, while the  $i_g$  values calibrated by NIST and by the quantum primary pressure standard agree for gauge “a”, the gauge factor for gauge “b” is significantly different [ $i_{ga} = 0.943(19)$  versus  $i_{gb} = 0.823(46)$ ]. Similarly, for the CO<sub>2</sub> gauge factors, there are significant discrepancies from gauge to gauge and with the manufacturers’ suggested values. Moreover, we found the calibrated gauge factors for CO<sub>2</sub> tend to increase as the background gas pressure increases, shown in Fig. 4.13 (b) and (c). In particular, the IG readings appear to be non-linear with the density of CO<sub>2</sub> molecules. This may be due to IG filament contamination by CO<sub>2</sub>. Due to its non-linearity, the gauge factor provided in Table. 4.2 for CO<sub>2</sub> only represent the effective gauge factors for the gauges under one specific pressure ( $P_{CO_2}^{IG,a} = 9.0 \times 10^{-9}$  Torr,  $P_{CO_2}^{IG,b} = 8.3 \times 10^{-9}$  Torr). We didn’t observe this

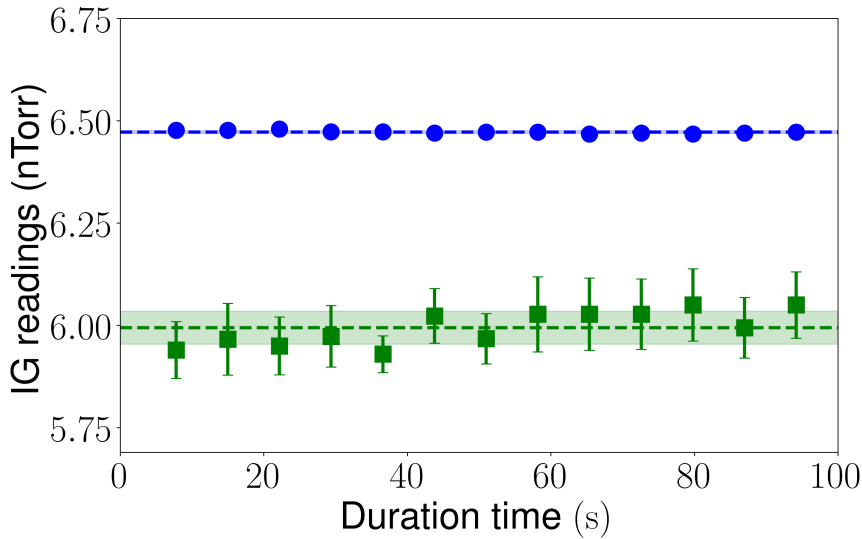


Figure 4.12: IG pressure readings as a function of measurement time. This shows an example of  $\text{N}_2$  pressure measured by both IG “a” (circles) and IG “b” (squares) during one decay rate measurement cycle. Each data point represents a pressure measurement averaged over more than 7 seconds, and the error bar shows the uncertainty. The dash lines represent the average pressure values over the entire measurement cycle, and the shadow areas display the overall uncertainty. For this example, the IG readings at the same  $\text{N}_2$  molecule density were,  $P_{\text{N}_2}^{\text{IG,a}} = 6.47(0.01) \times 10^9$  Torr,  $P_{\text{N}_2}^{\text{IG,b}} = 5.99(0.06) \times 10^9$  Torr.

gauge factor non-linearity for the other gases tested. Significantly, we verified that the measured values of  $\langle \sigma_{\text{tot}} v \rangle$  do not depend on the operating pressures.

These measurements underscore the flexibility of the new quantum pressure standard: any species with a long-range van der Waals interaction potential can be calibrated by the new standard. The orifice flow standards cannot easily be used with sticky molecules such as  $\text{CO}_2$ . At present, orifice flow standards are rarely used to calibrate IGs for gases other than Ar and  $\text{N}_2$ . The limitations of using IG for measuring non-inert species is also made clear by the results.

In summary, using an IG to measure the pressure of a noble gas is probably reliable within the 10% uncertainty quoted in [8]. However, when the ambient gas is  $\text{N}_2$ , gauge calibration is required to guarantee accurate measurements, with uncertainties that may lie outside the manufacturers’ quoted range of 10%. IG are even less reliable for measuring sticky species like  $\text{CO}_2$  because the gauge factors evidently vary with the density of background particles. These results offer some additional insight into the limitations of IG measurements. By contrast, the quantum pressure standard displays

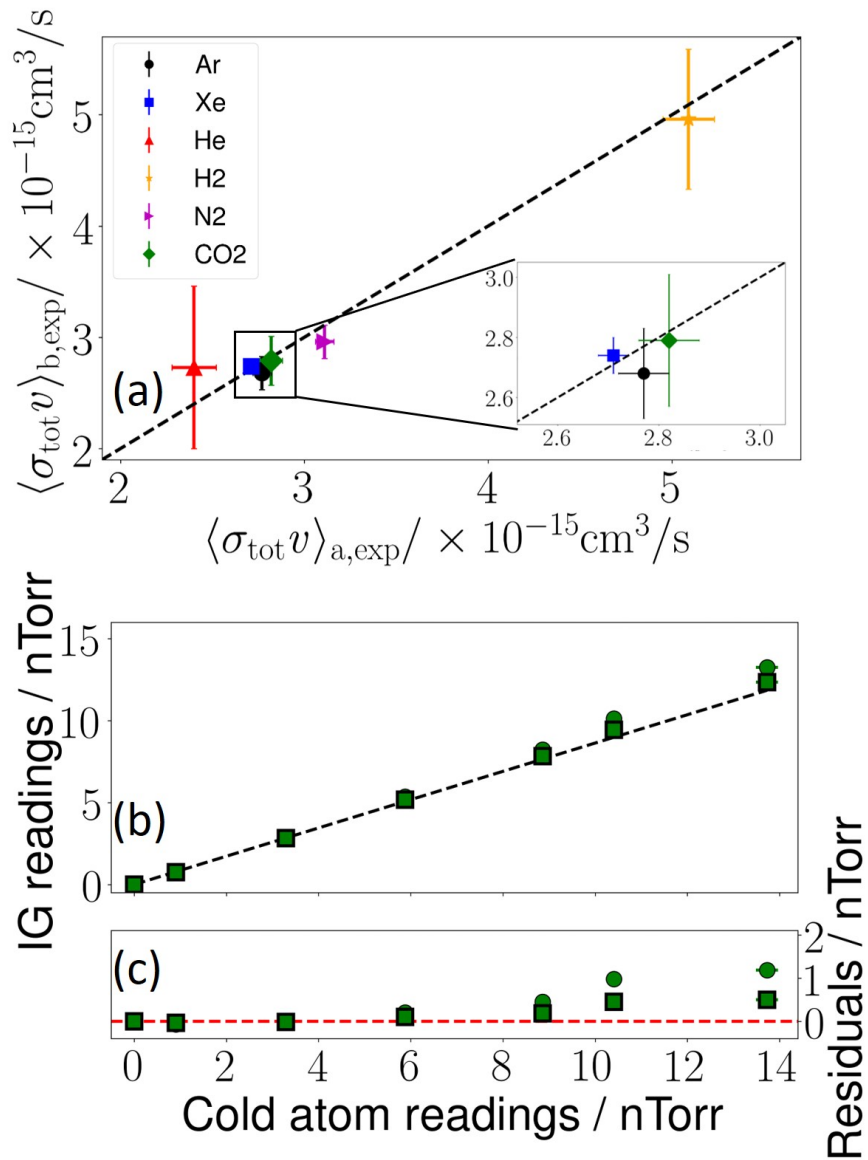


Figure 4.13: (a) A plot of  $\langle \sigma_{\text{tot}} v \rangle_a$  versus  $\langle \sigma_{\text{tot}} v \rangle_b$  measured against the two ionization gauges (IG “a” and IG “b”). The dash line indicates perfect agreement between the two values. Data of He (triangle), Xe (square), Ar (circle), H<sub>2</sub> (star), and N<sub>2</sub> (right triangle) is averaged over two different pressures, while CO<sub>2</sub> (diamond) is averaged over 7 different pressures, as stated in the text. A direct comparison between the IGs and the atom standard is in (b) plotting two IG “a” (circles), “b” (squares) readings versus the cold atom gauge readings with CO<sub>2</sub> as the test gas with a linear fit (dash line). The residuals of the data from the linear fit are plotted in (c) and the zero guideline is shown as the red dash line.

consistent values of the measured  $\langle \sigma_{\text{tot}} v \rangle$  for the different species against different ion gauges, as shown in Fig. 4.13 (a).

### 4.3 Rigorous Universal Fitting

We have reported the values of  $\langle\sigma_{\text{tot}}v\rangle$  by fitting the loss rate versus the mean trap depth to Eq. 4.16. However, this method can be viewed as the first-order approximation of the fitting routine since we view the whole cloud ensemble as a single atom with the trap depth of the mean trap depth of the cloud and only compute the loss rate coefficient at the mean trap depth. More rigorously, we should average the energy-dependent loss rate coefficient over the ensemble.

Recall the trap depth for a trapped atom with energy,  $E$ , is defined as  $U = E_{\text{max}} - E$ . Therefore, the mean trap depth,  $\bar{U}$ , of the sensor ensemble with energy below  $E_{\text{max}}$  is determined by averaging the trap depth of each atom,  $U$ , over the energy distribution of the selected ensemble,

$$\bar{U} = \frac{\int_0^{E_{\text{max}}} (E_{\text{max}} - E)\rho(E)dE}{\int_0^{E_{\text{max}}} \rho(E)dE} = \langle(E_{\text{max}} - E)\rangle_{\text{trunc}}. \quad (4.27)$$

Here “ $\langle\rangle_{\text{trunc}}$ ” indicates the ensemble average of the quantity in the bracket over the energy range,  $[0, E_{\text{max}}]$ , truncated by the RF radiation.  $\rho(E)$  represents the energy distribution of the whole ensemble before applying any RF field and can be measured experimentally. It is found to be modeled very well by a Maxwell-Boltzmann (MB) distribution of a mean temperature,  $T$ , shifted by a fixed amount of energy,  $E_{\text{min}}$  (owing to a slight misalignment of the MOT and MT used in the measurements),

$$\rho(E)dE = \Theta(E - E_{\text{min}}) \cdot 2 \left( \frac{E - E_{\text{min}}}{\pi} \right)^{\frac{1}{2}} \left( \frac{1}{k_B T} \right)^{\frac{3}{2}} e^{-\frac{E - E_{\text{min}}}{k_B T}} dE. \quad (4.28)$$

$\Theta(E - E_{\text{min}})$  is the Heaviside function, which indicates that there are no atoms with energies below  $E_{\text{min}}$  in the MT, and the remaining factor is a regular MB distribution in energy above  $E_{\text{min}}$ . Therefore, as a first approximation, we can directly insert the mean trap depth,  $\bar{U}$ , into Eq. 4.10 to calculate the loss rate coefficient as expressed in

the following,

$$\langle \sigma_{\text{loss}}(\bar{U}) v \rangle = \langle \sigma_{\text{tot}} v \rangle \left[ 1 - \sum_{j=1}^{\infty} \beta_j \left( \frac{\langle (E_{\text{max}} - E) \rangle_{\text{trunc}}}{U_d} \right)^j \right] \quad (4.29)$$

$$\begin{aligned} &= \langle \sigma_{\text{tot}} v \rangle \left[ 1 - \beta_1 \left( \frac{1}{U_d} \right) \langle (E_{\text{max}} - E) \rangle_{\text{trunc}} \right. \\ &\quad \left. - \beta_2 \left( \frac{1}{U_d} \right)^2 \langle (E_{\text{max}} - E) \rangle_{\text{trunc}}^2 - \dots \right]. \end{aligned} \quad (4.30)$$

A more rigorous approach is to average the loss rate coefficient  $\langle \sigma_{\text{loss}}(U) v \rangle$  of an atom at finite trap depth,  $U$ , over the energy distribution of the selected ensemble,

$$\overline{\langle \sigma_{\text{loss}}(U) v \rangle} = \frac{\int_0^{E_{\text{max}}} \langle \sigma_{\text{loss}}(E_{\text{max}} - E) v \rangle \rho(E) dE}{\int_0^{E_{\text{max}}} \rho(E) dE} \quad (4.31)$$

$$\begin{aligned} &= \langle \sigma_{\text{tot}} v \rangle \left[ 1 - \sum_{j=1}^{\infty} \beta_j \left( \frac{1}{U_d} \right)^j \frac{\int_0^{E_{\text{max}}} (E_{\text{max}} - E)^j \rho(E) dE}{\int_0^{E_{\text{max}}} \rho(E) dE} \right] \\ &= \langle \sigma_{\text{tot}} v \rangle \left\{ 1 - \beta_1 \left( \frac{1}{U_d} \right) \left[ \frac{\int_0^{E_{\text{max}}} (E_{\text{max}} - E) \rho(E) dE}{\int_0^{E_{\text{max}}} \rho(E) dE} \right] \right. \\ &\quad \left. - \beta_2 \left( \frac{1}{U_d} \right)^2 \left[ \frac{\int_0^{E_{\text{max}}} (E_{\text{max}} - E)^2 \rho(E) dE}{\int_0^{E_{\text{max}}} \rho(E) dE} \right] - \dots \right\} \end{aligned} \quad (4.32)$$

$$\begin{aligned} &= \langle \sigma_{\text{tot}} v \rangle \left[ 1 - \beta_1 \left( \frac{1}{U_d} \right) \langle (E_{\text{max}} - E) \rangle_{\text{trunc}} \right. \\ &\quad \left. - \beta_2 \left( \frac{1}{U_d} \right)^2 \langle (E_{\text{max}} - E) \rangle_{\text{trunc}}^2 - \dots \right]. \end{aligned} \quad (4.33)$$

One observes that these two expressions of the loss rate coefficient deviate from each other. The approximate loss rate coefficient expression (Eq. 4.29) replaces the  $j$ -th moment  $\langle (E_{\text{max}} - E)^j \rangle_{\text{trunc}}$  in each term of the polynomial with the  $j$ -th power of the first moment,  $\langle (E_{\text{max}} - E) \rangle_{\text{trunc}}^j$ . This discrepancy increases for higher powers of  $j$  and for lower values of  $U_d$  that increase the weighting of the higher-order terms. Due to the discrepancy between the approximate (Eq. 4.29) and the rigorous (Eq. 4.31) expression, the velocity averaged total collision cross sections,  $\langle \sigma_{\text{tot}} v \rangle$ , derived from fitting the experimental data to the two expressions are systematically different. We refit the experimental data to the new expression, Eq. 4.31, for all the gas species (Xe,

#### 4.4. Uncertainty Analysis

Ar, He, H<sub>2</sub>, N<sub>2</sub>, and CO<sub>2</sub>). The new values are labeled as  $\langle\sigma_{\text{tot}}v\rangle^*$  and are presented in table 4.3, along with the original values,  $\langle\sigma_{\text{tot}}v\rangle$ , reported in table 4.2. While they agree within statistical errors, the new values are systematically higher than the previous ones. As expected, the discrepancy is the largest (1.5%) for the collision partners with the lowest  $U_d$  (Rb-Xe) and least (0.4%) for Rb-He which has the largest  $U_d$ .

In addition to updating the values of  $\langle\sigma_{\text{tot}}v\rangle$ , we also report the revised gas calibration factors for the ionization gauge,  $i_g$ , used in the pressure calibration experiment. The gauge was calibrated only for N<sub>2</sub> gas by NIST (National Institute of Standards and Technology) using an orifice flow pressure standard. Our updated calibration factor,  $i_g = 0.950$  (19) agrees with the value reported by NIST,  $i_g = 0.940$  (26), within 1%.

	$\langle\sigma_{\text{tot}}v\rangle_a / 10^{-15} \text{m}^3/\text{s}$	$\langle\sigma_{\text{tot}}v\rangle_a^* / 10^{-15} \text{m}^3/\text{s}$	$\Delta\langle\sigma_{\text{tot}}v\rangle / \langle\sigma_{\text{tot}}v\rangle^* / \%$	$U_d / k_B / \text{mK}$	$i_g$
Rb-N <sub>2</sub>	3.11 (5) (2)	3.14 (5) (2)	0.9	9.4	0.950 (19)
Rb-He	2.40 (12) (8)	2.41 (12) (8)	0.4	32.3	0.164 (9)
Rb-Ar	2.77 (5) (2)	2.79 (5) (2)	0.7	8.8	1.245 (26)
Rb-Xe	2.71 (3) (3)	2.75 (3) (3)	1.5	5.0	2.549 (30)
Rb-H <sub>2</sub>	5.09 (14) (6)	5.12 (14) (6)	0.6	21.5	0.562 (18)
Rb-CO <sub>2</sub>	2.82 (6) (2)	2.84 (6) (2)	0.7	8.3	0.985 (15)

Table 4.3: A comparison of the experimentally determined values of  $\langle\sigma_{\text{tot}}v\rangle$  for Rb-X collisions (X = He, Ar, Xe, H<sub>2</sub>, N<sub>2</sub>, and CO<sub>2</sub>). The values of  $\langle\sigma_{\text{tot}}v\rangle$  in the second column, reported in table 4.2, are extracted by fitting the experimentally determined loss rate coefficients to the approximate expression, Eq. 4.29. The values in the column of  $\langle\sigma_{\text{tot}}v\rangle^*$  are determined by fitting the experimental data to the rigorous expression, Eq. 4.31. The discrepancy between the two values in column 2 and 3 is defined as  $\Delta\langle\sigma_{\text{tot}}v\rangle / \langle\sigma_{\text{tot}}v\rangle^* = (\langle\sigma_{\text{tot}}v\rangle^* - \langle\sigma_{\text{tot}}v\rangle) / \langle\sigma_{\text{tot}}v\rangle^* \times 100\%$  and is presented in column 4. The first bracket in the columns of  $\langle\sigma_{\text{tot}}v\rangle_a$  and  $\langle\sigma_{\text{tot}}v\rangle_a^*$  indicates the statistical error and the second one indicates the systematic error reported in table 4.2. The column of  $U_d$  presents the quantum diffractive energy of each collision pair, derived from the newly determined value of  $\langle\sigma_{\text{tot}}v\rangle^*$ . The last column reports the updated calibration factor,  $i_g$ , for the ionization gauge operated in the experiment, which was previously calibrated against NIST’s orifice flow pressure standard only for the gas of N<sub>2</sub>. The statistical error of the calibration factor is shown in the bracket.

#### 4.4 Uncertainty Analysis

Next, we assess, numerically and experimentally, the impact of the systematic and random errors associated with determining  $\langle\sigma_{\text{tot}}v\rangle$ . In this section, the magnitudes of the corresponding errors that limit the accuracy and precision of the Rb-N<sub>2</sub> measurements are provided. Note that the sizes of both the statistical and the systematic errors depend on the collision partners.

#### 4.4.1 Systematic Errors

First, heating of the ensemble gradually increases the average energy of the trapped atoms, reducing the effective trap depth over time. If not accounted for, this can lead to a systematic error in the measured  $\langle\sigma_{\text{tot}}v\rangle$ . There are two sources of ensemble heating: noise on the current source used to create the magnetic field, and heating induced by the quantum diffractive collisions which do not liberate the atoms from the MT. Measurements of current noise heating confirmed that it is negligible for the data presented here.

The dominant source of trap heating is due to collisions which fail to eject atoms from the trap [56, 131]. The rate of ensemble heating increases for deeper MTs (due to a larger fraction of collisions leading to retained sensor atoms) and the average temperature of the atom ensemble increases with hold duration in the MT. The heating effectively reduces the MT depth over time, leading to a systematic error in the measured  $\langle\sigma_{\text{tot}}v\rangle$  values. In the present work, this effect was suppressed by restricting the hold times used for the loss rate measurements to values that were less than twice the sensor atoms' lifetimes when the trap depth exceeded 1 mK. We estimate the effect of heating experimentally by measuring the change in the ensemble energy distribution between initially loading the atoms into the MT and after holding them in the trap for two lifetimes. The heating will reduce the effective trap depth of the atoms, changing the value of  $\langle\sigma_{\text{tot}}v\rangle$  that is measured. For our measurements with a trap depth of 2.2 mK, we estimate an upper bound of this uncertainty to be 0.4% corresponding to the percentage difference in the value of  $\langle\sigma_{\text{tot}}v\rangle$  computed for each of the two temperature extremes.

Second, this apparatus relies on a spherical quadrupole magnetic field, which has a zero in the field. Atoms traversing the zero-field region will experience Majorana loss [125, 132]. To accurately measure the background collision loss rate from a magnetic trap, one needs to consider the contributions from the spin-flip losses. This can be eliminated by using a different magnetic trap geometry, such as TOP trap [133] and Ioffe-Pritchard trap [112]. Given the Majorana loss rate,  $\Gamma_{\text{Maj}}$ , is constant as long as the field gradient and the temperature of the ensemble are not changing significantly over time. Here, we account for this constant loss rate contributing to the background loss rate by subtracting the background loss rate from the collision induced loss rate of interest.

Third, there is an unknown mixture of gases constituting the base pressure in the apparatus mostly due to backflow through the turbo pump and vacuum chamber outgassing [114, 129]. These background gases contribute a base loss rate,  $\Gamma_{\text{bg}}$ , to which the test gas loss rate is added. If the background constituents vary with time, this will lead to a systematic error in the measured loss rate for the pressure standard. For the turbopump system used in this work, it was found that the base pressure can change by about  $1 \times 10^{-10}$  Torr during the time a full trap depth characterization measurement is performed over 6 hours, and this contributes less than 0.4 % to the uncertainty of the final result when the test species is  $\text{N}_2$ .

In addition, sensor atom losses due to two-body elastic (evaporation), two-body inelastic [127] and three-body recombination losses [134] arising from intra-trap collisions are exceedingly small since the density of the trapped Rb atoms is below  $10^7 \text{ cm}^3$ , leading to the two body loss rate is on the order magnitude of  $10^{-5} \text{ s}^{-1}$ .

Finally, variations in the ambient temperature (the temperature of the vacuum chamber) during the measurements lead to uncertainties in the temperature of the gas being measured. This variation is less than 0.5 K contributing less than 0.01% uncertainty in the value of  $\langle \sigma_{\text{tot}} v \rangle$ .

#### 4.4.2 Random Errors

Besides these systematic errors, some random errors are reflected in the statistical uncertainties, limiting the precision of the measurements. First, the observed variation in the decay rate measurements (including the shot-to-shot variations in the atom number and the electronic noise in the photon detector) leads to a statistical uncertainty of 1.8% in the value of  $\langle \sigma_{\text{tot}} v \rangle$ . In addition, because we use the ion gauge readings to normalize away pressure variations during the measurement, random noise in the ion gauge readings  $P_x$  is written into  $\Gamma/P_x$  and introduces additional statistical error to the value of  $\langle \sigma_{\text{tot}} v \rangle$ . The shot-to-shot noise in IG “a” readings contributes about 0.2% in the statistical uncertainty while calibrating with the noisier IG “b” measurements introduces 1.0% uncertainty, as shown in Fig. 4.12. The error budget described in this section is summarized in Table 4.4. The systematic and random uncertainties together (added in quadrature) lead to an upper-bound total uncertainty of  $\pm 2.2\%$  on the measurements of  $\langle \sigma_{\text{tot}} v \rangle$ . A similar method has been applied to other test species, and the resulted

#### 4.4. Uncertainty Analysis

---

uncertainties are presented in column 2 of Table. 4.2.

<b>Source of Errors</b>	$\delta\langle\sigma_{tot}v\rangle/\langle\sigma_{tot}v\rangle$ /%
Heating effects	< 0.5
Base pressure changes	< 0.4
Majorana loss rate changes	< 0.06
Statistical uncertainty	< 1.9
Ambient temperature changes	< 0.01
<b>Total Estimate</b>	< 2.2

Table 4.4: Relative uncertainties for the total velocity averaged cross section  $\langle\sigma_{tot}v\rangle$  when the test species is  $N_2$ . The statistical uncertainty results from fitting the data, including variations due to fluctuations in the decay rate measurement 1.8% and fluctuations in the IG “a” readings 0.2% (1.0% for IG “b” readings). Note that the sizes of both the statistical and the systematic errors depend on collision species.

## Chapter 5

# Application of QDU: Precision Measurements of $\langle\sigma_{\text{tot}}v\rangle$

In Chapter 4, we used the full quantum scattering computations to demonstrate the quantum diffractive universality (QDU). Then we further validated this universal law by experimentally mapping out the loss rates as a function of trap depths in the MT. This allows us to construct a self-calibrating primary quantum pressure standard. Using the quantum universal pressure standard, we were able to measure the pressure of both atomic and molecular gas species within 2.0% uncertainty.

We found that fitting the loss rate versus trap depth data to the universal equation, Eq. 4.16, one can determine the total velocity averaging collision cross section,  $\langle\sigma_{\text{tot}}v\rangle$ . In return, this QDU provides us with a way of precisely determining  $\langle\sigma_{\text{tot}}v\rangle$  for the collision system we are interested in. In addition, applying the self-calibration method allows the experimental determination of  $\langle\sigma_{\text{tot}}v\rangle$  for a wide range of collision partners, many of which have not or cannot be characterized computationally. Thus, this technique provides an experimental measure to compare *ab initio* computations to and a method for measuring  $\langle\sigma_{\text{tot}}v\rangle$  for the vast majority of species where this quantity cannot be computed from first principles. This is an important application of the QDU, and the use of the QDU to perform precision measurements of the  $\langle\sigma_{\text{tot}}v\rangle$  for the Rb-Ar collision system will be shown in this chapter.

### 5.1 Trapping Rb Atoms in F=2 Ground State.

In the previous uncertainty analysis study, shown in table 4.4, we have found that the dominant error is the statistical uncertainty that comes from fitting the loss rate versus trap depth to the universal equation. There are two ways to reduce the fitting uncertainty: One is to reduce the size of the errorbar of each data point. The other is

to extend the range of trap depths included in the measurements, to sample more of the universal function and improve the precision of the fit  $\langle\sigma_{\text{tot}}v\rangle$  value. The former option is achieved by using a different measurement scheme, a two-point scheme, will be discussed in section 5.2. The latter is achieved by trapping  $^{87}\text{Rb}$  atoms in the  $|F = 2, m_F = 2\rangle$  state and is presented in this part.

In our case, the fitting range is the accessible range of the trap depths in the MT. Given the expression of the trap depth in Eq. 4.25, we can notice that the most efficient way to increase the trap depth is to increase the maximum achievable energy of atoms,  $E_{\text{max}}$ . As shown in Eq. 4.24,  $E_{\text{max}}$  depends on the size of the RF surface,  $z_{\text{min}}$ , the axial magnetic field gradient,  $dB/dz$ , and the quantum number of the trapped sublevel,  $m_F$ . The size of the RF surface is limited by the radius of the laser beams,  $r_{\text{beam}} \approx 1.2$  cm, and the value of the axial magnetic field gradient is limited by the maximum current we can run through the coil,  $I_{\text{max}} = 200$  A, which provides the axial field gradient of 272 G/cm. Therefore, for  $^{87}\text{Rb}$  atoms in  $|F = 1, m_F = -1\rangle$  state, the maximum trap depth we can achieve is 3.0 mK. To further increase the trap depth, we can trap atoms in  $|F = 2, m_F = 2\rangle$  state so that the value of the quantum number,  $m_F$ , is increased by a factor of 2, which leads to an increase of the maximum trap depth by a factor of 2.

### 5.1.1 Optical pumping

The experiment procedure of trapping  $^{87}\text{Rb}$  atoms in the  $|F = 2, m_F = 2\rangle$  state is similar to trapping them in the  $|F = 1, m_F = -1\rangle$  state, as introduced in section 4.2.1. We loaded atoms into the 3D MOT region by propelling atoms from the 2D MOT section. Then the atoms in the 3D MOT section are further cooled by turning down the pump laser power and shifting the pump laser frequency to 60 MHz below  $F = 2 \rightarrow F' = 3$  transition for 20 ms. Instead of extinguishing the repump laser first and leaving the pump light on as we operated in trapping atoms in the  $F=1$  state, we turned off the pump light first and left the repump light on.

Meanwhile, we applied a 50  $\mu\text{W}$  right-hand circularly polarized optical pumping (OP) light which drives  $F = 2 \rightarrow F' = 2$  transition, as shown in figure 3.9. An extra magnetic field, generated by the compensation coils, is also introduced along the direction of the OP light, as described in section 3.3.3. After 2 ms, the repump light, the optical pumping light and the compensation coils are extinguished, so the atoms are

transferred to the low-field seeking sublevels in  $F = 2$  state. We noticed that the optical pumping is essential to increase the signal-to-noise ratio (SNR) since it increases the efficiency of transferring atoms to the stretched states in  $F = 2$ . The inset of figure 5.1 shows the recapture fraction (atom number) in the MT with the OP light applied and the recapture fraction without the OP light. With the OP light, the total atom number in the MT has been increased by a factor of 7 while the energy distribution of the atoms is still kept the same, as demonstrated in figure 5.1.

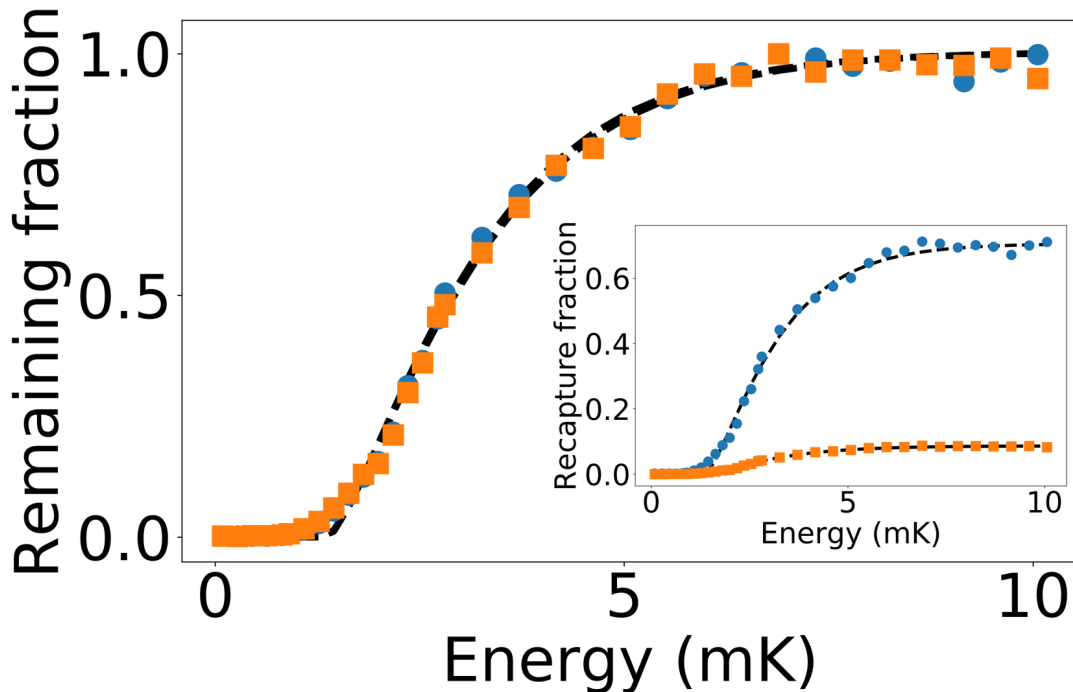


Figure 5.1: Fraction of atoms remaining in a MT as a function of energy, set by an RF pulse that ejects sensor atoms with energy above this. These data are fit to a cumulative MB distribution (dashed line) for the trapped atom ensemble. The remaining fraction is obtained by normalizing the recapture fraction to the maximum value, as shown in the inset. When the optical pumping beam is applied, more atoms can be transferred into  $|F = 2, m_F = +2\rangle$  state (blue circles). Here,  $|F = 2, m_F = +1\rangle$  state atoms have been gravitationally filtered out. On the contrary, fewer atoms will be transferred if the optical pumping beam is not applied (orange squares). However, the energy distribution is the same for both cases. The mean energy of both distributions is  $1332.28 \mu\text{K}$ , and the minimum energy (below which we find no atoms) is  $E_{\min} = 1360 \mu\text{K}$ .

### 5.1.2 Gravitational filtering

There are two trappable sublevels ( $m_F = 1$  and  $m_F = 2$ ) in  $F = 2$  state of  $^{87}\text{Rb}$ , as illustrated in figure 3.4. A mixture of atoms in these two states will experience different trap depths, complicating the loss rate measurements. Therefore, we need to ensure that atoms are trapped in pure  $|F = 2, m_F = 2\rangle$  state so that the MT loss rate can be measured from a single trap depth.

Given the minimum required magnetic field gradient to trap atoms depends on the sublevel,  $b'I = \frac{mg}{\mu_B g_F m_F}$ , we can distinguish them by ramping the coils to different magnetic field gradients, as demonstrated in figure 3.15. We found the minimum axial magnetic field gradient to trap  $|F = 2, m_F = 2\rangle$  state is 15.23 G/cm, which can be achieved by setting coil current to 11.2 A. While the minimum gradient to trap  $|F = 2, m_F = 1\rangle$  state is 30.46 G/cm when the coil current is set to 22.4 A. Therefore, to filter out  $|F = 2, m_F = 1\rangle$  state atoms, we ramp the coil current to a value,  $I_{\text{GF}}$ , between 11.2 and 22.4 A and wait an amount of time,  $t_{\text{GF}}$ , to allow the untrappable state atoms to leave from the trap. Finally, we ramp up the magnetic trapping current to a final target value to perform the loss rate measurements from an ensemble that contains solely atoms in the  $|F = 2, m_F = 2\rangle$  state.

However, extra care needs to be taken when choosing  $I_{\text{GF}}$  and  $t_{\text{GF}}$  since we have found that the atom cloud undergoes a damped oscillation during the GF step (see figure 5.2). If one chooses a  $t_{\text{GF}}$  that is not long enough to allow the cloud to reach equilibrium, one would have a larger uncertainty in measuring the decay rate and the energy distribution of the cloud.

To characterize the dynamics of the cloud in the GF step, we measured the energy distribution of the atoms at different GF times and different magnetic coil currents. This is achieved by increasing the coil current to the maximum value,  $I = 200$  A, immediately after the GF step is finished. This non-adiabatic increase of the magnetic field will not affect the final position of the atoms in the GF step. Therefore, by measuring the final energy distribution of the atoms under the high magnetic field, we will get a snapshot of the position of the atoms in the GF step.

We measured the final energy distributions at two different GF coil currents,  $I = 15$  A and  $I = 20$  A. We scanned the GF time from 0 ms to 2000 ms for each current. Figure 5.2 shows the cumulative energy distributions of the atoms in the GF step with

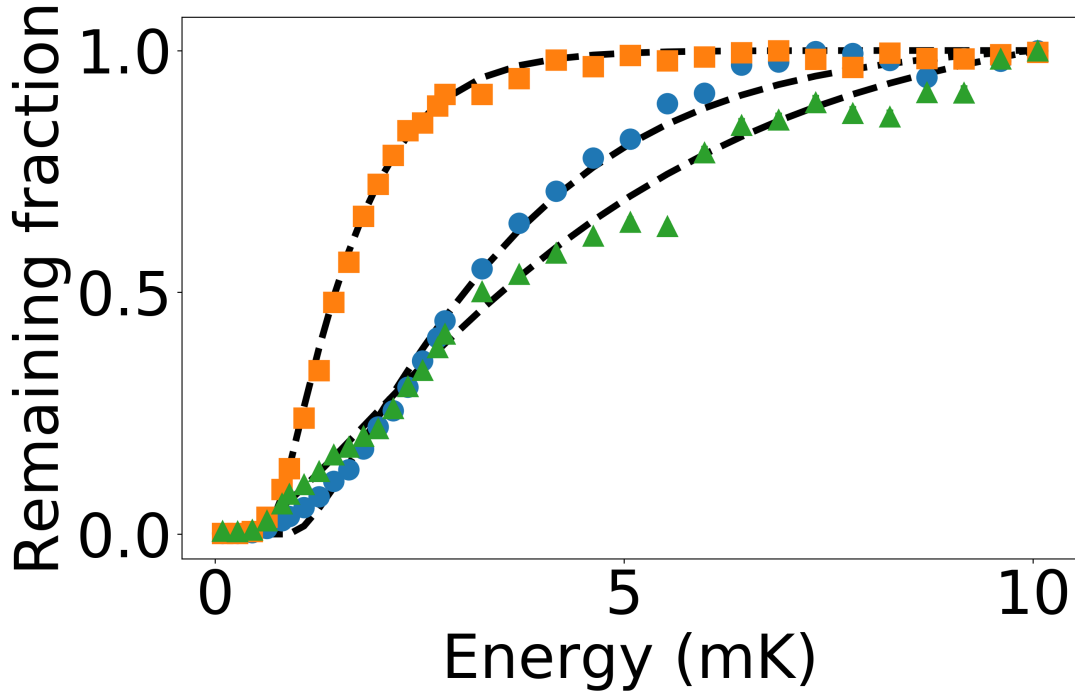


Figure 5.2: Fraction of atoms remaining in a MT as a function of energy after performing a gravitational filter step of various durations. It shows the cumulative energy distributions of the atoms in the GF step with the GF 15 A coil current and wait time for 0 ms (orange squares), 50 ms (green triangles), and 200 ms (blue circles). The mean fitted energies of the distribution for 0 ms, 50 ms, and 200 ms are 691.3  $\mu\text{K}$ , 1810.3  $\mu\text{K}$ , and 2998.0  $\mu\text{K}$ , respectively. The fitted minimum energy for 0 ms, 50 ms, and 200 ms are 649.7  $\mu\text{K}$ , 942.9  $\mu\text{K}$ , and 285.1  $\mu\text{K}$ , respectively.

the GF coil current equaling 15 A but at different GF times. We can notice that the energy distribution varies as a function of the GF times. Fitting the data to the energy shifted MB distribution, Eq. 4.28, we can extract the mean and minimum energy of the distribution. The mean energy of the distribution is proportional to the radius of the cloud in the radial direction, while the minimum energy of the distribution is proportional to the minimum position of the cloud.

The fitted mean and minimum energies are plotted as a function of GF time, shown in figure 5.3. We can see the cloud is ‘breathing’ in both the axial and radial directions. By fitting the results to the expression of the damped oscillator, we can characterize the oscillating periods. We have found the oscillating periods in the axial direction are 85 ms and 90 ms for the case of  $I_{\text{GF}} = 15$  A and  $I_{\text{GF}} = 20$  A, respectively. In comparison, the oscillating periods in the radial direction are 190 ms and 100 ms for the case of

$I_{\text{GF}} = 15$  A and  $I_{\text{GF}} = 20$  A, respectively. The ratio of the oscillating frequencies in the axial direction to the radial direction is about a factor of 2, which matches the ratio of the strength of their magnetic force in those 2 directions. The oscillation frequencies agree well with the results reported in ref.[135] even though the studies were on Li atoms. This suggests the dynamics of the cloud is caused by the magnetic force and is independent of the trapped species.

To obtain a stable energy distribution in the final MT, we need to choose the GF time long enough so that the cloud size is stable. Here, we chose the GF coil current to be 20 A and applied the GF step for 200 ms in order to have a stable cloud and to filter out all atoms in  $|F = 2, m_F = 1\rangle$  state.

### 5.1.3 Two-body elastic collisions

Another difficulty in performing trap loss rate measurements for atoms in the  $|F = 2, m_F = 2\rangle$  state is the enhanced two-body collisions. This is because the density of atoms trapped in  $F = 2$  state is higher than the density in  $F = 1$  state resulting from stronger spatial confinement. For a given trap depth, the trap volume of atoms can be estimated as,

$$V \approx (z_{\min})^3 = \left( \frac{h\nu_{\min}}{h\mu_B g_F |m_F| \left(\frac{dB}{dz}\right)} \right)^3. \quad (5.1)$$

Here, we substitute the axial radius of the RF surface,  $z_{\min}$ , with Eq. 4.23. From Eq. 5.1, we can conclude that the trap volume of atoms in  $m_F = 2$  state is roughly a factor of 8 less than the trap volume of atoms in  $m_F = \pm 1$  state for a given trap depth,  $h\nu_{\min}$ . Therefore, the density of the  $m_F = 2$  state atoms is about a factor of 8 higher, which enhances the two-body collisions.

We excluded the possibility that two-body spin-exchange collisions happen in the system since the atoms are all trapped in single  $m_F = 2$  state [136, 137]. Another inelastic two-body collision mechanisms is the spin relaxation collision which has a rate on the order of  $10^{-5} \text{ s}^{-1}$  [138]. This is negligible compared to the one-body collision rate, which is in the range of  $[10^{-2}, 10.0] \text{ s}^{-1}$ . However, the fact we still observed the obvious two-body collision loss at low trap depth, as shown in figure 5.4, showed that the two-body collision rate is comparable to the one-body collision rate. We have found

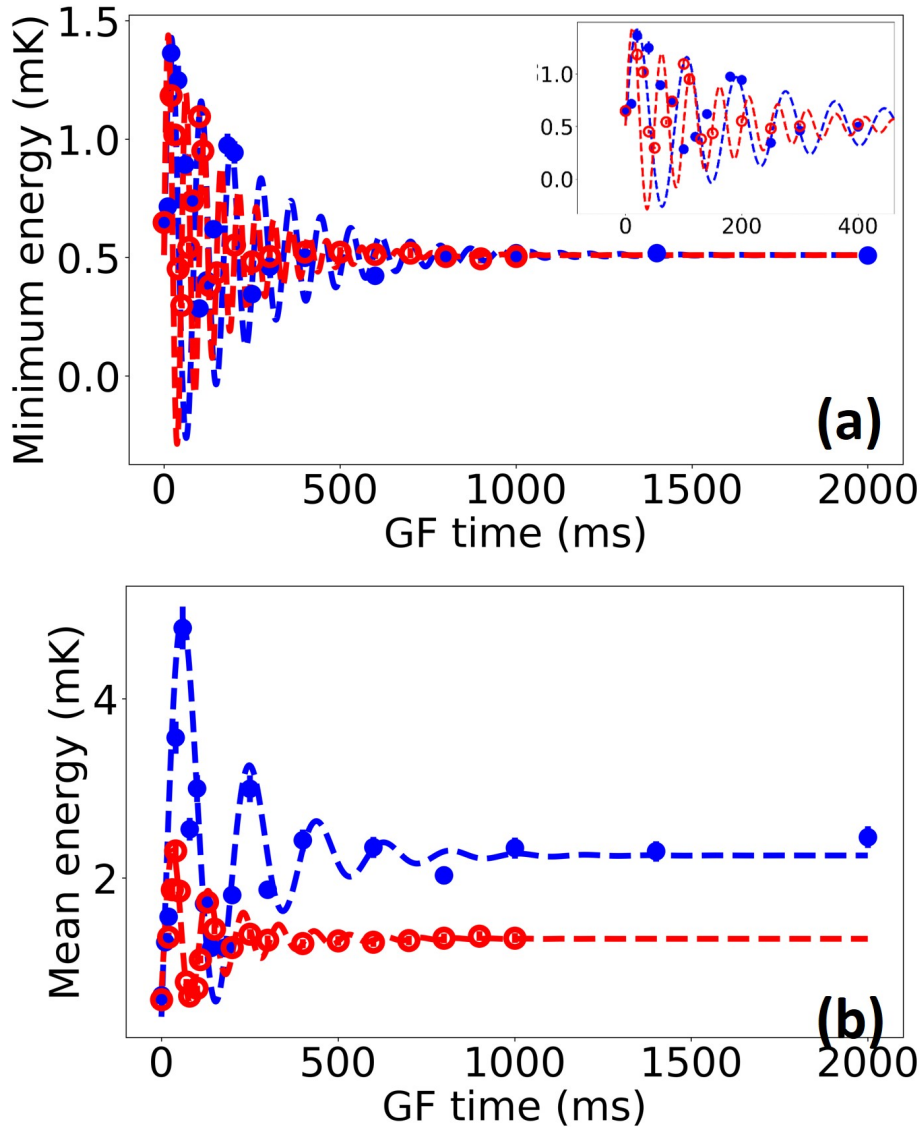


Figure 5.3: Panel (a) shows the fitted minimum energy as a function of the GF times at two different GF coil currents, 15 A (close circles) and 20 A (open circles). The fitted minimum energy is proportional to the minimum axial position of the cloud. The details of the plot between 0 and 400 ms are shown in the inset. Panel (b) shows the fitted mean energy as a function of GF time. The fitted mean energy is proportional to the radius of the cloud. The dashed lines represent the fitting to the expression of a damped oscillator. Damping results solely from dephasing of particles [135].

that the total loss rate at the long holding time converges to the one-body loss rate, and the loss rate curve is well modeled by a single exponential decay at large trap depths.

Therefore, we concluded that the two-body intra-trap collisions are elastic collisions. After an elastic collision, one of the partners will gain the extra momentum and energy,

the other will lose the same momentum and energy. When the trap depth is shallow, the one which gained momentum will leave the trap, while the other one will remain in the trap. This results in atom loss after the two-body elastic collisions at low trap depths. However, if the trap depth is large, both the particles stay in the trap after the elastic collisions, which matches the observation that the two-body loss disappears as the trap depth increases. We can model the dynamics of the atoms in the trap as [139],

$$\frac{dN}{dt} = -\Gamma N - bN^2, \quad (5.2)$$

where  $\Gamma$  is the total one-body loss rate.  $b = \beta/V_{eff}$ , where  $\beta$  is the two-body collision rate and  $V_{eff}$  is the effective volume of the atoms. The solution to Eq 5.2 is,

$$N(t) = \frac{N_0 \exp(-\Gamma t)}{1 + \frac{bN_0}{\Gamma}[1 - \exp(-\Gamma t)]}, \quad (5.3)$$

$N_0$  is the initial number of atoms in the MT. By fitting the data in figure 5.4 to Eq. 5.3 and estimating the  $V_{eff} = 1.55 \times 10^{-4} \text{cm}^3$  based the trap depth 190  $\mu\text{K}$ , we can obtain the two-body collision loss rate,  $\beta \approx 6.9 \times 10^{-12} \text{cm}^3/\text{s}$ .

To mitigate the two-body collisional loss, we need to decrease the density of atoms in the MT. This can be achieved by increasing the trap volume of the atoms by lowering the magnetic field gradient. Especially when the trap depth is shallow, we need to decrease the magnetic field gradient. However, we still kept the magnetic field high at higher trap depths where the contribution of the two-body loss is small compared to the one-body loss. We measured the loss rate of atoms in the MT as a function of the trap depth with the magnetic field axial gradient ranging from 40.8 G/cm ( $I = 30$  A) to 272.0 G/cm ( $I = 200$  A). The results are presented in figure 5.5. From the measurements, we found the threshold magnetic field gradient that eliminates the two-body collisional loss is 81.6 G/cm ( $I = 60$  A). The magnetic field gradient at 272 G/cm ( $I = 200\text{A}$ ) can be used when the trap depth is larger than 1.0 mK. Below 1.0 mK, we should run the coil at 60 A, which gives an 81.6 G/cm magnetic field axial gradient. In the following measurements, we used this "hybrid" method that runs a low gradient (81.6 G/cm) when the trap depth is below 1.0 mK and a high gradient (272 G/cm) when the trap depth is above 1.0 mK. This allows us to minimize the contributions from two-body

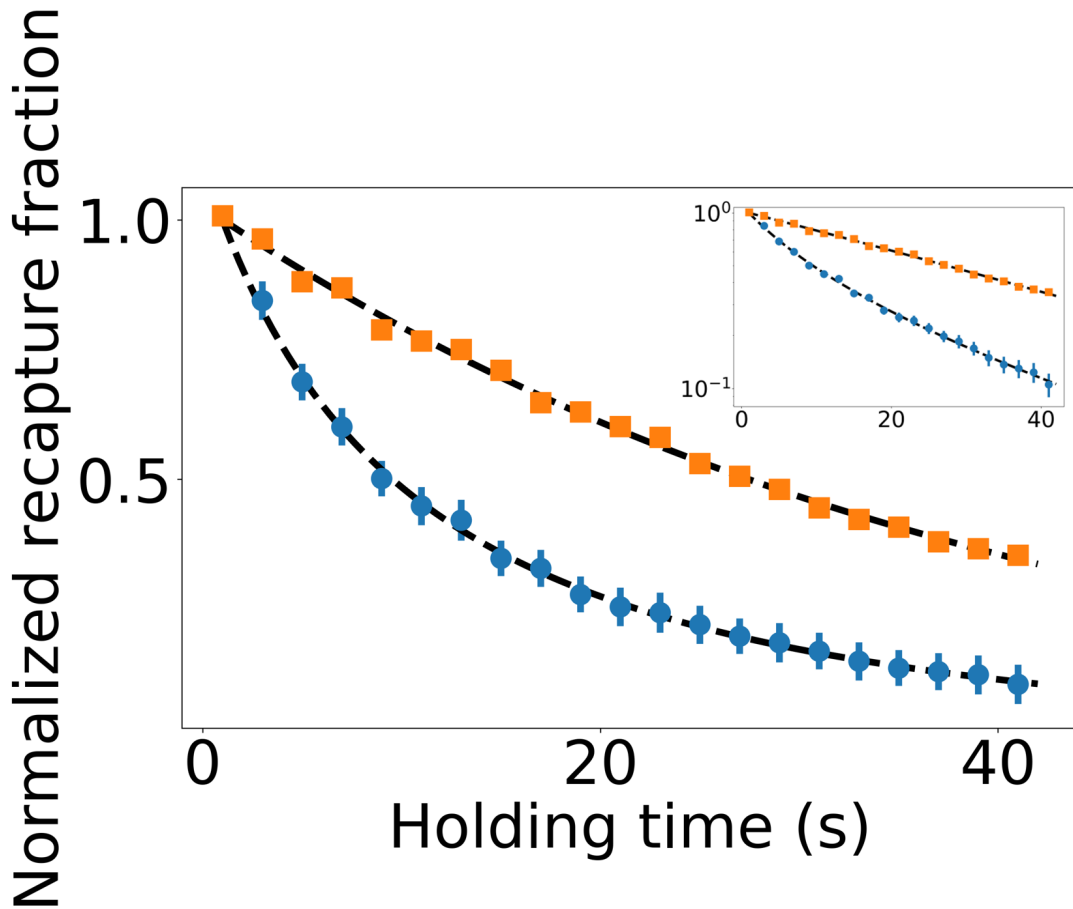


Figure 5.4: A plot of recapture fraction as a function of holding time in the MT. The blue circles represent the loss rate measurement with the trap depth of  $190 \mu\text{K}$ , while the orange squares represent the measurement that happens when the trap depth is  $3 \text{ mK}$ . The solid lines represent the two-body fitting function, as shown in Eq. 5.3. The log scale of y axis is shown in the inset.

collisions and still have a large trap depth range.

## 5.2 Two-point Decay Rate Measurement

After solving the two-body collision issue in the MT, the observed atom loss will follow a simple exponential decay, dominated by the 1-body collisions. A previous study on measuring the spin relaxation time in NMR experiment [140] has shown that the optimal sampling pattern is placing 22% of the sample points at zero time and the remaining 78% at  $1.28 \tau$ , where  $\tau$  is the lifetime. This data sampling prescription provided the best estimate of  $\tau$  with the lowest statistical uncertainty for a fixed number of data

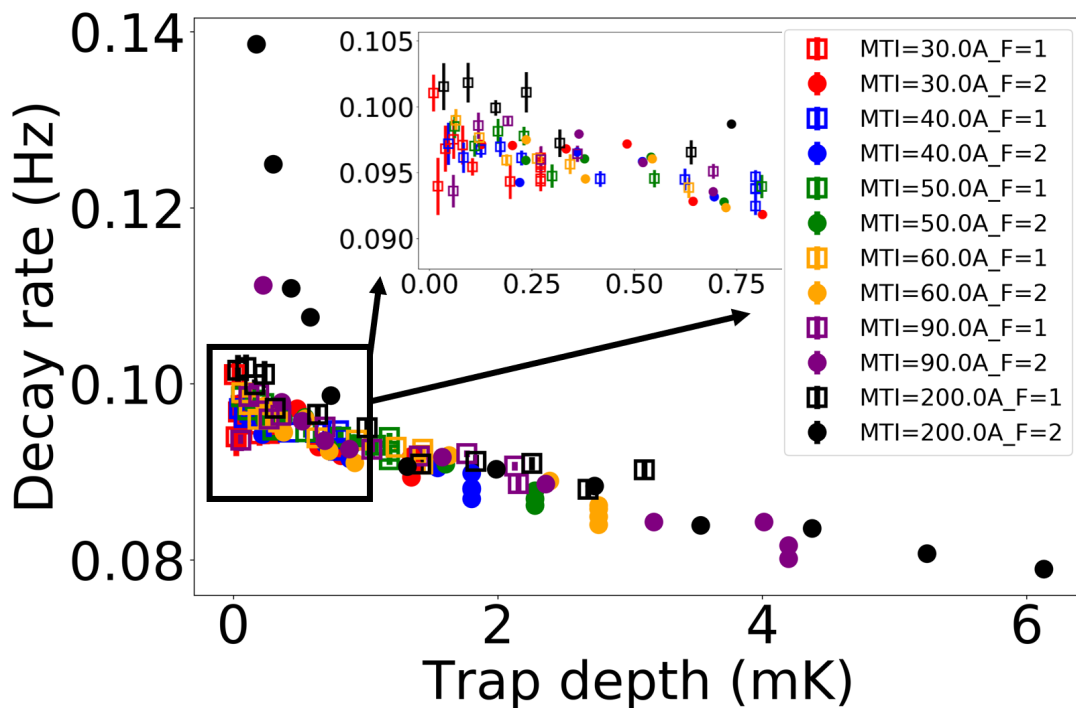


Figure 5.5: Decay rate versus the trap depth at different magnetic field gradients. The inset shows the details of the decay rate in the shallow trap depth regime. The rise of the decay rate indicates the two-body loss contributions. Squares represent the measurements for  $F=1$  state atoms, while circles represent the measurements for  $F=2$  state atoms.

points. An intuitive way of comprehending this is that this data selection pattern balances the need to have the points spread apart for improved precision of the value of  $\tau$  with the need for sufficient signal to noise to minimize the statistical uncertainty in the measurements. For any number of total sampling points, this two-point scheme produces a result with lower statistical uncertainty than the linearly spaced scheme. This method can be adapted here in order to reduce the statistical uncertainty in the decay rate measurement.

Here, we chose to place half of the sample points at the shortest holding time and the remaining half at  $1.28 \tau$ . We verified that this scheme provides a smaller uncertainty than the linearly spaced scheme. We used the two schemes to measure the decay rate at the same background density over 20 times. An example of showing the decay rate measurements with the two schemes is shown in figure 5.6 (a). Then we computed the relative uncertainty for each run by taking the ratio of the uncertainty,  $\Delta\Gamma$ , to the decay rate,  $\Gamma$ . The comparison results are presented in figure 5.6 (b). Using the two-point

scheme, we can reduce the uncertainty in the decay rate by a factor of 2 compared to the old method, while the decay rate results for both schemes agree well.

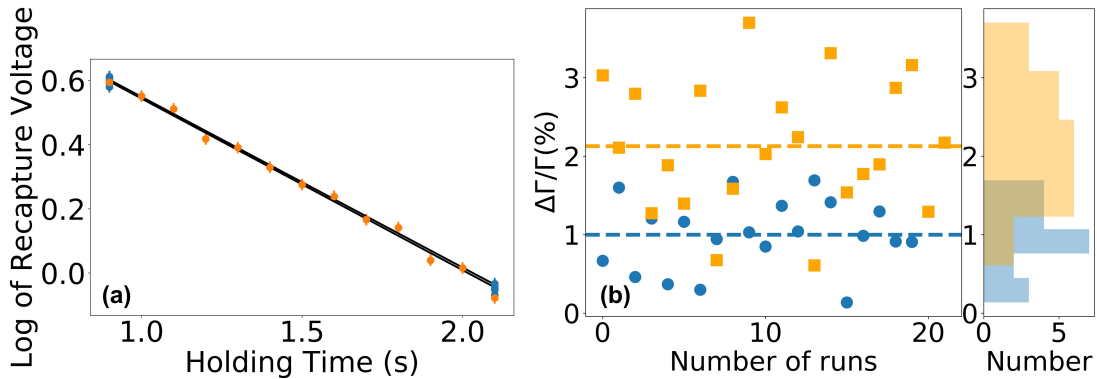


Figure 5.6: Panel(a) shows an example of the decay rate measurement with both the two-point scheme and the evenly spaced scheme. This comparison has been repeated over 20 times at the same background density. For each run, the relative uncertainty in the decay rate versus the number of runs is plotted in (b). The orange dots represent the decay rate measurements using the linearly spaced scheme. The blue dots represent the measurements with the two-point scheme. The dashed lines represent the average value of the relative uncertainty using each scheme. The right panel of (b) shows the histogram distribution of the relative uncertainty.

Another advantage of using this two-point method is that it allows us to extract a decay rate for each pair of data points while performing a point-by-point correction for variations in the pressure and ensemble initial atom number from shot to shot. In section 4.18, we introduced the ratiometric quantity (recapture fraction),  $f(t) = V_{\text{MT}}/V_{\text{MOT}}$ , to express the atom number in the MT normalized to the number of atoms in the original MOT used to load the MT. We can obtain the decay rate by measuring the recapture fraction,  $f(t)$ , as a function of holding times and fitting the data to the exponential function. This ratiometric quantity can be readily applied in the two-point scheme.

At the initial holding time,  $t_j$ , and the final holding time,  $t_f$ , we measured the recapture fraction as  $f_j(t_j)$  and  $f_k(t_k)$ , respectively. The expression of each recapture fraction is,

$$\begin{cases} f_j(t_j) = f_0 \exp(-\Gamma t_j) \\ f_k(t_k) = f_0 \exp(-\Gamma t_k), \end{cases}$$

where  $\Gamma = \Gamma_{\text{loss}} + \Gamma_0$  is the total loss rate as explained in section 4.2.1, and  $f_0$  is the

recapture fraction at zero time. Here, we performed recapture fraction measurements at the initial and final holding time sequentially in order to avoid the short-term fluctuations in the MOT condition, which affects the number of the zero time recapture fraction,  $f_0$ . This would allow us to make an assumption that the zero time recapture fraction is the same across two-point measurements. Therefore, we can take the log of the two equations in Eq. 5.4 and calculate the difference,

$$\begin{aligned} \ln \left[ \frac{f_j(t_j)}{f_k(t_k)} \right] &= \Gamma_{\text{loss}}(t_k - t_j) + \Gamma_0(t_k - t_j) \\ \ln \left[ \frac{f_j(t_j)}{f_k(t_k)} \right] &= \frac{(P_k - P_0)t_k}{i_g k_B T_k} \langle \sigma_{\text{loss}}(U) v \rangle \\ &\quad - \frac{(P_j - P_0)t_j}{i_g k_B T_j} \langle \sigma_{\text{loss}}(U) v \rangle + \Gamma_0(t_k - t_j). \end{aligned} \quad (5.4)$$

Here, we substitute  $\Gamma_{\text{loss}}$  with Eq. 4.16.  $P_j$  and  $P_k$  are the pressure readings from the IG at the holding time  $t_j$  and  $t_k$ , respectively. The IG readings for the test gas species can be obtained by subtracting the pressure of the ambient gas species,  $P_0$ .  $T_j$  and  $T_k$  are the temperature readings from the TCGs at each holding time. The last term in Eq. 5.4 indicates the contributions from the loss mechanisms that do not depend on the density of the test gas species and can be subtracted from the pre-baseline loss rate measurements. In our case,  $\Gamma_{\text{loss}}$  is two orders of magnitudes higher than  $\Gamma_0$ . An example of the recapture fraction measurement using the two-point method is shown in figure 5.7 (a).

Next, we can scale the holding time by its current pressure,  $p_i t_i$ , according to Eq. 5.4, so that we can eliminate the variation of the pressures and obtain the following expression,

$$\ln \left[ \frac{f_j(t_j)}{f_k(t_k)} \right] - \Gamma_0(t_k - t_j) = \frac{\langle \sigma_{\text{loss}}(U) v \rangle \left[ (P_k - P_0)t_k - (P_j - P_0)t_j \right]}{i_g k_B T}, \quad (5.5)$$

where we assume the change of the background temperature is slow, thus, the background temperature is the same across the two point measurements,  $T_j = T_k = T$ . Figure 5.7 (b) shows the pressure corrected results after scaling the holding time by the pressure. One can notice that the scaled holding times are radically different although the original holding times are the same.

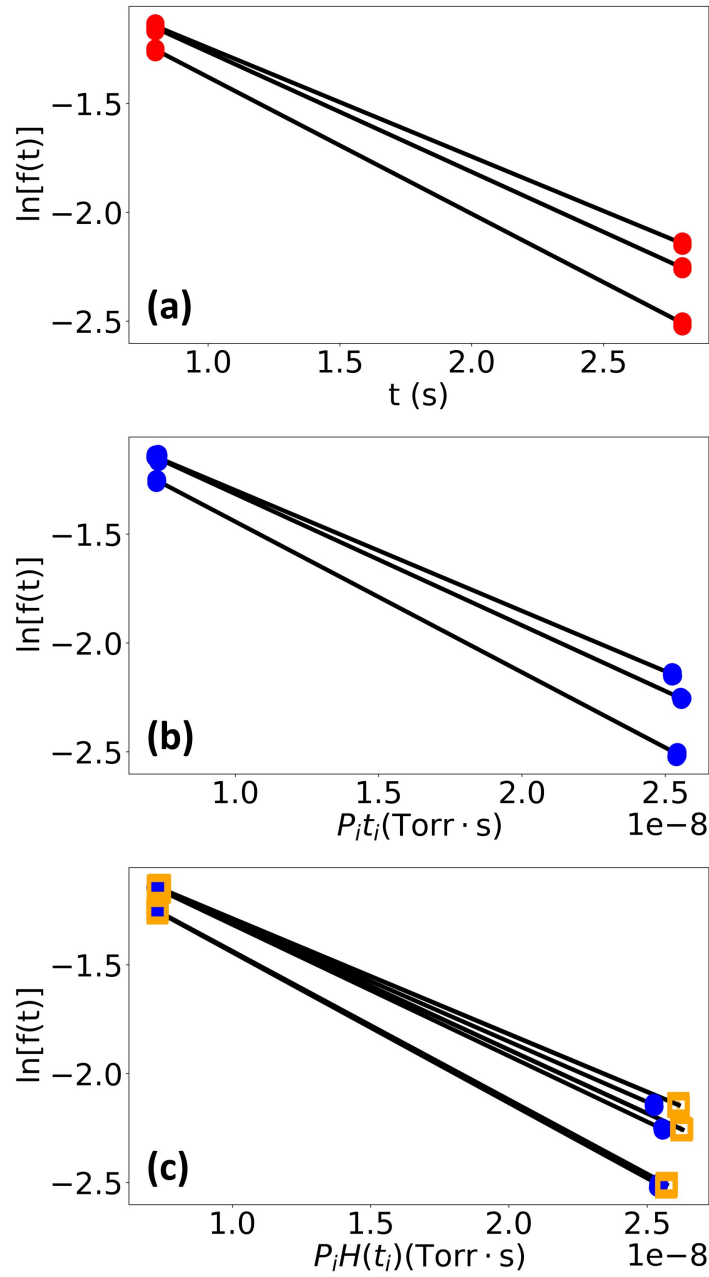


Figure 5.7: Panel (a) shows the log of the recapture fraction versus the holding time when atoms are trapped in  $F = 2$  state and the magnetic trapping is current,  $I = 200$  A. The fluctuations of the test gas density can be reduced by scaling the holding time by the present IG reading,  $P_i t_i$ , as shown in panel (b). The collisions induced heating can be corrected by scaling the holding time with the heating factor,  $H(t_i)$ , as defined in Eq. 5.9. After taking the pressure and the heating corrections into account, the final corrected plot is shown in panel (c). The blue dots in panel (c) are the same data in (b) and plotted for eye guidance.

Finally, we run the pair of measurements (initial and final holding time) at least six times each to acquire an average value of the recapture fraction ratio, which will further reduce the pressure and recapture fraction fluctuations. From Eq. 5.3 to Eq. 5.5, we made another assumption that the loss rate coefficients at the initial holding time and the final holding time are the same,  $\langle \sigma_{\text{loss}}(U) v \rangle_j = \langle \sigma_{\text{loss}}(U) v \rangle_k$ . However, this is not true if we consider the ensemble heating, especially when the trap depth increases. We will discuss the method of accounting for the trap heating next.

### 5.3 Heating Rate Correction

Another issue involved in achieving a higher trap depth is the collision-induced heating which is due to collisions that fail to eject atoms from the trap [56, 131]. As the trap depth increases, the fraction of collisions leading to retained trapped atoms increases, which results in the increase of the average energy of the atom ensemble with hold duration in the MT. Therefore, the trap depth of the atoms in the MT will decrease over time due to the effect of the heating, leading to a systematic overestimate of the measured  $\langle \sigma_{\text{tot}} v \rangle$  value. Although the fitting uncertainty decreases as the range of trap depths increases, the systematic error caused by the heating effect will increase. We have found that the heating error becomes dominant once the scaled trap depth,  $\frac{U}{U_a}$ , passes 0.3. The total uncertainty in determining  $\langle \sigma_{\text{tot}} v \rangle$  value is limited by the heating effect. Therefore, we need to correct the heating effect in order to achieve a lower total uncertainty. In the two-point decay rate measurement scheme, we can isolate the heating effect by taking the  $\langle \sigma_{\text{loss}}(U) v \rangle$  values differently at two different holding times in Eq. 5.4. We define  $\langle \sigma_{\text{loss}}(U) v \rangle_j$  as the initial loss rate coefficient at the initial holding time,  $t_j$ , and define  $\langle \sigma_{\text{loss}}(U) v \rangle_k$  as the final loss rate coefficient. Thus, we have the

new expression,

$$\begin{aligned}
 \ln \left[ \frac{f_j(t_j)}{f_k(t_k)} \right] - \Gamma_0(t_k - t_j) &= \frac{(P_k - P_0)t_k}{i_g k_B T} \overline{\langle \sigma_{\text{loss}}(U) v \rangle}_k - \frac{(P_j - P_0)t_j}{i_g k_B T} \overline{\langle \sigma_{\text{loss}}(U) v \rangle}_j. \\
 &= \frac{(P_k - P_0)t_k}{i_g k_B T} \frac{\int_0^{E_{\text{max}}} \langle \sigma_{\text{loss}}(E_{\text{max}} - E) v \rangle_k \rho(E, t_k) dE}{\int_0^{E_{\text{max}}} \rho(E, t_k) dE} \\
 &\quad - \frac{(P_j - P_0)t_j}{i_g k_B T} \frac{\int_0^{E_{\text{max}}} \langle \sigma_{\text{loss}}(E_{\text{max}} - E) v \rangle_j \rho(E, t_j) dE}{\int_0^{E_{\text{max}}} \rho(E, t_j) dE}. \tag{5.6}
 \end{aligned}$$

Here, we replace  $\langle \sigma_{\text{loss}}(U) v \rangle$  with  $\overline{\langle \sigma_{\text{loss}}(U) v \rangle}$  based on the rigorous analysis in section 4.3, which shows the rate coefficient averaging over the energy distribution of the ensemble,  $\rho(E, t)$ , at time  $t$ . Note the energy distribution of the ensemble is a time dependent function due to the collision-induced ensemble heating. Therefore, if we can characterize the energy distribution as a function of time, we can then evaluate the time dependent loss rate coefficient from zero time to the measurement time  $t$  to account for the changes due to the trap heating,

$$\begin{aligned}
 \ln \left[ \frac{f_j(t_j)}{f_k(t_k)} \right] - \Gamma_0(t_k - t_j) &= \frac{(P_k - P_0)}{i_g k_B T} \int_0^{t_k} \frac{\int_0^{E_{\text{max}}} \langle \sigma_{\text{loss}}(E_{\text{max}} - E(t)) v \rangle \rho(E, t) dE}{\int_0^{E_{\text{max}}} \rho(E, t) dE} dt \\
 &\quad - \frac{(P_j - P_0)}{i_g k_B T} \int_0^{t_j} \frac{\int_0^{E_{\text{max}}} \langle \sigma_{\text{loss}}(E_{\text{max}} - E(t)) v \rangle \rho(E, t) dE}{\int_0^{E_{\text{max}}} \rho(E, t) dE} dt. \tag{5.7}
 \end{aligned}$$

To simplify the expression, we can factor out the loss rate coefficient at zero time,  $\overline{\langle \sigma_{\text{loss}}(U) v \rangle}_{t=0}$ , which gives the following final expression,

$$\begin{aligned}
 \ln \left[ \frac{f_j(t_j)}{f_k(t_k)} \right] - \Gamma_0(t_k - t_j) &= \frac{\overline{\langle \sigma_{\text{loss}}(U) v \rangle}_{t=0}}{i_g k_B T} \left[ (P_k - P_0)H(t_k) - (P_j - P_0)H(t_j) \right], \tag{5.8}
 \end{aligned}$$

where we define the heating factor as,

$$\begin{aligned}
 H(t) &= \frac{\int_0^t \frac{\int_0^{E_{\max}} \langle \sigma_{\text{loss}}(E_{\max} - E(t)) v \rangle \rho(E, t) dE}{\int_0^{E_{\max}} \rho(E, t) dE} dt}{\frac{\int_0^{E_{\max}} \langle \sigma_{\text{loss}}(E_{\max} - E) v \rangle \rho(E, t) dE}{\int_0^{E_{\max}} \rho(E, t) dE} dt} \\
 &= \frac{\int_0^t \frac{\int_0^{E_{\max}} \langle \sigma_{\text{loss}}(E_{\max} - E(t)) v \rangle \rho(E, t) dE}{\int_0^{E_{\max}} \rho(E, t) dE} dt}{\langle \sigma_{\text{loss}}(U) v \rangle_{t=0}}.
 \end{aligned} \tag{5.9}$$

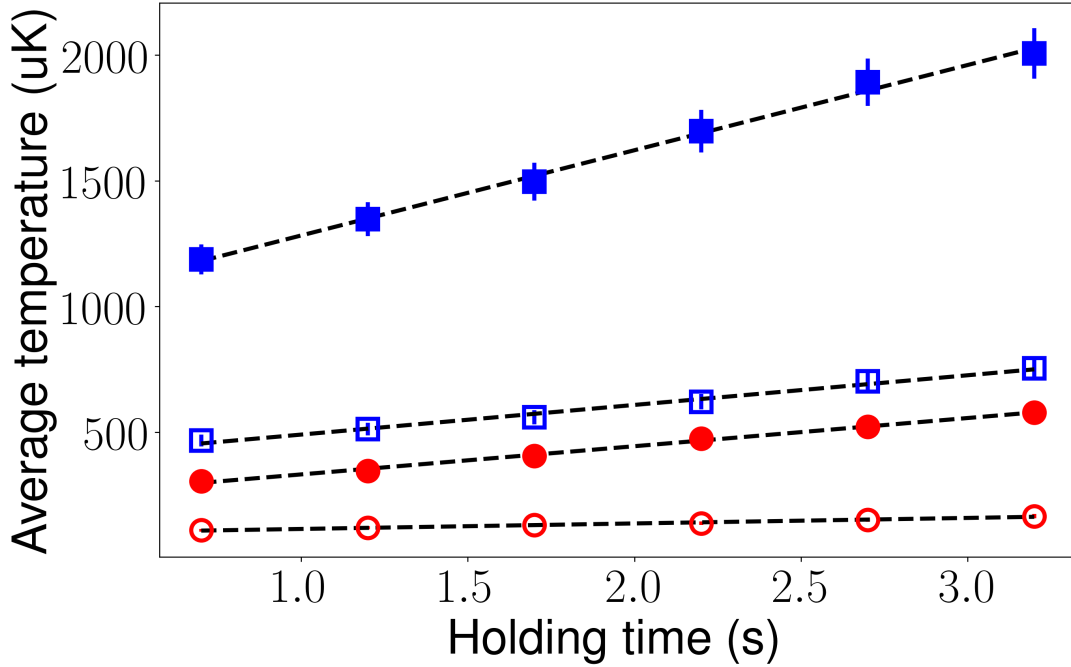


Figure 5.8: The average temperature of the cloud versus the holding time for atoms trapped in  $F = 1$  state at the magnetic trapping current,  $I = 60$  A (open blue squares) and  $I = 200$  A (blue closed squares) and in  $F = 2$  state at the magnetic trapping current,  $I = 60$  A (red open circles) and  $I = 200$  A (red closed circles). The average temperature is obtained by fitting the accumulated energy distribution of the ensemble, measured by the RF ‘knife’ method, to the accumulated MB distribution, as shown in Eq. 4.28. The average temperature of the ensemble is linearly increased with the holding time. The dashed lines are the best linear fit.

Next, we measured the energy distribution of the ensemble as a function of the holding time using the RF ‘knife’ method. We measured the  $\rho(E, t)$  when the atoms are trapped in both  $F = 1$  and  $F = 2$  state. For each state, we also measured the  $\rho(E, t)$  at two different trapping currents,  $I = 60$  A and  $I = 200$  A. The average temperature of the cloud is linearly increasing over time, as expected. The results are presented in

figure 5.8. Thus, we can express the time-dependent energy distribution as,

$$\rho(E, t) = \Theta(E - E_{\min}) \cdot 2 \left( \frac{E - E_{\min}}{\pi} \right)^{\frac{1}{2}} \left( \frac{1}{k_B T(t)} \right)^{\frac{3}{2}} e^{-\frac{E - E_{\min}}{k_B T(t)}}, \quad (5.10)$$

where  $T(t) = T_0 + mt$  and  $E_{\min}$  is found to be constant over time. The experimentally determined energy distribution as a function of time can be plugged in Eq. 5.9 to compute the heating factor,  $H(t)$  in order to account for the heating effect. Figure 5.7 shows the recapture fraction as a function of the final heating corrected quantity,  $H(t)P$ , as shown on the right-hand side of Eq. 5.8. Then, we can solve for the value of  $\overline{\langle \sigma_{\text{loss}}(U) v \rangle}_{t=0} / i_g$ , by plugging the computed heating factors into Eq. 5.8,

$$\frac{\overline{\langle \sigma_{\text{loss}}(U) v \rangle}_{t=0}}{i_g} = k_B T \frac{\ln \left[ \frac{f_j(t_j)}{f_k(t_k)} \right] - \Gamma_0(t_k - t_j)}{\left[ (P_k - P_0)H(t_k) - (P_j - P_0)H(t_j) \right]}. \quad (5.11)$$

However, one can notice that the right-hand side of Eq. 5.11 also has an unknown parameter,  $\langle \sigma_{\text{loss}}(U) v \rangle$  (included in the heating factor), which prevents us from directly computing the left-hand side. To solve this, we used an iteration fitting method to determine the final  $\langle \sigma_{\text{tot}} v \rangle$  and  $i_g$  values:

1. We feed an initial guess value of  $\langle \sigma_{\text{tot}} v \rangle$  into the expression of  $H$ , Eq. 5.9, to compute the values of  $H(t_j)$  and  $H(t_k)$  for the right-hand side of Eq. 5.11.
2. Plug in the computed  $H$  values, we can solve for the left-hand side,  $\frac{\overline{\langle \sigma_{\text{loss}}(U) v \rangle}_j}{i_g}$ , of Eq. 5.11.
3. Fit the computed results,  $\frac{\overline{\langle \sigma_{\text{loss}}(U) v \rangle}_j}{i_g}$ , in step 2 to the rigorous fitting function, we can get the fitted  $\langle \sigma_{\text{tot}} v \rangle$  and  $i_g$  values.
4. Replace the initial guess value with the new fitting result and repeat the steps from 2 to 4 until the fitted  $\langle \sigma_{\text{tot}} v \rangle$  is converged.

We have found this iteration method works well and were able to get a convergence of the  $\langle \sigma_{\text{tot}} v \rangle$  value after first 3 steps even if the initial guess is off by a factor of 6, as illustrated by the simulated results shown in figure 5.9. An intuitive way to think of this iteration method is that if the initial guess of  $\langle \sigma_{\text{tot}} v \rangle$  is overestimated, the heating

rate will then be also overestimated which leads to a smaller fitted  $\langle\sigma_{\text{tot}}v\rangle$  result, vice versa. Therefore, the next guess value will be more close to the true value. After several steps, the fitted result will converge. This iteration method provides us a nice feedback loop to determine  $\langle\sigma_{\text{tot}}v\rangle$  and eliminate the heating effect.

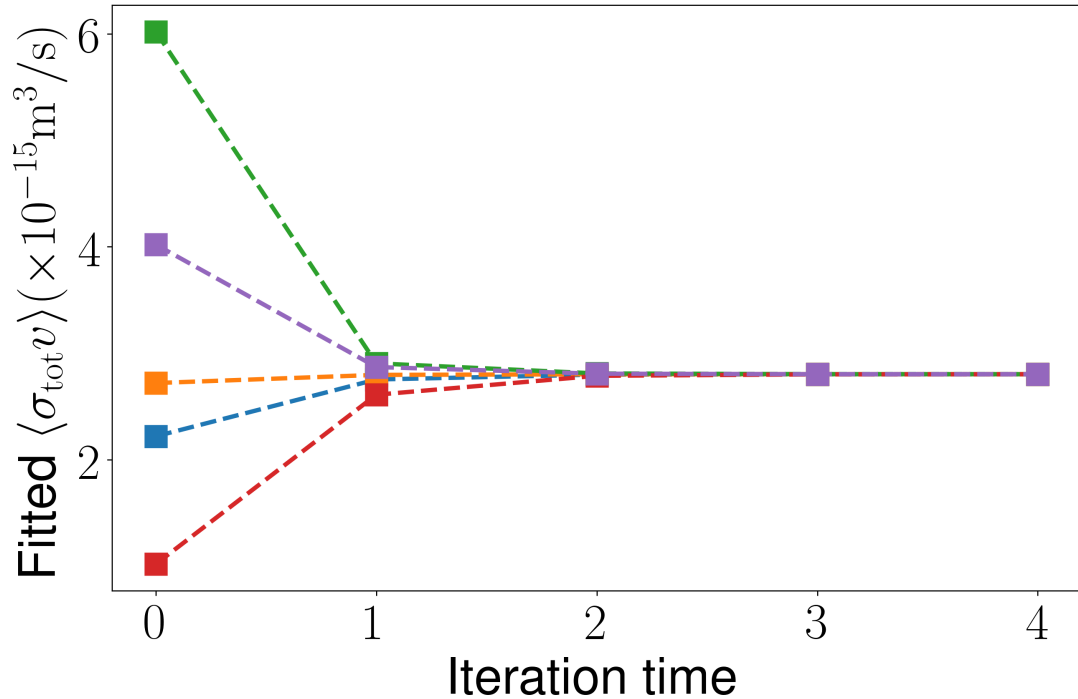


Figure 5.9: Fitted  $\langle\sigma_{\text{tot}}v\rangle$  results as a function of the iteration step for atoms trapped in  $F = 2$  state. The  $\langle\sigma_{\text{tot}}v\rangle$  value at zero iteration time represents the value of the initial guess. The initial guesses have been varied over a factor of 6 and they all converge to the same  $\langle\sigma_{\text{tot}}v\rangle$  value,  $2.8 \times 10^{-15}\text{m}^3/\text{s}$ .

## 5.4 Experiment Results

After taking into account the issues discussed above, we performed the precision measurements of  $\langle\sigma_{\text{tot}}v\rangle$  for collisions between trapped  $^{87}\text{Rb}$  and Ar atoms. We started by measuring the loss rate of Rb atoms without introducing Ar gas in order to determine the baseline decay rate,  $\Gamma_0$ , in Eq. 5.11. Then, to eliminate the two-body loss contributions, we run the magnetic field current at 60 A for the trap depth from 200  $\mu\text{K}$  to 2.0 mK, and run the magnetic field current at 200 A for the trap depth larger than 1.0 mK. There is an overlap trap depth region between the trapping current 60 A and 200

A, which is used to examine whether the loss rate coefficient depends on the trapping current.

We also examined the state dependence of  $\langle\sigma_{\text{tot}}v\rangle$  by performing the loss rate measurements for Rb atoms trapped in both  $F = 1$  and  $F = 2$  states. We altered the measurements for the loss rate of  $F=1$  and  $F=2$  state atoms in order to reduce the time-dependent systematic effects. Given that the magnetic moment for the Zeeman sublevel of  $F = 1$  state is a factor of 2 smaller than it of  $F = 2$  state, the largest accessible trap depth for  $F = 1$  state is around 3.0 mK, while the largest accessible trap depth for  $F = 2$  state is 6.0 mK.

Next, we leaked Ar gas into the system and brought up the pressure to around  $9.0 \times 10^{-9}$  Torr through a leak valve. When the pressure is stable, we then altered the measurement for the loss rate of Rb atoms in  $F = 1$  and  $F = 2$  states at trap depths chosen in random order. We repeated the loss rate measurement for each trap depth five times to further reduce the statistical uncertainty. Then we measured the energy distribution of the ensemble as a function of time in order to account for the heating effect.

Finally, we subtracted the decay rate at the base pressure from the decay rate measurements at the high Ar pressure. The subtraction results are then subjected to the pressure and heating correction procedures according to Eq. 5.11. The results are presented in figure 5.10. The measured  $\frac{\langle\sigma_{\text{loss}}(U)v\rangle}{i_g}$  at the trapping current 60 A agrees well with the values measured at the trapping current 200 A, which demonstrates the loss rate coefficient is only trap depth-dependent. Moreover, the overlap between the  $F = 2$  state results and  $F = 1$  state results shows the loss rate coefficient is independent to the hyperfine state as expected. The results in figure 5.10 are then fit to the rigorous function, as shown in Eq. 4.33, to extract the value of  $\langle\sigma_{\text{tot}}v\rangle$  and  $i_g$ . The extracted values are presented in table. 5.1. One can notice that the extracted  $\langle\sigma_{\text{tot}}v\rangle$  value agrees with the previous determinations in table 4.3 but with a much smaller statistical uncertainty. However, the  $i_g$  for Ar gas has been changed over 10 % over two years period of time. This instability of IG calibration factor again shows the advantages of the MT based CAPS.

This experimentally determined  $\langle\sigma_{\text{tot}}v\rangle$  value is compared with the full quantum scattering computations using two different forms of the PES; one is in the form of

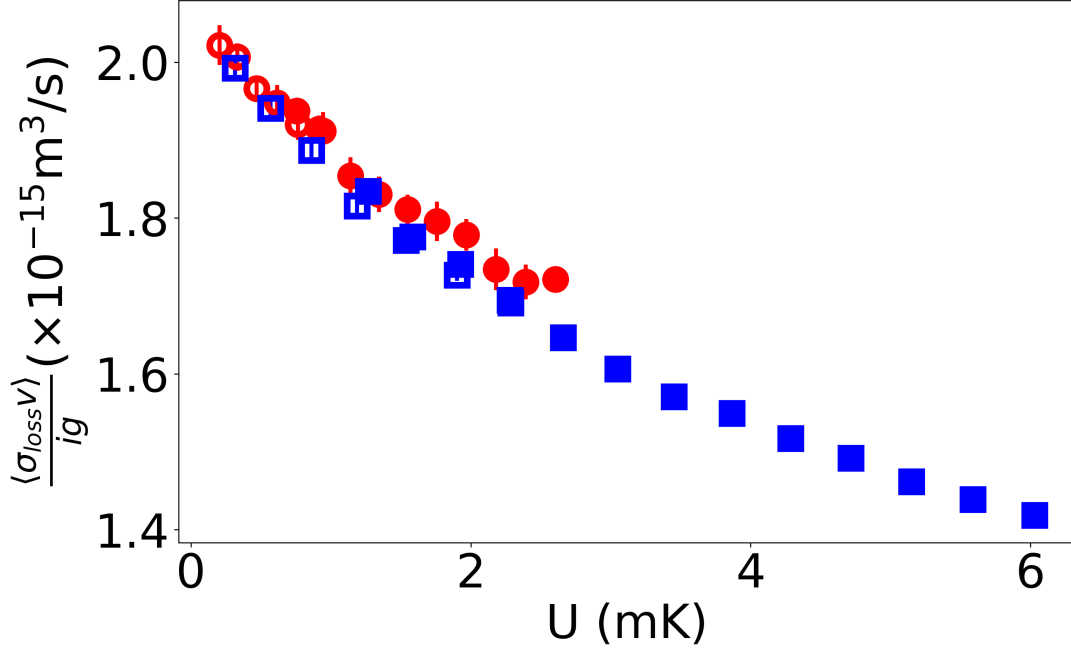


Figure 5.10: Measured  $\frac{\langle \sigma_{\text{tot}} v \rangle}{ig}$  as a function of trap depth for atoms trapped in both  $F = 2$  (blue markers) and  $F=1$  state (red markers). For each state, we run the magnetic trapping current at 60 A (open markers) for the trap depth below 2.0 mK, and run the trapping current at 200 A (closed markers) for the trap depth above 2.0 mK. Each data point is an average of five different measurements. The errorbar on each datapoint indicates the statistical uncertainty only.

L-J PES, the other is in the form of the modified Morse PES [12]. For each form of the PES, we chose the long-range coefficient,  $C_6 = 336.4 E_h a_0^6$ , and the depth of the potential,  $\epsilon = 38.06 \text{ cm}^{-1}$ , quoted from Ref.[12]. The comparisons are shown in table 5.1. The experiment result agrees well with both numerical computations. The agreement between the numerical result,  $2.82 \times 10^{-15} \text{ m}^3/\text{s}$ , using L-J form PES and the experiment results  $2.793(8)(25) \times 10^{-15} \text{ m}^3/\text{s}$  is better since the universal fitting function was generated based on the L-J form PES.

## 5.5 Error Analysis

The values for  $\langle \sigma_{\text{tot}} v \rangle_{\text{Rb-Ar}}^{\text{exp}}$  are listed in table 5.1. Each value is followed by two terms in brackets. The first term is the total statistical uncertainty in the experimental value, while the second bracket is the total systematic uncertainty. The dominant statistical uncertainty comes from the variation in the decay rate measurements as analyzed in

## 5.5. Error Analysis

Rb state	$\langle \sigma_{\text{tot}} v \rangle_{\text{Rb-Ar}}^{\text{num}} \times 10^{-15} \text{m}^3/\text{s}$	$\langle \sigma_{\text{tot}} v \rangle_{\text{Rb-Ar}}^{\text{exp}} \times 10^{-15} \text{m}^3/\text{s}$	$i_{\text{g,Ar}}$
$F = 1$		2.810(32)(30)	1.394(16)
$F = 2$	2.82 <sup>[1]</sup> , 3.02 <sup>[2]</sup>	2.793(8)(25)	1.404(5)

Table 5.1: The fitted values for  $\langle \sigma_{\text{tot}} v \rangle$  for collisions between Rb and Ar atoms and the ion gauge calibration factor for Ar gas. The first bracket in the column of  $\langle \sigma_{\text{tot}} v \rangle_{\text{Rb-Ar}}^{\text{exp}}$  indicates the total statistical error and the second one indicates the total systematic error. The numbers in the column of  $\langle \sigma_{\text{tot}} v \rangle_{\text{Rb-Ar}}^{\text{num}}$  are the numerically computed  $\langle \sigma_{\text{tot}} v \rangle$  for Rb-Ar collisions. The long-range coefficient,  $C_6 = 336.4 \text{E}_h a_0^6$ , and the depth of the potential,  $\epsilon = 38.06 \text{cm}^{-1}$ , are quoted from Ref.[12]. <sup>[1]</sup> represents the numerical result using the L-J PES form, while <sup>[2]</sup> represents the numerical result using the modified Morse PES in [12].

section 4.4. After applying the two-point measurement scheme, we have successfully reduced the statistical uncertainty in the decay rate down to the 1.0 % level. For atoms in the  $|F = 1, m_F = -1\rangle$  state, we have found that the statistical error in determining  $\langle \sigma_{\text{tot}} v \rangle$  is about 1.0%, while the error is decreased by a factor of 2 when trapping atoms in  $|F = 2, m_F = 2\rangle$  state since we have a larger data range to fit to mitigate the statistical error. In addition, there is random noise in the ion gauge readings, which is written into the scaled holding time,  $H(t)P$ , as shown in Eq. 5.8. This introduces additional statistical error to the value of  $\langle \sigma_{\text{tot}} v \rangle$ . The shot-to-shot noise in IG readings contributes about 0.2% in the statistical uncertainty in  $\langle \sigma_{\text{tot}} v \rangle$ .

Besides the statistical error, we also analyzed systematic errors associated with determining  $\langle \sigma_{\text{tot}} v \rangle$ . The systematic errors due to the Majorana loss, the two-body collision loss, the change of background constituents, and the change of the environment temperature have been analyzed in section 4.4. Here, we also experimentally and numerically assess the systematic error introduced by the change of the ensemble energy distribution during the measurements. The change of the ensemble energy distribution is due to the drifting in the laser frequency and the changes of the laser beam alignments in the trapping region. We measured the energy distribution of the ensemble with the same trapping conditions over the course of a day. The fitted average temperature of the ensemble changes within 3.0%, which contributes less than 0.1 % uncertainty to the value of  $\langle \sigma_{\text{tot}} v \rangle$ .

Finally, there is a measurement uncertainty in determining the heating rate (average energy as a function of the holding time), which introduces a systematic error in applying heating rate correction to the decay rate measurements. There is a  $< 5.0\%$  error in

## 5.5. Error Analysis

---

determining the heating rate, which adds a  $< 0.6\%$  systematic error in determining  $\langle\sigma_{\text{tot}}v\rangle$ . The total systematic error is presented in the second bracket in column 3 of table 5.1. The error budget in determining  $\langle\sigma_{\text{tot}}v\rangle$  with atoms in  $F = 2$  state is summarized in Table 5.2. The systematic and statistical uncertainties together (added in quadrature) lead to an upper-bound total uncertainty of  $\pm 0.9\%$  on the measurements of  $\langle\sigma_{\text{tot}}v\rangle$  for Rb-Ar collisions. A similar method has been applied to the measurements with  $^{87}\text{Rb}$  atoms in  $F = 1$  state.

Source of Errors	$\delta\langle\sigma_{\text{tot}}v\rangle/\langle\sigma_{\text{tot}}v\rangle$ /%
Heating rate changes	$< 0.6$
Ensemble temperature changes	$< 0.1$
Base pressure changes	$< 0.4$
Majorana loss rate changes	$< 0.06$
Ambient temperature changes	$< 0.01$
Statistical uncertainty	$< 0.5$
<b>Total Estimate</b>	$< 0.9$

Table 5.2: Relative uncertainties for the total velocity averaged cross section  $\langle\sigma_{\text{tot}}v\rangle$  for  $^{87}\text{Rb}$ -Ar collisions. The Rb atoms are trapped in  $F = 2$  ground state. The statistical uncertainty results from fitting the data which include variations due to fluctuations in the decay rate measurement 1.0% and fluctuations in the IG “a” readings 0.2% (1.0% for IG “b” readings).

We believe this measurement can be generalized to precisely measure  $\langle\sigma_{\text{tot}}v\rangle$  for the collisions between Rb and other test gas species where the PES is not/cannot be known as a priory.

## Chapter 6

# Magneto Optical Trap (MOT) Based CAPS

The MT-based CAPS is limited to an upper-pressure limit to a pressure of  $\approx 10^{-8}$  Torr ( $10^{-6}$  Pa). This limitation is imposed by several factors. First, as the gas pressure increases, the number of atoms in a MOT, used to load the MT, decreases. This is because the losses induced during the loading of the MOT increase and the loading rate of the MOT decreases. In addition, the transfer efficiency of the atoms from the MOT to the MT is less than 60% (even in the presence of the optical pumping stage), further reducing the signal-to-noise ratio for MT loss rate measurements.

Second, the RF “knife” used in this apparatus is located outside the vacuum housing, approximately 2 cm from the trapped atoms. The result is that the RF field needs to be applied for approximately 700 ms to ensure that the energetic atoms are completely removed from the trap to properly define the trap depth, making the minimum hold time for the MT measurements. At high pressures, the higher loss rate and lower atom number initially loaded into the MT reduces the number of atoms remaining in the MT after this period below our detection limit.

By contrast, the fluorescence signal from the 3D MOT is capable of being detected up to higher background pressures. Also the loss rate from the MOT is on the order of 4-5 times lower than the loss rate for the MT owing to the much larger trap depth of the MOT (1 K for the MOT compared to 1 mK for the MT). These features enable MOT loss rate measurements at pressures 60 times greater than that possible for MT measurements.

It would be advantageous to be able to operate the primary quantum pressure standard at pressures in the high vacuum (HV) regime  $1 \times 10^{-7}$  Torr ( $1.33 \times 10^{-5}$  Pa), the lower end of operation of spinning-rotary gauges (SRG). This would allow the pri-

mary standard for high- and ultra-high vacuum pressures defined and measured by the CAPS to be connected to the mercury manometer primary standard via the MOT loss measurements and the SRG measurements.

In this chapter, I will start by introducing the use of a MOT as a transfer pressure standard calibrated against the MT based CAPS. In our apparatus, we find the losses from a MOT can be measured for Argon pressures up to the mid  $10^{-7}$  Torr ( $10^{-5}$  Pa) range, making a MOT a good candidate for a transfer standard since this pressure overlaps SRG. Later, I will propose the idea of using a MOT to directly measure the pressure in the vacuum which involves the characterization of the excited state fraction (ESF) of atoms in a MOT and the determination of the loss rate coefficient between an excited state Rb atom and the test gas particle. The early-staged work of directly measuring the pressure with a MOT based CAPS will be presented in this chapter.

## 6.1 The Use of a MOT as a Transfer Standard.

The biggest roadblock of using a MOT based CAPS is to determine the loss rate coefficient. In contrast to the losses from a shallow MT, the losses from a MOT may not be well described by the universal law since the typical MOT has a trap depth in the 1-2 K range [141]. At the larger depths, the collision induced losses may be influenced significantly by the poorly characterized core repulsion part of the interaction potential (for both ground state and excited state Rb atoms), as well as any inelastic collision channels that may be present in the collision process. Thus, an *ab initio* computation of the effective velocity averaged collision loss rate coefficient,  $\langle \sigma_{\text{loss}}(U) v \rangle$ , may be required but not easily obtained.

A more effective strategy, employed here, is to use the quantum diffractive pressure standard (MT based CAPS) to calibrate the MOT. Namely, the loss rate from the MT and the loss rate from a MOT for a fixed background gas pressure can be measured in sequence. The MOT loss rate induced by background gas ‘x’ is,

$$\begin{aligned} \Gamma_{\text{MOT}} &= \langle \sigma_{\text{loss}} v \rangle_{\text{MOT}} n_x \\ &= \frac{\langle \sigma_{\text{loss}} v \rangle_{\text{MOT}}}{k_B T} P'_x = S \cdot P'_x, \end{aligned} \quad (6.1)$$

where  $P'_x$  is the pressure measured by the MT based CAPS for the test gas, x, at density

$n_x$ . The calibration is carried out over the pressure range accessible to the CAPS and extrapolated to higher pressures, assuming that the MOT loss rate continues to be linear in the background gas density. The measurement results are shown in the inset of figure 6.1. The calibration slope extracted from these measurements,  $S$ , can be used to determine the average  $\langle\sigma_{\text{loss}} v\rangle_{\text{MOT}} = S \cdot k_B T$  (note  $\langle\sigma_{\text{loss}} v\rangle_{\text{MOT}}$  is an average of the excited loss rate coefficient and the ground state loss rate coefficient).

An experiment was performed introducing Ar gas into the pressure standard apparatus with the results shown in Fig. 6.1. The magnetic trap depth used was 0.978 mK giving a value of  $\langle\sigma_{\text{loss}}(U) v\rangle_{\text{MT}} = 2.58(5) \times 10^{-15} \text{ m}^3/\text{s}$ . The inset of Fig. 6.1 which shows the low pressure region for which both the MT and MOT loss rates can be measured. This section is used to calibrate the MOT against the cold atom pressure standard. The slope was determined to be  $S = 2.29(1) \times 10^7 (\text{s}^{-1}/\text{Torr})$ , giving

$$\langle\sigma_{\text{loss}} v\rangle_{\text{MOT}} = 7.02(4) \times 10^{-16} \frac{\text{m}^3}{\text{s}}. \quad (6.2)$$

The MOT loss rate readings, in conjunction with Eq. 6.2, are then used to compute the gas pressures,  $P_{\text{MOT}} = k_B T \cdot \Gamma_{\text{MOT}} / \langle\sigma_{\text{loss}} v\rangle_{\text{MOT}}$ . The direct comparison between the MOT loss rate readings and the ion gauge ‘‘a’’ readings for Ar gas is shown in Fig. 6.1 which shows that the pressure can be calibrated up to the  $4.0 \times 10^{-7}$  Torr range based on the MOT loss rate. However, the calibration slope  $S$  will drift as the MOT trapping conditions change over time. If the steady-state excited state fraction in the MOT varies, the alignment of the MOT laser beams shifts, or the power in the MOT laser beams changes, then the calibration slope will change. Thus, this method relies strongly on calibrating against the MT based CAPS and periodically verifying this calibration.

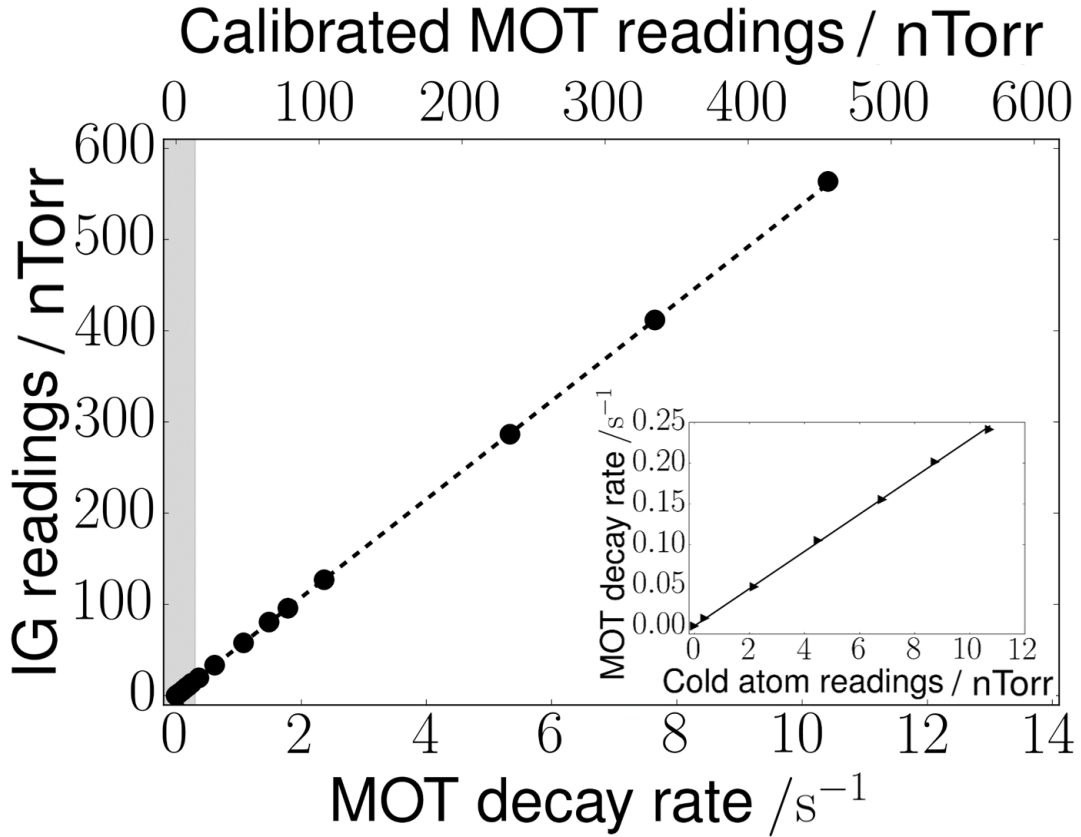


Figure 6.1: IG readings versus MOT decay rate for Ar gas (pressure up to  $6 \times 10^{-7}$  Torr). The shaded region in the figure indicates the region where the MOT decay rate can be calibrated by the MT cold atom gauge (primary), shown in the inset. The error bars are shown in the plot but are too small to be seen.

## 6.2 Proposal of Using a MOT as an Absolute Pressure Standard

In addition to using a MOT based CAPS as a transfer standard calibrated against a MT based CAPS, one could also use a MOT to measure the pressure in vacuum directly. However, the direct use of a MOT based CAPS must be carefully considered.

In a MOT there are trapped ground state  $^{87}\text{Rb}$  atoms along with a population of excited state  $^{87}\text{Rb}$  atoms. The loss rate coefficient,  $\langle \sigma_{\text{loss}}(U) v \rangle$ , between an excited state atom and the test gas particles will differ from the rate for a ground state Rb – test gas collision. Thus, changes to the ratio of excited state to ground state populations will lead to variations in the measured loss rate from the MOT, even at a fixed background gas pressure. In addition, the MOT trap depth is strongly influenced by the power,

detuning, size, and alignment of the laser beams used to form the MOT. Therefore, one needs to determine the ESF in a MOT and find a way to control the depth of atoms in a MOT before any meaningful loss rate pressure determinations can be undertaken. Given these complications, one anticipates that MOT based pressure measurement will have an inherently higher uncertainty than the one from the MT based pressure measurement [54, 53, 70].

In this section, we will first present a method of measuring the ESF of a MOT. Then a method of determining and varying the trap depth of a MOT will be introduced. Finally, a measurement of the loss rate coefficient between the excited state Rb atom and the Ar atom will be shown.

### 6.2.1 Excited state fraction characterization

In the past, people have shown that the photon scattering rate is useful in the calculations of the number of atoms in the MOT for measurements of the excited-state fraction [75, 73, 76]. In our experiment, a pump beam transfers atoms in the  $|F = 2\rangle$  to the  $|F' = 3\rangle$  state of the  $D_2$  ( $5^2S_{1/2} \rightarrow 5^2P_{3/2}$ ) manifold transitions for  $^{87}\text{Rb}$ . Since the pump transition is dominant, the atomic model can be approximately viewed as a two-level model which only considers the pump transition. Thus, the steady-state photon scattering rate per atom for a two-level atomic model,  $\gamma_{\text{sc}}$ , can be derived using the density matrix approach as [142],

$$\gamma_{\text{sc}} = \frac{\gamma}{2} \frac{s}{1 + s + (2\Delta/\gamma)^2}. \quad (6.3)$$

Here,  $\gamma = (2\pi)6.065(9)$  MHz is the natural decay rate of the  $^{87}\text{Rb}$  atoms in the excited states, and  $\Delta$  is the pump laser detuning, which is the difference between the laser's optical frequency and the resonance frequency of the  $F = 2 \rightarrow F' = 3$  pump transition. Here  $s = I/I_{\text{sat}}$ , where  $I$  is the intensity of the pump laser light experienced by the trapped atoms, and  $I_{\text{sat}}$  is the saturation intensity of the pump transition, which is the intensity needed for a beam to excite the pump transition at a rate equal to one half of its natural line width. Solving the rate equation in a two-level model [75], one can find

the ESF is given by

$$f_e = \frac{s}{2(1 + s + (2\Delta/\gamma)^2)} = \frac{\gamma_{sc}}{\gamma}. \quad (6.4)$$

Each atom that scatters a photon will be transferred to its excited state, therefore, the ESF in the MOT is determined by the photon scattering rate. For a given beam size, the laser power,  $W$ , is proportional to the intensity of the laser light,  $I$ . Thus, the parameter  $s$  in Eq. (6.3) can be simplified as  $s = I/I_{sat} = W/W_{sat}$ .  $W$  can be easily measured at a convenient location, under the assumption that this power and the power at the location of the trapped atoms are directly proportional to each other. The detuning,  $\Delta$ , can be precisely controlled in the experiment. Therefore, the only unknown factor is the effective saturation power  $W_{sat}$ , which can also be experimentally determined.

Based on Eq. 6.4, if one can measure the scattering rate as a function of the power and the detuning, then the data can then be fitted to Eq. 6.4 to extract the saturation power  $W_{sat}$ . We know the fluorescent light, collected on a PD, from each atom is proportional to the scattering rate. Therefore, measuring the fluorescent light will help us determine the scattering rate. The collected fluorescent light is converted to the electrical signal,  $V_{fluo}$ , through a PD and can be expressed as

$$V_{fluo} = \alpha\gamma_{sc}N, \quad (6.5)$$

where  $\alpha$  is the photon collection efficiency of the optical system times the photon-to-voltage conversion factor for the detector, and  $N$  is the number of atoms that emit photons. This equation is under the condition that each photon is only scattered from a single atom before leaving the dilute MOT (verified for our experimental conditions. See figure 4.5).  $\alpha$  is a constant and  $N$  is also kept constant during the measurements so that they don't contribute to the scattering rate measurements and can be normalized out later.

At first, we loaded atoms into a MOT using pre-selected "standard laser settings (power and detuning). Then we waited for the MOT to reach its steady state population. Next, the lasers' settings are suddenly switched to a set of test settings. The switching time ( $< 200 \mu s$ ) is short compared to the time for atoms to escape from the trap so

that the atom number  $N$  is constant during the switch. The ratio of the steady-state MOT fluorescence at the standard parameter settings,  $V_{\text{std}}$ , to the steady-state MOT fluorescence at the test settings,  $V_{\text{test}}$ , can be expressed as,

$$\begin{aligned} \frac{V_{\text{std}}}{V_{\text{test}}} &= \frac{\gamma_{\text{sc}}^{\text{std}}}{\gamma_{\text{sc}}^{\text{test}}} = \frac{s_{\text{std}}}{s_{\text{test}}} \frac{1 + s + (2\Delta_{\text{test}}/\gamma)^2}{1 + s_{\text{std}} + (2\Delta_{\text{std}}/\gamma)^2} \\ &= \frac{W_{\text{std}}}{W_{\text{test}}} \frac{1}{\xi_{\text{std}}} \left( A + \frac{W_{\text{test}}}{W_{\text{sat}}} \right), \end{aligned} \quad (6.6)$$

Here, the detuning-dependent quantity  $A = 1 + (2\Delta_{\text{test}}/\gamma)^2$  is defined here for convenience. The term  $\xi_{\text{std}} = A_{\text{std}} + s_{\text{std}}$  is a common scaling factor determined by the standard laser beam settings  $s_{\text{std}}$  and  $\Delta_{\text{std}}$ , which are constant values as the laser standard settings are fixed.

To speed up the cycle of the measurement, we don't reload the MOT and switch it to a new test setting. Instead, we switched the MOT back to the standard setting in between two test settings. Each new  $V_{\text{test}}$  is normalized to its previous  $V_{\text{std}}$  so that we strictly keep the number of atoms unchanged. An example of the fast switch measurement is shown in figure 6.2.

Then, we can eliminate the ratio of standard and test powers from the signal ratio in Eq. 6.6, and finally obtain,

$$G = \left( \frac{W_{\text{test}}}{W_{\text{std}}} \right) \left( \frac{V_{\text{std}}}{V_{\text{test}}} \right) = \frac{1}{\xi_{\text{std}}} \left( A + \frac{P_{\text{test}}}{P_{\text{sat}}} \right). \quad (6.7)$$

$G$  is an experimental parameter constructed from four easily measured quantities  $W_{\text{test}}$ ,  $W_{\text{std}}$ ,  $V$ , and  $V_{\text{std}}$ , which allows us to determine the effective, experimental pump saturation power parameter,  $W_{\text{sat}}$ , by fitting experimentally determined values of  $G$  to Eq. 6.7.

For a fixed pump detuning, the relation in Eq. (6.7) from the two-level atom model shows a linear relationship between the empirical parameter  $G$  and the pump power  $P$ . The deduced slope  $m_G$  is

$$m_G = \frac{1}{\xi_{\text{std}}} \frac{1}{W_{\text{sat}}}, \quad (6.8)$$

and the intercept  $b_G$  is

$$b_G = \frac{1}{\xi_{\text{std}}} A. \quad (6.9)$$

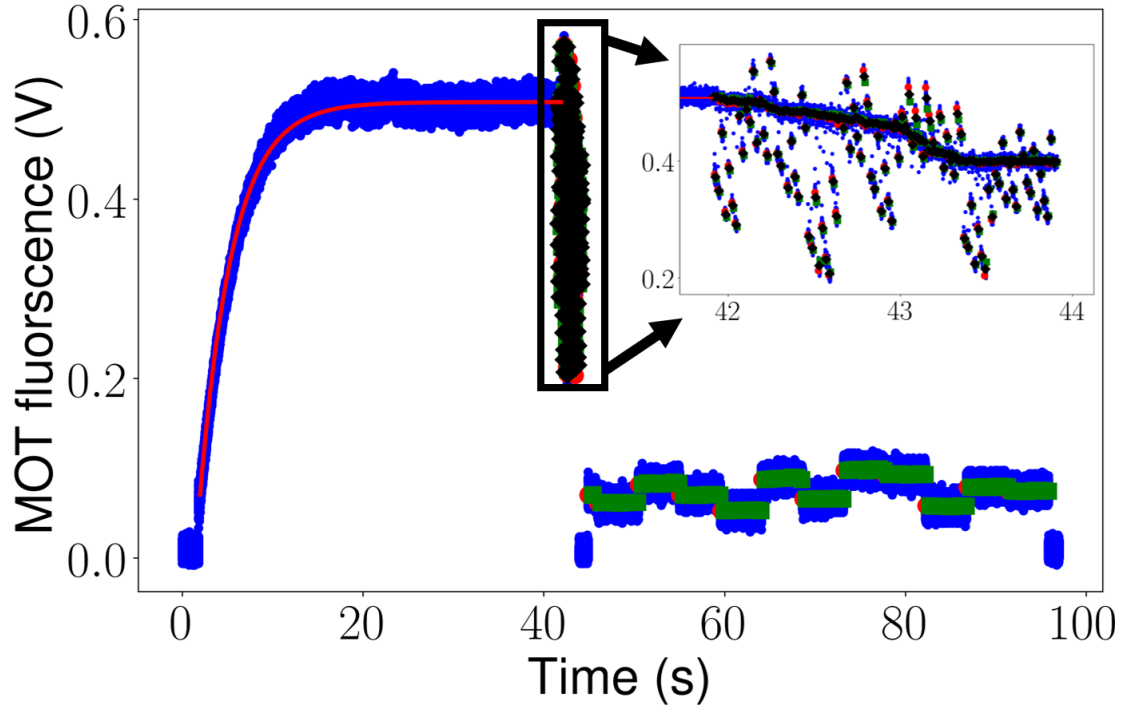


Figure 6.2: The fluorescence of a MOT (captured by a PD) versus time. The MOT is initially loaded with a standard setting and reached its equilibrium value,  $V_{\text{std}}$ . Then the lasers' settings are switched to the test settings and the new fluorescence level is  $V_{\text{test}}$ . Then, the lasers' settings are switched between the standard setting and a new test setting. The red dots in the inset indicate the instant MOT level after the quick switch, while the green dots indicate the level just before the new switch. The black dots indicate the average MOT level at this MOT setting. The bottom part of the plot shows the baseline level of the PD at each laser setting in order to be removed from the actual voltage to reflect the actual atom number.

Combining these two quantities, one can determine  $W_{\text{sat}}$  from the two-level model:

$$W_{\text{sat}} = \frac{b_G}{m_G A} \quad (6.10)$$

We performed the measurements by choosing the standard detuning to be 12 MHz, and the standard pump power to be 80 mW. The test power setting ranges from 35 mW to 160 mW, and the test detuning setting is chosen from 12 MHz to 26 MHz. The measured  $G$  values are shown in figure 6.3 (a). For each laser detuning, we can fit the  $G$  values as a function of pump power to Eq. 6.7 and extract the slope and intercept. For each pair of the slope and the intercept, we solved for the saturation power,  $W_{\text{sat}}$ . The calculated  $W_{\text{sat}}$  at different laser detunings are presented in figure 6.3 (b). The

results show that  $W_{\text{sat}}$  is independent of the laser detunings as expected and provided an effective saturation pump power  $W_{\text{sat}} = 2.12(8)$  mW. For a given pump power and the detuning, one can then compute the excited state fraction of a MOT using Eq. 6.4 and the pre-determined saturation power. Note, this determined saturation power is an experimentally determined value and depends on the alignment and polarization of the lasers. Thus, one must determine it every time before using the MOT based CAPS to perform pressure measurements.

In most cases, the above standard two-level model analysis can successfully determine the excited state fraction with the saturation intensity corresponding to the  $F = 2 \rightarrow F = 3'$  pump cycling transition while ignoring the scattering from any light tuned to the  $F = 1 \rightarrow F = 2'$  repump transition. However, if the repump power is very weak, the effects of the repump transition on the photon scattering rate must be taken into account. Thus, we need a more accurate model to describe the photon scattering rate, a four-level atomic transition model considering the hyperfine splittings can be used. The expression of the experimental parameter  $G$  is then needed to be updated. The details of the four-level model study can be found in Ref.[5]. We used a power of 28 mW of repump power and verified that the ESF is insensitive to the repump power. Therefore, we believe a two-level model is accurate enough to calculate the ESF.

### 6.2.2 Control of the trap depth of atoms in the MOT

Due to the presence of the excited state atoms in a MOT, the background collision induced loss rate,  $\Gamma_x^{\text{MOT}}$ , can be expressed as,

$$\Gamma_x^{\text{MOT}} = n_x \langle \sigma_{\text{loss}}(U) v \rangle (1 - f_e) + n_x \langle \sigma_{\text{loss}}(U) v \rangle^e f_e, \quad (6.11)$$

where  $\langle \sigma_{\text{loss}}(U) v \rangle$  and  $\langle \sigma_{\text{loss}}(U) v \rangle^e$  represent the ground state and the excited state loss rate coefficient, respectively.  $n_x$  is the density of the test gas, and  $f_e$  is the fraction of the atoms in the excited state in the MOT. The value of  $\langle \sigma_{\text{loss}}(U) v \rangle$  can be determined using a MT based CAPS. Therefore, one needs to know the value of  $\langle \sigma_{\text{loss}}(U) v \rangle^e$  in order to determine the test gas density,  $n_x$ .

The approach to determine the value of  $\langle \sigma_{\text{loss}}(U) v \rangle^e$  is to measure the loss rate of a MOT under a known test gas pressure at different ESFs. Since both  $\langle \sigma_{\text{loss}}(U) v \rangle$

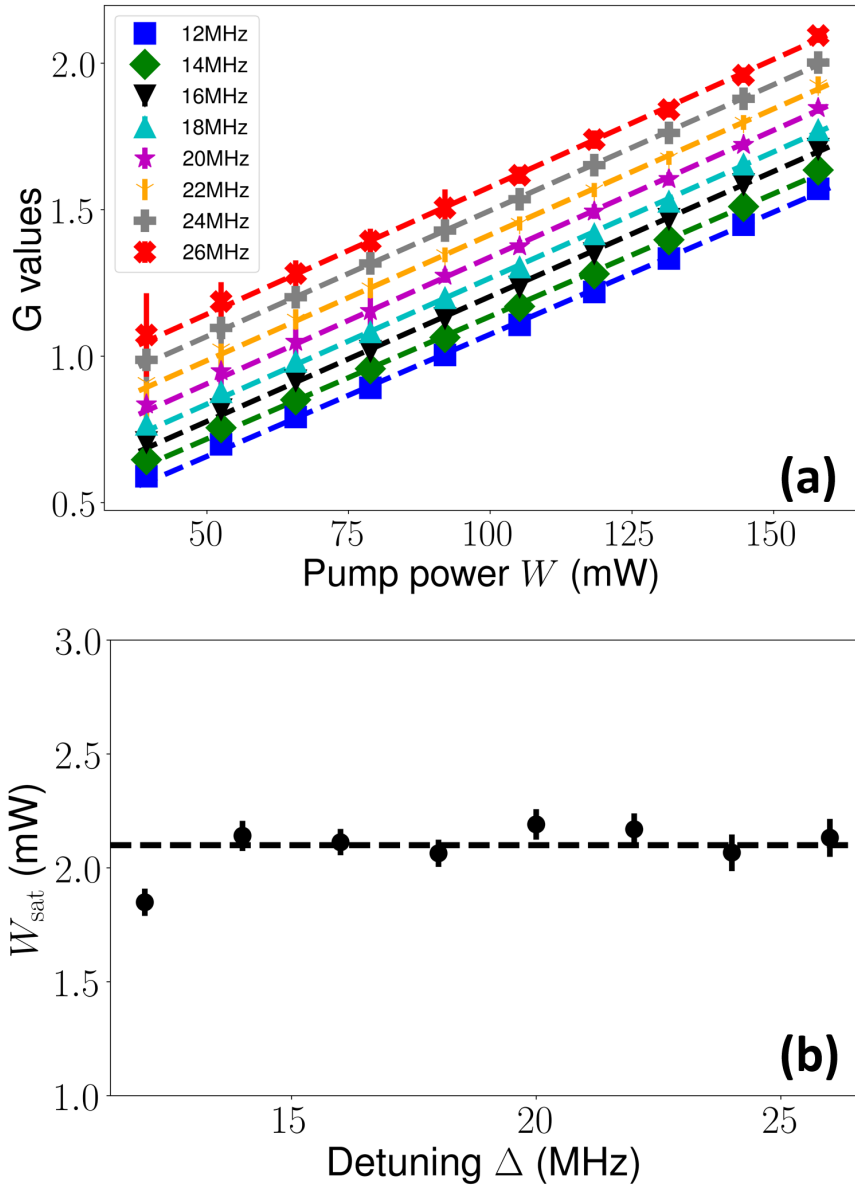


Figure 6.3: Panel (a) shows the  $G$  values as a function of the pump power for different laser detunings (12 MHz ■, 14 MHz ◆, 16 MHz ▼, 18 MHz ▲, 20 MHz ★, 22 MHz †, 24 MHz ‡, and 26 MHz ✖.) The dashed lines represent the best linear fit. The fitted slope and the intercept are used to compute the saturation power  $W_{\text{sat}}$  based on Eq. 6.7 and the results are shown in panel (b).

and  $\langle \sigma_{\text{loss}}(U) v \rangle^e$  are both a function of the trap depth, the trap depths of a MOT at different ESFs should be held unchanged. Therefore, one can solve for  $\langle \sigma_{\text{loss}}(U) v \rangle^e$  by plugging the measured/known quantities,  $\Gamma_x^{\text{MOT}}$ ,  $n_x$ ,  $f_e$ , and  $\langle \sigma_{\text{loss}}(U) v \rangle$  into Eq. 6.11. As one can see that the key to this method is to vary the ESF while keeping the trap depth constant.

Previous studies [66] have shown that the depth of the MOT depends on the area of the trap, thus, we can vary the trap beam size to vary the trap depth. Based on the two-model analysis in the last section, the ESF of a MOT is independent of the repump light. By contrast, the trap depth of the MOT depends on the spatial size of the trapping volume. Therefore, varying the size of the repump beam would allow us to change the trap depth while keeping the ESF unchanged.

We first studied the dependence of ESF on the repump beam size. We chose two different repump beam sizes; one is at the largest ( $1/e^2$  radius is 0.9 cm), the other is at the smallest repump beam ( $1/e^2$  radius is 0.025 cm) that still allows atoms to be trapped. The repump beam size is set using a motorized iris (Standa), as shown in figure 3.11. The calibration of the motorized iris is presented in appendix A. For each size of the repump beam, we performed the  $G$  measurements as introduced in the previous section. The “standard” setting is kept the same for both repump beam sizes,  $W_{\text{std}} = 80.0$  mW and  $\Delta_{\text{std}} = 12.0$  MHz. We varied the “test” power settings from 30 mW to 160 mW and the “test” detuning settings from 10 MHz to 26 MHz. Figure 6.4 (a) presents the  $G$  values at different repump beam sizes. If  $G$  values at different beam sizes agree with each other, we should expect the same ESF. The difference between the  $G$  values at different beam sizes are shown in the bottom part of figure 6.4. As we can see, the larger the pump power, the smaller variable range of the detunings we can choose to keep the same ESF at two different repump beam sizes. This is because when the trapped atoms inevitably fall into the  $|F = 1\rangle$  ground state and no longer interact with the pump laser beams, it takes a longer time for them to interact with the narrow diameter repump beam which sends them into the  $|F = 2\rangle$  state. This change in dynamics is no longer captured by the 2-level model. Therefore, we need to select the ‘stable’ range of the ESF at different repump sizes carefully, which gives total variable ESF range to be [0.16, 0.43]. The 2D map of the ESF as a function of the pump power and the detuning is shown in figure 6.4 (b).

Next, we verified that the trap depth changes as the repump beam size changes. To measure the trap depth of the MOT, we used the photoassociation method by introducing an additional laser, referred as ‘catalysis’ laser (CAL), to the MOT region [71, 66]. In a MOT, two colliding cold ground state atoms can resonantly absorb a photon from the ‘catalysis’ laser, which excites them to a repulsive molecular state. The molecule

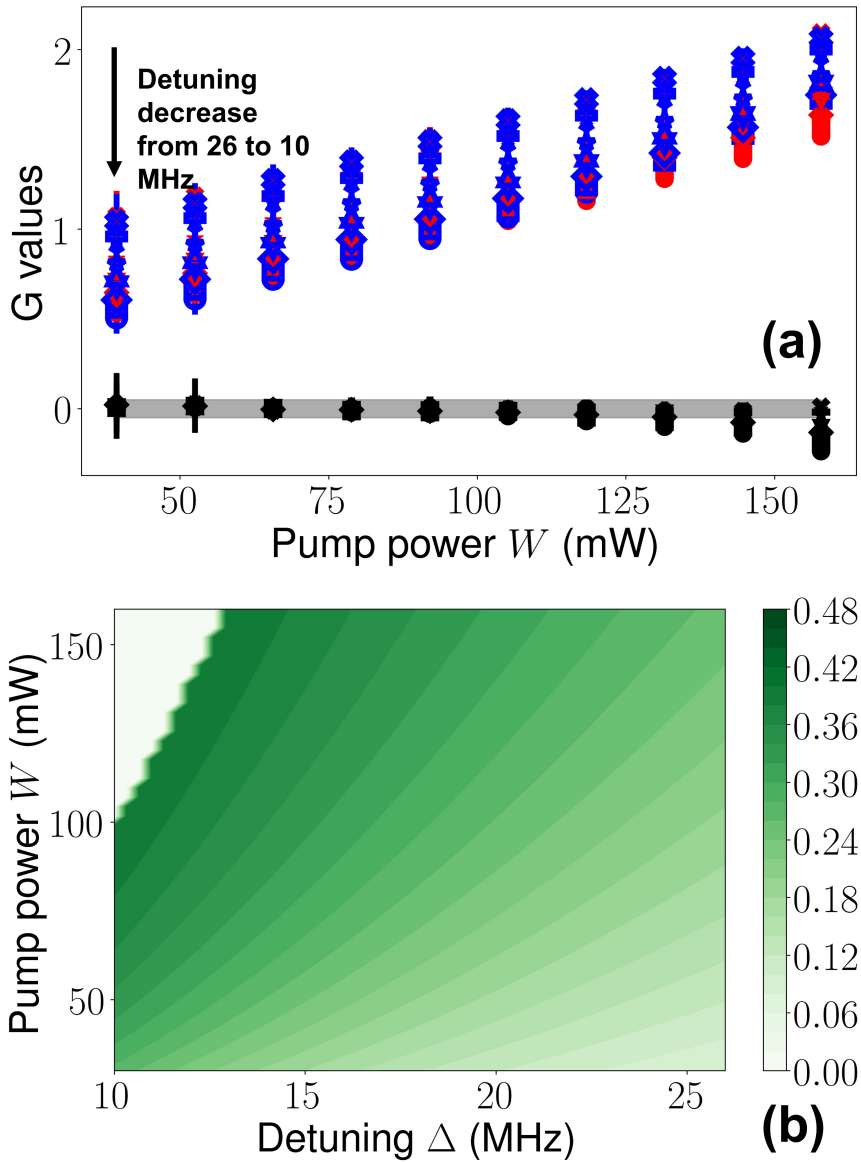


Figure 6.4: Panel (a) shows the  $G$  value as a function of the pump power at different detunings. The same measurements are repeated at two different repump beam sizes: One is at  $1/e^2$  radius 0.9 cm (blue dots), the other is at  $1/e^2$  radius is 0.025 cm (red dots). The bottom part shows the difference of the  $G$  values at different repump beam sizes. The overlap region represents the same ESF even though at different repump beam sizes. The pump powers and detunings in this overlap region are used to compute the corresponding ESFs. The results of the ESFs are plotted as a function of the power and detuning and shown in panel (b).

quickly dissociates, and the atoms move apart picking up kinetic energy and then spontaneously emitting back to the ground state. The kinetic energy picked up by each atom in the case of homonuclear collisions is  $\hbar\Delta_{cl}/2$  where  $\Delta_{cl}$  is the detuning of the

‘catalysis’ laser above the atomic resonance between the ground and the excited state ( $5^2S_{1/2}$  to  $5^2P_{3/2}$  in the case of  $^{87}\text{Rb}$ ). If  $h\Delta_{cl}/2 > U$ , where  $U$  is the trap depth, then the ‘catalysis’ laser will cause loss of the atoms from the trap. Therefore, by measuring the trap loss as a function of the ‘catalysis laser’s detuning, the average MOT trap depth can be determined.

The experimental setup of the ‘catalysis’ laser is presented in section 3.2.4. We used an  $f=250$  mm lens to focus the CAL laser onto the MOT region. The  $1/e$  radius of the CAL is around 0.1 mm when traveling to the atoms. The focusing lens is placed on a translation stage so that we can finely adjust the beam size at the MOT position. The total power of the CAL is about 200 mW, which gives the intensity  $636.6\text{W}/\text{cm}^2$ . The frequency of the CAL can be adjusted by the current and the temperature of the diode. The CAL frequency is on resonance with the pump transition ( $F = 2$  to  $F' = 3$  in the case of  $^{87}\text{Rb}$ ) when the current is 183 mA and the temperature is  $36.8^\circ\text{C}$ , and the frequency varies by  $-1.15\text{ GHz}/\text{mA}$  and  $-20.5\text{ GHz}/^\circ\text{C}$ . The current and the temperature of the CAL are both controlled by the controller from Vescent (D2-105) and are programmed by the external analog inputs. We have found that the output power of the CAL is stable with the current varying from 100 mA to 180 mA and the diode temperature varied from  $15^\circ\text{C}$  to  $40^\circ\text{C}$ . This provides the detuning range of the CAL over 600 GHz, which allows us to measure the trap depth as large as 14 K.

The MOT trap depth measurement starts by loading atoms into the 3D MOT from the 2D MOT with the CAL off. When the MOT reaches its equilibrium position, we shut down the atom loading by turning off the 2D MOT. At the same time, we turned on the CAL with a detuning  $\Delta_{cl}$  with respect to the pump transition. Without the atom loading, the dynamics of the atoms in a MOT can be expressed as,

$$\begin{aligned}\frac{dN}{dt} &= -\Gamma N - (\beta + \beta_{cl}) \int n_{\text{MOT}}^2 dV \\ \frac{dN}{dt} &= -\Gamma N - \frac{\beta + \beta_{cl}}{V_{eff}} N^2\end{aligned}\tag{6.12}$$

where  $N$  is the atom number in the MOT,  $\Gamma$  is the total one-body loss rate,  $\beta$  is the two-body loss rate coefficient without the CAL,  $\beta_{cl}$  is the CAL induced two-body loss rate coefficient through the photoassociation process, and  $n_{\text{MOT}}$  is the density of the MOT. Based on the assumption that the MOT is in the constant density regime, one

can solve Eq. 6.12,

$$N(t) = \frac{N_0 \exp(-\Gamma t)}{1 + \frac{(b+b_{cl})N_0}{\Gamma} [1 - \exp(-\Gamma t)]}. \quad (6.13)$$

Here  $N_0$  is the initial number of atoms in a MOT.  $b = \beta/V_{eff}$  and  $b_{cl} = \beta_{cl}/V_{eff}$  are the two-body loss rate with and without the CAL respectively. The total two-body loss rate  $b + b_{cl}$  can be extracted by fitting Eq. 6.13 to the MOT decay curve as shown in figure 6.5. With the detuning of the CAL resonant with photoassociation transition, we can see a factor of 10 increase in the total two-body loss rate.

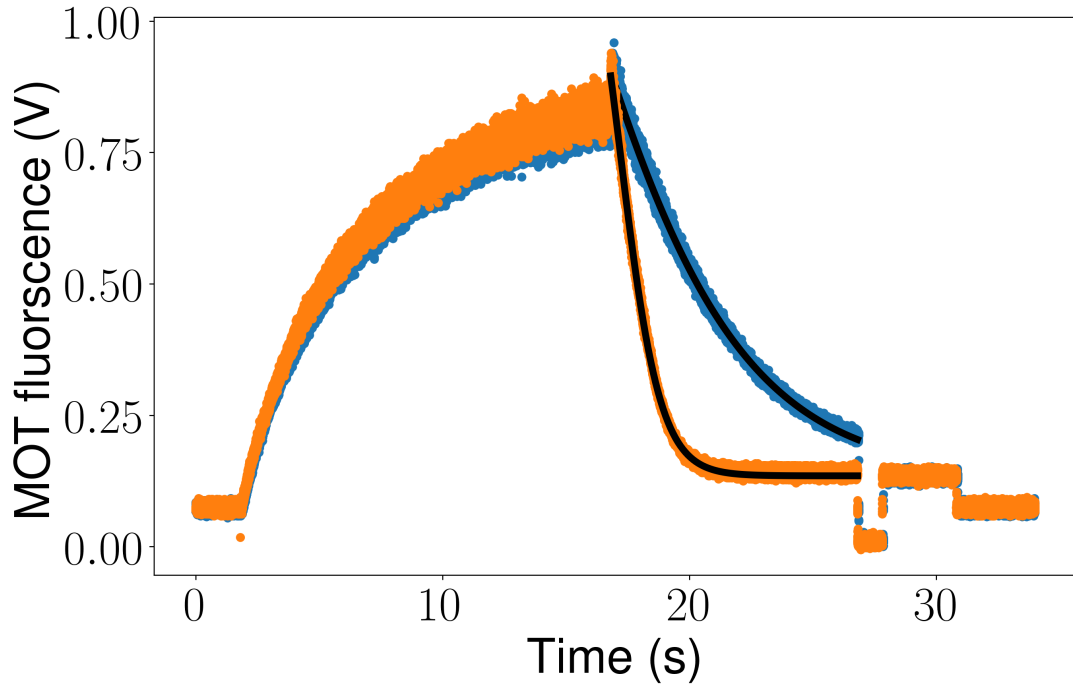


Figure 6.5: MOT fluorescence as a function of time. In this plot, the MOT is loaded for 15 s, then the loading beam is shut off and the CAL laser is turned on. The decay of the MOT is measured for 10 s. The orange dots represent the decay rate measurement with the CAL frequency close to the photoassociation transition, while the blue dots represent the decay rate measurement with the CAL frequency far from the photoassociation transition. The black lines are the two-body fitting function. The fitted two-body rate for orange data set is  $1.01 \text{ s}^{-1}$ , while the fitted two-body rate for blue data set is  $0.11 \text{ s}^{-1}$ .

We then varied the frequency of the CAL and repeated the decay rate measurement for each frequency of the CAL. An example of the full trap depth measurement is shown in the inset of figure 6.6. The average trap depth of the MOT can be calculated using

the x-axis (detuning) of the peak in the plot,  $U = h\Delta_{cl}/2$ .

Next, we measured the trap depth of the MOT at different repump beam sizes while keeping the pump laser parameters the same so that the ESFs are the same. We chose three different combinations of pump laser parameters that provide three different ESFs,  $f_e = 0.381$  (detuning 10 MHz, power 80 mW),  $f_e = 0.315$  (detuning 12 MHz, power 60 mW), and  $f_e = 0.166$  (detuning 16 MHz, power 30 mW). For each ESF, we varied the repump size from 0.9 cm  $1/e$  radius to the smallest one that can still achieve a stable MOT on the level of 0.1 cm  $1/e$  radius. The trap depth measurements are shown in figure 6.6. As we can see, there exists a small window when the trap depths are the same but the ESFs are different ( $f_e = 0.381, 0.315, 0.166$ ).

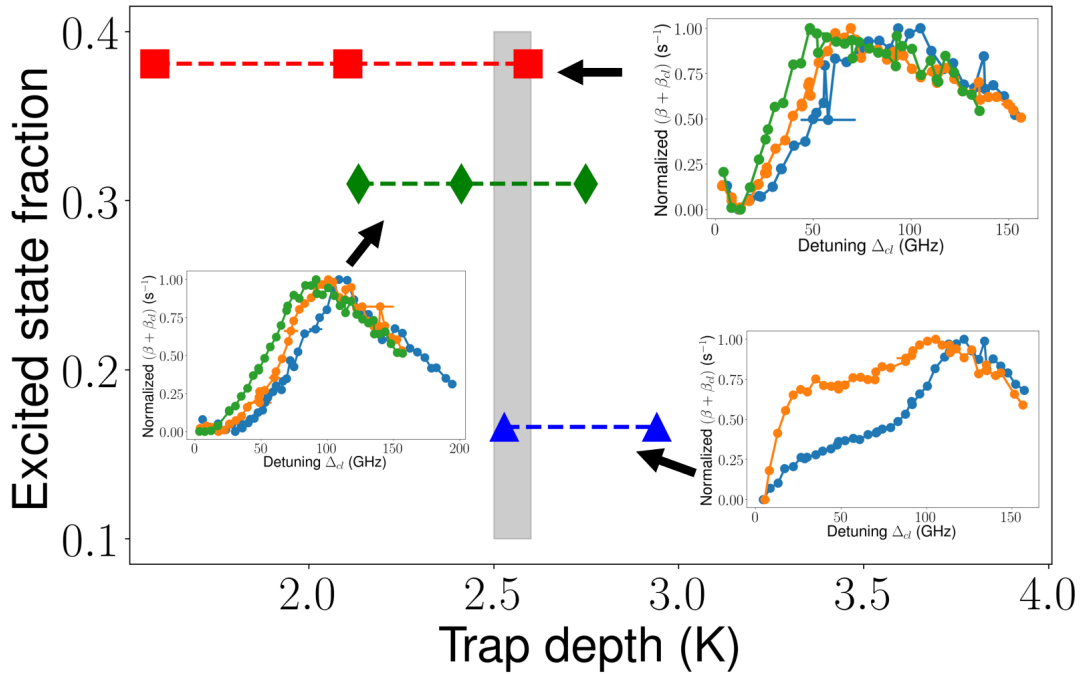


Figure 6.6: Excited state fraction of a MOT at different trap depths, controlled by the repump beam size. The red squares represent the MOT with a ESF 0.381 which is achieved when the pump power is 80 mW and the detuning is 10 MHz. The green diamonds represent the ESF of 0.315 with the pump power 60 mW and the detuning 12 MHz. The blue triangles represent the ESF of 0.166 with the pump power 30 mW and the detuning is 16 MHz. For each ESF, the trap depth of a MOT has been measured at different repump beam sizes by measuring the photoassociation induced two-body loss rate as a function of the detuning of the CAL,  $\Delta_{cl}$ . The corresponding detuning of the CAL at which the two-body loss rate reaches a maximum can be used to calculate the trap depth,  $U = h\Delta_{cl}/2$ . The results are shown in the insets.

### 6.2.3 Determination of loss rate coefficient of excited state Rb atoms

Now we have successfully realized the situation mentioned in the beginning of this section: Varying the ESF while keeping the trap depth constant. By measuring the decay of the MOT at each ESF, one would be able to solve the excited state loss rate coefficient at a particular trap depth,  $\langle \sigma_{\text{loss}}(U) v \rangle^e$ , based on Eq. 6.11.

As Eq. 6.12 shown, the two-body collision process in the MOT also generates atom loss, thus, one needs to isolate the two-body loss rate and the one-body loss rate due to the background collisions. One way is to fit the MOT decay rate measurement with the two-body fitting function, as shown in Eq. 6.12. The alternative approach, used in this work, is to increase the density of background particles so that the one-body collision loss dominates the loss process. This high one-body collision loss rate prevents too many atoms from being loaded into a MOT, which further decreases the two-body collision rate.

As a preliminary study, we decided to measure the excited state loss rate coefficient between Rb and Ar. We introduced Ar gas into the apparatus and kept the pressure always above the  $8 \times 10^{-9}$  Torr so that the one-body loss rate can dominate and the two-body collision loss contributions are negligible. We firstly measured the MOT decay rate at the  $8.2 \times 10^{-9}$  Torr Ar pressure. The extracted one-body decay rate is used as the baseline,  $\Gamma_b^{\text{MOT}}$ , and will be subtracted from the other decay rate measurements at higher pressures. Then, we increased the Ar pressure to  $1.04 \times 10^{-8}$  Torr,  $1.5 \times 10^{-8}$  Torr,  $2.46 \times 10^{-8}$  Torr, and  $3.41 \times 10^{-8}$  Torr sequentially. At each pressure, we measured the decay rates,  $\Gamma_{\text{loss}}^{\text{MOT}}$ , at three different ESFs,  $f_e = 0.381$  (detuning 10 MHz, power 80 mW),  $f_e = 0.315$  (detuning 12 MHz, power 60 mW), and  $f_e = 0.166$  (detuning 16 MHz, power 30 mW). At each ESF, the repump beam size is carefully adjusted so that they have the same trap depth at around 2.7 K measured by the ‘catalysis’ method.

Then the actual one-body loss rate due to collisions with Ar is given by,

$$\Gamma_{\text{Ar}}^{\text{MOT}} = \Gamma_{\text{loss}}^{\text{MOT}} - \Gamma_b^{\text{MOT}}. \quad (6.14)$$

Similarly, the actual Ar pressure is given by  $P_{\text{Ar}} = P - P_b$ , where  $P_b$  is the IG reading at the base pressure  $8.2 \times 10^{-9}$  and  $P$  is the IG reading at each test pressure. Since the IG has been calibrated against the MT based CAPS, we can compute the density of Ar

gas using  $n_{\text{Ar}} = P_{\text{Ar}}/i_{\text{g}}^{\text{Ar}}$ . Here,  $i_{\text{g}}^{\text{Ar}}$  is the gauge factor of the IG for Ar gas. The results of Ar collision induced loss rate,  $\Gamma_{\text{Ar}}^{\text{MOT}}$ , as a function of Ar density,  $n_{\text{Ar}}$ , for each ESF are presented in figure 6.7. The deviations in the decay rates at different ESFs suggest contributions from the excited state loss rate coefficient since they have the same ground state loss rate coefficient at the same trap depth.

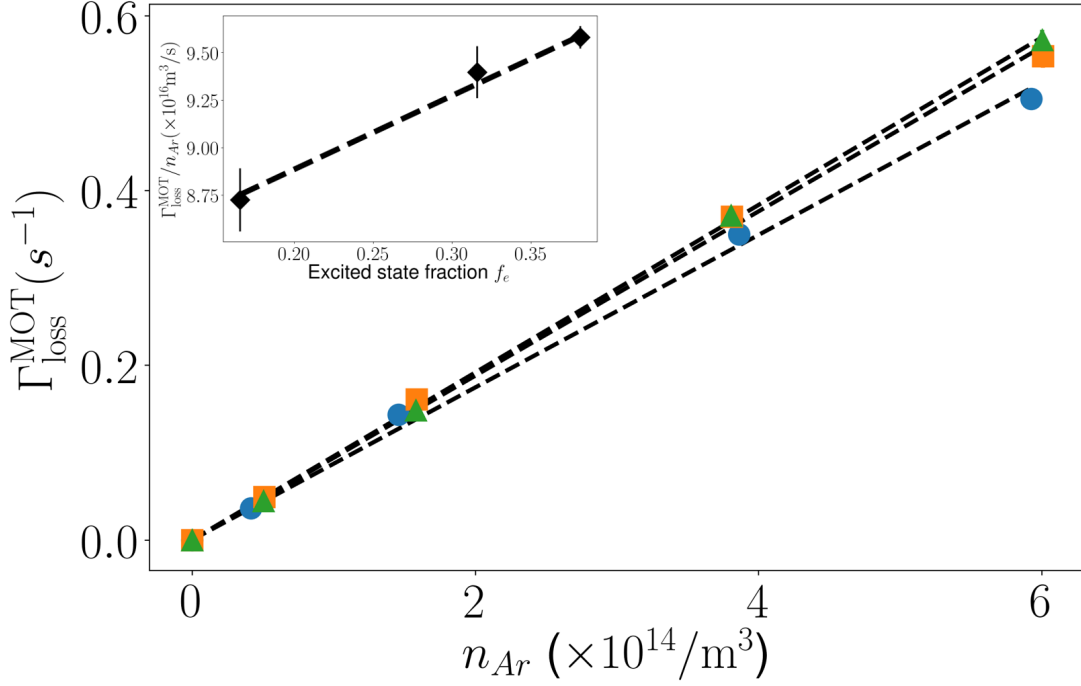


Figure 6.7: Ar collisions induced loss rate versus the density of Ar gas. The Ar density is reported by the IG, which is calibrated against the MT based CAPS. Blue circles represent the MOT at  $f_e = 0.381$  (pump light detuning at 10 MHz and power at 80 mW). Orange squares represent the MOT at  $f_e = 0.315$  (pump light detuning at 12 MHz and power at 60 mW), and green triangles represent  $f_e = 0.166$  with pumping detuning at 16 MHz and the power at 30 mW. The trap depth of the MOT at each ESF is set to be 2.7 K by adjusting the repump beam size. The dashed lines represent the linear best fit. The slope of each curve is plotted as a function of the ESF and shown in the inset. In the inset, the dashed line also represents the best linear fit. The extracted intercept represents the ground state loss rate coefficient, and the sum of the intercept and the slope gives the result of the excited state loss rate coefficient when the trap depth is 2.7 K.

The slope of each curve in figure 6.7 is a function of the ESF, thus, the ESF loss rate

coefficient can be obtained by fitting the slopes versus ESF to the following expression,

$$\begin{aligned} \frac{\Gamma_{\text{Ar}}^{\text{MOT}}}{n_{\text{Ar}}} &= \langle \sigma_{\text{loss}}(U) v \rangle (1 - f_e) + \langle \sigma_{\text{loss}}(U) v \rangle^e f_e \\ &= [\langle \sigma_{\text{loss}}(U) v \rangle^e - \langle \sigma_{\text{loss}}(U) v \rangle] f_e + \langle \sigma_{\text{loss}}(U) v \rangle. \end{aligned} \quad (6.15)$$

Through fitting, we can extract the excited state loss rate coefficient,  $\langle \sigma_{\text{loss}}(U) v \rangle^e$ , and the ground state loss rate coefficient,  $\langle \sigma_{\text{loss}}(U) v \rangle$ , at one trap depth. The fitting results are shown in the inset of figure 6.7. At 2.7 k depth of the MOT, the ground state loss rate coefficient is  $8.11 \times 10^{-16} \text{m}^3/\text{s}$  and the excited state loss rate coefficient is  $11.99 \times 10^{-16} \text{m}^3/\text{s}$ , which is a factor of 1.5 higher than the ground state. The determined ground state loss rate coefficient through this method agrees with the results obtained calibrating against the MT based CAPS ( $7.02(4) \times 10^{-16} \text{m}^3/\text{s}$ ) within 15 % uncertainty, as shown in previous section 6.1

One can repeat the measurements at many other different trap depths and characterize the both the ground and excited state loss rate coefficient as a function of the trap depth. Finally, the determined ground and excited state loss rate coefficients can be directly plugged in Eq. 6.11 to report the density of test gas species with the MOT loss rate measurements.

In summary, the procedure of using a MOT as an absolute pressure standard goes as:

1. One should determine the pump saturation power,  $W_{\text{sat}}$ , of the atoms in the MOT using the  $G$  measurements.
2. Measure the loss rate of a MOT at different ESFs but at the same trap depth, which is achieved by using the repump beam size.
3. The loss rate measurements of a MOT at different ESFs can be plugged in Eq. 6.15 to solve the excited and the ground state loss rate coefficient at a certain trap depth,  $U$ .
4. For a given new MOT in a new vacuum system, one needs to determine the pump saturation power  $W_{\text{sat}}$  and compute the ESF using Eq. 6.4. The trap depth of the MOT needs to be set to  $U$ .
5. Measure the loss rate of the MOT.

6. Given the pre-determined ground and excited state loss rate coefficients at trap depth,  $U$ , one can determine the density of test gas based on Eq. 6.11.

Although using the MOT based pressure standard to measure the loss rate coefficient requires lots of effort, we believe it is still advantageous. This is because the MOT can reach much higher depths than other traps, which allows measurements of much higher pressures by suppressing the loss rate. We also acknowledge that the simplest way of using the MOT based pressure standard is to use it as the transfer standard after being calibrated against the MT based pressure standard, as presented in section 6.1.

# Chapter 7

## Conclusion

In this thesis, we have discussed the developments of the first cold atom-based pressure standard. Rubidium atom has been used as the sensor atom in this CAPS since Rb atoms can be confined in a trap with a depth that is a factor of 10 higher than those that can be realized with Lithium. This larger trap depth range allow us to implement the self-calibrating method based on the universality of quantum diffractive collisions. We note that it is advantageous to use Li as the sensor atom for a practical implementation of a quantum pressure sensor due to its low vapor pressure at the room temperature and have been demonstrated somewhere else[83, 64].

We have shown the use of a differential pumping tube to separate the Rb source chamber and the measurement chamber in order to avoid the contamination of the measurement chamber by Rb atoms. We also added a UHV valve between the source chamber and the measurement chamber to further maintain the measurement chamber from Rb atoms contamination. We achieved a UHV environment ( $< 2 \times 10^{-10}$  Torr) in the measurement chamber through a high temperature baking. We want to emphasize again that the valve between the source chamber and the measurement chamber should be kept closed during the baking process.

In addition, we have shown that using two simple ECDLs to cool and trap  $^{87}\text{Rb}$  atoms. One is used here as the pump laser and the other is used as the repump laser. We have found the efficient way to stabilize lasers' frequencies is to lock the pump laser frequency with a saturated absorption spectroscopy (SAS) locking scheme, and stabilize the repump laser frequency with an offset locking scheme. The linewidth of these two lasers can be reduced to a FWHM of  $\sim 3$  MHz. To achieve enough laser power to the MOT region, we used the injection locking/amplifying systems to amplify their powers. We also have found stabilizing the powers of both pump and repump lasers is important to decreasing the statistical uncertainty in the pressure measurements.

We also have shown the design of the magnetic coils that provide trapping fields to the atoms. We chose the quadrupole field configuration for both 2-dimensional (2D) and 3-dimensional (3D) MOTs. We measured the axial field gradient of the 3D MOT coil to be 1.36 G/cm/A. A RF coil is used to set the trap depth of atoms in the MT. Due to the limited space between the cell and the coil, a single turn RF coil is used here, which produces the field with a Rabi frequency 0.1MHz and can clear the trap within 0.7 s. We acknowledge that more turns of RF coil can produce a higher Rabi frequency and a faster clear rate.

In chapter 4, we have demonstrated the realization of the MT-based CAPS. This standard employs a universal law that describes quantum diffractive collisions mediated by a long-range van der Waals interaction. Based on quantum scattering calculations and experimental measurements of the loss rate of trapped  $^{87}\text{Rb}$  atoms due to collisions with different test gases, He, Ar, Xe,  $\text{H}_2$ ,  $\text{N}_2$ , and  $\text{CO}_2$ , we determined the universal function describing quantum diffractive collisions by a single, experimentally measurable parameter  $\langle\sigma_{\text{tot}}v\rangle$ . The universal function for the trap loss rate can be used to determine thermally averaged total collision cross section,  $\langle\sigma_{\text{tot}}v\rangle$ , and ambient gas density without input from other measurements or theoretical calculations. The pressure measurement accuracy was verified against a NIST-calibrated ionization gauge: For  $\text{N}_2$ , NIST determined a gauge factor of  $0.94 \pm 2.8\%$  compared to  $0.950 \pm 2.0\%$  from the new pressure standard.

Following reference [6], a true primary quantum standard must obey the following laws: (1) The standard must be based on immutable, universal, and fundamental constants or quantum phenomena, (2) must report an accurate value of the measurement, and (3) must provide a quantifiable uncertainty fit for purpose. Therefore, the MT-based CAPS in this thesis fits in the Quantum SI standards paradigm with a zero-length traceability chain [143, 144]. Therefore, we also characterized the upper bound of the total uncertainty for the  $\langle\sigma_{\text{tot}}v\rangle$  measurements ( $\text{Rb-N}_2$ ) of the new standard are estimated to be 2.2 % in the current implementation. The dominant errors are the statistical uncertainty in decay rate measurements ( $< 1.9\%$ ) and the systematic uncertainty in the ensemble heating ( $< 0.5\%$ ) due to background collisions.

In chapter 5, we further reduced the statistical uncertainty and the systematic uncertainty in the measurements of  $\langle\sigma_{\text{tot}}v\rangle$ . To reduce the statistical uncertainty in decay

rate measurements, we rearranged our data measurements by placing 50 % of the sample points at the initial time and placing the rest 50 % of the sample points at  $1.28\tau$ , where  $\tau$  is the lifetime. This allows us to reduce the statistical uncertainty in decay rate measurements to a 1.0 % level. Furthermore, we trapped atoms in the  $F = 2$  ground state so that the trap depth range of the atoms can be increased by a factor of 2, which provides a wider range of  $U/U_d$  over which to fit the data and performs a more precise measurement of  $\langle\sigma_{\text{tot}}v\rangle$ . This helped reduce the total statistical uncertainty in  $\langle\sigma_{\text{tot}}v\rangle$  down to 0.5 % level. We also carefully considered the ensemble heating effect while increasing the trap depth of the atoms. We measured the energy distribution of the ensemble as a function of time in order to account for the collisional heating-induced energy distribution change. With the improvements in the precision, we have experimentally measured the  $\langle\sigma_{\text{tot}}v\rangle$  for Rb-Ar. The experimentally determined result,  $2.793(8)(25) \times 10^{-15} \text{m}^3/\text{s}$  agrees well with the full quantum scattering computed result  $2.82 \times 10^{-15} \text{m}^3/\text{s}$ , which is calculated based on the L-J formed potential with the depth quoted from [12]. This method can be generalized to precisely measure the  $\langle\sigma_{\text{tot}}v\rangle$  for other test gas species.

This MT based CAPS can only be operated in the pressure up to  $1.0 \times 10^{-8}$  Torr. To measure the pressure in the high vacuum (HV) regime ( $> 1.0 \times 10^{-7}$  Torr), the lower end of operation of SRGs, we utilized atoms trapped in a MOT to perform pressure measurements (MOT based CAPS). In chapter 6, We demonstrated trap loss from a MOT can be used as a transfer standard to extend the range of the MT-based CAPS above  $> 1.0 \times 10^{-7}$  Torr, allowing the cold atom standard to be connected, via SRGs, to the mercury manometer standard. In addition, we also proposed an idea of directly using a MOT to measure the pressure in the vacuum. At first, we have shown the method of characterizing the excited state fraction of a MOT using the photon scattering rate by the trapped atoms. Then we presented the details of measuring the excited state and the ground state loss rate coefficient, respectively. We have shown controlling the repumping beam size to vary the trap depth while keeping the excited-state fraction constant, which is key to this method. As a preliminary study, we have measured the excited state and the ground state loss rate coefficient for Rb-Ar at the trap depth of 2.7 K. We have found the excited state loss rate coefficient ( $11.99 \times 10^{-16} \text{m}^3/\text{s}$ ) is 1.5 times higher than the ground state loss rate coefficient  $8.11 \times 10^{-16} \text{m}^3/\text{s}$ . With the

information of both the excited state and the ground state loss rate coefficient, one can directly measure the pressure through the loss rate of a MOT. Future work can include measuring the excited state loss rate coefficients at different trap depths and examining if there exists a different universal.

# Chapter 8

## Future Outlook

We now turn to the future directions of developing the CAPS. We can divide the potential future work into two aspects: (1) complication, which is to further study the universality of quantum diffractive collisions and explore the limitations of this universality due to the impact from the short-range interaction, (2) simplification, which is to simplify the design and the use of CAPS in order to make a quick and accurate pressure measurement that requires us to build a portable version of the CAPS.

### 8.1 Complication

#### Explorations of quantum diffractive collisions

In section 4.1.2, we have shown that  $\langle\sigma_{\text{tot}}v\rangle$  is insensitive to the core potential for a given collision system by demonstrating the identical  $\langle\sigma_{\text{tot}}v\rangle$  values at three PESs with radically different depths,  $\epsilon$ , defined in Eq. 4.13. This reveals the effect of the thermal averaging that is averaging the cross section over one or more oscillations removes the core-dependent effects. Moreover, we also show that the shape of the loss rate versus trap depth is also independent of the short-range part of the potential at shallow trap depths. The values on the loss rate curve represent the retaining fraction of atoms after the collisions. The difference between the curve and the velocity averaged total collision cross section,  $\langle\sigma_{\text{tot}}v\rangle$ , at shallow trap depths indicates the loss due to quantum diffractive collisions that are insensitive to the short-range part of the potential. Therefore, if we scale the trap depth with its characteristic energy,  $U_d$  (shown as Eq. 4.12), which includes all the collision system dependent parameters, such as the  $\langle\sigma_{\text{tot}}v\rangle$ , the masses of the collision and the trapped particles, the shape of the function of the loss rate versus the scaled trap depth would be universal. This has been shown using the full quantum scattering computations for Rb, Li colliding with He, Ar, and Xe gas species, as shown

in figure 4.2.

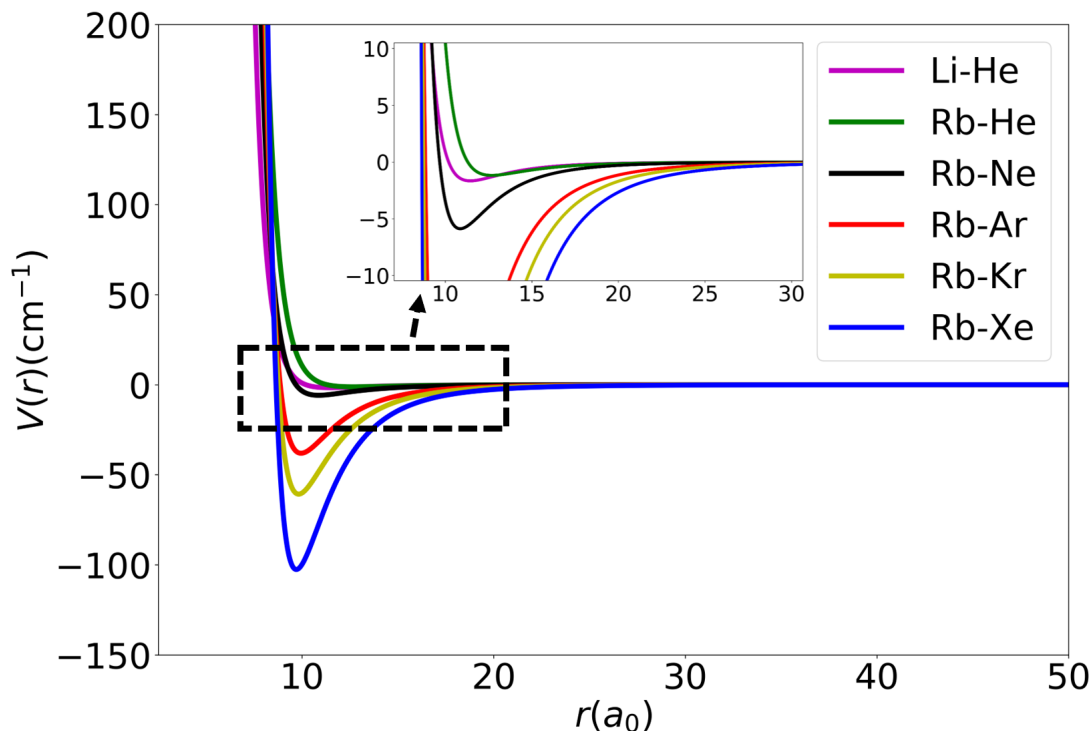


Figure 8.1: A plot of the interaction potential energy as a function of the inter-atomic distances. The form of the PES is chosen to be L-J form. The inset shows the details of the plot from inter-atomic  $5.0 a_0$  to  $25.0 a_0$ , where  $a_0$  is the Bohr radius.

In our previous studies, we chose the depth of the PES no smaller than  $50 \text{ cm}^{-1}$ . Given the PES expression in Eq. 4.13, we know the depth,  $\epsilon = C_6^2/4C_{12}$ , which shows the ratio of the contribution from the long-range to the short-range. The larger the depth, the smaller the short-range term compared to the long-range portion of the potential. Therefore, one question can be immediately raised will the description of the universality break if the depth of the PES keeps decreasing. In fact, this is a very realistic question since some of the collision systems have shallower trap depths than  $50 \text{ cm}^{-1}$ . In table 8.1, we listed the depths of the PES for different collision systems, Li-He [61], Rb-He, Ne, Ar, Kr, and Xe [12], and the L-J form of the PESs for different collision systems are shown in figure 8.1. When Rb is the sensor atom, the depths of the Rb-He, Ne PES are smaller than  $50 \text{ cm}^{-1}$ . Therefore, we run the full quantum scattering computations with the long-range coefficients and the depths listed in table 8.1. The results are shown in 8.2. As one can see, the results of Rb-He, Ne and Li-He do not follow the universal curve, while other noble gas species follow nicely.

### 8.1. Complication

Collision system	$C_6(E_h a_0^6)$	$\epsilon(\text{cm}^{-1})$	$\langle \sigma_{\text{tot}} v \rangle \times 10^{-15} \text{m}^3/\text{s}$	$Q$
Li-He <sup>[1]</sup>	22.535	1.661	1.50	1.65
Rb-He <sup>[2]</sup>	44.68	1.178	2.19	1.59
Rb-Ne <sup>[2]</sup>	88.0	5.878	1.72	2.60
Rb-Ar <sup>[2]</sup>	336.4	38.06	2.82	4.35
Rb-Kr <sup>[2]</sup>	498.0	60.75	2.64	4.95
Rb-Xe <sup>[2]</sup>	780.1	102.59	2.77	5.82

Table 8.1: Column 2 and 3 show the long-range coefficients,  $C_6$ , and the depths,  $\epsilon$ , of the PES for different collision systems, respectively. The values for Li-He are quoted from ref. [13], while the values for Rb colliding with noble gas species are quoted from ref. [12]. These coefficients are used to perform full quantum scattering computations to calculate  $\langle \sigma_{\text{tot}} v \rangle$  are presented in column 4. The  $Q$  factors, computed based on Eq. 8.3, are presented in the last column.

The deviations from the universal curve especially when the mass of the collision partner is light suggest that the short-range interaction even affects the quantum diffractive collisions. This is understandable since the lighter mass means higher kinetic energy at room temperature, which results in probing the core potential easier than the heavy particle. Also, the shallower the depth means the higher short-range part, which further helps the particle experience the core potential. We can define the ratio of the long-range part to the short-range part as a quantity to determine the relative contributions from the short-range potential. The J-B approximation provides an appropriate expression to calculate the phase shifts from either the long-range or the short-range, as shown in Eq. 2.49, since the scattered field is small compared to the incident field. For the long-range contribution, we can take  $s = 6$ , while for the short-range contribution, we can take  $s = 12$ . Then we can calculate the total collision cross section by plugging in the phase shifts for both long-range and short-range part,

$$\sigma_{C_6}(v_p) \approx 8.0827 \left[ \frac{C_6}{\hbar v_p} \right]^{\frac{2}{5}} \quad (8.1)$$

$$\sigma_{C_{12}}(v_p) \approx 6.5839 \left[ \frac{C_{12}}{\hbar v_p} \right]^{\frac{2}{11}}. \quad (8.2)$$

Here  $v_p$  is the most probable velocity of the background particles,  $\sigma_{C_6}(v_p)$  and  $\sigma_{C_{12}}(v_p)$  indicate the total collision cross section resulted by the long-range and the short-range

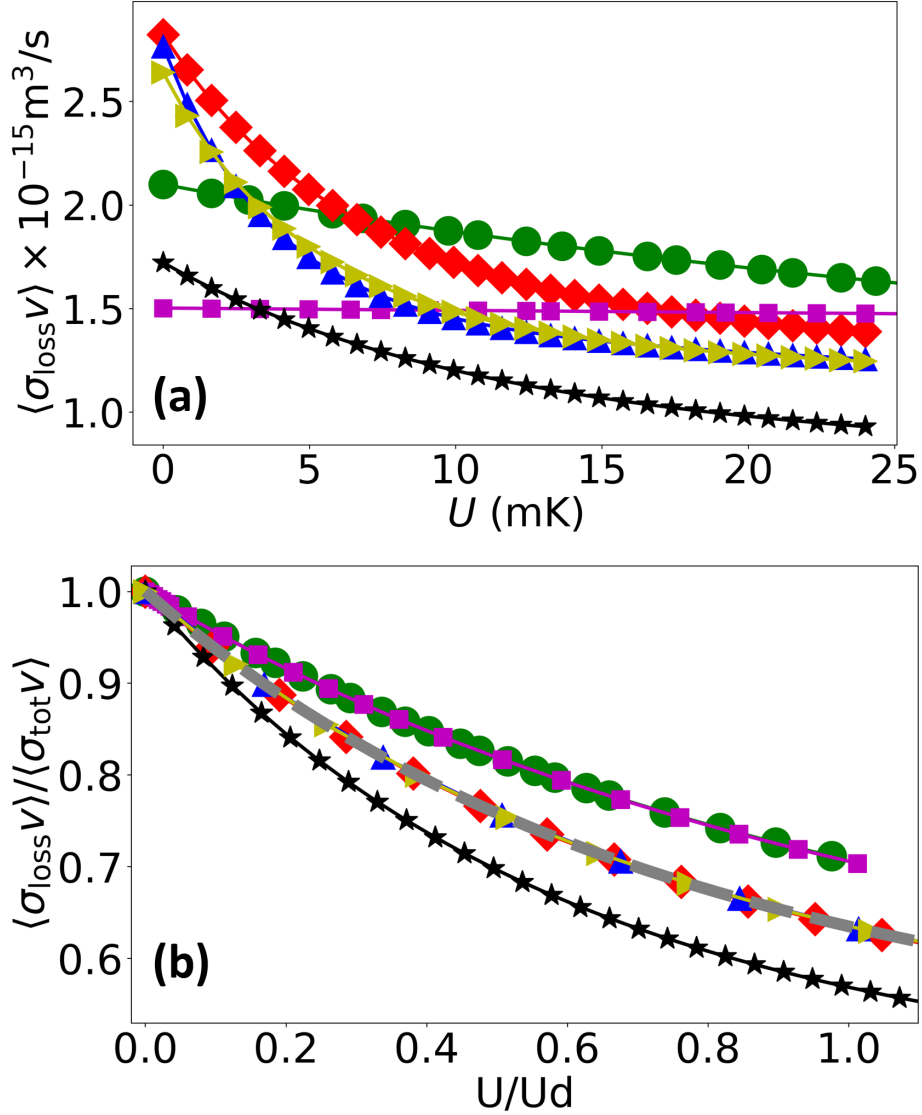


Figure 8.2: Velocity averaged collision loss cross sections versus trap depth for Rb-He (green circles), Ne (black stars), Ar (red diamonds), Kr (yellow right triangles), and Xe (blue up triangles), and Li-He (purple squares). In (b) these loss rate coefficients are normalized by their value at  $U = 0$  and plotted versus the scaled trap depth. Rb-He, Ne and Li-He results do not collapse to the universal curve (grey dashed line) nicely.

part of the potential, respectively. Therefore, we can define the  $Q$  quantity as

$$Q = \frac{\sigma_{C_6}(v_p)}{\sigma_{C_{12}}(v_p)} = 1.212(\hbar^2 k_B T)^{-\frac{6}{55}} [\epsilon^{10} C_6^2 m^6]^{\frac{1}{55}}, \quad (8.3)$$

where  $m$  is the mass of the collision partner, no mass of the trapped atom is involved. To check if  $Q$  factor is a sensitive measure for predicting deviations from the universal

curve, we compute the deviations (measured as the average orthogonal distance from the universal curve) for different collision systems. Finally, the deviation as a function of  $Q$  factor is plotted in figure 8.3. As we can see it nicely predicts when the collision system will not follow the universal curve due to the large contributions from the short-range part of the potential. When the  $Q$  factor is smaller than 3.2, one should expect the fall off from the universal curve.

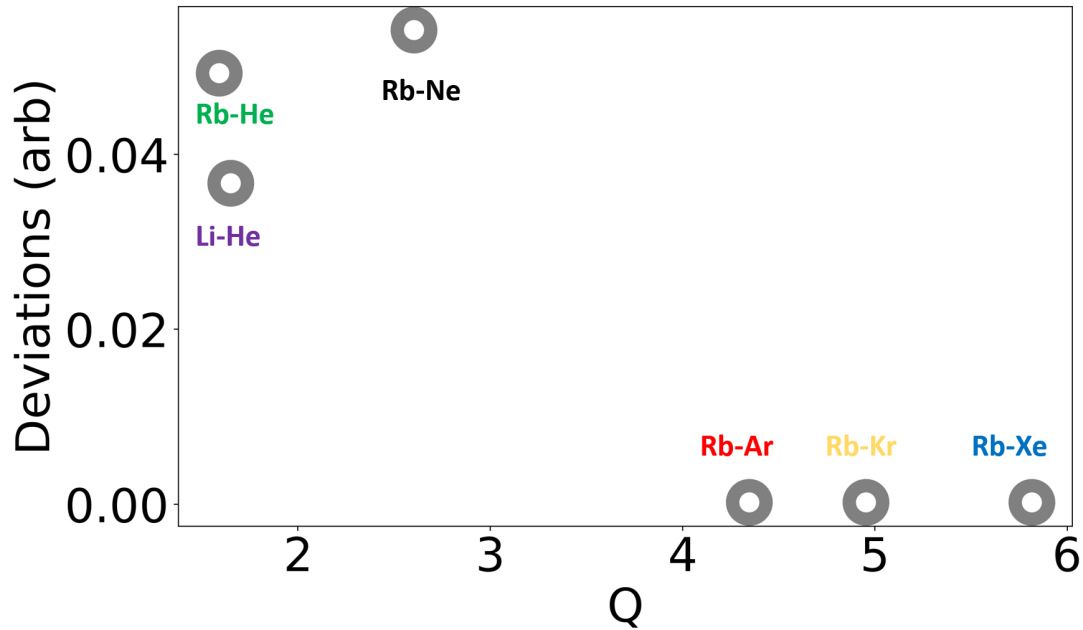


Figure 8.3: Averaged deviations from the universal curve as a function of the  $Q$  value. The results are nicely classified into two islands. When the value of  $Q$  is larger than 3.2, it shows that it will follow the universal curve. Otherwise, it will deviate from the universal curve.

More theoretical computations should be done to further support the prediction of the  $Q$  factor. However, the  $Q$  factor does not capture the sign of the deviations, namely whether the result is above (Rb-Ne) or below (Li-He, Rb-He) the universal curve. The role of the short-range interaction needs to be studied more carefully. Also, the results of Li-He and Rb-He overlap well which seems to suggest that there might exist a universality behavior determined by short-range interaction.

## 8.2 Simplification

### Portable CAPS

Another direction of this quantum sensing project is to simplify the operation of the pressure measurement, which will be beneficial to practical use. To achieve this goal, we are building a portable version of the CAPS. The vacuum chamber consists of a 2D MOT and a 3D MOT section, similar to the design of the apparatus in this thesis. A schematic of the vacuum chamber is shown in figure 8.4 (a). The whole vacuum chamber will be placed on a  $18 \times 30$  inches platform with essential optics, and the magnetic coils surrounded, as shown in figure 8.4 (b).

The design of the laser system in this portable CAPS is different from the one introduced in this thesis. In this portable version, we use the SAS locking method to frequency stabilize a reference laser. The pump laser is offset locked to this reference laser. Then, we used an EOM to generate the repump light, which helped achieve a perfect overlap between the pump and the repump light. The design of the coil system and the control system is similar to the ones introduced in this thesis. Eventually, the whole system will be integrated into a refrigerator-sized rack (60 inches tall  $\times$  25 inches wide  $\times$  36 inches deep ) so that it can be shipped to elsewhere in the world. The schematic of the whole system is shown in figure 8.4 (c).

The hope of this portable CAPS will be robust and easy to be operated. With the prior knowledge about the  $\langle \sigma_{\text{tot}} v \rangle$  determined with the standard in this thesis, one can simply perform the pressure measurements by measuring the decay rate of atoms using this portable CAPS. Next, this portable CAPS will be connected to the permanent CAPS in the lab to perform side-by-side pressure measurements to demonstrate the uniformity of the CAPS. In the future, this portable CAPS will be shipped to NIST to compare with its orifice flow pressure standard and a CAPS using Li as sensor atom [83].

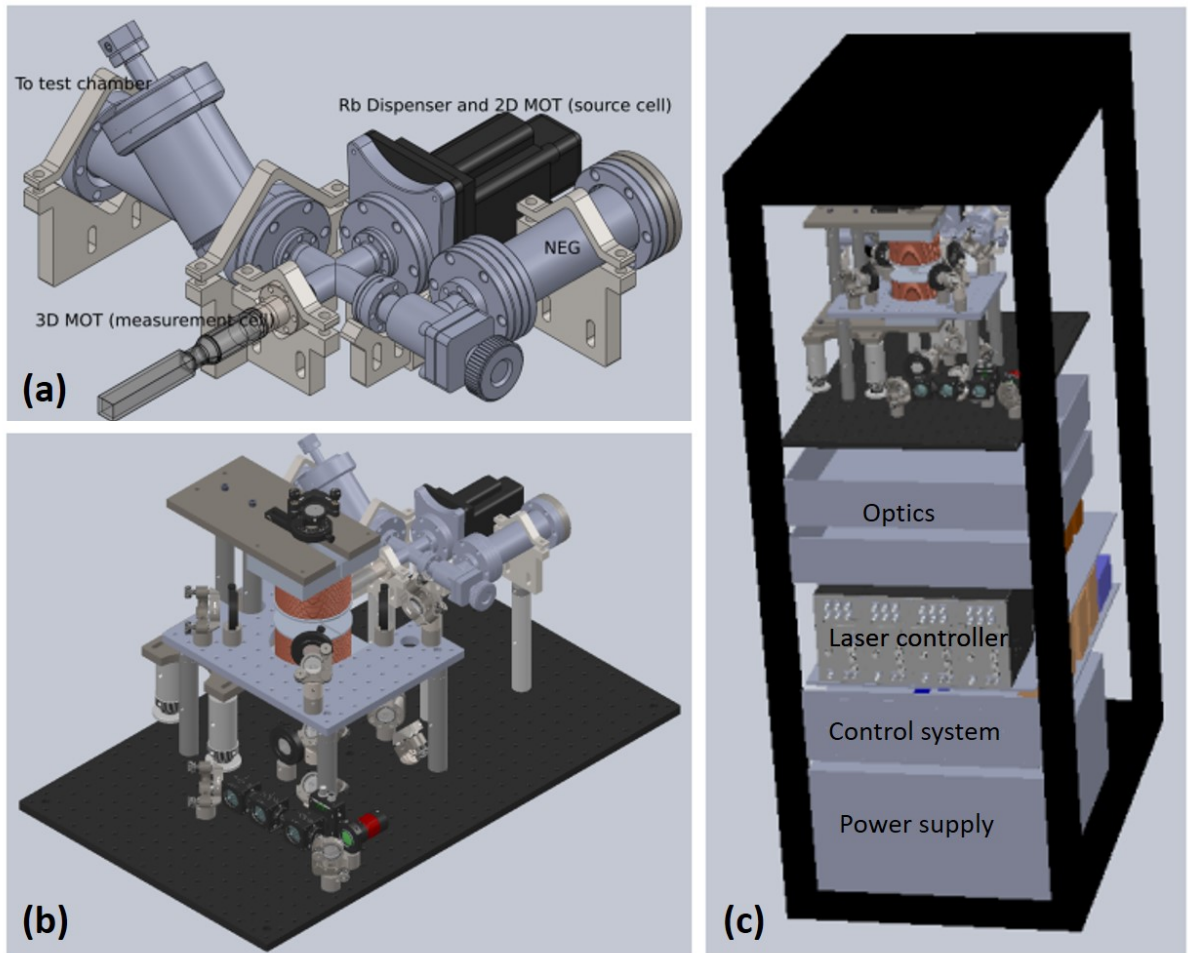


Figure 8.4: A schematic of the portable CAPS. Panel (a) shows the vacuum chamber design of the portable CAPS. A set of magnetic coils and optics are put around the chamber on a  $18 \times 30$  inches platform as demonstrated in panel (b). Then the whole platform, the laser controllers, the control system, and the power supply will be put together in a rack (60 inches tall  $\times$  25 inches wide  $\times$  36 inches deep), shown in (c).

# Bibliography

- [1] J. V. Dongen, *Study of background gas collisions in atomic traps*. PhD thesis, University of British Columbia, Jun 2014.
- [2] J. L. Booth, P. Shen, R. V. Krems, and K. W. Madison, “Universality of quantum diffractive collisions and the quantum pressure standard,” *New Journal of Physics*, vol. 21, p. 102001, Oct 2019.
- [3] P. Shen, K. W. Madison, and J. L. Booth, “Realization of a universal quantum pressure standard,” *Metrologia*, vol. 57, p. 025015, Mar 2020.
- [4] P. Shen, K. W. Madison, and J. L. Booth, “Refining the cold atom pressure standard,” *Metrologia*, vol. 58, p. 022101, Feb 2021.
- [5] Y. Shen, “Determination of the atom’s excited-state fraction in a magneto-optical trap.” Master thesis, The University of British Columbia, May 2018.
- [6] J. Scherschligt, J. A. Fedchak, D. S. Barker, S. Eckel, N. Klimov, C. Makrides, and E. Tiesinga, “Development of a new UHV/XHV pressure standard (cold atom vacuum standard),” *Metrologia*, vol. 54, pp. S125–S132, Nov 2017.
- [7] MKS Instrument Inc, *Granville-Phillips Series 370 Stabil-Ion Vacuum Measurement Controller User Manual*, Sep 2014.
- [8] R. Grinham and A. Chew, “Gas correction factors for vacuum pressure gauges,” *Vakuum in Forschung und Praxis*, Apr 2017.
- [9] A. Derevianko, S. G. Porsev, and J. F. Babb, “Electric dipole polarizabilities at imaginary frequencies for hydrogen, the alkali–metal, alkaline–earth, and noble gas atoms,” *Atomic Data and Nuclear Data Tables*, vol. 96, pp. 323 – 331, May 2010.

- [10] S. Bali, K. M. O'Hara, M. E. Gehm, S. R. Granade, and J. E. Thomas, "Quantum-diffractive background gas collisions in atom-trap heating and loss," *Phys. Rev. A*, vol. 60, pp. R29–R32, Jul 1999.
- [11] T. Arpornthip, C. A. Sackett, and K. J. Hughes, "Vacuum-pressure measurement using a magneto-optical trap," *Phys. Rev. A*, vol. 85, p. 033420, Mar 2012.
- [12] A. A. Medvedev, V. V. Meshkov, A. V. Stolyarov, and M. C. Heaven, "Ab initio interatomic potentials and transport properties of alkali metal (M = Rb and Cs)–rare gas (Rg = He, Ne, Ar, Kr, and Xe) media," *Phys. Chem. Chem. Phys.*, vol. 20, pp. 25974–25982, Jul 2018.
- [13] C. Makrides, D. S. Barker, J. A. Fedchak, J. Scherschligt, S. Eckel, and E. Tiesinga, "Collisions of room-temperature helium with ultracold lithium and the van der waals bound state of HeLi," *Phys. Rev. A*, vol. 101, p. 012702, Jan 2020.
- [14] M. Child, *Molecular Collision Theory*. Dover Books on Chemistry Series, Dover Publications, 1996.
- [15] W. Middleton, *The History of the Barometer*. Johns Hopkins University Press, Jan 1964.
- [16] T. Bock, H. Ahrendt, and K. Jousten, "Reduction of the uncertainty of the PTB vacuum pressure scale by a new large area non-rotating piston gauge," *Metrologia*, vol. 46, pp. 389–396, Jun 2009.
- [17] C. G. Rendle and H. Rosenberg, "New absolute pressure standard in the range 1 pa to 7 kPa," *Metrologia*, vol. 36, pp. 613–615, Dec 1999.
- [18] K. Jousten, "Gauges for fine and high vacuum," *CAS 2006 - CERN Accelerator School: Vacuum in Accelerators, Proceedings*, Jan 2007.
- [19] J. Ricker, J. Hendricks, T. Bock, k Dominik, T. Kobata, J. Torres, and I. Sadkovskaya, "Final report on the key comparison CCM.p-k4.2012 in absolute pressure from 1 pa to 10 kPa," *Metrologia*, vol. 54, pp. 07002–07002, dec 2016.

- [20] K. F. Poulter, “The calibration of vacuum gauges,” *Journal of Physics E: Scientific Instruments*, vol. 10, pp. 112–125, Feb 1977.
- [21] D. Li, M. Guo, Y. Cheng, Y. Feng, and D. Zhang, “Vacuum-calibration apparatus with pressure down to  $10^{-10}$  pa,” *Journal of Vacuum Science & Technology A*, vol. 28, pp. 1099–1104, Jun 2010.
- [22] E. Echmaeva and E. Osadchii, “Determination of the thermodynamic properties of compounds in the Ag – Au – Se and Ag – Au – Te systems by the emf method,” *Geology of Ore Deposits*, vol. 51, pp. 247–258, Jun 2009.
- [23] J. A. Fedchak and D. R. Defibaugh, “Accurate conductance measurements of a pinhole orifice using a constant-pressure flowmeter,” *Measurement*, vol. 45, no. 10, pp. 2449–2451, 2012. Special Volume.
- [24] K. Jousten, “Traceability to si units for vacuum measurement in industrial applications,” *Measurement*, vol. 45, pp. 2420 – 2425, Dec 2012.
- [25] P. Szwemin, “How to characterize gas in high vacuum?,” *Vacuum*, vol. 82, pp. 174–177, Oct 2007. Proceedings of the 11th Joint Vacuum Conference (JVC-11).
- [26] M. Stock, R. Davis, E. de Mirandés, and M. J. T. Milton, “The revision of the SI—the result of three decades of progress in metrology,” *Metrologia*, vol. 56, p. 022001, Feb 2019.
- [27] D. B. Newell, F. Cabiati, J. Fischer, K. Fujii, S. G. Karshenboim, H. S. Margolis, E. de Mirandés, P. J. Mohr, F. Nez, K. Pachucki, T. J. Quinn, B. N. Taylor, M. Wang, B. M. Wood, and Z. Zhang, “The CODATA 2017 values of  $h$ ,  $e$ ,  $k$ , and  $n_a$  for the revision of the SI,” *Metrologia*, vol. 55, pp. L13–L16, Jan 2018.
- [28] A. Possolo, S. Schlamming, S. Stoudt, J. R. Pratt, and C. J. Williams, “Evaluation of the accuracy, consistency, and stability of measurements of the planck constant used in the redefinition of the international system of units,” *Metrologia*, vol. 55, pp. 29–37, Dec 2017.
- [29] J. Fischer, “Progress towards a new definition of the kelvin,” *Metrologia*, vol. 52, pp. S364–S375, Aug 2015.

- [30] D. White and J. Fischer, “The boltzmann constant and the new kelvin,” *Metrologia*, vol. 52, pp. S213–S216, Oct 2015.
- [31] M. BORN and E. WOLF, “Chapter ii - electromagnetic potentials and polarization,” in *Principles of Optics (Sixth Edition)* (M. Born and E. Wolf, eds.), pp. 71–108, Pergamon, sixth edition ed., 1980.
- [32] I. Silander, M. Zelan, O. Axner, F. Arrhén, L. Pendrill, and A. Foltynowicz, “Optical measurement of the gas number density in a fabry–perot cavity,” *Measurement Science and Technology*, vol. 24, p. 105207, Sep 2013.
- [33] P. Egan and J. A. Stone, “Absolute refractometry of dry gas to 3 parts in 10<sup>9</sup>,” *Appl. Opt.*, vol. 50, pp. 3076–3086, Jul 2011.
- [34] P. F. Egan, J. A. Stone, J. H. Hendricks, J. E. Ricker, G. E. Scace, and G. F. Strouse, “Performance of a dual Fabry-Perot cavity refractometer,” *Opt. Lett.*, vol. 40, pp. 3945–3948, Sep 2015.
- [35] J. Ricker, J. Hendricks, P. Egan, J. Stone, K. Douglass, and G. Scace, “Towards photonic based pascal realization as a primary pressure standard,” *Journal of Physics: Conference Series*, vol. 1065, p. 162018, Aug 2018.
- [36] J. Stone, P. Egan, D. Gerty, J. Hendricks, D. Olson, J. Ricker, G. Scace, and G. Strouse, “Picometer metrology for precise measurement of refractive index, pressure, and temperature,” *NCSLI Measure*, vol. 8, no. 4, pp. 67–73, 2013.
- [37] J. A. Nwaboh, O. Werhahn, P. Ortwein, D. Schiel, and V. Ebert, “Laser-spectrometric gas analysis: CO<sub>2</sub>-TDLAS at 2  $\mu\text{m}$ ,” *Measurement Science and Technology*, vol. 24, p. 015202, Dec 2012.
- [38] A. O’Keefe and D. A. G. Deacon, “Cavity ring-down optical spectrometer for absorption measurements using pulsed laser sources,” *Review of Scientific Instruments*, vol. 59, pp. 2544–2551, Jul 1988.
- [39] G. Casa, A. Castrillo, G. Galzerano, R. Wehr, A. Merlone, D. Di Serafino, P. Laporta, and L. Gianfrani, “Primary gas thermometry by means of laser-absorption spectroscopy: Determination of the boltzmann constant,” *Phys. Rev. Lett.*, vol. 100, p. 200801, May 2008.

- [40] G. Giusfredi, S. Bartalini, S. Borri, P. Cancio, I. Galli, D. Mazzotti, and P. De Natale, “Saturated-absorption cavity ring-down spectroscopy,” *Phys. Rev. Lett.*, vol. 104, p. 110801, Mar 2010.
- [41] A. Roy, H. C. P. Movva, B. Satpati, K. Kim, R. Dey, A. Rai, T. Pramanik, S. Guchhait, E. Tutuc, and S. K. Banerjee, “Structural and electrical properties of mote2 and mose2 grown by molecular beam epitaxy,” *ACS Applied Materials & Interfaces*, vol. 8, pp. 7396–7402, Mar 2016.
- [42] A. Koma, “Van der waals epitaxy—a new epitaxial growth method for a highly lattice-mismatched system,” *Thin Solid Films*, vol. 216, pp. 72 – 76, Aug 1992. Papers presented at the International Workshop on Science and Technology of Thin Films for the 21st Century, Evanston,IL, USA, July 28-August 2, 1991.
- [43] B. J. May, E. C. Hettiaratchy, and R. C. Myers, “Controlled nucleation of monolayer MoSe<sub>2</sub> islands on Si (111) by MBE,” *Journal of Vacuum Science & Technology B*, vol. 37, p. 021211, Mar 2019.
- [44] G. W. Pröls, “Density perturbations in the upper atmosphere caused by the dissipation of solar wind energy,” *Surveys in Geophysics*, vol. 32, pp. 101–195, Mar 2011.
- [45] C. Pardini, L. Anselmo, K. Moe, and M. Moe, “Drag and energy accommodation coefficients during sunspot maximum,” *Advances in Space Research*, vol. 45, pp. 638 – 650, Mar 2010.
- [46] C. J. Rice, V. L. Carter, S. R. LaValle, W. T. CHater, D. A. Jones, C. G. King, and D. F. Nelson, “Atmosphere explorer pressure measurements: Ion gauge and capacitance manometer,” *Radio Science*, vol. 8, pp. 305–314, April 1973.
- [47] A. L. Migdall, J. V. Prodan, W. D. Phillips, T. H. Bergeman, and H. J. Metcalf, “First observation of magnetically trapped neutral atoms,” *Phys. Rev. Lett.*, vol. 54, pp. 2596–2599, Jun 1985.
- [48] J. E. Bjorkholm, “Collision-limited lifetimes of atom traps,” *Phys. Rev. A*, vol. 38, pp. 1599–1600, Aug 1988.

- [49] A. Cable, M. Prentiss, and N. P. Bigelow, “Observations of sodium atoms in a magnetic molasses trap loaded by a continuous uncooled source,” *Opt. Lett.*, vol. 15, pp. 507–509, May 1990.
- [50] C. R. Monroe, E. A. Cornell, C. A. Sackett, C. J. Myatt, and C. E. Wieman, “Measurement of cs-cs elastic scattering at  $t=30 \mu\text{k}$ ,” *Phys. Rev. Lett.*, vol. 70, pp. 414–417, Jan 1993.
- [51] K. J. Matherson, R. D. Glover, D. E. Laban, and R. T. Sang, “Measurement of low-energy total absolute atomic collision cross sections with the metastable  $^3p_2$  state of neon using a magneto-optical trap,” *Phys. Rev. A*, vol. 78, p. 042712, Oct 2008.
- [52] K. J. Matherson, R. D. Glover, D. E. Laban, and R. T. Sang, “Absolute metastable atom-atom collision cross section measurements using a magneto-optical trap,” *Review of Scientific Instruments*, vol. 78, p. 073102, Jul 2007.
- [53] A. M. Steane, M. Chowdhury, and C. J. Foot, “Radiation force in the magneto-optical trap,” *J. Opt. Soc. Am. B*, vol. 9, pp. 2142–2158, Dec 1992.
- [54] S. D. Gensemer, V. Sanchez-Villicana, K. Y. N. Tan, T. T. Grove, and P. L. Gould, “Trap-loss collisions of  $^{85}\text{Rb}$  and  $^{87}\text{Rb}$  : dependence on trap parameters,” *Phys. Rev. A*, vol. 56, pp. 4055–4063, Nov 1997.
- [55] H. C. W. Beijerinck, “Heating rates in collisionally opaque alkali-metal atom traps: Role of secondary collisions,” *Phys. Rev. A*, vol. 62, p. 063614, Nov 2000.
- [56] H. C. W. Beijerinck, “Rigorous calculation of heating in alkali-metal traps by background gas collisions,” *Phys. Rev. A*, vol. 61, p. 033606, Feb 2000.
- [57] D. E. Fagnan, J. Wang, C. Zhu, P. Djuricanin, B. G. Klappauf, J. L. Booth, and K. W. Madison, “Observation of quantum diffractive collisions using shallow atomic traps,” *Phys. Rev. A*, vol. 80, p. 022712, Aug 2009.
- [58] J. Booth, D. E. Fagnan, B. G. Klappauf, K. W. Madison, and J. Wang, “Method and device for accurately measuring the incident flux of ambient particles in a high or ultra-high vacuum environment,” 2011. US Patent 8,803,072.

- [59] J. Hendricks, Z. Ahmed, D. Barker, P. Egan, K. Douglass, S. Eckel, J. Fedchak, N. Klimov, J. Ricker, J. Scherschligt, and J. Stone, “The emerging field of quantum based measurements for pressure, vacuum and beyond,” *Journal of Physics: Conference Series*, vol. 1065, p. 162017, Aug 2018.
- [60] S. Eckel, D. S. Barker, J. A. Fedchak, N. N. Klimov, E. Norrgard, J. Scherschligt, C. Makrides, and E. Tiesinga, “Challenges to miniaturizing cold atom technology for deployable vacuum metrology,” *Metrologia*, vol. 55, pp. S182–S193, Sep 2018.
- [61] C. Makrides, D. S. Barker, J. A. Fedchak, J. Scherschligt, S. Eckel, and E. Tiesinga, “Elastic rate coefficients for  $\text{Li} + \text{H}_2$  collisions in the calibration of a cold-atom vacuum standard,” *Phys. Rev. A*, vol. 99, p. 042704, Apr 2019.
- [62] L. D. Landau and E. M. Lifshitz, *Quantum Mechanics (Non-relativistic Theory)*. Elsevier Ltd., 1977.
- [63] V. B. Makhalov, K. A. Martiyanov, and A. V. Turlapov, “Primary vacuumeter based on an ultracold gas in a shallow optical dipole trap,” *Metrologia*, vol. 53, pp. 1287–1294, Nov 2016.
- [64] V. B. Makhalov and A. V. Turlapov, “A vacuum gauge based on an ultracold gas,” *Quantum Electronics*, vol. 47, pp. 431–437, may 2017.
- [65] T. A. Savard, K. M. O’Hara, and J. E. Thomas, “Laser-noise-induced heating in far-off resonance optical traps,” *Phys. Rev. A*, vol. 56, pp. R1095–R1098, Aug 1997.
- [66] M. Haw, N. Evetts, W. Gunton, J. V. Dongen, J. L. Booth, and K. W. Madison, “Magneto-optical trap loading rate dependence on trap depth and vapor density,” *J. Opt. Soc. Am. B*, vol. 29, pp. 475–483, Mar 2012.
- [67] J.-P. Yuan, Z.-H. Ji, Y.-T. Zhao, X.-F. Chang, L.-T. Xiao, and S.-T. Jia, “Simple, reliable, and nondestructive method for the measurement of vacuum pressure without specialized equipment,” *Appl. Opt.*, vol. 52, pp. 6195–6200, Sep 2013.
- [68] R. W. G. Moore, L. A. Lee, E. A. Findlay, L. Torralbo-Campo, G. D. Bruce, and D. Cassettari, “Measurement of vacuum pressure with a magneto-optical trap: A

- pressure-rise method,” *Review of Scientific Instruments*, vol. 86, p. 093108, Sep 2015.
- [69] J. feng Xiang, H. nan Cheng, X. kai Peng, X. wen Wang, W. Ren, J. wei Ji, K. kang Liu, J. bo Zhao, L. Li, Q. zhi Qu, T. Li, B. Wang, M. feng Ye, X. Zhao, Y. yuan Yao, D.-S. Lü, and L. Liu, “Loss of cold atoms due to collisions with residual gases in free flight and in a magneto-optical trap,” *Chinese Physics B*, vol. 27, p. 073701, Jul 2018.
- [70] M. Prentiss, A. Cable, J. E. Bjorkholm, S. Chu, E. L. Raab, and D. E. Pritchard, “Atomic-density-dependent losses in an optical trap,” *Opt. Lett.*, vol. 13, pp. 452–454, Jun 1988.
- [71] D. Hoffmann, S. Bali, and T. Walker, “Trap-depth measurements using ultracold collisions,” *Phys. Rev. A*, vol. 54, pp. R1030–R1033, Aug 1996.
- [72] J. Van Dongen, C. Zhu, D. Clement, G. Dufour, J. L. Booth, and K. W. Madison, “Trap-depth determination from residual gas collisions,” *Phys. Rev. A*, vol. 84, p. 022708, Aug 2011.
- [73] M. H. Shah, H. A. Camp, M. L. Trachy, G. Veshapidze, M. A. Gearba, and B. D. DePaola, “Model-independent measurement of the excited fraction in a magneto-optical trap,” *Phys. Rev. A*, vol. 75, p. 053418, May 2007.
- [74] J. M. Kwolek, D. S. Goodman, S. A. Entner, J. E. Wells, F. A. Narducci, and W. W. Smith, “Model-independent measurements of the sodium magneto-optical trap’s excited-state population,” *Phys. Rev. A*, vol. 97, p. 053420, May 2018.
- [75] K. Jooya, N. Musterer, K. W. Madison, and J. L. Booth, “Photon-scattering-rate measurement of atoms in a magneto-optical trap,” *Phys. Rev. A*, vol. 88, p. 063401, Dec 2013.
- [76] G. Veshapidze, J.-Y. Bang, C. W. Fehrenbach, H. Nguyen, and B. D. DePaola, “Model-free measurement of the excited-state fraction in a  $^{85}\text{Rb}$  magneto-optical trap,” *Phys. Rev. A*, vol. 91, p. 053423, May 2015.

- [77] A. V. Durrant and J. Manners, “Collision cross sections for the noble-gas broadening of the cs 6s-7p doublet using photon echoes,” *Journal of Physics B: Atomic and Molecular Physics*, vol. 17, pp. L701–L706, Nov 1984.
- [78] A. Kumarakrishnan, U. Shim, S. B. Cahn, and T. Sleator, “Ground-state grating echoes from rb vapor at room temperature,” *Phys. Rev. A*, vol. 58, pp. 3868–3872, Nov 1998.
- [79] A. Kumarakrishnan, S. B. Cahn, U. Shim, and T. Sleator, “Magnetic grating echoes from laser-cooled atoms,” *Phys. Rev. A*, vol. 58, pp. R3387–R3390, Nov 1998.
- [80] A. Pouliot, G. Carlse, H. C. Beica, T. Vacheresse, A. Kumarakrishnan, U. Shim, S. B. Cahn, A. Turlapov, and T. Sleator, “Accurate determination of an alkali-vapor–inert-gas diffusion coefficient using coherent transient emission from a density grating,” *Phys. Rev. A*, vol. 103, p. 023112, Feb 2021.
- [81] P. R. Berman, T. W. Mossberg, and S. R. Hartmann, “Collision kernels and laser spectroscopy,” *Phys. Rev. A*, vol. 25, pp. 2550–2571, May 1982.
- [82] B. Dubetsky, P. R. Berman, and T. Sleator, “Grating stimulated echo,” *Phys. Rev. A*, vol. 46, pp. R2213–R2216, Sep 1992.
- [83] D. Barker, E. Norrgard, N. Klimov, J. Fedchak, J. Scherschligt, and S. Eckel, “Single-beam zeeman slower and magneto-optical trap using a nanofabricated grating,” *Phys. Rev. Applied*, vol. 11, p. 064023, Jun 2019.
- [84] A. Sitaram, P. K. Elgee, G. K. Campbell, N. N. Klimov, S. Eckel, and D. S. Barker, “Confinement of an alkaline-earth element in a grating magneto-optical trap,” *Review of Scientific Instruments*, vol. 91, p. 103202, Oct 2020.
- [85] W. R. McGehee, W. Zhu, D. S. Barker, D. Westly, A. Yulaev, N. Klimov, A. Agrawal, S. Eckel, V. Aksyuk, and J. J. McClelland, “Magneto-optical trapping using planar optics,” *New Journal of Physics*, vol. 23, p. 013021, Jan 2021.
- [86] J. Taylor, *Scattering Theory: The Quantum Theory of Nonrelativistic Collisions*. Dover Books on Engineering, Dover Publications, May 2006.

- [87] B. Johnson, “The multichannel log-derivative method for scattering calculations,” *Journal of Computational Physics*, vol. 13, no. 3, pp. 445–449, 1973.
- [88] I. Bloch, “Quantum gases,” *Science*, vol. 319, pp. 1202–1203, Feb 2008.
- [89] K. W. Madison, Y. Wang, A. M. Rey, and K. Bongs, *Annual Review of Cold Atoms and Molecules*. WORLD SCIENTIFIC, Feb 2013.
- [90] R. Clausius, “Ueber die bewegende Kraft der Wärme und die Gesetze, welche sich daraus für die Wärmelehre selbst ableiten lassen,” *Annalen der Physik*, vol. 155, pp. 500–524, Jan. 1850.
- [91] C. B. Alcock, V. P. Itkin, and M. K. Horrigan, “Vapour pressure equations for the metallic elements: 298-2500k,” *Canadian Metallurgical Quarterly*, vol. 23, pp. 309–313, Jul 1984.
- [92] D. Lide, *CRC Handbook of Chemistry and Physics, 85th Edition*. No. v. 85 in CRC Handbook of Chemistry and Physics, 85th Ed, Taylor & Francis, Jun 2004.
- [93] H. Metcalf, P. Van der Straten, J. Birman, J. Lynn, H. Stanley, M. Silverman, and M. Voloshin, *Laser Cooling and Trapping*. Graduate texts in contemporary physics, Springer-Verlag New York, 1999.
- [94] C. Foot, C. Foot, and D. Foot, *Atomic Physics*. Oxford Master Series in Physics, Oxford University Press, Feb 2005.
- [95] A. Corney, *Atomic and Laser Spectroscopy*. Oxford science publications, Clarendon Press, 1979.
- [96] G. Breit and I. I. Rabi, “Measurement of nuclear spin,” *Phys. Rev.*, vol. 38, pp. 2082–2083, Dec 1931.
- [97] W. Raith and T. Mulvey, *Constituents of Matter: Atoms, Molecules, Nuclei, and Particles*. De Gruyter Experimental Physics, Taylor & Francis, 2001.
- [98] P. Eugster and A. Keshet, “Unbelievable: The story of a laser.” NSERC USRA project, Aug 2005.

- [99] E. Bakke, P. Chen, and P. Djuricanin, “Frequency locking system for grating-stabilized diode lasers report.” APSC 459 Project, April 2007.
- [100] A. J. Wallard, “Frequency stabilization of the helium-neon laser by saturated absorption in iodine vapour,” *Journal of Physics E: Scientific Instruments*, vol. 5, pp. 926–930, Sep 1972.
- [101] D. W. Preston, “Doppler-free saturated absorption: Laser spectroscopy,” *American Journal of Physics*, vol. 64, pp. 1432–1436, Jul 1996.
- [102] J. E. Debs, N. P. Robins, A. Lance, M. B. Kruger, and J. D. Close, “Piezo-locking a diode laser with saturated absorption spectroscopy,” *Appl. Opt.*, vol. 47, pp. 5163–5166, Oct 2008.
- [103] R. Drever, J. Hall, F. Kowalski, J. Hough, G. Ford, A. Munley, and H. Ward, “Laser phase and frequency stabilization using an optical resonator,” *Appl. Phys. B*, vol. 31, pp. 97–105, Jun 1983.
- [104] P. Shen, “High-finesse cavity laser locking.” Master thesis, Northwestern University, Aug 2016.
- [105] E. D. Black, “An introduction to pound–drever–hall laser frequency stabilization,” *American Journal of Physics*, vol. 69, pp. 79–87, Dec 2001.
- [106] C. Buczek, R. Freiberg, and M. Skolnick, “Laser injection locking,” *Proceedings of the IEEE*, vol. 61, pp. 1411–1431, Oct 1973.
- [107] J.-P. Bouyer, C. Breant, and P. Schanne, “Injection-locking mechanisms in semiconductor lasers,” in *Frequency-Stabilized Lasers and Their Applications* (Y. C. Chung, ed.), vol. 1837, pp. 324 – 335, International Society for Optics and Photonics, SPIE, Apr 1993.
- [108] E. A. Donley, T. P. Heavner, F. Levi, M. O. Tataw, and S. R. Jefferts, “Double-pass acousto-optic modulator system,” *Review of Scientific Instruments*, vol. 76, p. 063112, Jun 2005.
- [109] D. EDVARDSSON, S. LUNELL, and C. M. MARIAN, “Calculation of potential

- energy curves for rb2 including relativistic effects,” *Molecular Physics*, vol. 101, no. 15, pp. 2381–2389, 2003.
- [110] R. Grimm, M. Weidemüller, and Y. B. Ovchinnikov, “Optical dipole traps for neutral atoms,” in *Advances In Atomic, Molecular, and Optical Physics* (B. Bederson and H. Walther, eds.), vol. 42 of *Advances In Atomic, Molecular, and Optical Physics*, pp. 95–170, Academic Press, 2000.
- [111] B. M. Garraway and V. G. Minogin, “Theory of an optical dipole trap for cold atoms,” *Phys. Rev. A*, vol. 62, p. 043406, Sep 2000.
- [112] D. E. Pritchard, “Cooling neutral atoms in a magnetic trap for precision spectroscopy,” *Phys. Rev. Lett.*, vol. 51, pp. 1336–1339, Oct 1983.
- [113] M. H. Anderson, J. R. Ensher, M. R. Matthews, C. E. Wieman, and E. A. Cornell, “Observation of bose-einstein condensation in a dilute atomic vapor,” *Science*, vol. 269, pp. 198–201, Jul 1995.
- [114] S.-S. Hong, Y.-H. Shin, and I. Arakawa, “Investigation of gas species in a stainless steel ultrahigh vacuum chamber with hot cathode ionization gauges,” *Measurement Science and Technology*, vol. 15, p. 359, Dec 2004.
- [115] S. J. Yu, “The study of field programmable gate array based servos in atomic, molecular and optical physics experiments.” Master thesis, University of British Columbia, 2017.
- [116] U. Kleinekathöfer, M. Lewerenz, and M. Mladenović, “Long range binding in alkali-helium pairs,” *Phys. Rev. Lett.*, vol. 83, pp. 4717–4720, Dec 1999.
- [117] A. J. Thakkar, H. Hettema, and P. E. S. Wormer, “Ab initio dispersion coefficients for interactions involving rare-gas atoms,” *The Journal of Chemical Physics*, vol. 97, pp. 3252–3257, May 1992.
- [118] H.-J. Werner, P. J. Knowles, G. Knizia, F. R. Manby, and M. Schütz, “Molpro: a general-purpose quantum chemistry program package,” *WIREs Computational Molecular Science*, vol. 2, pp. 242–253, Jul 2012.

- [119] D. Eichenauer, U. Harten, J. P. Toennies, and V. Celli, “Interaction potential for one-phonon inelastic he–cu(111) and he–ag(111) scattering,” *The Journal of Chemical Physics*, vol. 86, pp. 3693–3710, Aug 1987.
- [120] D. Cvetko, A. Lausi, A. Morgante, F. Tommasini, P. Cortona, and M. G. Doni, “A new model for atom–atom potentials,” *The Journal of Chemical Physics*, vol. 100, pp. 2052–2057, Sep 1993.
- [121] R. A. Aziz, “A highly accurate interatomic potential for argon,” *The Journal of Chemical Physics*, vol. 99, pp. 4518–4525, Aug 1993.
- [122] A. M. Arthurs, A. Dalgarno, and D. R. Bates, “The theory of scattering by a rigid rotator,” *Proceedings of the Royal Society of London. Series A. Mathematical and Physical Sciences*, vol. 256, pp. 540–551, Jul 1960.
- [123] R. V. Krems, “Molecular collisions in external fields,” in *Molecules in Electromagnetic Fields*, ch. 8, pp. 187–216, John Wiley Sons, Ltd, Jun 2018.
- [124] C. G. Townsend, N. H. Edwards, C. J. Cooper, K. P. Zetie, C. J. Foot, A. M. Steane, P. Szriftgiser, H. Perrin, and J. Dalibard, “Phase-space density in the magneto-optical trap,” *Phys. Rev. A*, vol. 52, pp. 1423–1440, Aug 1995.
- [125] C. V. Sukumar and D. M. Brink, “Spin-flip transitions in a magnetic trap,” *Phys. Rev. A*, vol. 56, pp. 2451–2454, Sep 1997.
- [126] W. Ketterle and N. V. Druten, “Evaporative cooling of trapped atoms,” in *Advances In Atomic, Molecular, and Optical Physics* (B. Bederson and H. Walther, eds.), vol. 37, pp. 181–236, Academic Press, 1996.
- [127] J. M. Gerton, C. A. Sackett, B. J. Frew, and R. G. Hulet, “Dipolar relaxation collisions in magnetically trapped  ${}^7\text{Li}$ ,” *Phys. Rev. A*, vol. 59, pp. 1514–1516, Feb 1999.
- [128] Y.-J. Lin, A. R. Perry, R. L. Compton, I. B. Spielman, and J. V. Porto, “Rapid production of  ${}^{87}\text{Rb}$  bose-einstein condensates in a combined magnetic and optical potential,” *Phys. Rev. A*, vol. 79, p. 063631, Jun 2009.

- [129] J. Bennett, S. Hughes, R. Elsey, and T. Parry, “Outgassing from stainless steel and the effects of the gauges,” *Vacuum*, vol. 73, no. 2, pp. 149 – 153, 2004. Proceedings of the European Vacuum Congress Berlin 2003, 23-26 June 2003, featuring the 8th European Vacuum Conference, 2nd Annual Conference of the German Vacuum Society.
- [130] J. A. Fedchak. private communication, 1 May 2012.
- [131] H. C. W. Beijerinck, “Heating rates in collisionally opaque alkali-metal atom traps: Role of secondary collisions,” *Phys. Rev. A*, vol. 62, p. 063614, Nov 2000.
- [132] D. M. Brink and C. V. Sukumar, “Majorana spin-flip transitions in a magnetic trap,” *Phys. Rev. A*, vol. 74, p. 035401, Sep 2006.
- [133] W. Petrich, M. H. Anderson, J. R. Ensher, and E. A. Cornell, “Stable, tightly confining magnetic trap for evaporative cooling of neutral atoms,” *Phys. Rev. Lett.*, vol. 74, pp. 3352–3355, Apr 1995.
- [134] E. A. Burt, R. W. Ghrist, C. J. Myatt, M. J. Holland, E. A. Cornell, and C. E. Wieman, “Coherence, correlations, and collisions: What one learns about bose-einstein condensates from their decay,” *Phys. Rev. Lett.*, vol. 79, pp. 337–340, Jul 1997.
- [135] D. Suchet, M. Rabinovic, T. Reimann, N. Kretschmar, F. Sievers, C. Salomon, J. Lau, O. Goulko, C. Lobo, and F. Chevy, “Analog simulation of weyl particles with cold atoms,” *Europhysics Letters*, vol. 114, p. 26005, Apr 2016.
- [136] A. E. Glassgold, “Spin exchange in collisions between atoms,” *Phys. Rev.*, vol. 132, pp. 2144–2154, Dec 1963.
- [137] W. Xiao, T. Wu, X. Peng, and H. Guo, “Atomic spin-exchange collisions in magnetic fields,” *Phys. Rev. A*, vol. 103, p. 043116, Apr 2021.
- [138] F. H. Mies, C. J. Williams, P. S. Julienne, and M. Krauss, “Estimating bounds on collisional relaxation rates of spin-polarized  $^{87}\text{Rb}$  atoms at ultracold temperatures,” *Journal of research of the National Institute of Standards and Technology*, vol. 101, pp. 521–535, Jul 1996.

- [139] J. Arlt, P. Bance, S. Hopkins, J. Martin, S. Webster, A. Wilson, K. Zetie, and C. J. Foot, “Suppression of collisional loss from a magnetic trap,” *Journal of Physics B: Atomic, Molecular and Optical Physics*, vol. 31, pp. L321–L327, Apr 1998.
- [140] J. A. Jones, P. Hodgkinson, A. L. Barker, and P. J. Hore, “Optimal sampling strategies for the measurement of spin-spin relaxation times,” *Journal of Magnetic Resonance, Series B*, vol. 113, pp. 25–34, Oct 1996.
- [141] J. Van Dongen, C. Zhu, D. Clement, G. Dufour, J. L. Booth, and K. W. Madison, “Trap-depth determination from residual gas collisions,” *Phys. Rev. A*, vol. 84, p. 022708, Aug 2011.
- [142] D. A. Steck, “Rubidium 87 d line data.” available online at <http://steck.us/alkalidata> (revision 2.1.5, 13 January 2015), Jan 2015.
- [143] E. O. Gebel, “Quantum standards in the international system of units (si).” Physics Colloquium at Columbia University in the City of New York, Sep 2005.
- [144] W. Nawrockt, “The New SI System of Units-The Quantum SI.” Springer International Publishing, Cham, Mar 2015.
- [145] D. A. Varshalovich, A. N. Moskalev, and V. K. Khersonskii, *Quantum Theory of Angular Momentum*. WORLD SCIENTIFIC, Oct 1988.

# Appendix A

## Motorized Iris Calibration

In this section, we present the calibration data of the motorized iris (MI). As introduced in section 6.2.2, we used the repump beam size to control the trap depth of the MOT. Therefore, we required that the repump beam size are reproducible and can be adjusted easily. Here, we used a motorized iris (8MID30-2.5-H) from Standa company, which can be controlled remotely through a PC. A picture of the MI is shown in figure A.1.



Figure A.1: A picture of the motorized iris. A one inch mirror is placed on the right to show a size comparison.

Before implementing this MI into the experiment, we calibrated the set diameter as a function of the set steps. To measure the set radius of the MI, we used the knife edge power measurement. A power of  $W_0 \approx 100$  mw parallel laser beam with a  $1/e$  waist 6.8 mm hit the center of the MI. We know with a beam centered on an aperture, the power

$W$  passing through a circle of radius  $r$  in the transverse plane at position  $z$  is,

$$\frac{W(r, z)}{W_0} = \left[ 1 - e^{-\frac{2r^2}{\omega^2(z)}} \right]. \quad (\text{A.1})$$

Here,  $\omega$  is the laser beam waist at the position  $z$ ,

$$\omega(z) = \omega_0 \sqrt{1 + (z/z_R)^2}, \quad (\text{A.2})$$

where  $z_R \approx 186$  m is the Rayleigh length of the laser beam. The power meter is 67 mm away from the MI, so  $z = 67$  mm.  $r$  in Eq.A.1 is the radius of the MI and can be expressed as,

$$r = \frac{(\text{steps}/\alpha + D_{\min})}{2.0}. \quad (\text{A.3})$$

Through measuring the power at the position,  $z = 67$  mm, as a function of the MI steps, one can extract the two unknown parameters,  $\alpha$ , the radius to step convert factor and  $D_{\min}$ , the minimum diameter of the MI. We repeated the calibrations for three times. Figure A.2 (a) shows the power measurement as a function of the steps and the converted radius versus the steps are shown in Figure A.2 (b). The uncertainty in setting the aperture radius is around 3%. Finally, three different calibration results are summarized in table A.1. We have also found the set radius are more reproducible if the steps of the MI are varied from large to small, which is due to the mechanical design.

Parameters	1	2	3	Factory
$\alpha$ (steps/mm)	80.7	81.8	79.7	75
$D_{rmin}$ (mm)	2.7	2.7	2.6	2.5

Table A.1: The calibration results of the MI at three different times. The last column shows the factory data.

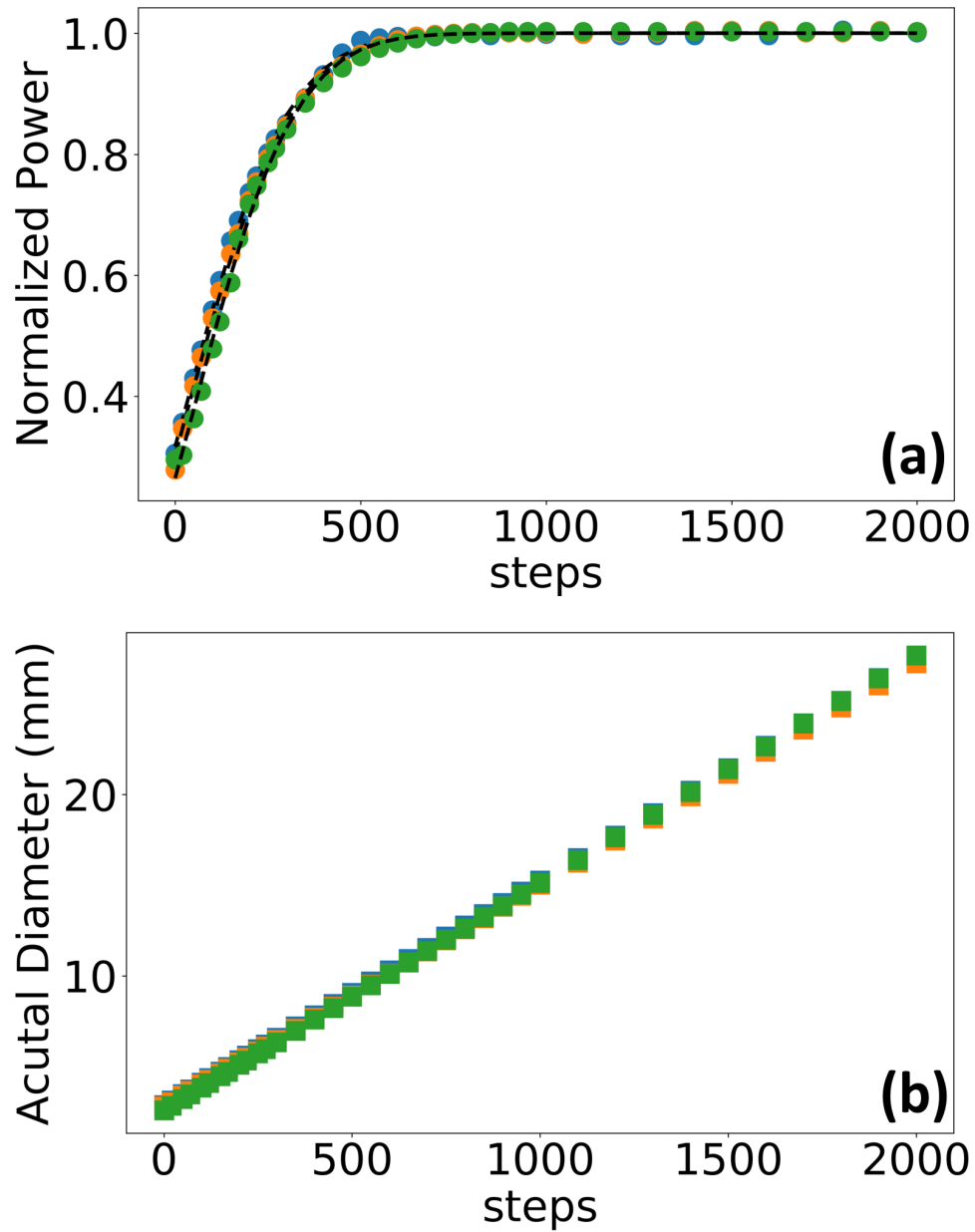


Figure A.2: Panel (a) shows the transmitted power as a function of the set steps of the MI. Different steps corresponding to different radius set by the MI. The measurements have been repeated three times (blue, green, and orange dots). The

## Appendix B

# Quantum Scattering Calculation

In this section, we provide the details of the quantum scattering calculations of the differential scattering cross sections, the total collision cross sections and  $\langle \sigma_{\text{loss}} v \rangle$ . The scattering event at a given collision energy is described by the  $T$ -matrix. We compute the  $T$ -matrices by solving the Schrödinger equation using the time-independent coupled channel (CC) approach and the total angular representation of Arthurs and Dalgarno [122]. The method is well described elsewhere [123]. Here, we only provide details pertinent to the calculations in the present work.

Within the CC approach, the Schrödinger equation is reduced to a set of coupled differential equations:

$$\left[ \frac{d^2}{dR^2} - k_\alpha^2 + \frac{l(l+1)}{R^2} \right] F_{\alpha,l;\alpha l}^J(R) = \sum_{\alpha'} \sum_{l'} U_{\alpha,l;\alpha' l'}^J F_{\alpha,l;\alpha' l'}^J(R), \quad (\text{B.1})$$

where  $R$  is the separation between the centers of mass of the colliding particles,  $k_\alpha$  represents the wave number of channel  $\alpha$ ,  $l$  is the orbital angular momentum for the rotation of the collision complex,  $J$  is the total angular momentum of the colliding particles and the matrix elements  $U_{\alpha,l;\alpha' l'}^J$  are parametrized by the interaction potential of the colliding particles. We integrate these equations by means of the log-derivative [87] and Numerov integration methods. Eq. B.1 are solved subject to the scattering boundary conditions and the elements  $T_{\alpha l, \alpha' l'}$  of the  $T$  matrix are extracted from the asymptotic solutions at large  $R$  [122, 123].

For atom - molecule scattering, we treat the molecule as a rigid rotor with rotational angular momentum  $j$ . In this case,  $\alpha = j$ . The differential scattering cross sections for elastic ( $j' = j$ ) and inelastic ( $j' \neq j$ ) collisions are computed from the  $T$ -matrix elements

as follows:

$$\frac{d\sigma_{j,j'}}{d\Omega} = \frac{(-1)^{j'-j}}{4(2j+1)k_j^2} \sum_{\lambda=0}^{\infty} A_{\lambda} P_{\lambda}(\cos \theta), \quad (\text{B.2})$$

where  $\theta$  is the scattering angle,  $P_{\lambda}$  is a Legendre polynomial of order  $\lambda$ , and the coefficients  $A_{\lambda}$  are given as

$$A_{\lambda} = \sum_{J_1}^{\infty} \sum_{J_2}^{\infty} \sum_{l_1=|J_1-j|}^{J_1+j} \sum_{l_2=|J_2-j|}^{J_2+j} \sum_{l'_1=|J_1-j'|}^{J_1+j'} \sum_{l'_2=|J_2-j'|}^{J_2+j'} Z(l_1 J_1 l_2 J_2; j \lambda) \times Z(l'_1 J_1 l'_2 J_2; j' \lambda) T_{j' l'_1; j l_1}^{J_1*} T_{j' l'_2; j l_2}^{J_2}, \quad (\text{B.3})$$

with

$$Z(abcd; ef) = (-1)^{\frac{1}{2}(f-a+c)} [(2a+1)(2b+1)(2c+1)(2d+1)]^{1/2} \langle a0, c0 | f0 \rangle W(abcd; ef), \quad (\text{B.4})$$

where  $\langle a0, c0 | f0 \rangle$  is the Clebsch-Gordan coefficient and  $W(abcd; ef)$  is the Racah W-coefficient [145].

The total cross section is computed from the differential cross sections by first integrating over the scattering angle and then summing over all final states of the collision products. To calculate the total collision rates, the energy dependence of the total collision cross sections is integrated over the Maxwell-Boltzmann distribution of collision velocities.

The potential energy surface (PES) for atom - rigid rotor interactions is a two dimensional function of  $R$  and the Jacobi angle  $\chi$  between the vector specifying the direction of the interatomic axis of the molecule and the vector joining the centers of mass of the colliding particles. We report calculations with three atom - molecule PESs. Our starting point is a PES that is represented as a Legendre expansion

$$V(R, \chi) = \sum_{s=0}^6 V_s(R) P_s(\cos \chi). \quad (\text{B.5})$$

The expansions coefficient  $V_{s>0}$  describe the anisotropy of the interaction potential giving rise to inelastic scattering, while the coefficient  $V_{s=0}$  is primarily responsible for

elastic scattering. Each of the coefficients  $V_s$  is represented by the proper (as permitted by symmetry) long-range expansion

$$V_s(R \rightarrow \infty) = \sum_n \frac{C_{n,s}}{R^n} \quad (\text{B.6})$$

at large values of  $R$ . In particular, the isotropic term  $V_{s=0}$  is represented at long range as

$$V_s(R \rightarrow \infty) = -\frac{C_{6,0}}{R^6} - \frac{C_{8,0}}{R^8} - \frac{C_{10,0}}{R^{10}}, \quad (\text{B.7})$$

with  $C_{6,0}$  chosen to be 350 a.u. characteristic of the long-range interaction between Rb atoms and  $\text{N}_2$  molecules. These long-range forms are smoothly joined with a short-range repulsive interaction giving the global PES. The coefficients  $V_s$  for the starting PES are chosen to generate a global potential that has a minimum of  $\approx 235 \text{ cm}^{-1}$  at  $R = 7.86$  a.u. These parameters are characteristic of van der Waals interactions of closed-shell molecules with alkali metal atoms. We denote this potential surface as PES-I. A cut of this PES is shown by the black line in the inset of figure 4.2 (a) in the main text.

The other PESs (hereafter denoted as PES-II and PES-III) are generated from PES-I by multiplying each of the coefficients  $V_s$  by the following function:

$$f(R) = \frac{ae^{2R} + b}{ae^{2R}} \quad (\text{B.8})$$

with the coefficients  $a$  and  $b$  chosen such that  $f(R) = 1$  when  $R > 12$  a.u. for PES-II and when  $R > 14.2$  a.u. for PES-III. The cross sections of PES-II and PES-III are shown in the inset of FIG. 1(a) of the main text. At  $R = 5$  a.u., PES-II is magnified by a factor of 102.7 and PES-III by a factor of 10058.3.

For the atom - atom scattering calculations, we approximate the interaction potentials as

$$V(R) = 4\epsilon [(R_0/R)^{12} - (R_0/R)^6] = [C_{12}/R^{12} - C_6/R^6] \quad (\text{B.9})$$

where the values of the  $C_6$  coefficients have been chosen to represent the long-range interactions of the Rb-He, Rb-Ar, Rb-Xe, Li-He, Li-Ar, and Li-Xe systems. The values

of the  $C_6$  coefficients were borrowed from the literature [9]. The parameter  $C_{12}$  was chosen to ensure a particular value of the energy at the potential energy minimum, as described in the main text.

For atom - atom scattering calculations,  $j = 0$  and  $J = L$ . This reduces Eq. B.1 to a single differential equation and greatly simplifies Eq. B.2. Eq. B.2 with  $j' = j = 0$ ,  $J_1 = l_1 = l'_1$  and  $J_2 = l_2 = l'_2$  produces the differential scattering cross section  $\sigma(v, \theta)$  for given collision velocity  $v$  and scattering angle  $\theta$ . This cross section is used to compute the loss cross section  $\sigma_{\text{loss}}(k, U)$  for each trap depth,  $U$ . Since the trap loss condition is  $U \geq (1 - \cos \theta) \mu^2 v^2 / m_t$ ,  $\sigma_{\text{loss}}(k, U)$  can be expressed in terms of  $\theta$  as

$$\sigma_{\text{loss}}(k = \mu v / \hbar, U) = \int_{\theta_{\text{min}}}^{\pi} \sigma_{\text{loss}}(v, \theta) \sin \theta \, d\theta. \quad (\text{B.10})$$

This cross section is then integrated over the Maxwell-Boltzmann distribution of collision velocities, to yield

$$\langle \sigma_{\text{loss}}(U) v \rangle = \int_0^{\infty} 4\pi v^3 \cdot \sigma_{\text{loss}}(v, U) \cdot \rho(v) \, dv \quad (\text{B.11})$$

The rates  $\langle \sigma_{\text{loss}} v \rangle$  were computed over trap depths ranging from 0 mK to 15 mK. A data set of  $\langle \sigma_{\text{loss}} v \rangle / \langle \sigma_{\text{tot}} v \rangle$  versus  $U/U_d$  was constructed for each collision pair and all six data sets combined and fit to equation C.6 by a sixth order polynomial. The results are shown in the first line of Table 2 in the main text of the paper. Over the trap depths investigated in this work, the deviations between the full QS calculations and equation C.6 are less than 0.1%, well below the experimental uncertainty of  $\approx 1\%$ . Thus the systematic deviations produced by the differences in the interactions between different collision partners are small out to the trap depths investigated, supporting the claim that the expression in Eq. 4.10 of the main text universally describes the collision loss rate.

## Appendix C

# Analytical Derivation of the Universal Form

In this section, I will provide the derivations of the analytical predictions of the universal coefficients. Let's start with the Eq. 4.7. To perform these integrations with the phase shift, shown in Eq. 4.8, leads to,

$$\langle \sigma_{\text{loss}} v \rangle \approx \langle \sigma_{\text{tot}} v \rangle - \alpha_1 \left( \frac{m_1 U}{\hbar^2} \right) + \alpha_2 \left( \frac{m_1 U}{\hbar^2} \right)^2 + \dots \quad (\text{C.1})$$

where,

$$\alpha_1 = \frac{0.0554929 \langle \sigma_{\text{tot}} v \rangle^2}{v_p} [1 - \epsilon_1] = \gamma_1 \frac{\langle \sigma_{\text{tot}} v \rangle^2}{v_p} \quad (\text{C.2})$$

$$\alpha_2 = \frac{0.004315 \langle \sigma_{\text{tot}} v \rangle^3}{v_p^2} [1 - \epsilon_2] = \gamma_2 \frac{\langle \sigma_{\text{tot}} v \rangle^3}{v_p^2} \quad (\text{C.3})$$

Here,

$$\epsilon_1 = \left( \frac{\langle \sigma_{\text{tot}} v \rangle_0}{\langle \sigma_{\text{tot}} v \rangle} \right)^2 \left[ \frac{0.2158}{v_p^{\frac{4}{5}}} \left( \frac{\hbar}{\mu} \right) \left( \frac{\hbar}{C_6} \right)^{\frac{1}{5}} - \frac{0.02795}{v_p^{\frac{8}{5}}} \left( \frac{\hbar}{\mu} \right)^2 \left( \frac{\hbar}{C_6} \right)^{\frac{2}{5}} \right] \quad (\text{C.4})$$

and

$$\epsilon_2 = \left( \frac{\langle \sigma_{\text{tot}} v \rangle_0}{\langle \sigma_{\text{tot}} v \rangle} \right)^3 \left[ \frac{0.6827}{v_p^{\frac{4}{5}}} \left( \frac{\hbar}{\mu} \right) \left( \frac{\hbar}{C_6} \right)^{\frac{1}{5}} + \frac{0.3356}{v_p^{\frac{8}{5}}} \left( \frac{\hbar}{\mu} \right)^2 \left( \frac{\hbar}{C_6} \right)^{\frac{2}{5}} - \frac{0.7891}{v_p^{\frac{12}{5}}} \left( \frac{\hbar}{\mu} \right)^3 \left( \frac{\hbar}{C_6} \right)^{\frac{3}{5}} \right] \quad (\text{C.5})$$

Combining these equations illustrates the emergence of the quasi-universal behaviour,

$$\begin{aligned}
 \langle \sigma_{\text{loss}} v \rangle &= \langle \sigma_{\text{tot}} v \rangle \left[ 1 - 4\pi\gamma_1 \left( \frac{m_1 \langle \sigma_{\text{tot}} v \rangle / v_p}{4\pi\hbar^2} \right) U \right. \\
 &\quad \left. + (4\pi)^2 \gamma_2 \left( \frac{m_1 \langle \sigma_{\text{tot}} v \rangle / v_p}{4\pi\hbar^2} \right)^2 U^2 + \dots \right] \\
 &= \langle \sigma_{\text{tot}} v \rangle \left[ 1 - 4\pi\gamma_1 \left( \frac{U}{U_d} \right) + (4\pi)^2 \gamma_2 \left( \frac{U}{U_d} \right)^2 + \dots \right] \\
 &= \langle \sigma_{\text{tot}} v \rangle \left[ 1 - \beta_1 \left( \frac{U}{U_d} \right) + \beta_2 \left( \frac{U}{U_d} \right)^2 - \dots \right] \\
 &= \langle \sigma_{\text{tot}} v \rangle (1 - p_{\text{QDU6}}).
 \end{aligned} \tag{C.6}$$

In Eq. C.6, the quantum diffractive energy has been defined as [10],

$$U_d = \frac{4\pi\hbar^2}{m_1 \langle \sigma_{\text{tot}} v \rangle / v_p}. \tag{C.7}$$

The universality of the coefficients in Eq. C.6 is disrupted by the  $\epsilon_i$  terms, defined in Eqs. C.4 and C.5 for  $i = 1, 2$ . These terms introduce a dependence on the room-temperature collision partner through the most probable velocity,  $1/v_p^{n/5}$ , terms. For lighter collision partners, these become more significant. Further, there are  $(1/C_6)^{n/5} \times (1/\mu)^n$  terms which introduce some dependence on the trapped atom mass and the long-range van der Waals coefficient. For lower reduced masses and smaller  $C_6$  coefficients, these corrections are more significant.

The qualitative nature of these and previous analytical predictions is demonstrated by the values of the coefficients,  $\beta_j$ , that are predicted. Table C.1 compares the predictions from the full quantum scattering computations (used in our data analysis) to those derived from [14] and derived in this Appendix. It is clear that the lowest order approximations ([14]) are further from the full computational results than the values determined in this Appendix, which use the next order approximation for expanding the Legendre polynomials. It must be emphasized that these analytical calculations are only a qualitative guide to the expected behavior of the universal function,  $p_{\text{QDU6}}$ .

	$\beta_1$	$\beta_2$
Full Numerical Computation	0.673	-0.477
Ref. [14] Values	0.764	-0.791
This Appendix		
Rb-He	0.693 $\epsilon_1 = 0.00597$	-0.669 $\epsilon_2 = 0.0188$
Rb-Ar	0.696 $\epsilon_1 = 0.00145$	-0.679 $\epsilon_2 = 0.00460$
Rb-Xe	0.697 $\epsilon_1 = 0.00104$	-0.680 $\epsilon_2 = 0.00328$
Li-He	0.690 $\epsilon_1 = 0.0104$	-0.660 $\epsilon_2 = 0.0325$
Li-Ar	0.692 $\epsilon_1 = 0.00817$	-0.664 $\epsilon_2 = 0.0256$
Li-Xe	0.690 $\epsilon_1 = 0.0099$	-0.661 $\epsilon_2 = 0.0309$

Table C.1: The coefficients  $\beta_1$  and  $\beta_2$  from the full quantum scattering computations averaged over 6 species (see text), based on the analytical expression for the small angle scattering amplitude from Ref. [14] (which predicts that all collision partners will have the same coefficients), and based on the analytical expressions used in this Appendix. The variation arising from the different  $C_6$  and masses of the collision partners from this analysis is shown for the different species listed.

### Generalization to $V(R) = -C^n/R^n$ Long-Range Potentials

The above methods can be generalized to other forms of long range potential, in particular to  $V(R) = -C_n/R^n$  for  $n = 3, 4, 5$ , etc. To begin, one generalizes the approximate angular momentum dependent phase shift,

$$\begin{aligned}
 \delta_L^{(n)} &= \left( \frac{\mu C_n k^{n-2}}{\hbar^2 L^{n-1}} \right) \left( \frac{\sqrt{\pi} \Gamma(\frac{n-1}{2})}{2\Gamma(\frac{n}{2})} \right) \\
 &= \left( \frac{\mu C_n k^{n-2}}{\hbar^2 L^{n-1}} \right) \xi(n)
 \end{aligned} \tag{C.8}$$

Table C.2 provides the values for the  $\xi(n)$  function for various values of  $n$ .

The corresponding cross sections are,

$$\begin{aligned}
 \sigma(k, n) &= \frac{2\pi}{k^2} \left[ (2a(n))^{\frac{2}{n-1}} \cos\left(\frac{\pi}{n-1}\right) \Gamma\left(\frac{n-3}{n-1}\right) \right. \\
 &\quad \left. + (2a(n))^{\frac{1}{n-1}} \cos\left(\frac{\pi}{2(n-1)}\right) \Gamma\left(\frac{n-2}{n-1}\right) \right] \\
 &= 2\pi \left[ \left(2\xi(n) \frac{C_n}{\hbar v}\right)^{\frac{2}{n-1}} \cos\left(\frac{\pi}{n-1}\right) \Gamma\left(\frac{n-3}{n-1}\right) \right. \\
 &\quad \left. + \left(\frac{\hbar}{\mu v}\right) \left(2\xi(n) \frac{C_n}{\hbar v}\right)^{\frac{1}{n-1}} \cos\left(\frac{\pi}{2(n-1)}\right) \Gamma\left(\frac{n-2}{n-1}\right) \right] \\
 &= c(n) \left(\frac{C_n}{\hbar v}\right)^{\frac{2}{n-1}} + d(n) \left(\frac{\hbar}{\mu v}\right) \left(\frac{C_n}{\hbar v}\right)^{\frac{1}{n-1}}
 \end{aligned} \tag{C.9}$$

which are valid for  $n > 3$ . The expressions are listed below in Table C.2.

The velocity averaged total elastic collision cross sections are,

$$\begin{aligned}
 \langle \sigma_{\text{tot}}(n) v \rangle &= \frac{2}{\sqrt{\pi}} \left[ c(n) v_p^{\frac{n-3}{n-1}} \Gamma\left(\frac{2n-3}{n-1}\right) \left(\frac{C_n}{\hbar}\right)^{\frac{2}{n-1}} \right. \\
 &\quad \left. + d(n) \frac{1}{v_p^{\frac{1}{n-1}}} \left(\frac{\hbar}{\mu}\right) \Gamma\left(\frac{3n-4}{2(n-1)}\right) \left(\frac{C_n}{\hbar}\right)^{\frac{1}{n-1}} \right] \\
 &= \langle \sigma_{\text{tot}}(n) v \rangle_0 \left[ 1 + \frac{d(n)}{c(n)} \frac{1}{v_p^{\frac{n-2}{n-1}}} \frac{\Gamma\left(\frac{3n-4}{2(n-1)}\right)}{\Gamma\left(\frac{2n-3}{n-1}\right)} \left(\frac{\hbar}{\mu}\right) \left(\frac{\hbar}{C_n}\right)^{\frac{1}{n-1}} \right]
 \end{aligned} \tag{C.10}$$

with the expressions summarized in column 3 of Table C.2. One observes that for all forms  $V(R) = -C_n/R^n$ , the description for  $\langle \sigma_{\text{tot}}(n) v \rangle$  follows the format described above for  $n = 6$ . Similarly, the description for  $\langle \sigma_{\text{loss}} v \rangle$  provided in Equation C.6 also applies to these long range potentials, with unique values for the expansion coefficients,  $\beta_j^{(n)}$ .

n	3	4	5	6	8	10
$\xi(n)$	1	$\frac{\pi}{4}$	$\frac{2}{3}$	$\frac{3\pi}{16}$	$\frac{5\pi}{32}$	$\frac{35\pi}{256}$
$c(n)$	-	10.0823	8.8352	8.0828	7.1703	6.6126
$d(n)$	-	8.0648	7.5347	7.1889	6.7486	6.4693

Table C.2: The values of  $\xi(n)$ ,  $c(n)$ , and  $d(n)$  as a function of  $n$  for potentials of the form,  $V(R) = -C_n/R^n$ .

# Appendix D

## Scattering Angle

In this appendix, I will derive the relationship between the scattering angle and the transferred energy. In our two-body system, the trapped particle 1 has a mass,  $m_1$ , and the collision partner has a mass,  $m_2$  as illustrated in figure 1.3. Before the collision, the trapped atom and the collision partner have the velocity  $\vec{v}_1$  and velocity  $\vec{v}_2$  separately. After the collision, their velocities are changed to  $\vec{v}_1'$  and  $\vec{v}_2'$ . Now, if we consider the system in the center of the mass (COM) frame, we can define the pre-collision relative velocity as  $\vec{v}_r = \vec{v}_1 - \vec{v}_2$  and the post-collision relative velocity as  $\vec{v}_r' = \vec{v}_1' - \vec{v}_2'$ . Also, the coordinate of COM is defined as,

$$\vec{R} = \frac{m_1 \vec{r}_1 + m_2 \vec{r}_2}{M}, \quad (\text{D.1})$$

and the velocity of COM is,

$$\vec{v}_C = \frac{m_1 \vec{v}_1 + m_2 \vec{v}_2}{M}. \quad (\text{D.2})$$

Following Eq. D.2 and the expression of  $\vec{v}_r$ , we can write the velocities in the lab frame,  $\vec{v}_1$  and  $\vec{v}_2$  in terms of the quantities defined in COM,

$$\vec{v}_1 = \vec{v}_C + \frac{\mu}{m_1} \vec{v}_r \quad (\text{D.3})$$

$$\vec{v}_2 = \vec{v}_C - \frac{\mu}{m_2} \vec{v}_r. \quad (\text{D.4})$$

Here, we define  $\mu = \frac{m_1 m_2}{m_1 + m_2}$  as the reduced mass, and thus, the relative momentum can be expressed as  $\vec{p}_r = \mu \vec{v}_r$ . Due to the conservation of the momentum,  $\vec{p}_1 + \vec{p}_2 = \vec{p}_1' + \vec{p}_2'$ ,

we have

$$\begin{aligned} m_1\vec{v}_1 + m_2\vec{v}_2 &= m_1\vec{v}_1' + m_2\vec{v}_2' \\ M\vec{v}_C &= M\vec{v}_C'. \end{aligned} \quad (\text{D.5})$$

We can see that the velocity of COM is unchanged,  $\vec{v}_C = \vec{v}_C'$ . Based on Eq. D.5, we can also have  $\vec{p}_1 - \vec{p}_1' = \vec{p}_2' - \vec{p}_2$ .

Given only the elastic collisions are taken into account, the energy is also conserved so that we have  $|\vec{v}_r| = |\vec{v}_r'|$ . Based on the expression of the relative momentum, we can find that the change of the relative momentum equals to the change of the trapped atom's momentum and the change of the collision atom's momentum,

$$\vec{p}_r - \vec{p}_r' = \mu(\vec{v}_r - \vec{v}_r') \quad (\text{D.6})$$

$$= \frac{m_1 m_2}{m_1 + m_2} (\vec{v}_1 - \vec{v}_2 - \vec{v}_1' + \vec{v}_2') \quad (\text{D.7})$$

$$= \vec{p}_1 - \vec{p}_1' = \vec{p}_2' - \vec{p}_2. \quad (\text{D.8})$$

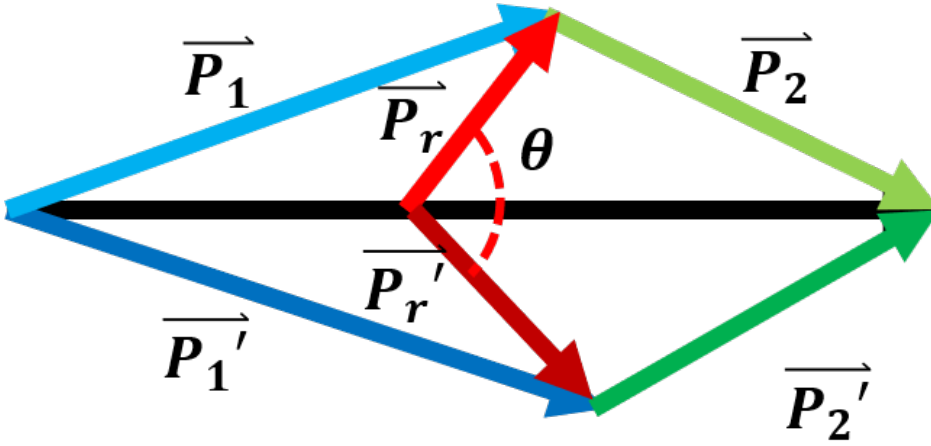


Figure D.1: Newton diagram

These equations allow us to draw the Newton diagram, as shown in figure D.1. Based

on the Newton diagram, we can further write Eq. D.8 into

$$\vec{p}_r - \vec{p}_r' = \vec{p}_1 - \vec{p}_1' \quad (\text{D.9})$$

$$\mu^2 |\vec{v}_r - \vec{v}_r'|^2 = m_1^2 |\vec{v}_1 - \vec{v}_1'|^2 \quad (\text{D.10})$$

$$2\mu^2 |\vec{v}_r|^2 (1 - \cos \theta) = m_1^2 |\vec{v}_1 - \vec{v}_1'|^2 \quad (\text{D.11})$$

$$1 - \cos \theta = \frac{m_1^2 |\vec{v}_1 - \vec{v}_1'|^2}{2\mu^2 |\vec{v}_r|^2}. \quad (\text{D.12})$$

If the initial velocity of the trapped atom is zero, then we can define the transfer energy to the trapped atom as,  $\Delta E = |\vec{v}_1'|^2/2m_1$ . Therefore, the relationship between the scattering angle and the transfer energy can be expressed as,

$$\cos \theta = 1 - \frac{m_1 \Delta E}{\mu^2 |\vec{v}_r|^2}. \quad (\text{D.13})$$